# A STUDY OF SYNCHRONOUS BURSTING IN THE PREBÖTZINGER COMPLEX

by

**Justin R. Dunmyre**

B.S. Computer Science, Pennsylvania State University, 2005

B.S. Mathematics, Pennsylvania State University, 2005

M.A. Mathematics, University of Pittsburgh, 2007

Submitted to the Graduate Faculty of

the Department of Mathematics in partial fulfillment

of the requirements for the degree of

**Doctor of Philosophy**

University of Pittsburgh

2011

UNIVERSITY OF PITTSBURGH

MATHEMATICS DEPARTMENT

This dissertation was presented

by

Justin R. Dunmyre

It was defended on

June 17th 2011

and approved by

Jonathan Rubin, Department of Mathematics

Bard Ermentrout, Department of Mathematics

Carson Chow, Department of Mathematics

Christopher Del Negro, Department of Applied Science, College of William and Mary

Dissertation Director: Jonathan Rubin, Department of Mathematics

# A STUDY OF SYNCHRONOUS BURSTING IN THE PREBÖTZINGER COMPLEX

Justin R. Dunmyre, PhD

University of Pittsburgh, 2011

The preBötzinger complex (preBötC) of the mammalian brainstem is a heterogeneous neuronal network underlying the inspiration phase of the respiratory rhythm. Through excitatory synapses and a nontrivial network architecture, a synchronous, network-wide bursting rhythm emerges. On the other hand, during synaptic isolation, preBötC neurons display three types of intrinsic dynamics: quiescence, bursting, or tonic activity. This work seeks to shed light on how the network rhythm emerges from the challenging architecture and heterogeneous population. Recent debate surrounding the role of intrinsically bursting neurons in the rhythmogenesis of the preBötC inspires us to evaluate its role in a three-cell network. We found no advantage for intrinsically bursting neurons in forming synchronous network bursting; instead, intrinsically quiescent neurons were identified as a key mechanism. This analysis involved only studying the persistent sodium (NaP) current. Another important current for the preBötC is the calcium-activated nonspecific cationic (CAN) current, which, when combined with a Na/K pump, was previously shown to be capable of producing bursts in coupled tonically active cells.

In the second part of this study, we explore the interactions of the NaP and CAN currents, both currents are ubiquitous in the preBötC. Using geometric singular perturbation theory and bifurcation analysis, we established the mechanisms through which reciprocally coupled pairs of neurons can generate various activity patterns. In particular, we highlighted how the NaP current could enhance the range of the strength of the CAN current for which bursts occur. We also were able to detail a novel bursting pattern seen in data, but not seen in

previous models.

With a foundation of understanding heterogeneity in the NaP and CAN currents, we again turned our attention to networks. For the third portion of the dissertation, we examine the effects that heterogeneity in the neuronal dynamics and coupling architecture can impose upon synchronous bursting of the entire network. We again found no significant advantage to including intrinsically bursting neurons in the network, and the best networks were characterized by an increased presence of quiescent neurons. We also described the way the NaP and CAN currents interact on the network scale to promote synchronous bursting.

## TABLE OF CONTENTS

## LIST OF TABLES

## LIST OF FIGURES

# PREFACE

This dissertation was supported by NSF awards EMSW21-RTG 0739261 and DMS-0716936, as well as NIH grants 1R01HL104127-01, 1R21NS070056-01. The content in Chapter 2 appeared as "Optimal intrinsic dynamics for bursting in a three-cell network" in the SIAM Journal on Applied Dynamical Systems- SIADS, vol. 9, no. 1, 2010, and has been modified for readability in this work. It is copyright to the Society for Industrial and Applied Mathematics, 2010. The content in Chapter 3 appeared in two separate publications, and have been modified only for readability. Portions appeared as "Interactions of persistent sodium and calcium-activated nonspecific cationic currents yield dynamically distinct bursting regimes in a model of respiratory neurons" in the Springer Journal of Computational Neuroscience with DOI: 10.1007/s10827-010-0311-y, and as "Qualitative validation of the reduction from two reciprocally coupled neurons to one self-coupled neuron in a respiratory network model" in the Springer Journal of Biological Physics vol. 37, no. 3, 307–316. They are copyright to Springer, 2011.

There are many people to whom I owe thanks for their support in the composition of this dissertation. My committee, G. Bard Ermentrout, Carson Chow, and Christopher Del Negro all contributed to this work. In particular, thank you Bard for questioning the stability of synchronous solutions of the unified model, this question alone lead me to a short publication! Carson's inquiries about the transition mechanisms between different bursting rhythms in the unified model were also very useful. Of course, Christopher's biological insights and mathematical understanding were extremely valuable for the entire document; thank you for your eternal patience, Christopher! My advisor, Jonathan Rubin, is owed a tremendous amount of gratitude. You provided a perfect balance of incredible insight, driving motivation and professional development, thank you Jon!

Of course, in the undertaking of any document such as this, professional support is could only carry me so far. More support came from my dearest friends. My sincerest thanks to Bruc(e), Chris, Josh, and Jer for conversations and games from near and afar. Nate, how did we juggle all of this? Thanks to Mark for withstanding a hundred lunches filled with computational neuroscience and finance. Kristen, you reenergized my passion for teaching, and, combined with your continued friendship, provided motivation for me to look past the present challenges to where I want to be. I cannot thank you enough, Lucy, for our late night conversations, for our coffee shop walks, but most importantly for your support in math and in life!

Where would I be without family? Mother, father, how could I begin to enumerate what you've done for me? Thanks for everything! Perhaps the biggest thank you that I can give though, is to my newest family member, Liz. Thank you for enduring without ever looking back, and for your unwavering and unfathomable support!

## 1.0 INTRODUCTION

The preBötzinger complex (preBötC) of the mammalian ventral respiratory brainstem contains a heterogeneous neuronal network that generates the inspiratory phase of the respiratory rhythm [64, 20]. In isolation from the rest of the brainstem, the preBötC sustains robust, network-wide, rhythmic bursts that can be studied in reduced preparations *in vitro* [64]. The preBötC is located within a ring of other networks, many of which provide inhibition to the preBötC. During phenomena like hypoxia, this inhibition may be released as the activation in these networks fades out, and so it falls on the preBötC to drive the respiratory rhythm [63, 52]. Thus, a significant component of understanding the respiratory cycle involves understanding the intrinsic dynamics of the preBötC. Excitatory synaptic connections between neurons within the preBötC are essential for rhythm generation, while the preBötC rhythm persists under blockade of chloride-mediated inhibition [21, 3, 60, 48]. Neurons within the preBötC are endowed with a persistent sodium (NaP) current [44] and a calcium activated nonspecific cationic (CAN) current [42]. The CAN current can be activated via second-messenger mediated synaptic pathways [42]. The NaP current is voltage dependent and has sub-threshold activation [13, 45, 31]. Both currents are relevant to rhythmicity within the preBötC. Previous analysis of preBötC activity has primarily focused on each of these currents individually, in the context of distinct neuronal models [4, 56].

The NaP current is found in every preBötC neuron [44], and has been shown to play a role in generating robust bursts in the preBötC [44, 45, 31, 13, 57], at least in certain conditions, such as when the respiratory brainstem is challenged by hypoxia, anoxia, or hypercapnia [52, 63, 59]. Butera et al. developed an ODE model (henceforth called the "Butera model") of preBötC neurons that is characterized by the presence of the NaP current, but does not include the CAN current [4, 5]. In the Butera model, by varying the strength of

the NaP current, model neurons can be made to exhibit quiescence (spiking rarely if at all), intrinsic tonic activity (spiking with regular frequency), or instrinsic bursting (alternating active phases containing multiple spikes with quiescence); all of these patterns are observed in synaptically isolated preBötC neurons, though an individual neuron need not be capable of all three patterns. In fact, for individual neurons in the preBötC, the NaP current is necessary for intrinsic bursting dynamics [13]. The Butera model can exhibit network bursting and reproduce important features of the *in vitro* respiratory rhythm. However, recent experimental results suggest that under pharmacological nullification of the NaP current [12], via the drug Riluzole, the preBötC still generates an inspiratory-like rhythm [43]. There must be another mechanism that functions independent of the NaP current that is capable of maintaining inspiratory-like rhythms. Nevertheless, the NaP current is ubiquitous within the preBötC, and given its capacity to enhance neuronal activity [34], investigation of the NaP current is critical to efforts to fully understand preBötC rhythmicity.

Experimental observations suggest that most cells in the preBötC, when considered in isolation, either are tonically active or are quiescent; however, there is also a significant population of cells that engage in intrinsic bursting behavior when they are decoupled from the rest of the network [20]. Intrinsically bursting neurons in the preBötC are not necessary for the overall network rhythm, since this rhythm persists when the persistent sodium current is pharmacologically blocked (see also [55]). On the other hand, such intrinsically bursting neurons may contribute to the bursting rhythm in normal circumstances. Chapter 2 considers the role of intrinsically bursting neurons in a network containing three model neurons. The model used is a reduced version of the Butera model, and therefore does not include the CAN current, but is still able to represent intrinsically quiescent, tonic, and bursting neurons. We develop a set of necessary conditions, as well as a separate set of sufficient conditions, for which the three model neurons, when coupled by synaptic excitation, will generate synchronous bursting activity. We expand upon these conditions by performing numerical simulations to evaluate the effect of adding model neurons with various intrinsic dynamics to a network already containing a pair of neurons: one quiescent and one tonically active. Prior numerical results using the Butera model indicate that neurons that are intrinsically bursting, at least for some range of applied tonic input, enhance the robustness and frequency

range of preBötC bursting [46]. Throughout, when we say a neuron has a certain kind of intrinsic dynamics, we mean that the neuron is tuned to have those intrinsic dynamics under baseline conditions. We found that of those so called burst capable neurons, intrinsically quiescent neurons best support synchronous bursting over a broad frequency range when embedded within a network, as long as intrinsically tonic neurons are also present. In fact, we found that intrinsically bursting neurons are not well suited for promoting synchronous bursts in the network of three neurons. Since these neurons do not promote synchronous network bursts and network bursts persist in the absence of the NaP current, we turn our attention to the CAN current, a network mechanism for generating network bursts.

The CAN current is found in up to 96% of preBötC neurons [42]. Experimental results indicate that the CAN current plays an important role in rhythmogenesis within the preBötC [7, 37, 42, 43]. A recent model (we will call it the Rubin-Hayes model) was used to study the CAN-based mechanism for rhythmogenesis by focusing on the role of excitatory synaptic interactions in activating the CAN current [56]. In its core form, this model included the CAN current and a Na/K ATPase electrogenic pump current. It was shown that qualitative features of model dynamics were preserved when the pump was replaced by any of a variety of other currents that cause the loss of positive charge at high voltage, including the NaP current. Analysis was done mostly in the absence of the NaP current, however, to focus on emergent network properties achieved through recruitment of postsynaptic burst-generating conductances by network activity.

Flufenamic acid (FFA) is a pharmacological agent that blocks the CAN current, but also interferes with other network properties such as gap junctions. Nevertheless, when the strength of the CAN current is significantly reduced by FFA, the preBötC is still able to achieve synchronous bursting patterns. Simultaneous application of FFA and Riluzole, however, abolishes the rhythmicity of the preBötC until the drugs are washed out. Therefore, to understand how rhythmicity is generated in the preBötC it is important to understand the interactions of the persistent sodium and CAN currents.

In Chapter 3 we introduce a unified model, which includes the CAN current, Na/K pump, and persistent sodium current within one differential equation model. Numerical simulations validate the reduction from two reciprocally coupled neurons to the self-coupled

case. Within one self-coupled model neuron, we simultaneously vary the strengths of the persistent sodium and CAN currents, and catalogue the dynamics that emerge by partitioning parameter space into regions of like dynamics. Employing geometric singular perturbation theory and bifurcation analysis, we explain how the dynamics in each region arise. We are also able to analyze the transition mechanisms between each region, and use this to verify the boundaries between the various regions. In particular, we elucidate the circumstances through which a novel bursting pattern arises from the model; the pattern is experimentally observed in preBötC neurons and highlights the interactions of the CAN and persistent sodium currents. Heterogeneity is a known feature of preBötC networks, and our analysis provides a framework through which we can understand larger networks when heterogeneity is included in the strengths of the persistent sodium and CAN currents.

The study of long term behavior for large networks is a developing field that spans many disciplines, including dynamical systems and graph theory [66]. A large network can be thought of as having heterogeneity in two ways: the network architecture and the dynamics at each node. Large bodies of research have explored the two natural limits of this dichotomy, irregular architectures with identical dynamics for each node, or very regular architecture with heterogeneous dynamics distributed across the nodes of the network. Heterogeneity in dynamics for the individual nodes is often considered in the case of coupled oscillators, where each node intrinsically oscillates at its own frequency. Studying coupled oscillators may not necessarily yield good insights for analysis in the preBötC because of the heterogeneity in the individual neurons. Indeed this can be seen in the wide variety of activity patterns for a reciprocally coupled pair of neurons in Chapter 3. On the other hand, regular connectivity patterns, such as all-to-all connectivity, which is often deployed in numerical simulations of preBötC models [5, 46, 62, 33], may not be appropriate for elucidating the rhythmicity of the preBötC, as it trivializes interneuronal distances between synaptically coupled neurons; these distances are now known to be nontrivial [25].

Experimental data regarding the connectivity architecture of preBötC neurons are relatively rare. The data that exist show that the neurons are organized into spatial clusters, with dense intracluster connectivity and very sparse intercluster connectivity [25]. For neurons modeled with the Butera model, simulations of network architectures adhering to these

data, as well as networks adhering to a catalogue of other architectures, were recently performed by Gaiteri and Rubin [24]. They found that networks inspired by the experimental data performed poorly. Their analysis did not include the CAN current, the addition of which may improve network bursting. Nevertheless, it is clear that the preBötC sustains stable synchronous bursting despite the apparent handicap of its architecture. How do the clusters of a large network synchronize with each other despite the challenges of heterogeneous intrinsic dynamics and sparse connectivity? In Chapter 4, we address this question by creating artificial networks that adhere to the connectivity statistics from the data [25] and endowing each node of the network with dynamics governed by the unified model from Chapter 3.

Data based, randomly generated networks have poor performance, so we developed a genetic algorithm to search parameter space for well performing networks with both heterogeneous neuronal dynamics and heterogeneous cluster structure. Through the genetic algorithm we found families of networks that produce bursting rhythms that are stable and synchronized. The genetic algorithm makes apparent two mechanisms that promote network bursting. When connections between clusters are sparse, those few neurons with intercluster connections rise to elevated importance because of their role in communicating activity from the rest of the network to their cluster, or vice versa. The best networks we found through the genetic algorithm contained significantly more quiescent neurons than the networks we used to initialize the search. Moreover, we found that, with a greater frequency than expected by chance, intrinsically quiescent neurons were harnessed to serve as the communicative neurons between clusters. We also found that the CAN current plays a crucial role in rhythmogenesis. Interestingly, the average strength of the CAN current across the networks we found through the genetic algorithm is different from the average at initialization. In Chapter 4 we explore the ramifications of these findings, as well as other phenomena found in our search.

## 2.0 INTRINSIC DYNAMICS FOR BURSTING IN 3-CELL NETWORKS

Most cells in the preBötC, when considered in isolation, either are tonically active (firing spikes repeatedly) or are quiescent (spiking rarely if at all); however, there is also a significant population of cells that engage in intrinsic bursting (alternating spiking and prolonged quiescence) behavior when they are decoupled from the rest of the network [20]. This chapter attempts to answer the question of what is the role of these neurons that burst in isolation in the control of preBötC dynamics.

In [4, 5], Butera et al. developed an ODE model of a class of neurons in the preBötC characterized by the presence of a persistent sodium current. Working with the model from [4, 5], Rubin provided conditions for the emergence of synchronous bursting in a pair of burst-capable cells, one tuned to be intrinsically quiescent and the other to be intrinsically tonic, coupled with synaptic excitation [55], thereby proving that burst-capable neurons need not be tuned to be intrinsically bursting in the absence of inputs in order for them to generate network bursting when coupled (see also [50]). Purvis et al. used simulations of a network including a mixture of intrinsically burst-capable and burst-incapable cells to show that the presence of significant numbers of burst-capable cells enhances the parameter range over which synchronous bursts occur and the frequency range that bursts achieve under variation of a control parameter [46]. Together, these findings highlight the importance of burst-capable cells for synchronous bursting within the preBötC but also lead us to ask, given that cells that are tuned to burst in isolation are not necessary for network-wide synchronous bursting, how do they contribute to such activity patterns?

Given the heterogeneity of dynamics observed in isolated preBötC cells (see also [47]) and the evidence for the involvement of burst-capable cells in network activity, we explore the role of intrinsically bursting cells in the preBötC by considering heterogenous networks,

each containing three burst-capable cells. Such networks are large enough to include representatives of all three types of intrinsic dynamics (quiescence, bursting, and tonic spiking), and hence for the role of intrinsically bursting cells in a heterogeneous network to become apparent, but are also small enough to allow for the analysis of the dynamic effects of the presence of intrinsic bursters.

Including this introduction, this chapter is partitioned into 6 sections. Section 2.1 introduces the model we will use for our analysis and provides a heuristic introduction to the theory of relaxation oscillators, including the effects of synaptic coupling. Section 2.2 provides a set of necessary conditions for periodic, synchronous bursting oscillations to occur within our three-cell network, as well as a separate set of sufficient conditions for such a solution to exist in the network. Although these conditions are presented for a three-cell network, the interested reader may refer to Section 2.3, which provides a guideline for extending these conditions to an arbitrarily sized network. Section 2.4 provides results and analysis of two numerical experiments. The first experiment explores which cells promote synchronous oscillations if added to a network already containing an intrinsically quiescent and an intrinsically tonic cell. The second simulation addresses the issue of frequency control in the three-cell network. Finally, we summarize our work and suggest directions for future research in the discussion contained in Section 2.5.

## 2.1 INTRODUCTORY THEORY

### 2.1.1 Models

Throughout this work, we will focus on a reduced version of the Butera model developed in [4, 5]. The original model for an individual cell in isolation is

$$v' = (-I_{NaP}(h,v) - I_{Na}(n,v) - I_K(n,v) - I_L(v) - I_{tonic-e}(v) + I_{app})/C_m \quad (2.1)$$

$$n' = (n_\infty(v) - n)/\tau_n(v) \quad (2.2)$$

$$h' = \varepsilon(h_\infty(v) - h)/\tau_h(v) \quad (2.3)$$

$$s' = \alpha_s(1-s)s_\infty(v) - s/\tau_s \quad (2.4)$$

with $I_{NaP}(h,v) = g_{NaP}m_{p,\infty}(v)h(v-E_{Na})$, $I_{Na}(n,v) = g_{Na}m_{\infty}^3(v)(1-n)(v-E_{Na})$, $I_K(n,v) = g_K n^4(v-E_K)$, $I_L(v) = g_L(v-E_L)$ and $I_{tonic-e} = g_{ton}(v-E_{syn-e})$. Equation (2.4) relates to the strength of synaptic signals generated by the cell. The variable $s$ does not feed back to equations (2.1)–(2.3) in the isolated cell case but will play an important role in coupled networks, later in the chapter. Values for the parameters and the definitions of the other functions appearing in this model can be found in Subsection 2.1.2. Typically, the small parameter $\varepsilon$ is absorbed into the function $\tau_h(v)$, however, for clarity of analysis, we have factored it out.

Neurons modeled by these equations are classified as quiescent, bursting or tonic depending on their activity patterns. After a transient that depends on the initial conditions of the system, a quiescent neuron will not spike, and a tonic neuron will repeatedly fire spikes at a regular frequency. A bursting neuron will switch between active and silent phases. During the active phase a bursting neuron emits spikes, while during the silent phase it does not. Thus, a quiescent neuron can be thought of as being stuck in the silent phase, while a tonic neuron is stuck in the active phase. Depending on the relative magnitudes of its ionic conductances, each quiescent or tonic cell may be burst-capable, meaning that it can burst for some level of $g_{ton}$, or not; for example, a large $g_L$ relative to $g_{NaP}$, or vice versa, can eliminate burst-capability.

In the given model, when the neuron is in the active phase, the currents $I_K$ and $I_{Na}$ are what cause the rapid fluctuations in the $v$ variable that we interpret as spikes. In the silent phase, these currents do not contribute much to the $v$ dynamics. Removing these terms from the $v$ equation also allows us to remove equation (2.2) to obtain a reduced model that is more amenable to analysis. This reduced model has been used previously for the analysis of synchronous oscillations in a heterogeneous network combining intrinsically bursting and intrinsically quiescent cells as well as for a coupled intrinsically quiescent and intrinsically tonic cell pair [53, 55]. The model takes the form

$$v' = (-I_{NaP}(h,v) - I_L(v) - I_{tonic-e}(v) + I_{app})/C_m \tag{2.5}$$

$$h' = \varepsilon(h_\infty(v) - h)/\tau_h(v) \tag{2.6}$$

$$s' = \alpha_s(1-s)s_\infty(v) - s/\tau_s \tag{2.7}$$

where $I_{NaP}(h, v)$ and $I_L(v)$ are as given above.

The $s$ variable in equation (2.7) is slaved to $v$, and it does not appear in equations (2.5) and (2.6), so it is useful to do analysis on the $vh$ phase plane. A nice feature of this reduced model is that if we make biologically reasonable assumptions on the parameters, then equations (2.5) and (2.7) operate on a fast time scale, while (2.6) evolves on a slow time scale, due to the small size of $\varepsilon$. Further, within a broad, biologically relevant parameter range, the $v$-nullcline (the algebraic equation $v' = 0$) can be written as a twice differentiable function $F(v)$ with a cubic shape, while the $h$-nullcline is a sigmoidal curve that is monotone decreasing as a function of $v$. We follow the work of Rubin in [55] to perform analysis on this model. Insights based on the shapes and positions of the nullclines often suffice to analyze the model. When $F(v)$ is cubic, we call its branches the left, middle, and right branch, respectively. The left branch satisfies $F'(v) > 0, F''(v) < 0$, the middle branch has $F'(v) < 0$, and the right branch has $F'(v) > 0, F''(v) > 0$. Where the left branch meets the middle branch there is a local maximum of the nullcline, which we will call the left knee. Similarly, where the middle branch meets the right branch there is a local minimum of the nullcline, which we will call the right knee. See Figure 2.1 for an example chosen to illustrate these definitions. If we make a further assumption that the nullclines intersect exactly once, then it is a straightforward calculation to determine the stability of the resulting critical point.

### 2.1.2 Function definitions and parameter values

Below we record the definitions of the individual functions that make up equations (2.1)–(2.4) which were introduced in Refs. [4, 5]. In these equations, for $x \in \{h, m, m_P, n, s\}$, the function $x_\infty(v)$ takes the form $x_\infty(v) = \{1 + \exp[(v - \theta_x)/\sigma_x]\}^{-1}$, and also for $x \in \{h, n\}$, the function $\tau_x(v)$ has the form $\tau_x(v) = \bar{\tau}_x / \cosh[(v - \theta_x)/(2\sigma_x)]$. The parameter values used in the simulations are listed in Table 2.1. These parameters appear as they did in Ref. [55], except that we set $\theta_h = -40$mV. Heterogeneity was introduced by the parameters $g_{NaP}$ and $g_L$ so they do not appear in Table 2.1.

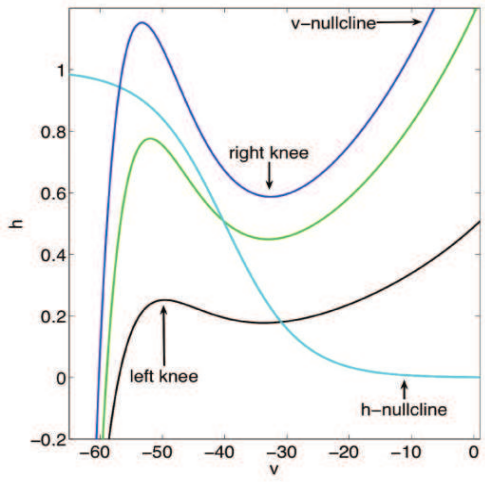


Figure 2.1: Example nullclines for three different instances of the reduced model. For $\varepsilon$ sufficiently small, the dark blue nullcline corresponds to a quiescent cell, the green nullcline represents a bursting cell, and the black nullcline represents a tonic cell. All three cells in this case share the same h-nullcline, which is light blue. All parameters are as in Table 2.1, except: for the quiescent cell we have $g_{NaP} = 2, g_L = 2.5$, for the bursting cell we have $g_{NaP} = 2, g_L = 2$ and for the tonic cell $g_{NaP} = 3.5, g_L = 1.5$.

Table 2.1: Common parameter values for equations (2.1)–(2.4)

| Parameter | Value | Parameter | Value | Parameter | Value |
|---|---|---|---|---|---|
| $\alpha_s$ | 0.2 ms$^{-1}$ | $I_{app}$ | 12 mV | $\bar{\tau}_h$ | 1 ms |
| $C_m$ | 0.1 pF | $\sigma_h$ | 6 mV | $\bar{\tau}_n$ | 10 ms |
| $E_K$ | −85 mV | $\sigma_m$ | −33 mV | $\tau_s$ | 6.25 ms |
| $E_L$ | −65 mV | $\sigma_{m_P}$ | −5 mV | $\theta_h$ | −40 mV |
| $E_{Na}$ | 50 mV | $\sigma_n$ | −4 mV | $\theta_m$ | −34 mV |
| $E_{syn-e}$ | 0 mV | $\sigma_s$ | −1 mV | $\theta_{mp}$ | −38 mV |
| $g_{ij}$ | 0.35 nS | | | $\theta_n$ | −29 ms |
| $g_{ton}$ | 0 nS | $\varepsilon$ | 1/100 | $\theta_s$ | −33 mV |

### 2.1.3 Review of the Dynamics of a Relaxation Oscillator

In this subsection we simply provide a brief, heuristic discussion of relaxation oscillator dynamics relevant for our analysis of system (2.5)–(2.6). Analysis of the dynamics of relaxation oscillators in arbitrary dimensions can be done using the tools of geometric singular perturbation theory [22, 32, 28].

For $0 < \varepsilon << 1$ and $v \in \mathbb{R}, h \in \mathbb{R}$ consider a system of the form:

$$v' = f(v,h) \tag{2.8}$$

$$h' = \varepsilon g(v,h) \tag{2.9}$$

Suppose further that the $v$-nullcline can be written as a cubic shaped function $h = F(v)$ with $\lim_{v\to\infty} F(v) = \infty$. Allow the $h$-nullcline to be a monotonically decreasing function of $v$. We will use again the terminology from Section 2.1.1 to describe the knees and branches of the $v$-nullcline, see Figure 2.1. Figure 2.1 contains three different $v$-nullclines, one where the intersection with the $h$-nullcline is on the left branch, another where the intersection is on the middle branch, and at last one where the intersection falls on the right branch. If the $h$-nullcline intersects the $v$-nullcline near one of the knees, we risk the existence of canards, which are outside of the scope of this work. Let $(v_p, h_p)$ be the intersection point of the $v$ and $h$-nullclines, and let $(v_{LK}, h_{LK}), (v_{RK}, h_{RK})$ denote the left and right knee, respectively. For a given $\varepsilon > 0$, there is a $\delta = \delta(\varepsilon) > 0$, such that if $\min\{|v_p - v_{LK}|, |v_p - v_{RK}|\} > \delta$, then canards will not exist. For the remainder of the work, we assume that this inequality holds.

It is useful at this point to define a way to measure the distance of a point from the $v$-nullcline. For any fixed $h$ there are between 1 and 3 values of $v$ such that $F(v) = h$. We will only concern ourselves with those $v$ that correspond to the left and right branches of the $v$-nullcline. Allow $v_{LB}(h)$ to be the $v$ such that $F(v_{LB}) = h$ and $(v_{LB}, h)$ is on the left branch of the $v$-nullcline, and if there is no such $v$ then set $v_{LB}(h) = \infty$. Similarly, allow $v_{RB}(h)$ to be the value of $v$ such that $F(v_{RB}) = h$ and $(v_{RB}, h)$ is on the right branch of the $v$-nullcline, and set $v_{RB}(h) = \infty$ if no such $v$ exists. Let $\Gamma_v(t)$ be the $v$-coordinate at time $t$ of a trajectory $\Gamma(t)$ of the ODE. Similarly, allow $\Gamma_h(t)$ to be the $h$-coordinate at time

$t$ for the trajectory $\Gamma(t)$. Now we can define the distance from $\Gamma(t)$ to the $v$-nullcline as $D(\Gamma(t)) = \min\{|\Gamma_v(t) - v_{LB}(\Gamma_h(t))|, |\Gamma_v(t) - v_{RB}(\Gamma_h(t))|\}$.

The intersection of the $v$ and $h$-nullclines is a critical point of system (2.8)–(2.9). Suppose now that $v' < 0$ below the $v$-nullcline and $v' > 0$ above it. Similarly, assume that $h' > 0$ below the $h$-nullcline and $h' < 0$ above it. These assumptions, together with the critical point being bounded away from the knees, imply that critical points on the middle branch of the $v$-nullcline are unstable, while critical points on the left and right branches of the $v$-nullcline are stable. If for some time $t$, $D(\Gamma(t))$ is large relative to $\varepsilon$, then $|v'| >> 0$ and comparatively $h' \approx 0$. So we consider that the dynamics holds $h$ fixed, and $\Gamma(t)$ quickly approaches a neighborhood of the $v$-nullcline for this fixed $h$. Once $D(\Gamma(t))$ is small enough, then $|v'| \approx 0$ and the $h$ dynamics becomes relevant.

First, consider the case that critical point lies on the middle branch of the $v$-nullcline. Suppose we start with $\Gamma(0)$ on the left branch of the $v$-nullcline. Since the critical point is on the middle branch of the $v$-nullcline, $\Gamma_h(0)$ is below the $h$-nullcline, and so $\Gamma_h'(0) > 0$. The $\varepsilon$ in equation (2.9) implies that the $h$ dynamics are slow, so we say that the trajectory oozes up toward the $h$-nullcline, remaining close to the $v$-nullcline. Eventually $\Gamma_h(t) > h_{LK}$. In this situation, we find that $D(\Gamma(t))$ is large, because for $\Gamma_h(t)$ there is only one corresponding point on the $v$-nullcline, and it is on the right branch. So suddenly $\Gamma_v'(t) >> 0$, and the trajectory quickly jumps over to the right branch of the $v$-nullcline, with $\Gamma_h(t)$ barely changing. Now $\Gamma_h(t)$ is above the $h$-nullcline, so $\Gamma(t)$ begins to ooze down toward the right knee. Since the $h$-nullcline is below the right knee, $\Gamma$(t) will eventually drift below the right knee, and as before, it is suddenly the case that $D(\Gamma(t)) >> 0$. So $\Gamma$(t) will quickly fall down to the left branch of the $v$-nullcline, completing one cycle. This alternation of prolonged phases of slow change interrupted by fast transitions between phases is the hallmark of relaxation oscillations. In the two dimensional case, the Poincaré-Bendixon theorem implies the existence of periodic relaxation oscillations in this situation.

Suppose instead that the critical point is on the left branch of the $v$-nullcline. If $\Gamma(t)$ is on the right branch of the $v$-nullcline, it will ooze down until it drifts below the right knee, at which point it falls down to the left branch of the $v$-nullcline, as before. However, since the critical point on the left branch of the $v$-nullcline is asymptotically stable, the trajectory

will not be able to get above the left knee. So instead of jumping back to the right branch of the $v$-nullcline, the trajectory simply approaches the critical point. Similarly, if the critical point is on the right branch of the $v$-nullcline, the trajectory will eventually converge to the critical point.

The $v$-nullcline for equation (2.1) or equation (2.5) may or may not be cubic, depending on parameters such as $g_L$ and $g_{NaP}$. In either case, in the full model (2.1)–(2.4), spiking activity evolves due to the $I_K$ and $I_{Na}$ currents, and spiking only occurs for $v$ above some threshold. This spiking behavior is encoded in the reduced model by the variable $s$, representing synaptic output. We see that equation (2.7) involves $s_\infty(v)$, which is a steep sigmoidal function (Section 2.1.2) since $\sigma_s$ is small. $s_\infty(v)$ takes the value $\frac{1}{2}$ at $v = \theta_s$, which we call the synaptic threshold. For values of $v$ arising during spiking, corresponding to the right branch of the $v$-nullcline when it is cubic, $s_\infty(v) \approx 1$, and the cell is producing synaptic output as would be generated with spiking in the full model, which we represent with $s = s_{max}$. On the other hand, for values of $v$ arising when the cell is quiescent, corresponding to the left branch of the $v$-nullcline when it is cubic, $s_\infty(v) \approx 0$, representing an absence of spiking. Should the $v$-nullcline be cubic with a critical point on its middle branch, the cell will oscillate between phases of low $s$ and phases of $s \approx s_{max}$, corresponding to intrinsic bursting. We will use the location of the critical point to classify our modeled cells as intrinsically bursting (cubic $v$-nullcline with critical point on its middle branch), quiescent (cubic $v$-nullcline with critical point on its left branch or monotone $v$-nullcline with critical point below $\theta_s$), or tonic (cubic $v$-nullcline with critical point on its right branch or monotone $v$-nullcline with critical point above $\theta_s$).

### 2.1.4 Heterogeneity in $g_{NaP}$ and $g_L$

The preBötC is a heterogeneous network of cells that are quiescent, tonically active, or bursting in isolation [20]. Following [46], in order to reflect this heterogeneity in our work, we consider heterogeneity in two parameters: the conductance $g_{NaP}$ of the persistent sodium current $I_{NaP}$ and the conductance $g_L$ of the leak current $I_L$. Such heterogeneity is observed in experimental data [46]. Increasing $g_L$ has the effect of raising the entire $v$-nullcline, in

particular, the left knee. This moves the intersection of the $v$ and $h$-nullclines to lower $v$ values. Numerically, we observe that increasing $g_{NaP}$ has the effect of moving the intersection of the $v$ and $h$-nullclines to higher $v$ values. Below, in Figure 2.2, we show the partitioning of $g_{NaP}g_L$ space into regions where the resultant cell is quiescent (blue), bursting (green), or tonically active (black). For each $g_{NaP}g_L$ pair, we find the branch on which the $h$-nullcline intersects the $v$-nullcline, if the nullcline is cubic on $0 \leq h \leq 1$. If the intersection is on the left branch, middle, or right branch the cell is declared quiescent, bursting, or tonic, and is colored blue, green, or black, respectively. The coloring in Figure 2.2 does not take into account those small neighborhoods around the knee where the intersection of the nullclines may result in a canard explosion, or where the Andronov-Hopf bifurcation does not occur precisely at the knee, as these cases only occur on very small parameter ranges, due to the disparity in timescales of $v$ and $h$, and thus are not significant for our results. If the $v$-nullcline is not cubic (e.g., large $g_{NaP}$ relative to $g_L$) or if it is only single branched for $0 \leq h \leq 1$ (e.g., large $g_L$ relative to $g_{NaP}$), then we classify the cell as quiescent or tonic depending on the position of the critical point relative to the synaptic threshold, $\theta_s$. Further detail on the effects of varying $g_{NaP}$ and $g_L$ can be found in Section 2.4.3.

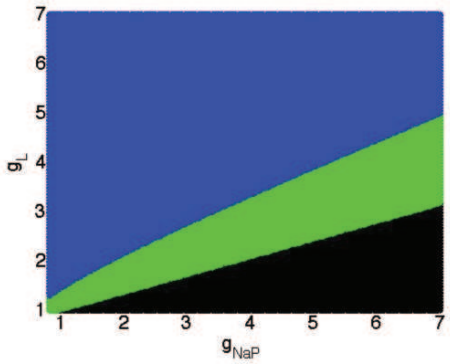


Figure 2.2: Partitioning of $g_{NaP}g_L$ space into regions where the cells are quiescent, bursting, or tonic. The blue region represents quiescent cells, the green consists of bursting cells, and the black region contains tonic cells.

### 2.1.5 Effects of Synaptic Coupling

In a network of coupled cells, each individual cell in the network will have its own $v$,$h$ and $s$ variables. The rest of this chapter concerns a network of three cells, so for $i = 1, 2, 3$, we adopt the vector notation $cell_i = [v_i, h_i, s_i]$, where

$$v_i' = (-I_{NaP,i}(h_i, v_i) - I_{L,i}(v_i) - I_{tonic-e}(v_i) + I_{app} - \sum_{j \neq i} g_{ij} s_j (v_i - E_{syn-e}))/C_m \quad (2.10)$$

$$h_i' = \varepsilon(h_\infty(v_i) - h_i)/\tau_h(v_i) \quad (2.11)$$

$$s_i' = \alpha_s(1 - s_i)s_\infty(v_i) - s_i/\tau_s \quad (2.12)$$

with $I_{NaP,i}(v_i, h_i) = g_{NaP,i} m_{p,\infty}(v_i) h_i (v_i - E_{Na})$, $I_{L,i}(v_i) = g_{L,i}(v_i - E_L)$ and $I_{tonic-e}(v_i) = g_{ton}(v_i - E_{syn-e})$. Note that Equation (2.10) excludes self-coupling, yet self-coupling could be easily included in the analysis if desired (see Section 2.3). We henceforth assume that the $v$-nullcline for each neuron is cubic, with associated active and silent phases corresponding to its right and left branches, respectively, since this assumption is only violated on the edges of the parameter range illustrated in Figure 2.2, away from where the important dynamic effects occur.

In Section 2.2.2 we will prove that when $s_j$ increases, the knees of the coupled cells have lower $h_i$ coordinates, see Figure 2.3. Here, we will use this result without proof, to briefly illustrate the mechanism by which a network of these modeled neurons may produce synchronous bursts. Recall that we do not have spiking oscillations in this reduced model, so $s_j$ is relatively constant when $v_j$ is above the synaptic threshold. Therefore, the $v_i$ nullclines for $i \neq j$ experience a quick shift when $v_j$ crosses the synaptic threshold, but the changes are otherwise gradual, see Subsection 2.2.1. We continue to assume $\varepsilon$ is small so that the $h$ dynamics are slow relative to the $v$ and $s$ dynamics, see Section 2.1.3. Thus, in a network architecture where $cell_1 = [v_1, h_1, s_1]$ is coupled to $cell_2 = [v_2, h_2, s_2]$ and both cells are initially in the silent phase, if the trajectory for $cell_1$ transitions to the active phase, then there is an instantaneous change in the $v_2$-nullcline. It may happen that the left knee for $cell_2$ has dropped below the current value of $h_2$, in which case $cell_2$ immediately transitions to the active phase. A similar effect may happen when one cell transitions to the silent phase. Such fast threshold modulation [65] can yield rapid convergence to synchronous oscillations

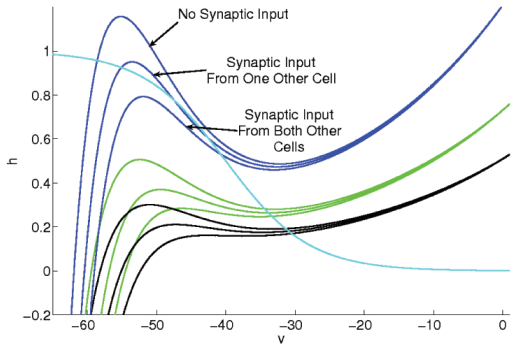


Figure 2.3: Various levels of synaptic input to sample instances of the reduced model. The blue, green and black nullclines represent respectively a quiescent, a bursting, and a tonic cell under various levels of synaptic input. The key feature is that synaptic input from another cell lowers both the left and the right knee of the receiving cell. In this way, a quiescent cell can become bursting, and a bursting cell can become tonic.

by allowing the trailing cell to catch up to the cell ahead of it, although order switching may complicate the dynamics. A great amount of detail on this mechanism is provided in [55, 2, 65, 53].

### 2.1.6 Illustration of Three Coupled Cells

In this section, we illustrate how the dynamics in which we are interested, synchronous bursting, can arise in an all-to-all coupled network of three cells, modeled by equations (2.10),(2.11),(2.12), with heterogeneity introduced through $g_{NaP}$ and $g_L$, such that one cell is intrinsically quiescent, one is intrinsically bursting, and one is intrinsically tonic. Analysis of such systems can yield insights into how these three types of intrinsic dynamics interact. We define a solution as a synchronous bursting oscillation if all three cells transition repeatedly, via fast excursions controlled by their $v$ dynamics, between the silent and active phases and, after one cell undergoes a transition from one phase to another, all the other cells join it in its new phase before any cell undergoes a transition out of that phase. We will study this system

by projecting the solution onto three separate phase planes: $(v_1, h_1)$, $(v_2, h_2)$, and $(v_3, h_3)$, while keeping in mind that the position of $v_j$ in the $(v_j, h_j)$ phase plane directly affects $s_j$ and so changes the shapes of the $v$-nullclines in the other two phase planes. Suppose that in the absence of coupling $cell_1$ is quiescent, $cell_2$ is bursting, and $cell_3$ is tonic. We will use the shorthand $Q$, $B$, and $T$, for $cell_1$, $cell_2$ and $cell_3$ respectively. We start with all three cells in the silent phase, and view the evolution of the trajectory as a series of snapshots, laid out in Figures 2.4–2.15. Though the $v_j$-nullclines actually change continuously as a function of $s_i$ for $i \neq j$, we assume that the change is fast enough to be considered instantaneous relative to the slow $h$ dynamics.

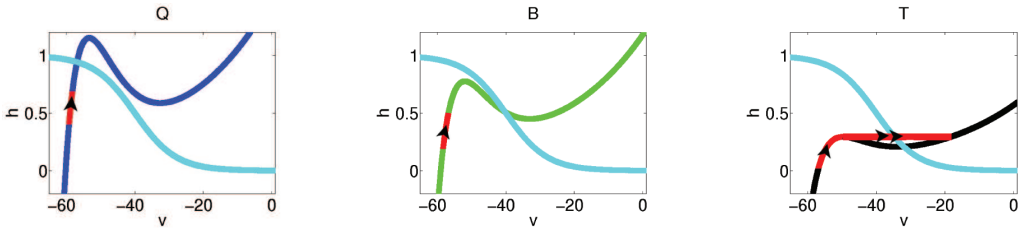


Figure 2.4: Starting with all cells silent, T is the first to reach its left knee and enter the active phase. In this figure and for Figures 2.5–2.15, the dark blue, green, and black curves represent the $v$-nullclines for the $Q$, $B$, and $T$ cells respectively. The light blue curve is the $h$-nullcline. Red represents the trajectory of the system. One black arrow indicates slow evolution, while two black arrows indicates a fast evolution.

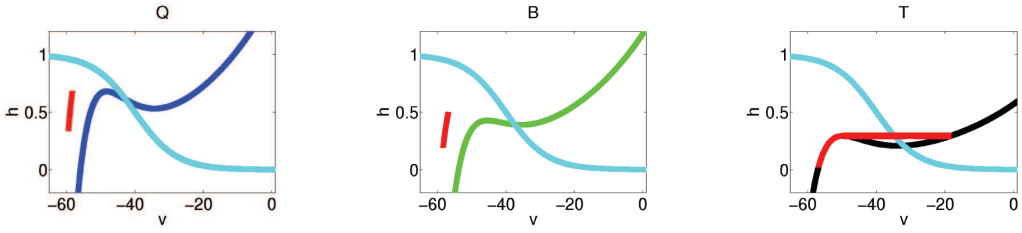


Figure 2.5: Now that T is in the active phase, it sends synaptic input to the other two cells, and their $v$-nullclines change abruptly.

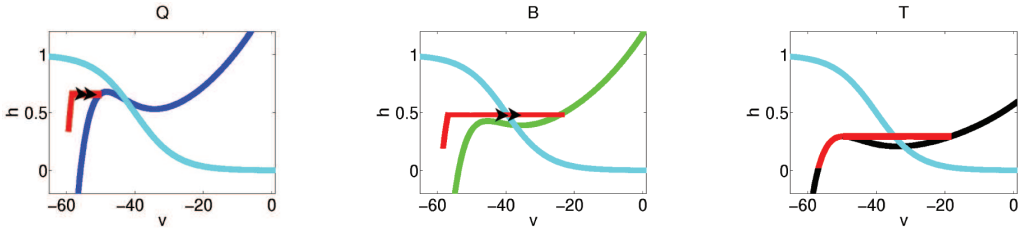


Figure 2.6: Due to the synaptic input from T, B is suddenly above its left knee, so it immediately enters the active phase. Meanwhile, Q quickly approaches its $v$-nullcline.

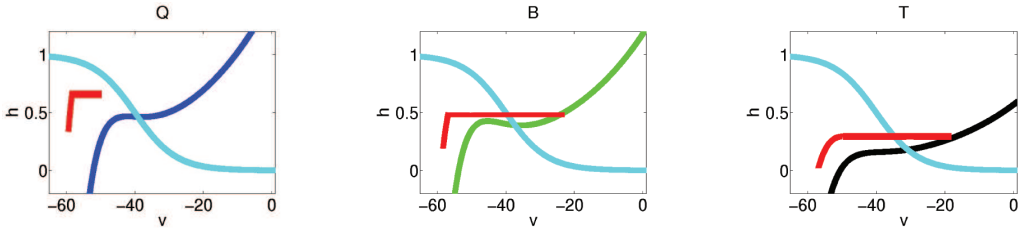


Figure 2.7: Now that B is in the active phase, it sends synaptic input to both Q and T, and their $v$-nullclines are updated accordingly.

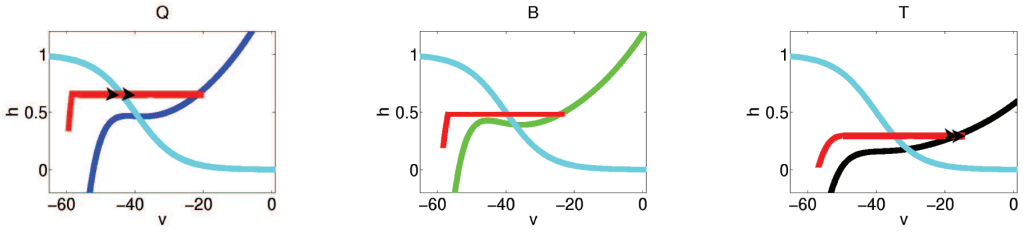


Figure 2.8: Q is now above its left knee, and so it enters the active phase.

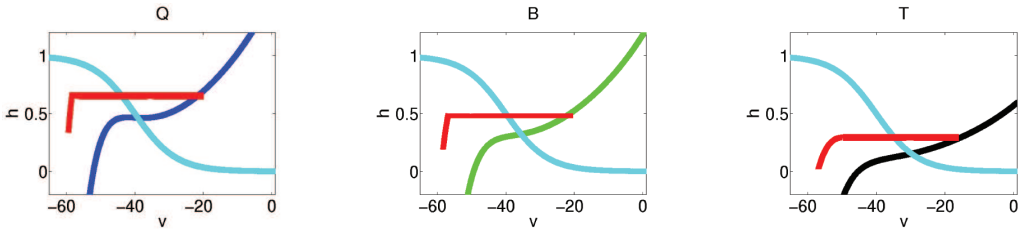


Figure 2.9: Now that Q is in the active phase, it sends synaptic signals to B and T, so their $v$-nullclines are updated.

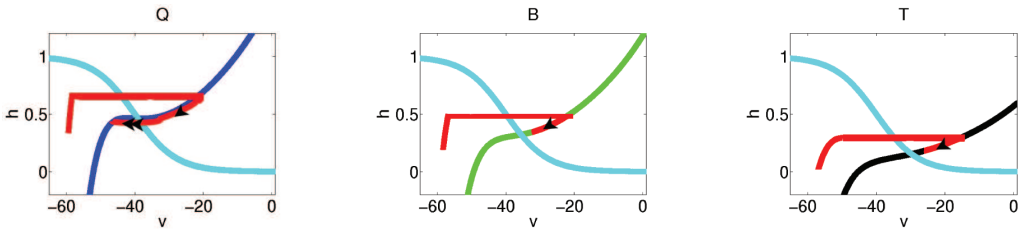


Figure 2.10: The system evolves until one of the cells reaches its right knee. In this case, the Q cell must be the first to do so, because the other two cells become tonic under the current input levels.

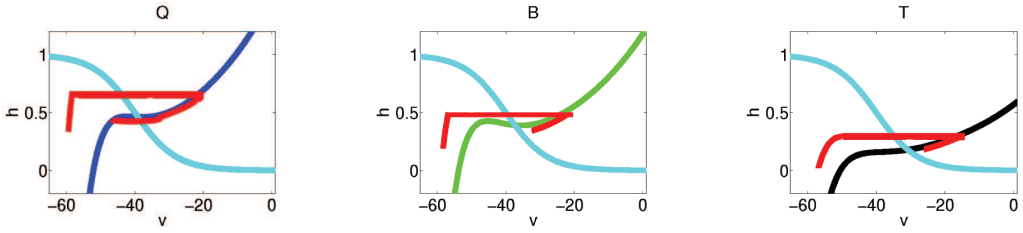


Figure 2.11: Q has returned to the silent phase, so the $v$-nullclines are updated for cells B and T. Note that Q could return to the silent phase because the synaptic input from B and T were not strong enough to push Q's critical to the right branch of its $v$-nullcline.

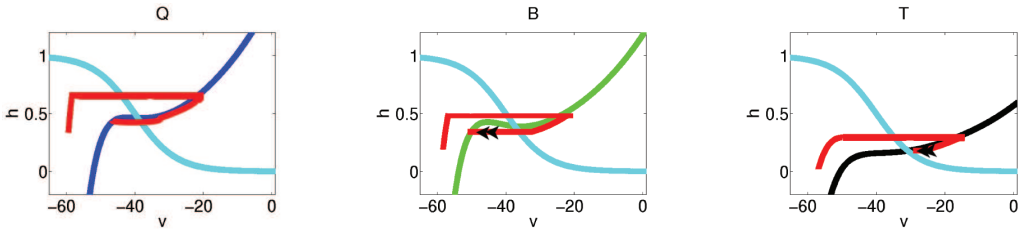


Figure 2.12: With the synaptic input from Q removed, B is below its right knee and enters the silent phase.

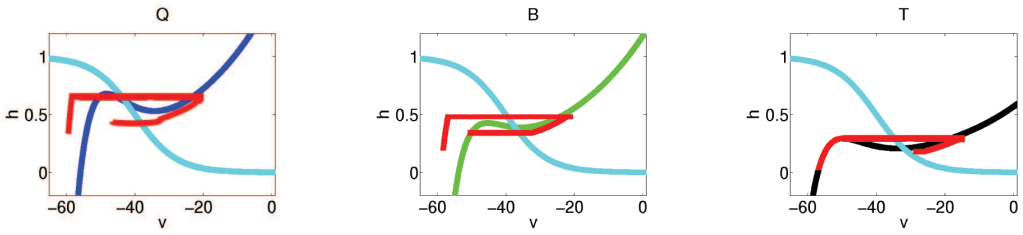


Figure 2.13: Now that B is in the silent phase, synaptic inputs to Q and T are removed, and their $v$-nullclines are updated.

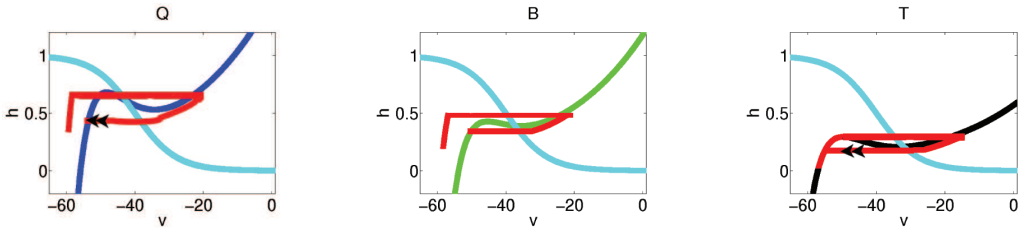


Figure 2.14: Finally T is below its right knee, so it falls down to the silent phase.

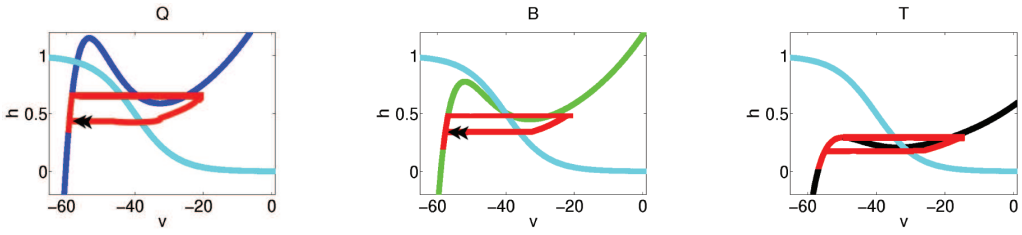


Figure 2.15: All cells have returned to the silent phase, so all synaptic inputs are removed. This completes one cycle of the synchronous bursting oscillation.

### 2.1.7 Remarks on Synaptic Adaptation

The cartoon presented in Figures 2.4–2.15 omits one feature of equation (2.12). Typically, $s_\infty(v)$ is a sigmoidal function. However, if the sigmoid is not steep, then there is a significant range of values of $v$ where the synaptic output of the cell is reduced from its maximal value but remains nonzero. This effect can represent synaptic adaptation, if the relevant range of $v$-values overlaps the right branch of the $v$-nullcline (i.e., the active phase). That is, $v$ effectively evolves on the slow timescale for a cell on the right branch, and a slow change in $v$ yields a slow change in $s$ and hence a gradual change in the $v$-nullclines of the other cells. This may have far reaching ramifications; for instance, if the $v$-nullcline of a quiescent cell does not change fast enough, then the cell may not be able to transition to the active phase. Further consideration on the effects of synaptic adaptation can be found in [69, 9].

## 2.2 SYNCHRONOUS OSCILLATIONS IN THREE-CELL NETWORKS

### 2.2.1 Necessary Conditions for Synchronous Bursting

Our definition of synchronous does not require cells to transition between the active and silent phases at precisely the same time. Instead, we call a solution synchronous if the following conditions are always met after some transient time. When $cell_i$ transitions to the active phase, every other $cell_j$, for $j \neq i$, must have been in the active phase before $cell_i$ returns to the silent phase. Similarly, after the return to the silent phase, $cell_i$ does not transition to the active phase until all other cells have visited the silent phase. For an $n$-cell network, these conditions can be formulated in terms of the time it takes each cell to reach the left or right knee, as appropriate.

We will consider iterations on two sets of integers, one set contains the indices of cells in the active phase, while the other set contains the indices of cells in the silent phase. An iteration involves moving an index between the two sets. We let $i \in S_m \subseteq \{1, 2, .., n\}$ if $cell_i$ is in the silent phase at iteration $m$. Similarly, $i \in A_m \subseteq \{1, 2, .., n\}$ if $cell_i$ is in the active phase at iteration $m$. Let $T_{LK}(i, m)$ be the time it takes $cell_i$ to reach the left knee from

its current position, which depends heavily on the current state of the network, implicitly encoded in the iteration number $m$. Similarly define $T_{RK}(i,m)$ as the time it takes $cell_i$ to reach the right knee from its current position in iteration $m$. There are two network-wide stages to consider: the first is "cells are transitioning from the silent to the active phase" and the other is "cells are transitioning from the active to the silent phase." Assume that $S_0 = \{1, 2, ..., n\}$ and $A_0 = \emptyset$. Let $k$ be the index such that $k = \underset{i\in\{1,2,...,n\}}{\operatorname{argmin}} T_{LK}(i,0)$. Then we write $S_1 = S_0 \backslash k$ and $A_1 = A_0 \cup k$. This completes one iteration on the sets. We then consider the system again after time $T_{LK}(k,0)$.

With this notation, the necessary condition that no cell in the active phase may return to the silent phase until there are no cells in the silent phase during the $m$th iteration can be phrased as:

$$\inf_{i\in S_m}\{T_{LK}(i,m)\} < \inf_{j\in A_m}\{T_{RK}(j,m)\} \tag{2.13}$$

That is, for fixed $m$, as long as (2.13) holds, the first cell to jump up can be moved from $S_m$ to $A_{m+1}$ to complete the $m^{\text{th}}$ iteration. If (2.13) holds for $m = 0, 1, ..., n-1$, then all cells enter the active phase before any cell leaves it. Then, after the first cell returns to the silent phase, the condition is reversed for the "cells returning to the silent phase" network stage. We must have $\inf_{j\in A_m}\{T_{RK}(j,m)\} < \inf_{i\in S_m}\{T_{LK}(i,m)\}$, in this case, until all cells are back to the silent phase. In order for a network to maintain synchronous bursting, these conditions must be satisfied for all $m \in \mathbb{N}$.

*Remark.* For fast-slow networks of arbitrary size, classification of cells into finer bins, depending on slow variable values in the silent phase, can be used to develop a Markov chain representation of network dynamics [51]. For the study of synchronous bursting solutions as we have defined them, two bins suffice.

### 2.2.2 Sufficient Conditions for Synchronous Bursting

In this section we provide sufficient conditions for the existence of synchronous bursting oscillations in a three-cell network of cells with all-to-all coupling modeled by equations (2.10)–(2.12). The results in this section generalize to networks with an arbitrary number of

cells with all-to-all coupling. The technique used can also be generalized to other architectures; see Section 2.3 for details. Also for convenience, we assume one cell in this network is intrinsically quiescent and another cell is tonic in the absence of input. We will place some restrictions on the third cell, again for notational convenience. These restrictions will arise in the context of the proof. The proof that the provided conditions are sufficient for synchronous bursting works in the $\varepsilon = 0$ limit, though with sufficient effort it may be extended to $0 < \varepsilon << 1$, see [32]. We also assume without loss of generality that $g_{ton} = 0$, because the arguments below are based on the shapes of the nullclines and the times of flight, which are qualitatively independent of $g_{ton}$.

Suppose that $j \in \mathbb{Z}_3$. Let $j = 0$ correspond to the intrinsically quiescent cell, which we shall also call $Q$ for short. Let $j = 2$ correspond to the intrinsically tonic cell, also called $T$ below. Further, $j = 1$ will denote the other cell, which we will abbreviate by $A$ for "added." The architecture is such that cell $j$ receives synaptic input from cells $j - 1$ and $j + 1$.

In the $\varepsilon = 0$ limit, the dynamics for $v_j$ and $s_j$ are reduced to algebraic equations, and the $h_j$ dynamics becomes relevant. For a fixed $s_{j-1}$ and $s_{j+1}$ and a given $h_j$, there are up to three corresponding values of $v_j$, one for each branch of the $v_j$-nullcline. However, if we restrict our view to each branch individually, the monotonic nature of these branches permits us to write $v_j = v_j^X(h_j, s_{j-1}, s_{j+1})$ for $X \in \{L, M, R\}$. Further, since $s_j$ can be considered as a function of $v_j$, we can write $s_j = s_j^X(h_j, s_{j-1}, s_{j+1})$, for $X \in \{L, M, R\}$. Since there are three cells and each could be on either the left or right branch of the $v$-nullcline, there are many possible slow subsystems. Due to the algebraic dependencies detailed above, to describe the dynamics for $\overrightarrow{h} = [h_0, h_1, h_2]$, we use the notation $\dot{\overrightarrow{h}} = G_{XYZ}(h)$ if $v_0$, $v_1$, $v_2$ are on the $X$, $Y$, $Z$ branches of their respective $v$-nullclines, for $X, Y, Z \in \{L, M, R\}$.

For each cell $j$ we label the $h$ coordinate of the left knee, right knee, and fixed point by $LK(s_{j-1}, s_{j+1}; j), RK(s_{j-1}, s_{j+1}; j), FP(s_{j-1}, s_{j+1}; j)$ respectively. Below, we justify this functional notation by the implicit function theorem. We will carry through the analysis for equations (2.10)–(2.12), though it is clear that the techniques apply to any model with similar structure.

**Lemma 2.2.1.** *The $h$-coordinates of the left and right knees and the fixed point of cell$_j$,*

*modeled by equations (2.10)–(2.12), are monotonically decreasing functions of the synaptic input variables $s_{j-1}$ and $s_{j+1}$.*

*Proof.* Note that $v_j$ obeys the equation:

$$\begin{aligned} \dot{v_j} &= (-g_{NaP} m_{P,\infty}(v_j)(v_j - E_{Na}) h_j - g_L(v_j - E_L) - \\ & \quad g_{j,j-1} s_{j-1}(v_j - E_{syn-e}) - g_{j,j+1} s_{j+1}(v_j - E_{syn-e}))/C_m \end{aligned} \tag{2.14}$$

We solve $\dot{v_j} = 0$ for $h_j$ to find $F(v_j, s_{j-1}, s_{j+1})$, the $v$-nullcline:

$$h_j = F(v_j, s_{j-1}, s_{j+1}) := \frac{-g_{j,j-1} s_{j-1}(v_j - E_{syn-e}) - g_{j,j+1} s_{j+1}(v_j - E_{syn-e}) - g_L(v_j - E_L)}{g_{NaP} m_{p,\infty}(v_j)(v_j - E_{Na})} \tag{2.15}$$

For fixed synaptic input variables $s^*_{j-1}, s^*_{j+1}$, the $v$-coordinate of the right knee of cell $j$, denoted by $v_j^{RK}$, satisfies

$$\begin{aligned} \left.\frac{\partial F}{\partial v_j}\right|_{(v_j^{RK}, s^*_{j-1}, s^*_{j+1})} =: F_{v_j}(v_j^{RK}, s^*_{j-1}, s^*_{j+1}) &= 0 \\ \left.\frac{\partial^2 F}{\partial v_j^2}\right|_{(v_j^{RK}, s^*_{j-1}, s^*_{j+1})} =: F_{v_j v_j}(v_j^{RK}, s^*_{j-1}, s^*_{j+1}) &> 0 \end{aligned}$$

The Implicit Function Theorem applied to $F_{v_j}(v_j^{RK}, s^*_{j-1}, s^*_{j+1})$ asserts the existence of a unique $a_j(s_{j-1})$ and a neighborhood $N_1$ around $s^*_{j-1}$ such that for all $s_{j-1} \in N_1$ we have $F_{v_j}(a_j(s_{j-1}), s_{j-1}, s^*_{j+1}) = 0$, and so

$$\begin{aligned} RK(s_{j-1}, s^*_{j+1}; j) &= F(a_j(s_{j-1}), s_{j-1}, s^*_{j+1}) \\ \left.\frac{\partial RK}{\partial s_{j-1}}\right|_{(s_{j-1}, s_{j+1})} =: RK_{s_{j-1}}(s_{j-1}, s^*_{j+1}; j) &= F_{v_j}(a_j(s_{j-1}), s_{j-1}, s^*_{j+1}) a_j'(s_{j-1}) + F_{s_{j-1}}(a_j(s_{j-1}), s_{j-1}, s^*_{j+1}) \\ RK_{s_{j-1}}(s_{j-1}, s^*_{j+1}; j) &= \frac{-g_{j,j-1}(a_j(s_{j-1}) - E_{syn-e})}{g_{NaP} m_{p,\infty}(a_j(s_{j-1}))(a_j(s_{j-1}) - E_{Na})} \end{aligned}$$

Since $a_j(s_{j-1}) - E_{syn-e} < 0$ and $a_j(s_{j-1}) - E_{Na} < 0$, and all other terms are positive, we conclude that

$$RK_{s_{j-1}}(s_{j-1}, s^*_{j+1}; j) < 0$$

A similar argument grants that there is a unique function $b_j(s_{j+1})$ and a neighborhood $N_2$ of $s^*_{j+1}$ such that for all $s_{j+1} \in N_2$ we may conclude

$$RK_{s_{j+1}}(s_{j-1}, s_{j+1}; j) < 0$$

Similar arguments also yield that the left knee is a monotonically decreasing function of both synaptic inputs. Also, solving $\dot{h_j} = 0$ for $h_j$ yields $h_j = H(v_j)$, the $h_j$-nullcline. The intersection of the $v$ and $h$-nullclines satisfies $F(v_j, s_{j-1}, s_{j+1}) - H(v_j) = 0$. For $v_j$ corresponding to the left and right branches of the $v_j$-nullcline, by assumption $F_{v_j}(s_{j-1}, s_{j+1}) > 0$, and also by assumption $H_{v_j}(v_j) < 0$, so the implicit function theorem again applies, yielding a function $\psi(s_{j-1})$ or $\phi(s_{j+1})$, each describing the change of the $v$ coordinate of the fixed point under variation of $s_{j-1}$ or $s_{j+1}$ respectively. Straightforward differentiation yields that $\psi'(s_{j-1}) > 0$ and $\phi'(s_{j+1}) > 0$, and combined again with the fact that the $h_j$-nullcline is a monotonically decreasing function of $v_j$, we see that $\frac{\partial FP}{\partial s_{j-1}}\Big|_{(v_j, s_{j-1}, s_{j+1})} < 0$. Similarly, the $h$ coordinate of the fixed point is a monotonically decreasing function of $s_{j+1}$. □

The monotonicity of the knees justifies the functional definition of $D_Q, D_A, D_T, I_Q, I_A, I_T$ in Table 2.2 below.

The proof we provide for the existence of a periodic orbit corresponding to synchronous bursting relies on the Brouwer Fixed Point theorem, for which there is a constructive proof.

**Theorem 2.2.2.** *Let $D_1, D_2, D_3$ be closed and bounded intervals in $\mathbb{R}^3$. Consider a set $D = D_1 \times D_2 \times D_3$, and a continuous function $B : D \to D$. There is an $x^* \in D$ such that $B(x^*) = x^*$.*

*Proof.* See reference [30]. □

We work in the $\varepsilon = 0$ limit, so that for any particular triple $(h_1, h_2, h_3)$ we precisely know the possible states of the entire solution via the algebraic relations previously mentioned. We will begin by considering the set $\Omega$ consisting of all possible $(h_1, h_2, h_3)$ coordinates where all three cells can enter the silent phase simultaneously, with $v_j = v_j^L(h_j, 0, 0)$ and $s_j = 0$ for all $j$, corresponding to all cells being in the silent phase. We will construct a continuous

function $M : \Omega \to \Omega$, by considering the evolution of a trajectory with arbitrary initial condition in $\Omega$ until all cells return to the silent phase. Due to the fact that solutions to ODEs depend continuously on their initial conditions, since $M$ simply evolves a trajectory with initial conditions in $\Omega$, $M$ will be a continuous function. In order to construct $M$ in such a way that it will map $\Omega$ to $\Omega$, we need estimates on the time it will take each cell to change phases, and it is on these estimates that we will place our assumptions. We note that $M$ can be viewed as a Poincaré map on the 3 dimensional section $\Omega$ of the 9d phase space. The proposition below states that under certain assumptions on times of passage associated with trajectories with initial conditions in $\Omega$, there exists a periodic synchronous bursting solution to equations (2.10)–(2.12). Roughly speaking, the assumptions set an order in which the cells enter the active phase; first $T$ will enter the active phase, then $A$ will follow, and at last $Q$ will enter the active phase before $A$ can return to the silent phase ((A2) and (A3)). Finally, we set an assumption (A4) that will guarantee that all cells enter the silent phase simultaneously, which ensures that $M$ will map $\Omega$ to $\Omega$ (otherwise, a cell that entered the silent phase first may have time to evolve such that its $h$ coordinate leaves $\Omega$). To prove this result, we will show that these assumptions imply that even in the absolute worst case scenario, every cell will jump from the silent to the active phase before any cell falls from the active to the silent phase and all cells will eventually enter the silent phase together, with respect to the fast timescale.

Rather than writing out each mathematical definition relevant to the proof individually, we have collected these definitions in Table 2.2. The reader may find it useful to consult this table in conjunction with Table 2.3, which gives heuristic interpretations of the mathematical definitions. The reader may also find it illuminating to refer to Figures 2.16,2.17,2.18, 2.19, and 2.20 for a graphical representation of some of the critical times involved in the proof of the existence of a synchronous bursting solution given below.

Figure 2.17 illustrates the definition of $\tau^*_{\frac{1}{3}}$. We have omitted a similar figure for $T_0$. The idea behind these two quantities is that we want to ensure that $T$ enters the active phase before $A$. Therefore, we need to compare the shortest possible time $A$ could take to reach its left knee from the silent phase with the longest possible time $T$ could take to reach its left knee from the silent phase.

Figure 2.18 illustrates the definition of $\tau_{\frac{2}{3}}(h_Q, h_T, h_A)$. For a given coordinate $(h_Q, h_T, h_A)$ in the silent phase, this gives the time it takes for $Q$ to reach the active phase from that point. An upper bound on $\tau_{\frac{2}{3}}(h_Q, h_T, h_A)$ is given by $T_{\frac{2}{3}}$. This bound must be compared against $\tau^*_{\frac{2}{3}}$, which is the shortest possible time it could take for $A$ to enter the silent phase from the active phase (Figure 2.19).

Finally, Figure 2.20 illustrates the quantity $T_A$. As stated above, we will require all cells to enter the silent phase simultaneously, though we prescribe a particular falling order to track the corresponding change in the nullclines. First, $Q$ will enter the silent phase, and then $A$ will follow. For $A$ to be able to enter the silent phase upon the sudden removal of synaptic input from $Q$, the coordinate $h_A$ must be below $RK(0, s_T; A)$, which takes its lowest possible value if $s_T = s_{max}$. Correspondingly, $T_A$ is defined using $RK(0, s_{max})$ as shown in Figure 2.20. $T_T$ denotes a similar longest active time for the tonic cell, and a similar figure could be generated to illustrate how it is defined. If $T_A$ and $T_T$ are both less than $T_1$, then both the $A$ and $T$ cells will return to the silent phase when $Q$ does.

We make the following assumptions about some of the quantities defined in Table 2.2:

(A1) Let the added cell $A$ be such that when $s_T = \tilde{s}_T$ and $s_Q = \tilde{s}_Q$ the fixed point for the $A$ subsystem occurs on the right branch of the $v_A$-nullcline.

(A2) $T_0 < \tau^*_{\frac{1}{3}}$

(A3) $T_{\frac{2}{3}} < \tau^*_{\frac{2}{3}}$

(A4) $\max(T_A, T_T) < T_1$

**Proposition 2.2.3.** *Under assumptions (A1)–(A4), with the definitions in Table 2.2, the system of three cells modeled by equations (2.10)(2.11)(2.12) admits a periodic orbit representing synchronous bursting.*

Before stating the proof of the above proposition, we introduce one more bit of notation.

**Definition 2.2.4.** *Allow $x \cdot t$ to represent the result of applying the flow of equations (2.10)–(2.12) to the initial condition $x$ for $t$ units of model time.*

*Proof.* Assume that (A1)–(A4) hold. Given the definitions in Table 1, the proof is rather concise. First, let $x_0 = (h_Q^0, h_A^0, h_T^0) \in \Omega$. Because $T_0 < \tau_{\frac{1}{3}}^*$ (A2), $T$ is the first cell to enter the active phase, after time $\tau_0(x_0)$. We then allow $x_1 = x_0 \cdot \tau_0(x_0)$. Since $Q$ is silent under input from $T$, we evolve until $A$ enters the active phase, after an additional time $\tau_{1/3}(x_0)$, and set $x_2 = x_1 \cdot \tau_{\frac{1}{3}}(x_1)$. The condition $T_{\frac{2}{3}} < \tau_{\frac{2}{3}}^*$ (A3) asserts that $Q$ will always join the active phase before $A$ can fall down to the silent phase. Synaptic input from $A$ lowers T's fixed point. The result of this is that $T$ cannot return to the silent phase until the synaptic input is removed. Thus, we call $x_3 = x_2 \cdot \tau_{\frac{2}{3}}(x_2)$, and after time $\tau_0(x_0) + \tau_{\frac{1}{3}}(x_1) + \tau_{\frac{2}{3}}(x_2)$, all three cells are in the active phase simultaneously. When $Q$ falls down to the silent phase, $h_Q \in D_Q$ by the definition of $D_Q$. Finally, the condition $\max(T_A, T_T) < T_1$ (A4) asserts that when $Q$ falls down to the silent phase, $h_A \in D_A$ and $h_T \in D_T$ and both $A$ and $T$ will return to the silent phase. If we define $x_4 = x_3 \cdot \tau_1(x_3)$, then we have $x_4 \in \Omega$. Thus, the map $M : x_0 \to x_4$ is a continuous map from $\Omega$ into $\Omega$, and by Brouwer's fixed point theorem, there is an $x^*$ such that $M(x^*) = x^*$. Thus, in the $\varepsilon = 0$ limit, the solution with initial condition corresponding to $x^*$ is a periodic orbit. By construction, this orbit meets our definition of a synchronous bursting solution. □

Numerical explorations indicate that assumptions (A1)–(A4) are easy to satisfy in the case where two cells are intrinsically tonic and the third is intrinsically quiescent. Parameter sets for which the model satisfied (A1)–(A4) with one cell intrinsically tonic, one intrinsically bursting, and one intrinsically quiescent were harder to find. An example of such a set consists of the parameter values from Table 2.1, except $g_{ij} = 0.0875$, $g_{NaP,1} = 0.795$, $g_{NaP,2} = 1.6945$, $g_{NaP,3} = 0.705$, $g_{L,1} = 0.898$, $g_{L,2} = 1.94709$, $g_{L,3} = 1.209$.

### 2.2.3 Observations on Failures to Produce Synchronous Bursts

In searching for parameters sets for which (A1)–(A4) hold and one cell is intrinsically bursting, the condition $T_{\frac{2}{3}} < \tau_{\frac{2}{3}}^*$ proved to be the hardest to satisfy. While it is true that this condition is fairly restrictive, it reveals a key feature of three-cell networks that include a cell that intrinsically bursts: if the synaptic input from the tonic cell is not strong enough to cause the bursting cell to become tonic itself, then the bursting cell has an opportunity to

re-enter the silent phase before the quiescent cell can enter the active phase. More precisely, suppose that $s_T = \tilde{s}_T$ and $s_Q = 0$. Suppose that under the corresponding level of input, the fixed point for cell $A$ falls on the middle branch of the $v_A$-nullcline. In this case, the condition $T_{\frac{2}{3}} < \tau^*_{\frac{2}{3}}$ can be violated. If this occurs, then there may be an $(h_1, h_2, h_3)$ such that $Q$ fails to enter the active phase before $A$ enters the silent phase, which would violate our necessary conditions for synchronous bursting. In our numerical explorations of these three-cell networks, we identified this premature return to the silent phase as the most common cause for a network to fail to burst synchronously. Addition of a tonic cell instead of a bursting cell ensures that the added cell will not fall down from the active phase to the silent phase before the quiescent cell has a chance to jump up, while addition of a quiescent cell yields a relatively late entry of the added cell into the active phase, which makes it less likely that the original quiescent cell will get stuck in the silent phase.

## 2.3 SUFFICIENT CONDITIONS: SYNCHRONOUS BURSTING FOR OTHER ARCHITECTURES AND $N \geq 3$

The conditions presented in Section 2.2.2 applied to a network of 3 relaxation oscillators. These conditions generalize naturally for a network of $n$ cells, even if the architecture is not all-to-all. Recall that the network as a whole can be thought of as being in one of two stages, "cells moving to the active phase" and "cells moving to the silent phase." Consider a starting set $D_1 \times D_2 \times \ldots \times D_n$, where the $D_j$ are analogous to $D_Q, D_A, D_T$ in table 2.2. When the network is in the stage where cells are moving to the active phase, the following rules should be used to generate the sufficient conditions. First, an order in which the cells are going to enter the active phase must be decided upon, and conditions must be placed to ensure that this will be the order for any initial condition on the cross product of possible locations where the cells could re-enter the silent phase. Once this order is established, then use $C$ to denote the next cell in line to enter the active phase. Consider $T_C$ to be the longest possible time $C$ could take to enter the active phase. Next, look at all the cells currently in the active phase. Calculate the fastest-case scenario for a cell to return to the silent phase. As in Figure 2.19,

realize that the $h$ coordinate of a cell in the active phase evolves fastest under maximal input from the other cells in the active phase. If it happened that all synaptic inputs decayed to some minimal value by the time the $h$ coordinate reached the right knee height, the cell would transition to the silent phase. Make this calculation for each active cell, and allow $T_A$ to be the smallest of all these times. Then the sufficient condition becomes $T_C < T_A$. Repeat this process for every cell in the silent phase, each time evolving the network until $C$ enters the active phase.

When the network is returning cells to the silent phase, numerical results suggest an approach to derive a reasonable set of sufficient conditions for synchrony to be maintained. As in the first case, decide on an order for the cells to return to the silent phase. Then the sufficient conditions become a cascade; as each cell enters the silent phase, the right knees of all other cells are raised. The sufficient condition is then, that the next cell that is to return to the silent phase must be below its new right knee. Repeat this condition for each cell until all of the cells have returned to the silent phase.

This return condition in particular can be relaxed a bit. The Brouwer fixed point theorem requires a map to return a closed set to itself. Thus, if the cells do not return to the silent phase simultaneously, as long as the last cell enters the silent phase before any cell leaves the starting set, we construct a map that evolves the system until the last cell returns to the silent phase. This map will return the starting set to itself, and so the fixed point theorem yields a fixed point, which will be a periodic orbit of the ODE.

For a network with a different architecture, the same steps as above must be applied. However, care must be taken when determining the order for the cells transitioning between phases. A network other than all-to-all coupling is more complicated because when a cell switches between the active and silent phases, it may not update the nullclines of every other cell in the network. As long as this variation is handled properly in calculating the sheet of knees each cell must reach to switch phases, the proof does not change. In fact, calculating the fastest time in which a cell can return to the silent phase can be kept the same, again because the $h$ dynamics are fastest under full input. This shortcut may be undesirable; with less than full connectivity the bound will be significantly tighter if the network coupling architecture is incorporated properly.

On the other hand, an architecture including self coupling may promote synchronous oscillations. We identified in Section 2.2.3 that intrinsically bursting cells that do not become tonic under synaptic input from the tonic cell may prematurely fall down to the silent phase before the rest of the network can join the active phase. However, should these intrinsically bursting cells provide synaptic input to themselves, that extra kick may be enough to push their critical point to the right branch, inducing a tonic behavior. As long as the intrinsically quiescent cell can fall down to the silent phase under full synaptic input, the all-to-all architecture with self-coupling should support synchronous oscillations more robustly than the architecture considered throughout this work.

## 2.4 NUMERICAL EXPERIMENTS

### 2.4.1 Implementation

The numerical results presented in this section were gathered with the MATLAB programming language (The MathWorks, Natick, MA). The equations (2.10),(2.11),(2.12) are very stiff, and speed became an issue due to the large number of simulations we ran. To speed up our simulations, we used a C implementation of the CVODE package from SUNDIALS [26] for the differential equation integration, compiled as a MATLAB function by way of the mex command.

We allowed a transient of 1000 milliseconds of model time before any conditions on bursting were checked. Typically, integration was done for 10000 milliseconds. When a cell's synaptic output increased beyond 60% of the maximum possible output value, we recorded that the cell entered the active phase. On the other hand, when the cell's synaptic output decreased below 20%, we recorded that the cell entered the silent phase. For purposes of approximating the frequency of synchronous activity, we track each time when all three cells have re-entered the silent phase after all three cells have been in the active phase.

The necessary conditions given in Section 2.2.1 provide a guideline for checking if a solution is synchronous. We implemented these conditions by using a series of boolean flags

that track the states for cells $j+1$, $j-1$ relative to cell $j$. Should a solution fail to meet the necessary conditions at any time after the initial transient, the integration stops and the solution is declared to be asynchronous. One shortcoming of this implementation is that a solution may be declared synchronous if the first time the necessary conditions are violated occurs after 10000 milliseconds. A second shortcoming is that we may be misled by parameter values supporting bistability. Although we cannot guarantee that bistability does not arise, additional numerical explorations suggested that it was rare in the parameter regimes considered.

### 2.4.2 Which Cells Promote Synchronous Bursting?

Intuitively, a cell that is intrinsically bursting seems like a safe cell to add to a network to promote synchronous bursting; however, Section 2.2.3 casts doubt on this intuition. We tested this intuition more systematically by performing the following numerical experiment. First, pick at random one cell that is intrinsically tonic and another that is intrinsically quiescent. Next, partition $g_{NaP}g_L$ space into a mesh, and use each mesh point to form a third cell to be coupled with the other two into a three-cell network. For each network, integrate equations (2.10)–(2.12) and check whether the network sustains synchronous bursting. We present a colorization of $g_{NaP}g_L$ space as follows. If the third cell failed to create a synchronous burst, we color the coordinate red. Otherwise we color the coordinate blue if the added cell was intrinsically quiescent, green if it was intrinsically bursting, and black if it was intrinsically tonic. We repeated this experiment with many different random choices of the $Q, T$ pair. After this numerical exploration, certain patterns emerged in these colorizations. Below, in Figure 2.21, we provide examples that qualitatively cover the breadth of our numerical findings. It may be useful to refer to Figure 2.2 to recall the division of $g_{NaP}g_L$ space into regions where the resultant cell is quiescent, bursting, or tonic. We also direct the web-enabled reader to Figure 2.22 for an animated comparison between the original partition of $g_{NaP}g_L$ space and one example of the numerical experiment detailed here. A brief analysis of which underlying cell pairs yielded each type of synchronization configuration shown in Figure 2.21 can be found in Section 2.4.6.

### 2.4.3 Explanation of the Mechanisms Involved in Synchronous Bursting

In each panel of Figure 2.21, large $g_L/g_{NaP}$ or small $g_L/g_{NaP}$ in the added cell leads to an absence of synchronous bursting in the network. These failures correspond to cases when the third cell is "too quiescent," that is, even under full input from the other two cells it cannot activate, or "too tonic," in that when input is removed, it cannot transition to the silent phase. Outside of these extreme ranges of $g_L$ and $g_{NaP}$, it was often those coordinates that represent the addition of an intrinsically bursting cell that failed to produce synchronous network wide bursting. In this section we attempt to explain the mechanisms underlying the changes in network dynamics that occur at the boundaries between the red region and non-red regions of the parameter space.

To explain the results of our experiments, we will for convenience provide arguments based on the positions of the knees of various nullclines. It should be noted that more precise arguments should be expressed in terms of times of flight, as in the proof of the existence of synchronous solutions in Section 2.2.2. However, numerically we observe that the time of flight to the knee in the silent phase is an increasing function of the $h$-coordinate of the left knee, and a decreasing function of the $h$-coordinate of the right knee. This result allows an easy translation from knee-based arguments to the time-based analogue.

We consider four basic movements in $g_{NaP}g_L$ space corresponding to increasing or decreasing $g_{NaP}$ or $g_L$ independently. Keeping in mind the insight from Section 2.2.3, that the most common source of network failure is for a cell to prematurely return to the silent phase, we will explain how varying $g_{NaP}$ or $g_L$ may affect the bursting behavior of the system. Specifically we are interested in what happens to induce a switch from a red region to a non-red region. That is, we seek to explain the bifurcation from non-synchronous solutions to synchronous solutions resulting from changes in $g_{NaP}$ or $g_L$.

As we did in Section 2.2.2, we can use the implicit function theorem to write the $h$-coordinates of the left knee and right knee each as a function of $g_L$. By straightforward differentiation of equation (2.15), it is then easy to see that the $h$-coordinates of the left and right knees are monotone functions of $g_L$, but an important difference is that the $h$-coordinate of the left knee is much more sensitive to changes in $g_L$, so that for fixed $(h_Q, h_A, h_T) \in$

$W, \tau_{\frac{1}{3}}(h_Q, h_A, h_T)$ is a monotonically increasing function of $g_L$. Consider then the crossing from a red-region to a non-red region as $g_L$ increases. The result of the added cell having a higher $g_L$ is that it spends more time in the silent phase. This means that the difference between the times when the $A$ cell and $Q$ cell will enter the active phase is smaller, and thus it is less likely to be the case that $A$ will prematurely return to the silent phase. This explains the transition through the red-non-red border as $g_L$ increases for all the panels in Figure 2.21, except for Figure 21(b). In Figure 21(b), the only cell within a reasonable parameter regime that could not be successfully added to the network to achieve synchronous bursting was another tonic cell. The explanation for the transition in this case is that the $Q$ for this particular experiment, under synaptic input from the other cells, has a nullcline where the left and right knees have very similar $h$ coordinates. The result is that assumption (A4) is violated. In particular, $T$ will not return to the silent phase with $Q$ each time, because $Q$ does not spend enough time in the active phase for $h_T$ to fall below the $h$-coordinate of the required knee. Increasing $g_L$ to the added cell in this case still causes the $A$ to spend more time in the silent phase, but the beneficial effect is that when $Q$ enters the active phase, $h_T$ is lower, and thus more likely to sink below the knee as required for $T$ to join the silent phase when $Q$ does.

This is not the whole picture, however. Consider those added cells such that when they receive input from a tonic source, they have a fixed point on the right branch of the $v$-nullcline. Such cells will not return to the silent phase until $Q$ first enters the active phase and then returns to the silent phase. If we increase the added cell's value of $g_L$ from such a configuration, it can happen that the intersection of the $v_A$ and $h_A$-nullclines will occur on the middle branch of the $v_A$-nullcline. Suddenly, it becomes possible for $A$ to reenter the silent phase before $Q$ can join the active phase. Reversing this process reveals a mechanism by which lowering $g_L$ for the added cell can allow the network to burst synchronously, and so explains the transition from a red region to a non-red region by lowering $g_L$.

To understand the result of changing $g_{NaP}$, we again use the implicit function theorem, but this time we write the $v$-coordinates of the left knee and right knee each as a function of $g_{NaP}$, say $v = \psi(g_{NaP})$. Unfortunately, it is not true that the $h$-coordinates of the knees of a cell are monotonically dependent on $g_{NaP}$, and so our analysis of crossing the red-to-non-red

border is more restricted. Increasing $g_{NaP}$ has the general effect of sliding the $v_A$-nullcline to the left, which causes the intersection with the $h_A$-nullcline to move to the right, possibly causing the intersection point to change from the center to the right branch. We claim that the mechanism for creating synchronous bursting by increasing $g_{NaP}$ is analogous to the one generated by lowering $g_L$, consistent with the positive slopes of the boundary curves in Figure 2.21. That is, increasing $g_{NaP}$ puts the intersection point of the $v_A$ and $h_A$-nullclines for the added cell on the right branch of the $v_A$-nullcline when $T$ is in the active phase. Conversely, lowering $g_{NaP}$ should have an effect analogous to raising $g_L$. Indeed, in the absence of synaptic coupling, lowering $g_{NaP}$ increases the $h$-coordinate of the knees. When $A$ is receiving synaptic input from $T$, the situation is not as obvious. We seek conditions for which the left knee will increase as $g_{NaP}$ decreases. Allowing $v = \psi(g_{NaP})$ and differentiating equation (2.15) with respect to $g_{NaP}$ yields the relation

$$g_L > \frac{-g_{s_{j+1}} s_{j+1}(\psi(g_{NaP}) - E_{syn-e})}{\psi(g_{NaP}) - E_L} \tag{2.16}$$

For $g_L$ satisfying (2.16), the left knee is a monotone decreasing function of $g_{NaP}$, when $T$ is in the active phase. In this case when $g_{NaP}$ is lowered, the left knee's $h$-coordinate again increases more than the right knee's $h$-coordinate, and the analysis is the same as that of the variation of $g_L$ we presented previously.

In summary, we identified two primary transitions from asynchronous network dynamics to synchronous network oscillations. One transition mechanism is to eliminate the possibility of the added cell prematurely entering the silent phase. If the added cell can prematurely return to the silent phase, it must be because under input from the tonic cell the intersection of the $v_A$ and $h_A$-nullclines is on the middle branch of the $v_A$-nullcline. When this intersection is moved (by changing $g_L$ or $g_{NaP}$) to the right branch of the $v_A$-nullcline, the added cell no longer can return to the silent phase until after the quiescent cell first enters the active phase and then re-enters the silent phase. The other transition mechanism involves keeping the quiescent cell in the silent phase for an extended period of time, which allows the tonic cell to approach the intersection of the $v_T$ and $h_T$-nullclines. The closer the tonic cell is to this intersection point, the more likely it is to have its $h$-coordinate sink below the right knee when the quiescent cell returns to the silent phase. The mechanism provided for buying this

extra time is to make the added cell not only quiescent, but to ensure that the $h$-coordinate of its left knee is high even under synaptic input from the tonic cell, though not so high that it intersects the $h$-nullcline on the left branch of the $v_A$-nullcline, preventing it from being active. In this way, the quiescent cell and the added cell will spend more time in the silent phase and will enter the active phase at similar times, which prevents one cell from returning to the silent phase before the other cell is ready to follow.

This analysis of the bifurcation from asynchronous network dynamics to synchronous network oscillations reveals what may be called a weakness of a neuron with intrinsically bursting dynamics. When such a bursting cell is added and receives synaptic input from the tonic cell, the intersection of the $v_A$ and $h_A$-nullclines may still be on the center branch of the $v_A$-nullcline. This presents the opportunity for $A$ to enter the silent phase before $Q$ enters the active phase. There are two primary ways to correct this phenomenon. We can increase the $h$-coordinate of $A$'s left knee, thereby giving $Q$ more time to enter the active phase, or we can change the position of $A$'s right knee enough that the intersection of the $v_A$ and $h_A$-nullclines falls on the right branch of the $v_A$-nullcline. Such adjustments are required less frequently for added cells with intrinsically quiescent or tonic dynamics. When a cell is added with intrinsically tonic dynamics, it cannot prematurely return to the silent phase. Therefore the only concern is that $Q$ spends enough time in the active phase to allow $T$ and $A$ to return to the silent phase. On the other hand, if the added cell is intrinsically quiescent, we potentially must still face the issue of $A$ returning to the silent phase before $Q$ enters the active phase. However, the left knees of $Q$ and $A$ have more similar $h$-coordinates than if $A$ were not intrinsically quiescent and hence the times at which they enter the active phase will differ by less than if $A$ had any other intrinsic dynamics. Therefore it is more likely that $Q$ will follow $A$ into the active phase. Keeping such results in mind, it is perhaps unsurprising that when adding a third cell to a network already containing a quiescent and tonic cell, it is those added cells which are intrinsically bursting that are most likely to fail to create synchronous oscillations.

### 2.4.4 Which Cells Promote Frequency Modulation?

Another important aspect of the preBötC is that it exhibits a wide range of bursting frequencies, perhaps influenced by an outside population of tonically active cells. Biologically, control over frequency for the preBötC would allow it to adapt to changes in environmental and metabolic demands. Further, the system should not be too sensitive to variation of a control parameter, such as the conductance $g_{ton}$ of the tonic drive current $I_{tonic}$ (i.e., $|\frac{dfrequency}{dg_{ton}}|$ should not be too big). Intuitively, it may seem that a cell that is intrinsically bursting may enhance this dynamic range of network bursting, given that it is naturally tuned to burst. We performed a numerical experiment, however, which suggests that this may not be the case. In our experiment, we repeatedly selected two cells, one intrinsically quiescent and one intrinsically tonic, at random. For each such pair, we added a third cell with $g_{NaP} = 2$ and varied $g_L$ systematically in the interval $(.5, 4)$. Finally, for each value of $g_L$, we varied $g_{ton} \in (0, .25)$, taking $g_{ton} = 0$ as the baseline value without loss of generality. For each $(g_L, g_{ton})$ pair, we recorded the frequency of the network, if it bursted, as the inverse of the average period of synchronous oscillations, recording 0 if synchronous oscillations were not obtained. Figure 2.23 illustrates some of the results from this experiment.

Our simulations showed that adding an intrinsically bursting cell to the network did not promote synchronous oscillations particularly well, even under variation of the control parameter $g_{ton}$. Even in those cases where the network demonstrated synchronous oscillations over a wide range of $g_{ton}$ when an intrinsically bursting cell was added, we did not observe a wide range of frequencies for these synchronous oscillations. On the other hand, we saw that adding a quiescent cell often promoted synchronous oscillations under a broad range of $g_{ton}$, and further, when the network produced synchronous oscillations over a wide frequency range, it was commonly an intrinsically quiescent cell that had been added.

### 2.4.5 Explanation of the Mechanisms Involved in Frequency Control

The numerical experiments illustrated in Figure 2.23 have a trait reminiscent of those in Figure 2.21: it is common for the network to fail to exhibit synchronous oscillations when the added cell is intrinsically bursting. This experiment gives us information about more

than just the existence of synchronous oscillations, however. It also indicates the range of frequencies that the three-cell networks can produce, as well as their robustness to variation of the control parameter $g_{ton}$. We rescaled the parameters relating to the time constants from Butera's original model in [4] to speed up the simulations, so the frequencies recorded here do not match the frequencies seen in the preBötC. However, our qualitative results should carry over to biologically relevant time scales. Based on the criteria discussed in Section 2.4.4, an optimal network should generate a significant color variation extending over a wide range of $g_{ton}$ values. We consistently find that it is the addition of a quiescent cell to the network that allows the network to burst at a wide range of frequencies over a wide range of values of $g_{ton}$.

We offer an explanation for this result by analyzing the $v$-nullclines of the cells. Suppose we have a network consisting of two quiescent cells and one tonic cell. The control parameter $g_{ton}$ changes the strength of the excitatory synaptic current $I_{tonic-e}$ in equation (2.14), and mathematically, varying $g_{ton}$ is analogous to varying a synaptic conductance variable $s$. Therefore, an argument similar to those in Section 2.2.2 implies that the $h$-coordinate of the left knee of the $v$-nullcline is a monotonic decreasing function of $g_{ton}$. Suppose that input from the tonic cell is insufficient to activate either quiescent cell; that is, they still have their fixed points on the left branches of their $v$-nullclines. Then it is variation of $g_{ton}$ that can push the knees low enough that one of the quiescent cells can activate through a singular Andronov-Hopf bifurcation where there is a $O(\varepsilon)$ pure imaginary eigenvalue corresponding to the change in the intersection point of the $v$ and $h$-nullclines of the activating cell. In the $\epsilon = 0$ case, for values of $g_{ton}$ beyond this bifurcation but still nearby, the quiescent cell can take arbitrarily long to activate, which yields an arbitrarily low network oscillation frequency. Thus, in the $\epsilon > 0$ case, this slow activation may account for the wide range of frequencies observed, even though arbitrarily low frequencies may no longer be achieved.

Interestingly, in some cases, adding a $T$ cell to a given $(Q, T)$ pair gives a similarly broad range of frequencies to that achieved by adding a $Q$ cell, as in Figures 23(a) and 23(b). Let $T$ and $Q$ be the intrinsically tonic and intrinsically quiescent cells fixed for this experiment and let $A$ be the added cell. We observe that the added cells that yield synchronous oscillations in this experiment for low levels of $g_{ton}$ are either intrinsically tonic or have high values of

$g_L$, corresponding to a high value of the $h$-coordinate of the left knee. For intermediate values of $g_L$, a high value of $g_{ton}$ is required to induce the network to burst synchronously. These observations together indicate that the left knee of the quiescent cell has a high $h$-coordinate, even under synaptic input from the tonic cell. With this insight in mind, it makes sense that adding a cell that will become tonic under input from $T$ will provide the $Q$ cell with adequate time to become active over a broad range of $g_{ton}$, with a correspondingly wide range of frequencies of synchronous oscillations. The mechanism for achieving this frequency range will be the same as before: two cells, $A$ and $T$, are stuck in the active phase, so increasing $g_{ton}$ lowers $LK(s_T, s_A; Q)$, which hastens the $Q$ cell's jump to the active phase. As $Q$ jumps into the active phase progressively faster with increased values of $g_{ton}$, the network frequency increases, since $Q$ always controls the network's return to the silent phase. On the other hand, an added cell that is intrinsically quiescent, with the $h$-coordinate of its left knee at a high value similar to that of the $Q$ cell's left knee, will jump up close to the time when $Q$ does, and so also generates synchronous network oscillations.

### 2.4.6 Additional analysis

Figure 2.24 highlights an auxiliary experiment designed to increase our understanding of the relative frequency of occurrence of the various configurations represented by the individual panels of Figure 2.21, and of which pairs of intrinsically quiescent and intrinsically tonic cells give rise to each configuration. For the numerical experiment, we selected a set of intrinsically quiescent and intrinsically tonic cells. For each pair, we explored network dynamics over a range of added cell parameters as in Section 2.4.2 and produced a diagram of the results, as Figure 2.21. We qualitatively categorized each pair based on the similarity of the resulting diagram to the individual panels from Figure 2.21. Figure 2.24 illustrates the pairs identified for two such panels.

One result of this experiment is, for each panel in Figure 2.21, Q cells with diverse $(g_{NaP}, g_L)$ values appear to generate similar synchrony configurations, and they do so by pairing with different T cells. This observation suggests that there may be multiple mechanisms through which each configuration represented in Figure 2.21 can arise. Interestingly,

the ratio $\frac{g_L}{g_{NaP}}$ for the quiescent cell seems to be important in selecting the configuration that results, although the parameters for the T cell participate as well.

We performed one more simulation to investigate this idea further. For each category from the above numerical experiment, we took the average value of the $g_L$ values for the intrinsically quiescent cells together with the average value of the $g_{NaP}$ values of those cells, to form an average intrinsically quiescent cell. Similarly, we formed an average intrinsically tonic cell for that category. We performed the simulation from Section 2.4.2.

We found that in several cases, the results from the intrinsically quiescent and intrinsically tonic pair generated with the averaged parameters did not match those generated from the individual pairs that were averaged. While this result may initially seem surprising, it reflects the fact that there may be multiple clusters of pairings that produce each configuration, whereas the average across all relevant pairs may lie outside all such clusters.

## 2.5 DISCUSSION

This chapter was motivated by the current debate about the source of synchronous rhythmic bursting in the heterogeneous network of cells coupled with synaptic excitation within the preBötC, which includes some intrinsically bursting neurons. Previously, it has been shown that cells that intrinsically burst are not required for sustained network-wide bursting in the preBötC [5, 55, 46, 56]. Numerical results do suggest, however, that the presence of neurons that burst under some range of tonic input current does enhance the robustness and frequency range of preBötC bursting. We have furthered this result by explaining why, of all such burst-capable cells, it is the ones that are intrinsically quiescent that best support synchronous bursting over a broad frequency range when embedded within a network, as long as intrinsically tonic cells are also present.

To arrive at this conclusion, we provided a definition of synchronous bursting and stated sufficient conditions under which a three-cell network will support a solution that satisfies this definition. To expand upon these results, we numerically explored the effects of adding intrinsically quiescent, bursting, or tonic cells to various (quiescent,tonic) pairs to form var-

ious three-cell networks with all-to-all coupling architectures. The central result from these experiments and analysis is that typically, if we start with a network containing an intrinsically quiescent and an intrinsically tonic cell, then it is preferable to add an intrinsically quiescent cell instead of an intrinsically bursting cell to endow the network with the capacity to burst synchronously and to achieve a wide frequency range under variation of the strength $g_{ton}$ of an excitatory synaptic drive. In brief, tonic cells play a key role in spreading synaptic excitation throughout the network and meanwhile remain active, ensuring that all other cells can enter the active phase. Intrinsically bursting neurons can also recruit quiescent cells, but they tend to return to the silent phase too soon, before quiescent cells can become active or before the persistent sodium current for the tonic cells can inactivate sufficiently to allow them to become silent along with the bursters. Intrinsically quiescent cells offer three advantages relative to bursters: because they enter the active phase more slowly, they (1) allow for slower overall burst frequencies to be achieved (see also [9]), (2) provide tonic cells with more inactivation time, decreasing their chances of being stuck in the active phase, and (3) provide extra time for other, even less excitable cells to be recruited to the active phase.

In our simulations, consistent with these features, we observe tightly synchronized transitions from the active phase to the silent phase, whereas the transitions from silent to active may be much less unified. Interestingly, single cells in the preBötC appear to be unable to initiate network bursts, which instead arise through a gradual recruitment [47], reflected in a diversity in active phase onset times observed experimentally [5, 6, 27]. On the other hand, too much spread could pose disadvantages for a strong activation of muscles associated with inspiration; thus, some of the oscillations on the low end of the frequency range we consider may not be biologically relevant. Clearly, less heterogeneous networks would yield tighter synchronization, but heterogeneity is a known feature of the preBötC. Beyond the possibility that our definition of synchrony is over-generous, another limitation of our study is the omission of spikes. Spiking effects may make important contributions to preBötC network bursting. For example, two intrinsically tonic preBötC model cells coupled with synaptic excitation may engage in synchronous bursting at a very low frequency, due to asynchrony at the level of spikes within bursts [1]. Nonetheless, our main qualitative result should encompass such spike-related phenomena: To maintain synchronous bursting over a broad range

of frequencies, it is optimal to introduce intrinsically quiescent cells into the network, such that a full range of dynamic regimes can be sampled by gradually turning up the strength of the drive (e.g. $g_{ton}$) to these cells, as long as there are enough tonically active cells in the network to recruit the quiescent cells to become active in the first place. Once these cells join the active phase, similar spike asynchrony effects should apply to the network dynamics, regardless of what behavior these added cells exhibited in the absence of coupling.

Since our results rely on synaptic activity for synchronization, the relative strengths of the synapses merit discussion. Changing $g_{syn}$ will change which neurons promote synchronous bursting and frequency control in Section 2.4.2 and Section 2.4.4. Decreasing $g_{syn}$ means that an intrinsically bursting cell is less likely to become tonic under synaptic input from another cell. Increasing $g_{syn}$ has the opposite effect, it will improve synchrony as long as at least one cell in the network can return to the silent phase. In light of Subsection 2.2.3, lower $g_{syn}$ will accentuate the fact that intrinsically quiescent cells promote synchronous bursting and frequency control. When $g_{syn}$ is elevated, intrinsically quiescent cells will still play this role, but to a lesser extent.

There are many ways to extend this work. In particular, this chapter focused on strong excitatory synaptic coupling and the results may change with weak synaptic excitation, or synaptic inhibition [73], or synaptic plasticity [29]. Further, to understand the dynamics of the preBötC, it is important to realize that the persistent sodium current is not the only mechanism that may yield intrinsically bursting dynamics. Rubin *et al.* developed a computational model for an experimentally grounded group pacemaker, showing that a calcium-activated nonspecific cation (CAN) current present in at least some cells in the preBötC can give rise to synchronous network bursting that depends crucially on synaptic interactions [56]. As such, an important next step will be to analyze the role of such a group pacemaker within a small heterogeneous network also including some cells featuring bursting dependent on the persistent sodium current. It may also be important to understand how the CAN and persistent sodium currents work together within the same cell, to help with the interpretation of various pharmacological experiments. This extension is the focus of Chapter 3.

Another important direction for future work is to consider the effect of noise on the overall

dynamics. In particular, a study of which network configurations sustain robust synchronous oscillations in the presence of noise is critical to an understanding of the overall picture of the preBötC. Headway into analysis of noise in the slow-fast dynamics of the preBötC has been made by Nesse et al. [39].

Ultimately, this chapter identified no significant advantage of adding intrinsically bursting neurons to a network of intrinsically quiescent and intrinsically tonic cells. In this model, changing $g_{NaP}$ or $g_L$ switches a cell's intrinsic behavior from quiescent to bursting to tonic, or from tonic to bursting to quiescent. The fact that intrinsically bursting neurons are in the center of this slice of parameter space may account for their presence in the preBötC. Indeed, if there were a similar region of the brain exhibiting network-wide synchronous bursting oscillations, and the mathematical model for the individual cells transitioned under parameter variation from intrinsically quiescent directly to tonic and then to bursting, then we would predict that cells with intrinsically bursting dynamics would not be prominent in the network.

Table 2.2: Mathematical definitions of symbols in Subsection 2.2.2

| Symbol | Mathematical Definition |
|---|---|
| $D_Q$ | $[RK(s_{max}, s_{max}; Q), RK(0, 0; Q)]$ |
| $D_A$ | $[RK(s_{max}, s_{max}; A), RK(0, 0; A)]$ |
| $D_T$ | $[RK(s_{max}, s_{max}; T), RK(0, 0; T)]$ |
| $\Omega$ | $D_Q \times D_A \times D_T$ |
| $U_Q$ | $[LK(s_{max}, s_{max}; Q), FP(0, 0; Q))]$ valid by (A3) |
| $I_Q$ | $[RK(s_{max}, s_{max}; Q), FP(0, 0; Q))$ |
| $I_A$ | $(FP(s_{max}, s_{max}; A), LK(0, 0; A)]$ valid by (A1) |
| $I_T$ | $(FP(s_{max}, s_{max}; T), LK(0, 0; T)]$ |
| $W$ | $I_Q \times I_A \times I_T$ |
| $\tau_0(h_Q, h_A, h_T)$ | time of flight (t.o.f.) from $(h_Q, h_A, h_T) \in \Omega$ to $h_T = LK(0, 0; T)$ under the flow $\dot{\overrightarrow{h}} = G_{LLL}(\overrightarrow{h})$ |
| $\tau_{\frac{1}{3}}(h_Q, h_A, h_T)$ | t.o.f. from $(h_Q, h_A, h_T) \in W$ to $h_A = LK(0, s_T; A)$, under the flow $G_{LLR}(\overrightarrow{h})$; see Figure 2.16 |
| $\tau^*_{\frac{1}{3}}$ | t.o.f. from $h_Q \in I_Q, h_T \in I_T, h_A = RK(0, 0; A)$ to $h_A = LK(0, 0, A)$, under the flow $\dot{\overrightarrow{h}} = G_{LLL}(\overrightarrow{h})$, with $s_Q = s_T = 0$ and held constant; see Figure 2.17 |
| $\tau_{\frac{2}{3}}(h_Q, h_A, h_T)$ | t.o.f. from $h_Q \in I_Q, h_T \in (FP(0, 0; T), LK(0, 0; T)], h_A = LK(0, s_T; A)$ to $h_Q = LK(s_T, s_A; Q)$ under the flow $\dot{\overrightarrow{h}} = G_{LRR}(\overrightarrow{h})$; see Figure 2.18 |
| $\tilde{v}_A$ | $v_A$ corresponding to $h_A = LK(0, 0; A)$ and $s_T = s_{max}$ |
| $\tilde{v}_Q$ | $v_Q$ corresponding to $h_Q = LK(s_{max}, s_{max}; Q)$ and $s_T = s_A = s_{max}$ |
| $\tilde{s}_T$ | $s_T$ corresponding to $h_T = FP(0, 0; T)$, with $v_T = v_{RB}(h_T)$ |
| $\tilde{s}_A$ | $s_A$ corresponding to $h_A = RK(\tilde{s}_T, 0; A)$ for $v_A = v_{RB}(h_A)$ |
| $\tilde{s}_Q$ | $s_Q$ corresponding to $h_Q = RK(\tilde{s}_T, \tilde{s}_A; Q)$ for $v_Q = v_{RB}(h_Q)$ |
| $\tau^*_{\frac{2}{3}}$ | $\tau_h(\tilde{v}_A)) \log(\frac{LK(0, s_{max}; A)}{RK(0, \tilde{s}_T; A)})$ |
| $\tau_1(h_Q, h_A, h_T)$ | t.o.f. from $h_Q \in U_Q$, $h_A \in [LK(0, 0; A), RK(0, s_{max}; A))$, $h_T \in [LK(0, 0; T), FP((s_{max}, 0; T)]$ to $h_Q = RK(s_T, s_A; Q)$ under the flow $\dot{\overrightarrow{h}} = G_{RRR}(\overrightarrow{h})$; see Figure 2.19 |
| $T_A$ | t.o.f. from $h_Q \in I_Q$, $h_A = LK(0, 0; A)$,$h_T \in I_T$, to $h_A = RK(0, s_{max}; A)$ under the flow $\dot{\overrightarrow{h}} = G_{RRR}(\overrightarrow{h})$; see Figure 2.20 |
| $T_T$ | t.o.f. from $h_Q \in I_Q$, $h_A \in I_A$,$h_T = LK(0, 0; T)$, to $h_T = RK(0, s_{max}; T)$ under the flow $\dot{\overrightarrow{h}} = G_{RRR}(\overrightarrow{h})$ |
| $T_0$ | t.o.f. from $h_Q \in D_Q, h_A \in D_A$, $h_T = FP(s_{max}, s_{max}; T)$ to $h_T = LK(0, 0; T)$ under the flow $\dot{\overrightarrow{h}} = G_{LLL}(\overrightarrow{h})$ with $s_Q = s_A = 0$ fixed |
| $T_{\frac{2}{3}}$ | $\tau_h(\tilde{v}_Q)) \log(\frac{RK(s_{max}, s_{max}; Q)}{LK(\tilde{s}_A, \tilde{s}_T; Q)})$ |
| $T_1$ | t.o.f. from $h_Q = LK(s_{max}, s_{max}; Q)$, $h_A \in I_A$, $h_T \in I_T$ to $h_Q = RK(\tilde{s}_T, \tilde{s}_A; Q)$ under the flow $\dot{\overrightarrow{h}} = G_{RRR}(\overrightarrow{h})$ with $s_T = s_A = s_{max}$ held constant |

Table 2.3: Explanation of symbols in Table 2.2

| Symbol | Interpretation |
|---|---|
| $D_Q$ | range of possible $h$ values at which the Q cell can enter the silent phase. |
| $D_A$ | range of possible $h$ values at which the A cell can enter the silent phase. |
| $D_T$ | range of possible $h$ values at which the T cell can enter the silent phase. |
| $\Omega$ | box containing all possible $(h_T, h_A, h_Q)$ coordinates at which the network can enter the silent phase. |
| $U_Q$ | range of possible $h$ values at which the Q cell can enter the active phase. |
| $I_Q$ | range of $h$ values that $Q$ can achieve. |
| $I_A$ | range of $h$ values that $A$ can achieve. |
| $I_T$ | range of $h$ values that $T$ can achieve. |
| $W$ | all possible $(h_T, h_A, h_Q)$ coordinates. |
| $\tau_0(h_Q, h_A, h_T)$ | the time $T$ takes to enter the active phase, that is, the time for $h_T$ to reach the left knee. |
| $\tau_{\frac{1}{3}}(h_Q, h_A, h_T)$ | the time $A$ takes to enter the active phase, taking into account that the position of the left knee changes based on $s_T$. |
| $\tau^*_{\frac{1}{3}}$ | the minimum time $A$ can spend in the silent phase, without input from $T$. |
| $\tau_{\frac{2}{3}}(h_Q, h_A, h_T)$ | the time it takes $Q$ to enter the active phase after $A, T$ have entered the active phase. |
| $\tilde{v}_A$ | the maximal value attainable by $v_A$ when only $T$ is in the active phase. |
| $\tilde{v}_Q$ | the maximal value attainable by $v_Q$ while $Q$ is still in the silent phase. |
| $\tilde{s}_T$ | the minimal synaptic output from cell $T$ when it is in the active phase. |
| $\tilde{s}_A$ | the minimal synaptic output from cell $A$ when both $A$ and $T$ are in the active phase. |
| $\tilde{s}_Q$ | a lower bound on the minimal synaptic output from cell $Q$ when all three cells are in the active phase. |
| $\tau^*_{\frac{2}{3}}$ | the minimal time $A$ can spend in the active phase, if $T$ is also in the active phase. |
| $\tau_1(h_Q, h_A, h_T)$ | the time it takes $Q$ to reach its right knee from the time it enters the active phase. |
| $T_A$ | maximum time it takes $A$ to reach a point where it will enter the silent phase when $Q$ does. |
| $T_T$ | maximum time it takes $T$ to reach a point where it will enter the silent phase when $A$ does. |
| $T_0$ | upper bound on the time $T$ can spend in the silent phase. |
| $T_{\frac{2}{3}}$ | upper bound on the time $Q$ can spend in the silent phase. |
| $T_1$ | a lower bound on the time $Q$ can spend in the active phase. |

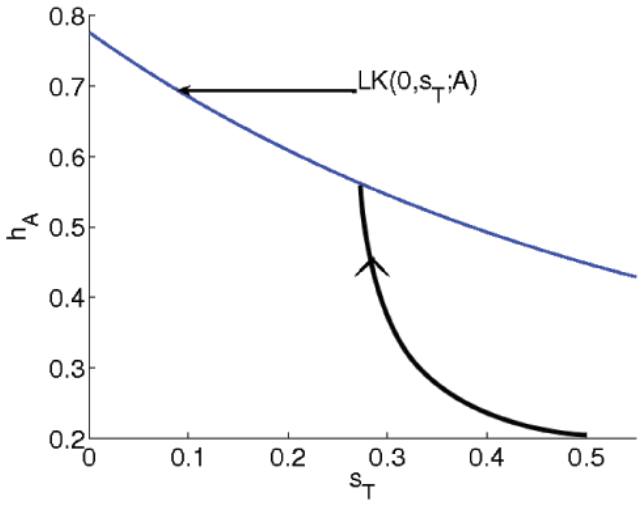


Figure 2.16: Plot of $h_A$ against $s_T$. The blue curve is the curve of the left knees of the $v_A$-nullcline as a function of $s_T$. When the black trajectory reaches the curve of left knees, the added cell $A$ will jump up to the active phase. The time it takes to reach the curve of left knees is $\tau_{\frac{1}{3}}(h_Q, h_A, h_T)$ for initial conditions $h_Q, h_A, h_T \in W$. In this figure, the blue curve $LK(0, s_T; A)$ was generated numerically for one particular added cell $A$, while the black trajectory is a schematic included for illustrative purposes. For the added cell $A$, all parameters are as in Table 2.1, except $g_{NaP} = 2, g_L = 2$.

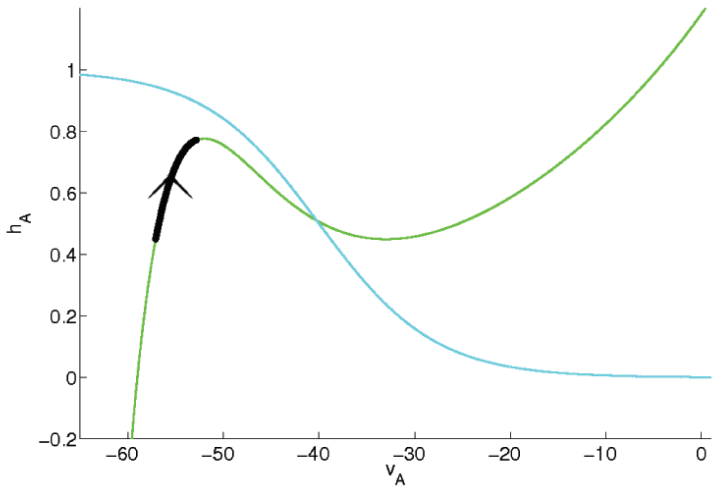


Figure 2.17: Plot of $h_A$ against $v_A$. The green curve is the $v_A$-nullcline, while the light blue curve is the $h_A$ nullcline. In the worst case, shown here, the trajectory starts as high as possible, namely at $RK(0,0;A)$, and continues to the left knee $LK(0,0;A)$. This evolution takes time $\tau^*_{\frac{1}{3}}$. In this figure, the light blue and green nullclines were generated numerically for a particular choice of the added cell $A$, while the black trajectory is fictive and included for illustrative purposes. For the added cell $A$, the parameters are as in Table 2.1, except $g_{NaP} = 2, g_L = 2$.

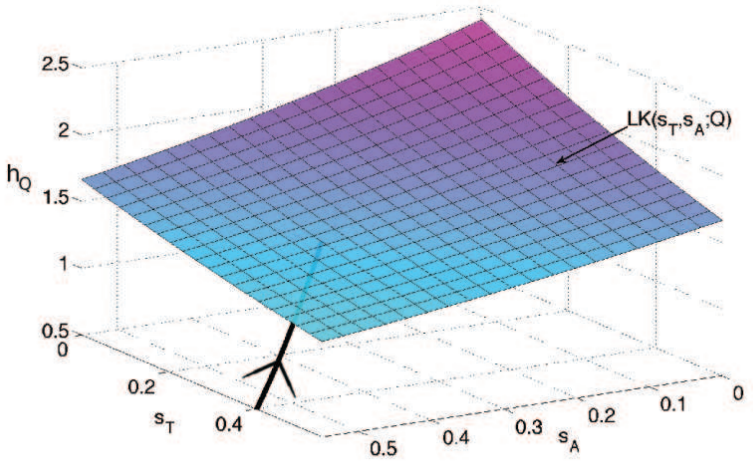


Figure 2.18: Plot of $h_Q$ against $s_T$ and $s_A$. The multicolored surface is the sheet of $Q$'s left knees as a function of $s_T$ and $s_A$. The black curve is the $h_Q$ coordinate of the $Q$ subsystem under the flow $G_{LRR}(h_Q, h_A, h_T)$. The trajectory evolves towards the sheet as $s_T$ and $s_A$ experience some decay. When trajectory reaches the sheet $LK(s_T, s_A)$, $Q$ enters the active phase. From initial conditions $h_Q, h_A, h_T$, the time it takes the trajectory to reach the sheet is $\tau_{\frac{2}{3}}(h_Q, h_T, h_A)$. In this figure, the sheet of left knees $LK(s_T, s_A; Q)$ for the quiescent cell was generated numerically, while the black trajectory is included for illustrative purposes only. For the quiescent cell $Q$, the parameters are as in Table 2.1, except $g_{NaP} = 2, g_L = 4$.

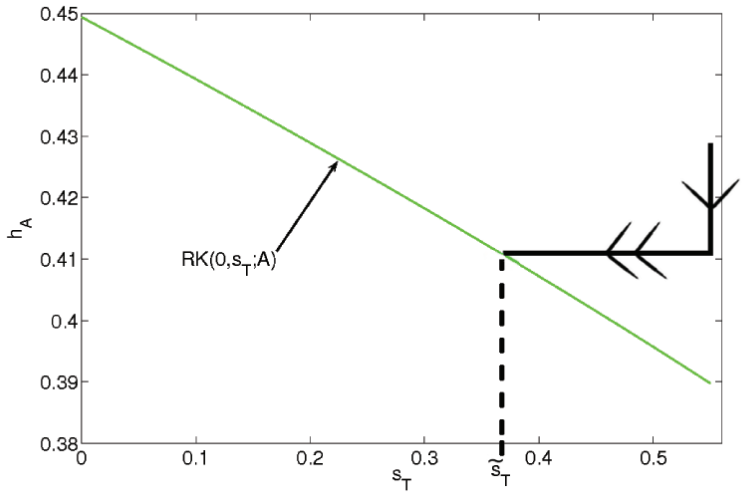


Figure 2.19: Plot of $h_A$ against $s_T$. The green curve is the curve of right knees of $A$ as a function of $s_T$. The trajectory begins at $LK(0, s_{max})$ and has maximum velocity while $s_T = s_{max}$. The point with the largest value at which $A$ can enter the silent phase is $RK(0, \tilde{s}_T; A)$. $\tau^*_{\frac{2}{3}}$ is defined such that if $s_T$ suddenly dropped to $s_T = \tilde{s}_T$ after time $\tau^*_{\frac{2}{3}}$, then the trajectory of A would exactly hit the curve of knees at $RK(0, \tilde{s}_T; A)$. In this figure, the green curve $RK(0, s_T; A)$ of right knees was generated numerically for a particular choice of the added cell $A$. For the added cell $A$, the parameters are as in Table 2.1, except $g_{NaP} = 2, g_L = 2$. The black trajectory is an illustration of the worst-case trajectory and may not be realized.

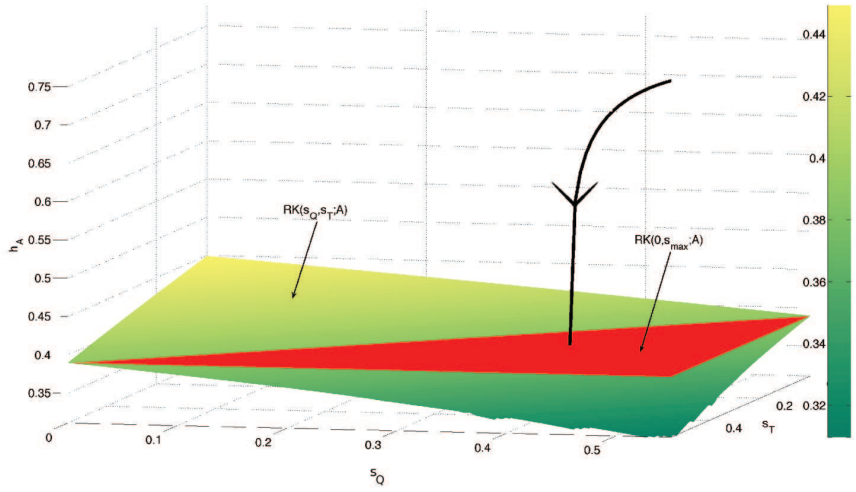


Figure 2.20: Plot of $h_A$ against $s_T$ and $s_Q$. The green-hued surface is the sheet $RK(s_Q, s_T; A)$ of right knees for $A$ as a function of $s_T$ and $s_Q$. The red plane is $h = RK(0, s_{max}; A)$, the $h$ value of the lowest possible right knee for $A$ when $Q$ has entered the silent phase. In order for $A$ to return to the silent phase simultaneously with $Q$, $h_A$ must be below the red sheet when $Q$ enters the silent phase. We define $T_A$ as the time it takes a trajectory starting from $LK(0, 0; A)$ to reach the red sheet. Here, the green-hued sheet $RK(s_Q, s_T; A)$ and the red sheet $RK(0, s_{max}; A)$ were generated numerically for a particular choice of the added cell $A$. For the added cell $A$, the parameters are as in Table 2.1, except $g_{NaP} = 2, g_L = 2$. The black trajectory, on the other hand, is fictive and included for illustrative purposes.

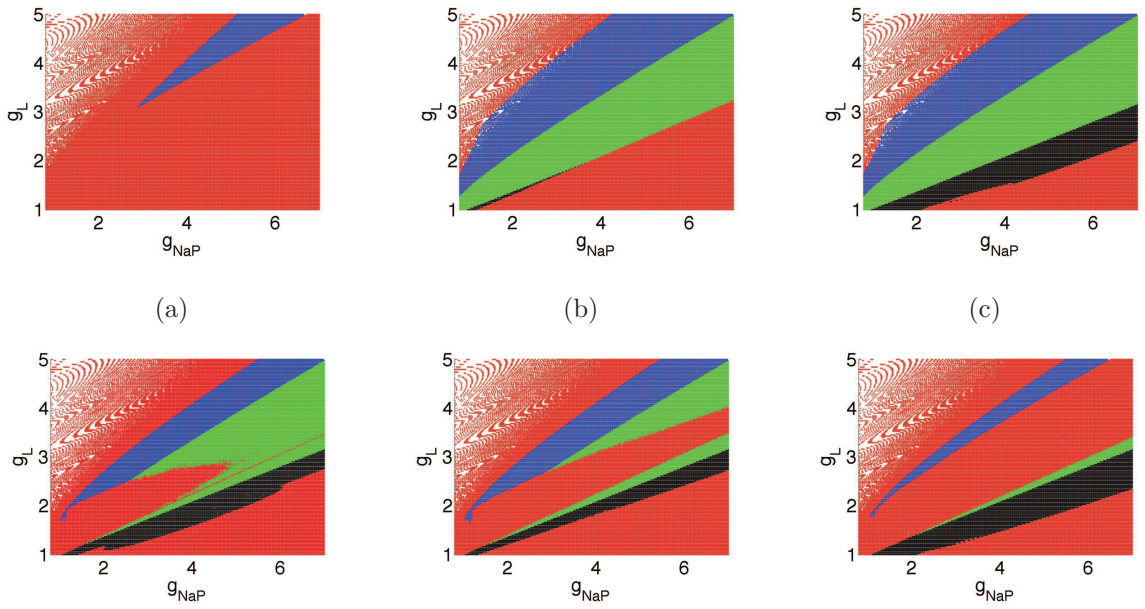


Figure 2.21: Each panel is a plot of $g_{NaP}$ vs. $g_L$ and represents a numerical experiment with a different pair of fixed intrinsically quiescent and intrinsically tonic cells. For each such experiment, we choose a third cell with parameters $g_{NaP}$ and $g_L$, and color the point $(g_{NaP}, g_L)$ red if the network failed to exhibit synchronous bursting. Otherwise, we color the point according to the added cell's intrinsic dynamics, using blue for quiescent, green for bursting, and black for tonic. For each cell, all parameters are as in Table 2.1, except: $(g_{NaP,1}, g_{L,1}, g_{NaP,2}, g_{L,2})$ = (a) (5.772, 1.842, 2.043, 2.552), (b) (4.529, 1.842, 2.043, 2.552), (c) (4.529, 2.236, 5.772, 4.342), (d) (4.529, 2.000, 3.286, 4.105), (e) (4.529, 1.921, 3.286, 4.105), (f) (4.529, 2.000, 5.772, 5.815).

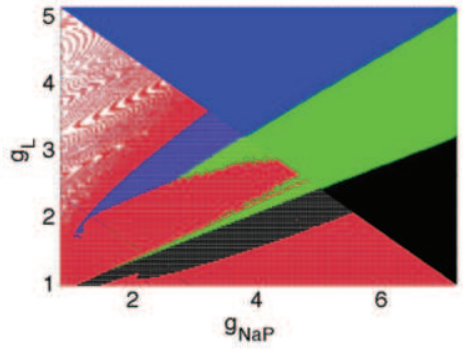


Figure 2.22: Animated comparison between the original partition of $g_{NaP}g_L$ space and one example of the numerical experiment detailed in Section 2.4.2. Click here to view the animation.

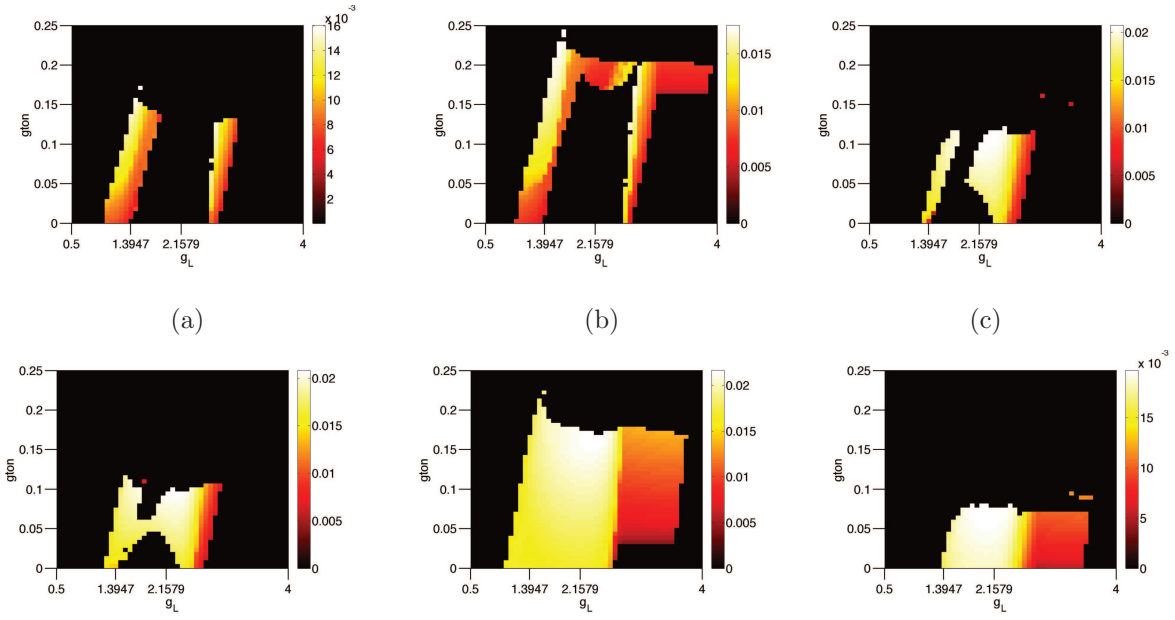


Figure 2.23: Frequency variation by $g_{ton}$ depends on the added cell. Each panel shows an individual experiment where an intrinsically quiescent cell and an intrinsically tonic cell were chosen at random. Then, with $g_{NaP} = 2$ and a range of values of $g_L$ between .5 and 4, we added a third cell to the network. For this network, we varied $g_{ton}$ from 0 to .25, and at each mesh point we recorded the average period of synchronous oscillations (recording 0 if synchronous oscillations did not occur). The frequency is color coded here as the inverse of this average period, unless the period was 0, in which case we recorded the frequency as 0 as well. As indicated on the $g_L$ axis, $g_L = 1.3947$ and $g_L = 2.1579$ represent, for $g_{NaP} = 2$, where the added cell's intrinsic dynamics transitions from tonic to bursting and from bursting to quiescent, respectively. The black regions indicate a failure by the network to burst synchronously. The parameters for each cell are as in Table 2.1, except:
$(g_{NaP,1}, g_{L,1}, g_{NaP,2}, g_{L,2})$ = (a) (4.5293, 2.0789, 5.7724, 5.8158), (b) (5.7724, 2.6316, 5.7724, 5.8158), (c) (5.7724, 2.3158, 3.2862, 4.1053), (d) (4.5293, 2.0000, 3.2862, 4.1053), (e) (4.5293, 2.2368, 4.5293, 4.4474), (f) (5.7724, 2.1579, 4.5293, 4.4474).

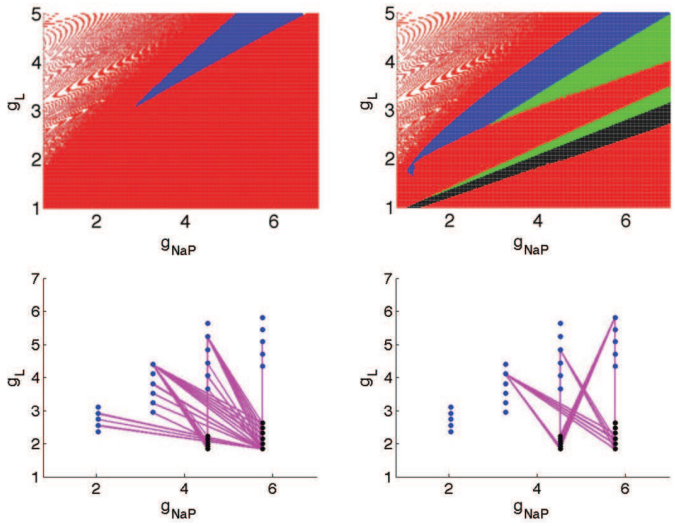


Figure 2.24: An illustration of which pairs of (Q,T) cells give rise to two classes of synchrony outcomes. The top row shows two examples from Figure 2.21. In the bottom row, dots corresponding to quiescent cells are blue, and dots corresponding to tonic cells are black. In each panel, the dots for each intrinsically quiescent and intrinsically tonic pair are connected if, using the procedure discussed in Section 2.4.2, this pair generated a synchrony diagram like the one in the panel above.

# 3.0 ON THE INTERACTION OF THE CAN AND NaP CURRENTS

## 3.1 INTRODUCTION

In the previous chapter, we concluded that intrinsically bursting neurons did not promote synchronization in small model networks of respiratory neurons. Heuristically this is because intrinsically bursting neurons need not become tonically active when receiving synaptic input from the rest of the population; this allows them to prematurely return to the silent phase before the rest of the network could enter the active phase. Under tonic input, quiescent neurons using the reduced model in Chapter 2 were able to return to the silent phase. The loss of the synaptic output from the quiescent neuron would return the rest of the network to the silent phase, in an excitatory analogue of post-inhibitory rebound. This chapter highlights another mechanism for returning tonically active neurons to the silent phase, the CAN current.

Recently, the Rubin-Hayes model was used to show how the CAN current may, when coupled with another outward current such as the NaP current or Na/K ATPase pump, generate robust bursting rhythms in small network of intrinsically tonic neurons [56]. However, analysis for the self-coupled neuron mostly done in the absence of the NaP current. Given the prevalence of the NaP current, in this chapter we study its interaction with the CAN current, and the roles each current play in preBötC rhythmogenesis.

We analyze a unified model by extending the core Rubin-Hayes model to include the NaP current, with all of its associated dynamic effects. This is a crucial step in understanding the rhythmicity of the preBötC. Indeed, although the previous modeling work done on these neurons for the most part separated out the CAN and NaP components of preBötC dynamics, it is likely that in the majority of preBötC neurons, it is the interaction of these currents

that produces the cellular activity that underlies the bursting rhythm. Our unified model provides a framework with which we can understand this interaction.

We use a slow-fast decomposition involving three slow variables to analyze dynamics of the unified model. We approach this problem by reviewing bifurcation mechanisms present in the NaP-only and CAN-only limits of the unified model, which have one and two slow variables, respectively, and then consider how these interact when both currents are present. Specifically, in Section 3.2, we introduce the unified model. In Section 3.3, we review, in the context of the unified model, the mechanisms by which the Butera model and Rubin-Hayes model generate bursting rhythms. Section 3.4 discusses the particulars of our numerical implementations of the unified model. In Section 3.5 and Section 3.6 we provide an analysis of the unified model by considering dynamic regimes that emerge under variation of the CAN and NaP conductances. Section 3.7 highlights the coexistence of bursting and tonically active solutions for some regions of conductance space. In Section 3.8 we break the symmetry of a self-coupled neuron by considering two reciprocally coupled neurons that are identical except for their initial conditions. Overall, this chapter shows that the interaction of the synaptically activated CAN conductance with the voltage dependent NaP conductance yields a rich spectrum of behaviors, most of which are prevalent in experimental recordings of neurons of the preBötC. These results suggest that the diversity of observed preBötC neuron outputs reflects an intrinsic heterogeneity across neurons in this population, which should be taken into account in future preBötC network models.

## 3.2 PRELIMINARIES

We present and analyze a model that extends the Rubin-Hayes model to include the NaP current. As a starting point for developing this model, we used the Rubin-Hayes model containing the CAN current together with a Na/K ATPase pump. In the Rubin-Hayes model, individual model neurons isolated from synaptic inputs can be quiescent or tonically active, with transitions between these regimes governed by the reversal potential, $E_L$, of the leak current, or equivalently by $I_{app}$, the applied current. Excitatory synaptic coupling between

two tonically active model neurons, or between a quiescent model neuron and a tonically active model neuron, allows the pair to burst via interactions of the CAN current and the Na/K ATPase pump. We analyze a self-coupled model neuron that, considered in synaptic isolation, would be tonically active. We review the mechanisms underlying the bursting behavior in the Rubin-Hayes model resulting from synaptic excitation in Section 3.3.2. We model the NaP current based on the data given for the Butera model [4].

The Butera model differs from the Rubin-Hayes model in that isolated model neurons, without self-coupling, may have quiescent, bursting, or tonically active spiking patterns, with transitions between these dynamics as appropriate parameters are varied [46]. In the Butera model, introducing self-coupling for a model neuron that would intrinsically be tonically active may yield a bursting rhythm [1]. In Chapter 2 we noted that quiescent and tonically active model neurons may also be coupled together to generate a bursting rhythm (see also [55]). In the Butera model, the NaP current is responsible for transitions from the silent to the active phase and for the return from the active phase to the silent phase, as reviewed in Section 3.3.1.

Parameters have been adjusted from those values found in [56] and [4] such that the unified model can be tuned to generate qualitatively identical dynamics to the Rubin-Hayes model and the Butera model. Using the notation $\dot{x}$ for the time derivative of the variable $x$, the unified model is

$$\begin{aligned}\dot{v} = &-\{I_L(v) + I_{Na}(v,h,m) + I_{\mathrm{K}}(v,n) + I_{\mathrm{NaP}}(v,hp) + I_{\mathrm{CAN}}(v,Ca) \\ &+ I_{pump}(Na) - I_{app} + I_{syn}(v,s)\}/C_m \end{aligned} \tag{3.1}$$

$$\dot{h} = (h_\infty(v) - h)/\tau_h(v) \tag{3.2}$$

$$\dot{m} = (m_\infty(v) - m)/\tau_m(v) \tag{3.3}$$

$$\dot{n} = (n_\infty(v) - n)/\tau_n(v) \tag{3.4}$$

$$\dot{Ca} = \varepsilon_{Ca}(k_{IP_3}s - k_{Ca}(Ca - Ca_{base})) \tag{3.5}$$

$$\dot{Na} = \alpha(-I_{\mathrm{CAN}}(v,Ca) - I_{pump}(Na)) \tag{3.6}$$

$$\dot{hp} = \varepsilon_{hp}(hp_\infty(v) - hp)/\tau_{hp}(v) \tag{3.7}$$

$$\dot{s} = ((1-s)s_\infty(v) - k_s s)/\tau_s \tag{3.8}$$

Table 3.1: Common parameter values for Equations (3.1)–(3.8)

| Parameter | Value | Parameter | Value | Parameter | Value |
|---|---|---|---|---|---|
| $\alpha$ | $6.6 \times 10^{-5}$ mM pA$^{-1}$ms$^{-1}$ | $g_K$ | 30 nS | $Na_{base}$ | 5 mM |
| $Ca_{base}$ | 0.05 µM | $g_L$ | 3 nS | $r_{pump}$ | 200 pA |
| $C_m$ | 45 pF | $g_{Na}$ | 160 nS | $\sigma_{\text{CAN}}$ | −0.05 µM |
| $E_{\text{K}}$ | −75 mV | $g_{syn}$ | 2.5 nS | $\sigma_h$ | 5 mV |
| $E_{Na}$ | 65 mV | $I_{app}$ | 0 mV | $\sigma_{hp}$ | 6 mV |
| $\varepsilon_{Ca}$ | 0.0007 | $k_{IP_3}$ | 1200 µM ms$^{-1}$ | $\sigma_m$ | −8.5 mV |
| $\varepsilon_{hp}$ | 0.001 | $k_s$ | 1 | $\sigma_{m,p}$ | −6 mV |
| $E_{\text{CAN}}$ | 0 mV | $k_{Na}$ | 10 mM | $\sigma_n$ | −5 mV |
| $E_{syn}$ | 0 mV | $k_{Ca}$ | 22.5 ms$^{-1}$ | $\sigma_s$ | −3 mV |
| $E_L$ | −61 mV | $k_{\text{CAN}}$ | 0.9 µM | $\bar{\tau}_h$ | 15 ms |
| $\bar{\tau}_{hp}$ | 1 ms | $\bar{\tau}_m$ | 1 ms | $\bar{\tau}_n$ | 30 ms |
| $\tau_s$ | 15 ms | $\theta_h$ | −30 mV | $\theta_{hp}$ | −48 mV |
| $\theta_m$ | −36 mV | $\theta_{m_p}$ | −40 mV | $\theta_n$ | −30 mV |
| $\theta_s$ | 15 mV | | | | |

where $\varepsilon_{Ca}$, $\alpha$, and $\varepsilon_{hp}$ are relatively quite small, and $I_L(v) = g_L(v - E_L)$, $I_{Na}(v,h,m) = g_{Na}m^3h(v - E_{Na})$, $I_{\text{K}}(v,n) = g_{\text{K}}n^4(v - E_{\text{K}})$, $I_{syn}(v,s) = g_{syn}s(v - E_{syn})$, $I_{\text{CAN}}(v,Ca) = g_{CAN}(v - E_{\text{CAN}})/(1 + \exp((Ca - k_{\text{CAN}})/\sigma_{\text{CAN}}))$, $I_{\text{NaP}}(v,hp) = g_{NaP}mp_\infty(v)hp(v - E_{Na})$, $I_{pump}(Na) = \phi(Na) - \phi(Na_{base})$, where $\phi(x) = x^3/(x^3 + k_{Na}^3)$. For each $x \in \{h, hp, mp, n, s\}$, the function $x_\infty(v)$ takes the form $x_\infty(v) = \{1 + \exp[(v - \theta_x)/\sigma_x]\}^{-1}$. Also for each $x \in \{h, hp, m, n\}$, the function $\tau_x(v)$ is given by $\tau_x(v) = \bar{\tau}_x/\cosh[(v - \theta_x)/(2\sigma_x)]$. In Table 3.1 we record the baseline parameter values used for equations (3.1)–(3.8). A value for $E_L$ is included, although we also comment on variations away from this baseline. Values of $g_{CAN}$ and $g_{NaP}$ are discussed throughout the text, so these parameters do not appear in Table 3.1.

In the Rubin-Hayes model and the unified model (3.1)–(3.8), the value for $k_{IP_3}$ is large, and represents a signaling cascade that begins with presynaptic glutamate and terminates with the release of intracellular calcium stored in the post synaptic endoplasmic reticulum. When enough intracellular calcium is released (represented by $Ca \approx k_{CAN}$) the CAN current activates. The Rubin-Hayes model includes an outward current denoted $I_{pump}(Na)$ with corresponding dynamic variable $Na$, that represents the effects of ATPase pumps that are activated during CAN current dominated activity [56].

When two neurons modeled by (3.1)–(3.8) are coupled with excitatory synapses, the pair can produce robust bursts analogous to those exhibited by the Rubin-Hayes model, when $g_{NaP} = 0$, or to those exhibited by the Butera model, when $g_{CAN} = 0$. With the unified model, we seek to analyze the forms of rhythmic activity produced by interactions of the CAN and NaP currents. To understand this interaction, we systematically vary $g_{CAN}$, the conductance of the CAN current, and $g_{NaP}$, the conductance of the NaP current.

In a real preBötC neuron, synaptic recruitment of the CAN current and the Na/K ATPase pump activity occur primarily in dendrites [41, 37, 38], whereas sodium channels are likely to be most prevalent near the axon hillock, where they can strongly influence action potential generation. However, simultaneous somatic voltage recordings and dendritic calcium imaging from preBötC neurons suggest that preBötC neurons are electrotonically compact. Figure 3.1 shows an example of the temporal proximity of somatic and dendrite responses, which is representative of a large set of recordings [10]. In particular Figure 3.1(e) demonstrates that the difference between the time when the onset of activity occurs in the dendrite (green trace in panel (e)) and the time when activity begins in the soma (black trace at the top of panel (e)) is sufficiently small that we may justify using a one compartment model, which simplifies the analysis. Another way we have simplified analysis is by focusing on one self-coupled model neuron, instead of a network of two model neurons. We provide numerical justification for this simplification in Section 3.4.

Our primary tool for analysis will be geometric singular perturbation theory [22] (for thorough review see [28]). This analysis exploits the fact that $\varepsilon_{Ca}$, $\alpha$ and $\varepsilon_{hp}$ are small, and so $Ca$,$Na$,$hp$ (the "slow subsystem") evolve on a timescale separate from the dynamic variables $v, h, m, n, s$ (the "fast subsystem"). Here we briefly summarize the interactions of the slow and fast subsystems. From the perspective of the fast subsystem, the slow subsystem's dynamic variables are fixed at some values. The fast subsystem then approaches some stable orbit or critical point based on the current values of the slow variables. From the slow subsystem's perspective, the dynamics of the fast subsystem is instantaneous. Based on the asymptotic limit of the fast subsystem dynamics, the slow subsystem slowly evolves. This drift updates the appropriate stable orbit for the fast subsystem, but the fast subsystem instantly tracks these updates, and the slow subsystem continues to drift in a way that is

determined by the fast subsystem's limits.

## 3.3 REVIEW OF THE LIMITING CASES $g_{NAP} = 0$ AND $g_{CAN} = 0$

We begin our analysis by reviewing model dynamics in the two extremal parameter regimes, $g_{CAN} = 0$ and $g_{NaP} = 0$. Analysis of these regimes isolates key mechanisms that will combine to yield the rich dynamics of the general case.

### 3.3.1 Dynamics without the CAN current

First, we set $g_{CAN} = 0$ and allow $g_{NaP}$ to vary for a self-coupled model neuron. With $g_{CAN} = 0$, we can safely ignore the calcium dynamics given in Equation (3.5) and the sodium dynamics will equilibrate at $Na = Na_{base}$. Thus, after a transient, we need only consider one slow variable, $hp$, which simplifies the analysis. In this case, the model is similar to the Butera model, though the parameter values differ slightly. Importantly, the bifurcation structure is similar to the one from the Butera model[1]. Here we will briefly recall how a slow-fast decomposition can be used to describe the dynamics in the case $g_{CAN} = 0$. First we present the bifurcation structures associated with equations (3.1)–(3.4),(3.8) in Figure 3.2 by projecting the bifurcation diagram generated by treating $hp$ as a parameter, along with the graph of the curve satisfying equation $hp' = 0$ (also called the $hp$-nullcline), into $(v, hp)$ coordinates.

We have marked three key features in Figure 3.2, a saddle-node (SN) bifurcation (visible in the inset), a family P of stable periodic orbits, and the family's termination point: a critical point of the fast subsystem (3.1)–(3.4),(3.8) that is the asymptotic limit of a homoclinic orbit (HC). At the SN bifurcation the family of asymptotically stable critical points of the fast subsystem that correspond to quiescence ceases to exist. The family P is born in a supercritical Andronov-Hopf (AH) bifurcation at $hp > 1.2$ but is is not visible in Figure 3.2.

The features illustrated in Figure 3.2 will be visited in succession by the evolving tra-

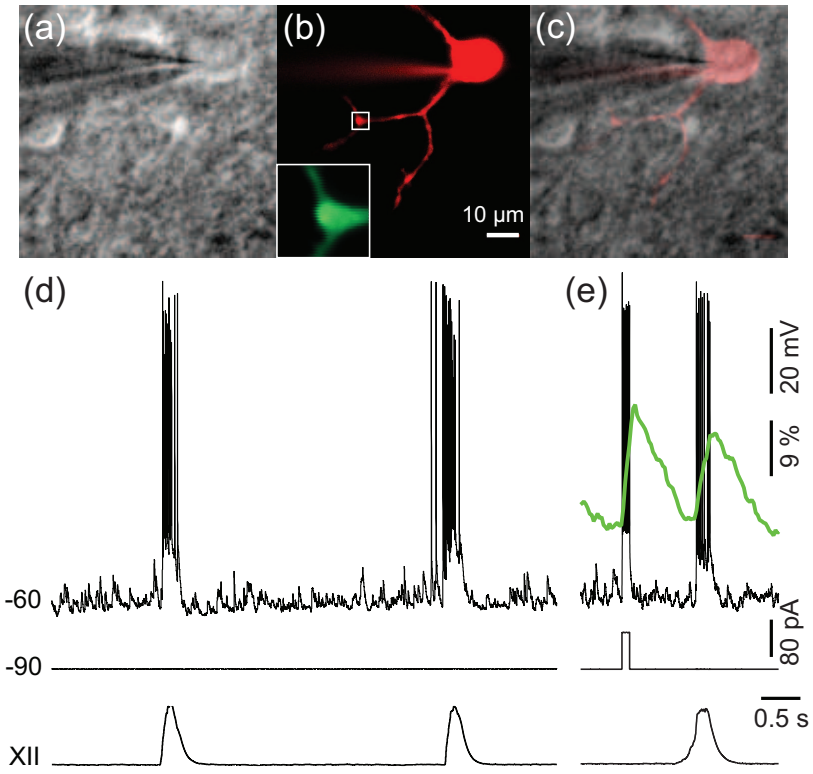


Figure 3.1: Neurons in the preBötC are electrotonically compact; these data were collected from the Del Negro laboratory. (a) Videomicroscopic image of a whole-cell patch-clamp recording in the preBötC of a neonatal mouse. (b) Neuronal soma and dendrites imaged via Alexa 568 hydrazide (fast diffusing) fluorescent dye. The white box in (b) shows the dendrite region subsequently imaged using Oregon-Green BAPTA 2, a calcium-sensitive dye, and two-photon excitation [11]. The inset shows this dendrite region imaged via Oregon-Green BAPTA 2. (c) Superimposition of (a) and (b). (d) Inspiratory bursts recorded immediately after achieving a whole-cell recording in the neuron (a–c). A bias current of -90 pA was applied to maintain a -60 mV baseline membrane potential. At first, the Alexa dye quickly dialyzes the cell (panel (b)) to reveal its full morphology. However, the Oregon-Green dye diffuses more slowly and does not reach the dendrite until 20-30 min later. (e) Whole-cell recording and dendritic imaging after 30 min. A 300 ms current step command is also illustrated to show that calcium fluorescent changes in the dendrite occur closely in time with somatic voltage changes.

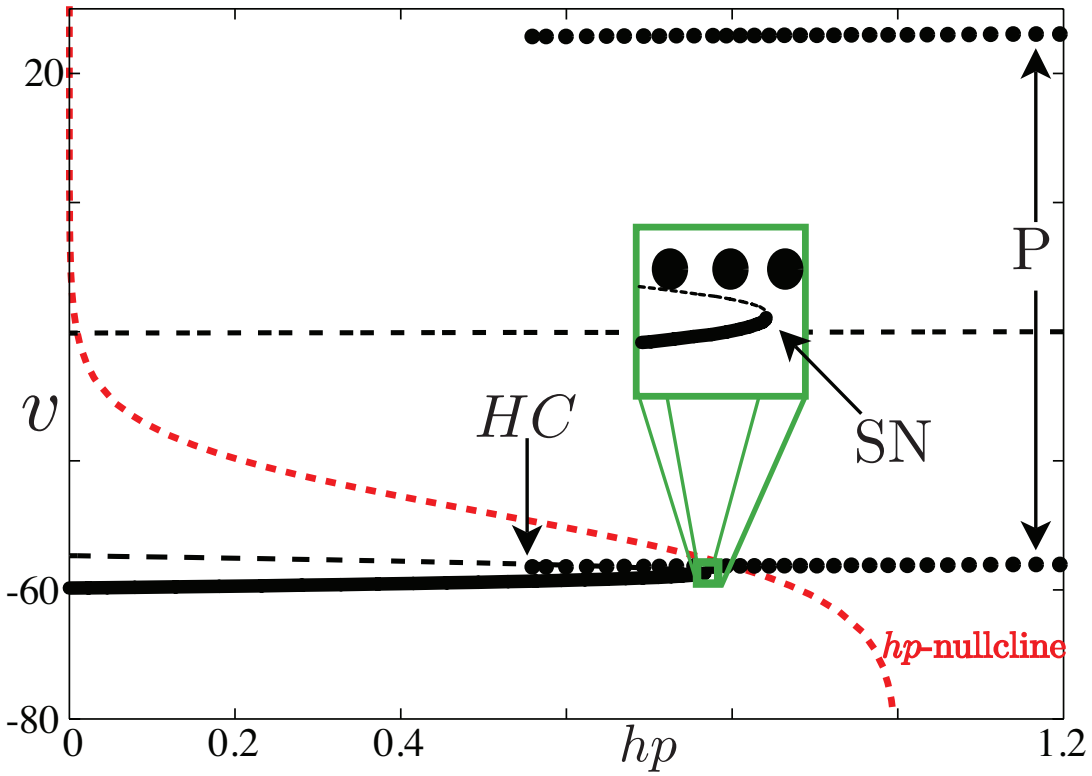


Figure 3.2: Bifurcation diagram for $g_{CAN} = 0$ formed by treating $hp$ as a bifurcation parameter. P is a family of stable periodic orbits, the maximum and minimum $v$ values of the periodic orbits are indicated by solid black circles. P terminates in a homoclinic orbit with homoclinic point HC. Solid lines indicate stable critical points, while black dashed lines are unstable critical points, and the sigmoidal red dashed curve is the $hp$-nullcline.

jectory to create the dynamics for the $g_{CAN} = 0$ system. We will work in the $\varepsilon_{hp} = 0$ limit so that the methods of geometric singular perturbation theory allow us to first consider the slow variable $hp$ as fixed. For each fixed $hp \in [0,\ 1]$ each solution of the fast subsystem is quickly attracted to one of the stable structures highlighted in Figure 3.2.

To facilitate our analysis we introduce the following notation. Considering $hp$ fixed as a parameter, we call $(v, h, m, n, s)$ the fast subsystem, with associated fast dynamics given by Equations (3.1)–(3.4),(3.8).

Let $x \cdot t$ be the result of applying the flow of the fast dynamics to initial condition $x$ for time $t$. Allow $d(x, y)$ to be the usual euclidean distance between points $x = (v_x, h_x, m_x, n_x, s_x)$ and $y = (v_y, h_y, m_y, n_y, s_y)$, that is, $d(x, y) = \sqrt{(v_x - v_y)^2 + (h_x - h_y)^2 + \ldots + (s_x - s_y)^2}$. We use the dynamics of equations (3.1)–(3.4),(3.8) to define $F_{g_{CAN}=0}(hp, x_0) = \{x$: for fixed $hp$ and any given $\delta > 0$ there exists $t_n \to \infty$ such that for each $t_n$, $d(x_0 \cdot t_n, x) < \delta\}$. Note that $F_{g_{CAN}=0}(hp, x_0)$ can be thought of as $\lim_{t\to\infty} x_0 \cdot t$ for $hp$ fixed, when this limit exists. $F_{g_{CAN}=0}(hp, x_0)$ may be either a nontrivial orbit or a critical point and may depend critically on $x_0$ for choices of $hp$ where the fast subsystem exhibits bistability. We construct a solution for the full system by allowing $hp$ to drift based on the dynamics of equation (3.7) averaged over $F_{g_{CAN}=0}(hp, x_0)$. We define $hp_{SN}$ to be the $hp$ coordinate of the SN bifurcation. In Figure 3.2 the AH bifurcation (with $hp$-coordinate $hp_{AH}$) is not seen because it occurs at $hp_{AH} > 1.2$. Further, for $hp$ fixed in $[0,\ hp_{SN})$, we define $Q(hp)$ to be the unique stable critical point of the fast subsystem corresponding to quiescence for that fixed $hp$, see Figure 3.2. We will call $hp_{HC}$ the $hp$ coordinate of the homoclinic orbit. For $hp_{HC} \leq hp < 1$ we define $P(hp)$ to be the unique stable periodic orbit with large amplitude and high voltage corresponding to fast subsystem spiking for that given value of $hp$, see Figure 3.2.

Without loss of generality, we begin our analysis of the model dynamics with $g_{CAN} = 0$ and an initial condition $(hp, x_0)$ on the lower stable branch in Figure 3.2, that is, $(hp, x_0) = (hp, Q(hp))$ for $0 < hp < hp_{SN}$. $F_{g_{CAN}=0}(hp, x_0) = Q(hp)$ is below the $hp$-nullcline, so that $hp$ will slowly begin to increase toward $hp_\infty(v)$. As $hp$ slowly increases, $F_{g_{CAN}=0}(hp, x_0) = Q(hp)$ initially persists. If the $hp$-nullcline intersects the curve of stable quiescent states, then the system converges to this intersection point, and the resultant solution will exhibit quiescent dynamics. Otherwise, $hp > hp_{SN}$ eventually holds, and $Q(hp)$ is not defined for such values

of $hp$. For $hp_{AH} > hp > hp_{SN}$, $F_{g_{CAN}=0}(hp, x_0) = P(hp)$, so a spiking or active phase begins once $hp > hp_{SN}$.

During the active phase, the relation $F_{g_{CAN}=0}(hp, x_0) = P(hp)$ is maintained, based on the $x_0$ values visited. If the right hand side of equation (3.7) averaged over $P(hp)$ is negative for each fixed $hp \in (hp_{HC}, hp_{SN}]$, then there is a negative net drift for $hp$, so that $hp$ decreases until $hp \approx hp_{HC}$. The location of the $hp$-nullcline relative to the homoclinic orbit will determine the resultant dynamics of the solution. More precisely, let $T(P(hp))$ be the period of $P(hp)$ and let $D(hp) = \varepsilon_{hp} \int_0^{T(P(hp))} (hp_\infty(v) - hp)/\tau_{hp}(v)\ dt$ where $(v, m, n, h, s)$ evolve according to $P(hp)$. The net drift of $hp$ across the homoclinic is $D = \lim_{hp \to hp_{HC}^+} D(hp)$. Suppose $D < 0$. Under this assumption, $hp < hp_{HC}$ eventually holds (and $P(hp)$ is no longer defined) and again $F_{g_{CAN}=0}(hp, x_0) = Q(hp)$, resulting in the termination of the active phase, after which the full cycle repeats. Such dynamics represent square-wave bursting. On the other hand, if $D \geq 0$, even if $hp < hp_{HC}$ for some time, then eventually $hp > hp_{HC}$ again, and $F_{g_{CAN}=0}(hp, x_0) = P(hp)$ for all subsequent time. The full system will eventually settle onto a periodic orbit, resulting in tonic spiking.

Modulation of $g_{NaP}$ or $E_L$ shifts the location of the SN bifurcation and the location of the homoclinic orbit. For some range of $E_L \leq -61$ and $E_L = -61$ in particular, increasing $g_{NaP}$ from 0 to 5, the stable dynamics changes from quiescence to bursting, and eventually from bursting to tonic spiking. For some range of $E_L \geq -60$ and $g_{NaP} \in [0,\ 5]$, the full system always exhibits tonic spiking.

### 3.3.2 Dynamics without the NaP current

We now consider a self-coupled model neuron with $g_{NaP} = 0$ and $g_{CAN}$ nonzero. With $g_{NaP} = 0$, we may safely ignore the dynamics of $hp$, and so may reduce our system to one that has two slow variables: $Ca$ and $Na$. In this case, with the exception of a few parameter values, the model is the same as the Rubin-Hayes model [56]. For a sample voltage trace of a burst when $g_{NaP} = 0$, together with its projection into the ($Na$,$Ca$) plane, see Figure 3.3. There are several bifurcation structures we must consider to explain the dynamics when $g_{NaP} = 0$. In Figure 3.4, we present the bifurcation diagram of the fast subsystem projected

into $(Ca, v)$ coordinates with $Na > Na_{base}$ fixed. As in the $g_{CAN} = 0$ regime, there is a supercritical AH bifurcation that gives rise to a family of small amplitude periodic orbits, which quickly coalesce with a family of unstable periodic orbits at a SNP bifurcation; it is important to note that the $Ca$-coordinate of the AH bifurcation will be attainable by the full system, unlike the $g_{CAN} = 0$ case. The unstable family of periodic orbits meets the stable family of periodic orbits P at another SNP bifurcation. P contains periodic orbits with large amplitude and generally short period, again representative of neuronal spiking. As above, P terminates at a homoclinic orbit; however, this homoclinic orbit precisely coincides with a SN bifurcation, resulting in a saddle-node on an invariant circle (SNIC) bifurcation.

In this section, we consider two slow variables, but our definitions will be analogous to

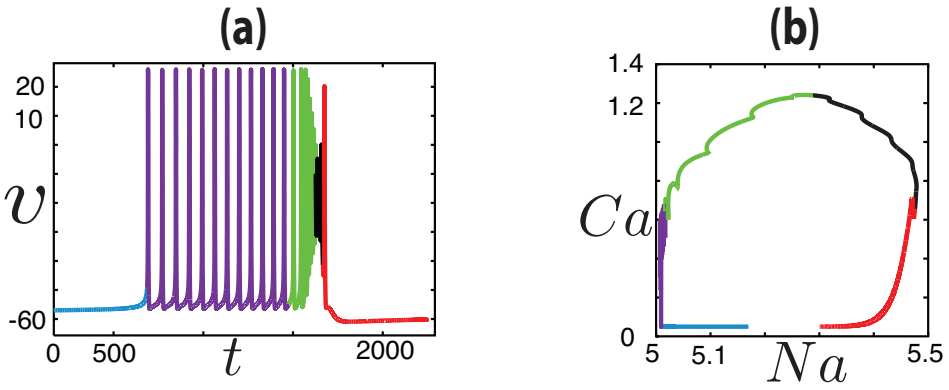


Figure 3.3: Sample trajectory for a burst in the $g_{NaP} = 0$ case. (a) Voltage trace. The colors correspond to those in panel (b). (b) Projection of the trajectory into the $(Na, Ca)$ plane. As the model neuron spikes (purple), $Ca$ exhibits several sharp increases until the CAN current activates (green), which drives both $Ca$ and $Na$ to higher values, eventually leading to depolarization block (black) and the termination of the burst (red).

those in Section 3.3.1. In Section 3.3.1 we defined $Q(hp)$ as the branch of stable quiescent critical points for the fast subsystem. Those critical points were not defined for $hp > hp_{SN}$. Analogously, in this section, instead of a single SN bifurcation point, there is a curve of SNIC bifurcations in the $(Ca, Na)$ plane. Setting $Ca = Ca_{base}$ and considering $Na$ as a bifurcation parameter, there is a SNIC bifurcation of the critical points corresponding to quiescence at $Na = Na_{SNIC}$. For $Na > Na_{SNIC}$ we define $Ca_{SNIC}(Na)$ to be the unique

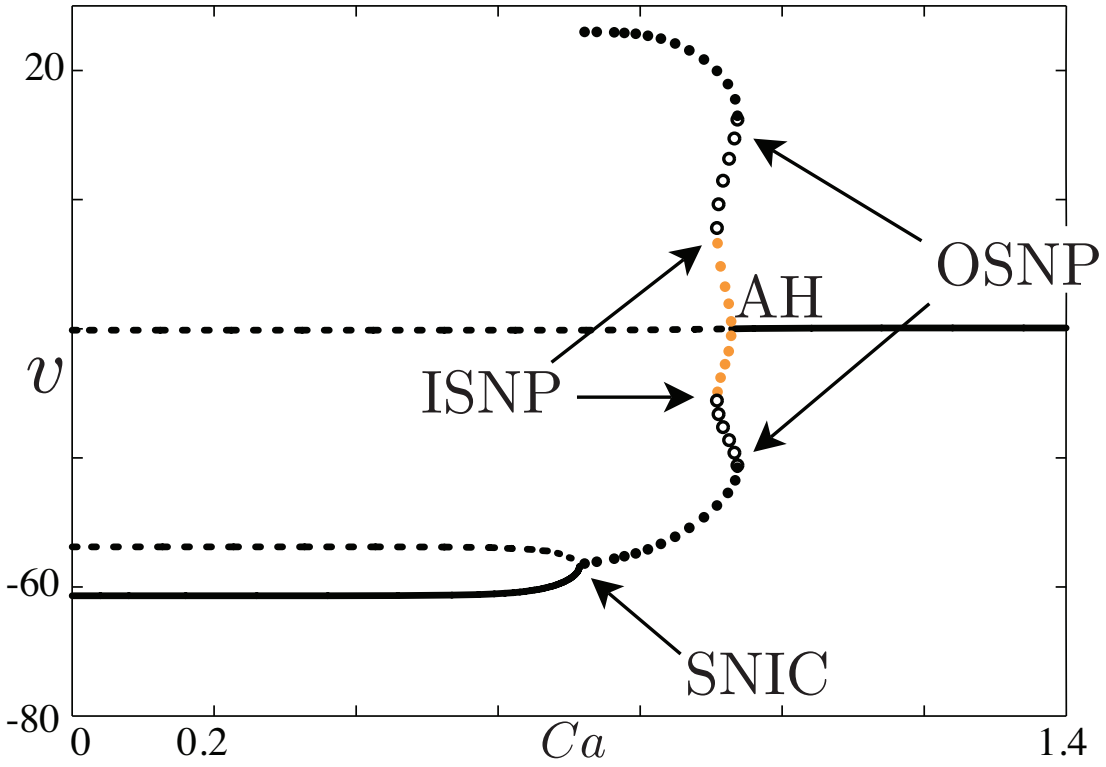


Figure 3.4: Bifurcation diagram of the fast subsystem with $g_{NaP} = 0$ generated by treating $Ca$ as a bifurcation parameter. $Na$ has been fixed at a level higher than $Na_{base}$. Solid lines indicate stable critical points of the fast subsystem, and the line at low $Ca$ corresponds to the silent phase. Dashed lines indicate unstable critical points of the fast subsystem. Open or closed circles mark the maximum and minimum $v$ coordinates of a periodic orbit. Closed black circles indicate stable periodic orbits P of the fast subsystem that correspond to spiking. Open black circles correspond to unstable periodic orbits for the fast subsystem. Orange circles correspond to high voltage low amplitude oscillations L of the fast subsystem. A SN bifurcation coincides with a homoclinic bifurcation of P, resulting in a SNIC bifurcation. P meets the unstable periodic orbits at a SNP bifurcation, labeled OSNP here. The unstable periodic orbits meet L at another SNP bifurcation, labeled ISNP here. L collapses down to the branch of stable critical points corresponding to depolarization block at an AH bifurcation.

$Ca$ coordinate of the curve of SNIC bifurcations. For $(Ca, Na)$ such that $Na > Na_{SNIC}$ and $Ca < Ca_{SNIC}(Na)$ there is a unique stable critical point of the fast subsystem, $Q(Ca, Na)$, corresponding to hyperpolarized quiescence. In particular, $Ca_{base} < Ca_{SNIC}(Na)$ for almost all $Na > Na_{SNIC}$.

Similarly to subsection 3.3.1, we use the dynamics of equations (3.1)–(3.4),(3.8) to define $F_{g_{NaP}=0}(Ca, Na, x_0) = \{x :$ for fixed $(Ca, Na)$ and any given $\delta > 0$ there exists $t_n \to \infty$ such that for each $t_n$, $d(x_0 \cdot t_n, x) < \delta\}$. Again, $F_{g_{NaP}=0}(Ca, Na, x_0)$ may be either a nontrivial orbit or a critical point. We use this definition to consider various types of trajectories for the full system. We begin our construction with $Ca = Ca_{base}$ and $Na > Na_{SNIC}$ so that $F_{g_{NaP}=0}(Ca, Na, x_0) = Q(Ca, Na)$. In this state, $s \approx 0$ and thus $\dot{Ca} \approx 0$, and we need only consider the $Na$ dynamics, which will initially cause $Na$ to decrease toward $Na_{base}$. If $Na_{SNIC} < Na_{base}$, then $Na$ will stagnate at $Na_{base}$, resulting in a solution to the full system that exhibits quiescence. On the other hand, if $Na_{SNIC} > Na_{base}$, the system may exhibit bursting or tonic spiking dynamics. As $Na$ decreases toward $Na_{base}$, eventually $Na < Na_{SNIC}$ holds and $Q(Ca, Na)$ is no longer defined; the full system exits the quiescent state, see Figure 3.5.

For fixed $Na$, treating $Ca$ as a bifurcation parameter yields two SNP bifurcations, which we label as ISNP ("inner SNP"), for the one with a lower $Ca$ coordinate, and OSNP ("outer SNP"), for the bifurcation at higher $Ca$ coordinate. We define $Ca_{ISNP}(Na)$ to be the $Ca$ coordinate of ISNP for the given value of $Na$, and similarly, $Ca_{OSNP}(Na)$ is defined to be the $Ca$ coordinate of OSNP for the given value of $Na$. For $Ca_{SNIC}(Na) \leq Ca < Ca_{OSNP}(Na)$ we can define $P(Ca, Na)$ to be the unique high voltage large amplitude stable periodic orbit of the fast subsystem that corresponds to spiking.

As the full system exits the quiescent state, it follows that $F_{g_{NaP}=0}(Ca, Na, x_0) = P(Ca, Na)$. The model neuron is self-coupled, and as a result of the spiking the $s$ dynamic variable increases, which induces a positive drift in $Ca$, see Equation (3.5). Increased $Ca$ activates the CAN current, which for sufficiently high $g_{CAN}$ leads to increased spiking frequency. This increased spiking frequency further drives $Ca$ by sustaining a higher synaptic level $s$, see Equations (3.1) and (3.8). The dynamics may enter a voltage-dependent spike inactivation state called depolarization block, and to explain this, we consider the location

of the AH bifurcation relative to the trajectory of the slow subsystem. There is a curve of AH bifurcations in the $(Ca, Na)$ plane, so we define $Ca_{AH}(Na)$ to be the $Ca$ coordinate of the AH bifurcation for a provided value of $Na$. For $(Ca, Na)$ satisfying $Ca_{AH}(Na) < Ca$, we define $DB(Ca, Na)$ to be the unique stable critical point of the fast subsystem corresponding to depolarization block (e.g., the solid branch of critical points near $v = -20$ in Figure 3.4). As $Ca$ increases, eventually $Ca > Ca_{OSNP}(Na) > Ca_{AH}(Na)$ holds, and $P(Ca, Na)$ is no longer defined; $F_{g_{NaP}=0}(Ca, Na, x_0) = DB(Ca, Na)$ so that the dynamics no longer exhibits spiking. Instead, through damped oscillations, it winds down to the depolarization block state.

With the full system in depolarization block, the $s$ dynamic variable decays due to the spike attenuation (see Equation (3.8), and in particular $s_\infty(v)$ and $\theta_s$ in Section 3.2). From Equation (3.5) we note that low levels of $s$ cause $Ca$ to decay, so that $Ca < Ca_{AH}(Na)$ eventually holds. For $(Ca, Na)$ satisfying $Ca_{ISNP}(Na) < Ca < Ca_{AH}(Na)$, we define $L(Ca, Na)$ to be the unique high voltage low amplitude stable periodic orbit of the fast subsystem corresponding to the given $(Ca, Na)$ pair. For $Ca_{ISNP}(Na) < Ca < Ca_{AH}(Na)$ there is bistability between $L(Ca, Na)$ and $P(Ca, Na)$ for the fast subsystem; however, a solution just exiting depolarization block will be in the basin of attraction for $L(Ca, Na)$. Periodic orbits for $L(Ca, Na)$ have a maximal voltage less than $\theta_s$; see Figure 3.4 for an example of this situation. These sub-threshold oscillations do not yield an increase in the $s$ dynamic variable, so that $Ca$ continues to have a negative drift, at least until $Ca < Ca_{ISNP}(Na)$, so that $L(Ca, Na)$ is no longer defined and $F_{g_{NaP}=0}(Ca, Na, x_0) = P(Ca, Na)$. However, due to the activated CAN current, $Na$ continues to have a positive net drift throughout the active phase that we have described, see Equation (3.6). As $Na$ increases, so does $Ca_{SNIC}(Na)$. If the combined changes in $Na$ and $Ca$ push $Ca < Ca_{SNIC}$, then $P(Ca, Na)$ is not defined, yielding $F_{g_{NaP}=0}(Ca, Na, x_0) = Q(Ca, Na)$ so that the full system returns to the silent phase. We summarize the $(Na, Ca)$ coordinates corresponding to different dynamics for $F_{g_{NaP}=0}(Ca, Na, x_0)$ in Figure 3.5.

A solution that encompasses all of these components has a burst that exhibits depolarization block during its active phase, which we will call a DB burst. If $g_{CAN}$ is low, then, for $Na \geq Na_{base}$, $Ca_{AH}(Na)$ may be beyond the maximum attainable value of $Ca$, so the

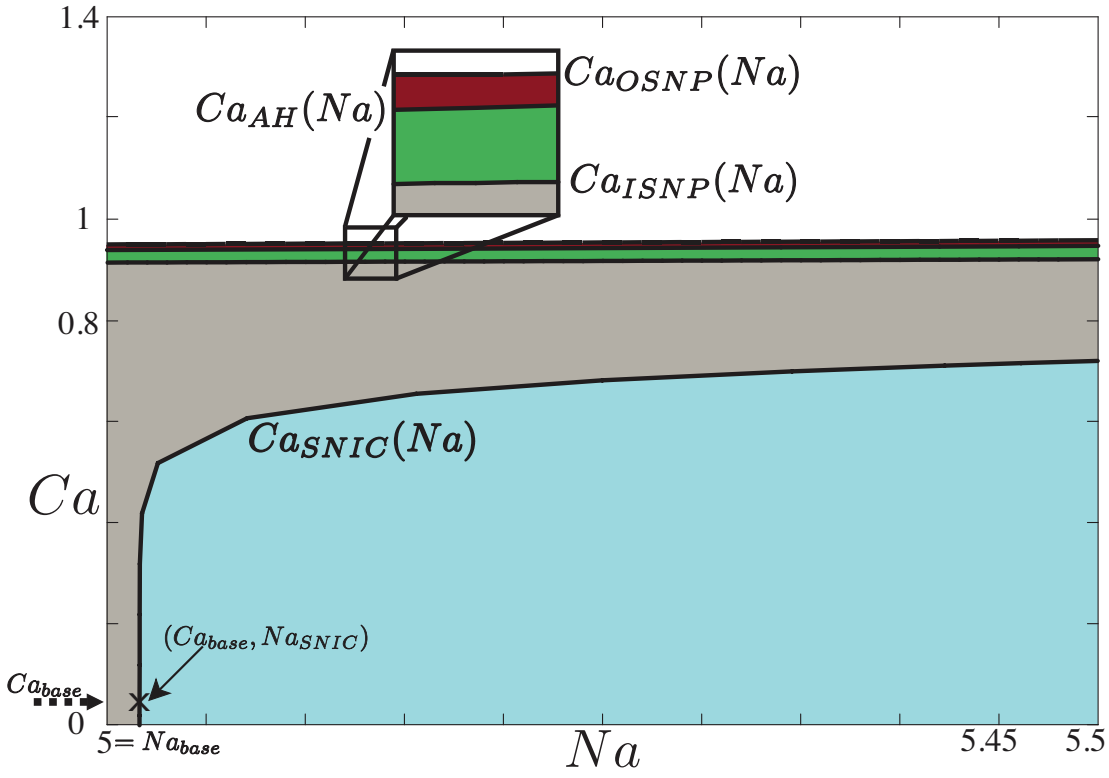


Figure 3.5: Plot of various bifurcation curves and resultant dynamics of the fast subsystem when $g_{NaP} = 0$. For $(Na, Ca)$ corresponding to the light blue region $F_{g_{NaP}=0}(Ca, Na, x_0) = Q(Ca, Na)$. For $(Na, Ca)$ corresponding to the light grey region, $F_{g_{NaP}=0}(Ca, Na, x_0) = P(Ca, Na)$. For $(Na, Ca)$ in the green region, there is bistability in the fast subsystem, either $F_{g_{NaP}=0}(Ca, Na, x_0) = P(Ca, Na)$ or $F_{g_{NaP}=0}(Ca, Na, x_0) = L(Ca, Na)$. Similarly, for $(Na, Ca)$ in the red region, there is also bistability in the fast subsystem such that either $F_{g_{NaP}=0}(Ca, Na, x_0) = P(Ca, Na)$ or $F_{g_{NaP}=0}(Ca, Na, x_0) = DB(Ca, Na)$ holds. Finally, for $(Ca, Na)$ in the white region, $F_{g_{NaP}=0}(Ca, Na, x_0) = DB(Ca, Na)$. These regions are bounded by various curves of SNIC, AH, or SNP bifurcations.

model neuron will not reach the depolarization block state, see Section 3.5.5. This may lead either to square-wave bursting or to tonic activity. We say that a function $f(x)$ blows up for finite $x = x_0$ if $\lim_{x \to x_0} f(x) = \infty$. When the coordinate of a bifurcation blows up, the trajectory may be captured by this bifurcation. For instance, if $Ca_{SNIC}(Na)$ blows up for finite $Na = Na_0$ then as $Na$ approaches $Na_0$, the trajectory's $Ca$ and $Na$ coordinates satisfy $Ca < Ca_{SNIC}(Na)$, and so $F_{g_{NaP}=0}(Ca, Na, x_0) = Q(Ca, Na)$ and we say that the trajectory has been captured by the SNIC bifurcation. Specifically, if $g_{CAN}$ is low, then $Ca_{SNIC}(Na)$ may blow up for finite $Na$, see Section 3.5.6.

If the activated CAN current can pull $Na$ up to such a value that the $Ca_{SNIC}(Na)$ blows up, then $F_{g_{NaP}=0}(Ca, Na, x_0) = Q(Ca, Na)$. Thus, the trajectory will have a period of quiescence, so that $Ca$ and $Na$ will decay. As $Na$ decays during the quiescence, $Ca_{SNIC}(Na)$ takes finite values again. Eventually $Na < Na_{SNIC}$ holds and triggers re-entry to the active phase, which, via activation of the CAN current, brings $Na$ high enough that $Ca_{SNIC}(Na)$ blows up, resulting in a return to the silent phase. A solution with such dynamics exhibits square-wave bursting with a long period and we note that this version of square-wave bursting is distinct from the square-wave bursts see in Section 3.3.1. Should this blowup of the $Ca_{SNIC}(Na)$ not occur, the resultant solution has no way to return to the silent phase and so will be tonically active.

The dynamics of the $g_{NaP} = 0$ system depends on $E_L$ as well. If $E_L \leq -61$, then $Na_{base} > Na_{SNIC}$, so that the solution cannot enter the active phase and quiescence results. If $E_L = -60$, then increasing $g_{CAN}$ from 0 to 5 first yields tonically active solutions and then DB bursting solutions. For $E_L = -59.5$, increasing $g_{CAN}$ from 0 to 5 first yields solutions that are tonically active, then square-wave bursting, then tonic activity again, and finally DB bursting. Desirable bursting solutions persist for a range of $E_L \geq -59.5$; however, when $E_L$ is not sufficiently negative, $I_{pump}$ is unable to terminate the burst by causing a prolonged silent phase [56]. Instead, for sufficiently high $g_{CAN}$ and $E_L$, the trajectory will wind back and forth through the AH bifurcation, resembling an elliptic burster. The mechanisms underlying these different solutions will be described in detail, for the more general case with both $I_{\mathrm{NaP}}$ and $I_{\mathrm{CAN}}$ in the model, in Sections 3.5 and 3.6.

## 3.4 NUMERICS

Most of our numerical work was done in the MATLAB programming language (The MathWorks, Natick, MA). Systems such as our unified model that have multiple timescales are stiff, so to speed up integration we used a C implementation of the CVODE package from SUNDIALS [26], interfaced with MATLAB via the mex command. Absolute and relative tolerances were set to $10^{-6}$. Two dimensional bifurcation diagrams such as Figure 3.2 were generated with XPPAUT [19], and three dimensional bifurcations were created by the MATCONT package for MATLAB [16] as well as XPPAUT.

In Figure 3.6, we present a colorization of $(g_{NaP}, g_{CAN})$ parameter space based on the dynamics of the model under different parameter choices, using blue for quiescence, black for tonic, and green for bursting. To classify a parameter set based on neuronal activity, we use initial conditions corresponding to the silent phase, with elevated $Na$ and low $Ca$ and $hp$, and after a transient of $10,000$ msec, we apply an algorithm to the spiking pattern of the model neuron recorded over the next 9999 msec. The algorithm records that the model neuron has spiked each time $V = 0$ and $V' > 0$, since most spikes peak at about $V = 20$, and $V$ stays below 0 during both the spike attenuation leading into depolarization block that sometimes occurs and the sub-threshold oscillations that emerge upon exit from depolarization block. If there are no spikes after the initial transient, then we classify the model neuron as quiescent. Otherwise, we compute the standard deviation of the interspike intervals (ISI). The ISI of a tonically active model neuron will have a standard deviation very close to zero milliseconds. On the other hand, due to the long time between the last spike of a burst and the first spike of the next burst, in the bursting case the standard deviation of the ISI is significantly increased relative to the tonically active case. We classified the model neurons as follows: if the standard deviation of the ISI was less than 10 msec, we considered the model neurons to be tonically active; otherwise, they were considered to be bursting. All of the tonically active model neurons observed before automating the procedure had ISI standard deviations well below 10 msec. Most bursting solutions yielded ISIs with standard deviations greater than 50 msec, so a threshold of 10 msec is reasonable for partitioning the parameter space.

We include white labels in Figure 3.6 to facilitate later discussion. Figure 3.7 provides representative voltage traces from these labeled regions. The bursting dynamics in region II (Figure 3.7(a)) is square-wave bursting as seen in the Butera model [4], while that in region III (Figure 3.7(b)) is DB bursting as seen in the Rubin-Hayes model [56]. Both of these are prevalent in voltage traces recorded from mouse preBötC slices, as are the patterns found in region * (Figure 3.7(c)). Figure 3.8 gives several sample recordings and agrees well with model output for the various bursting regimes.

In Section 3.8.2, we discuss the differences between considering a reciprocally coupled pair of model neurons, and one self-coupled neuron. For two reciprocally coupled neurons, we find that the synchronous state is weakly unstable, but nevertheless, the activity patterns of the two neurons are very similar. Except for the precise spike synchrony, all of the dynamics observed in the self-coupled case have been observed in the two-neuron case. The result of this analysis yields that the self-coupled case will yield good insight into the two-neuron case.

Variations in $E_L$ have been used to explore robustness of model dynamics in past work, for various reasons (see Discussion). We generated Figure 3.6 with $E_L = -61$, although the figure would be qualitatively similar for a range of $E_L$ values. In particular, for $E_L < -61$, a higher value of $g_{NaP}$ is required for solutions to be able to enter the active phase, so all of the regions will shift to the right in $g_{NaP}$ space. On the other hand, for $E_L > -61$ and large enough such that the system fails to produce quiescence or bursts when $g_{CAN} = 0$, then the $g_{CAN} \neq 0$ case will not exhibit region I-like or region II-like dynamics, but the other regions persist. We note that region * is lost for a value of $E_L$ close to that which causes the loss of region II. For $E_L$ insufficiently negative, $I_{pump}$ and the NaP current will be unable to cause a prolonged silent phase (as seen in the $g_{NaP} = 0$ case), and the system may exhibit activity that resembles elliptic bursts.

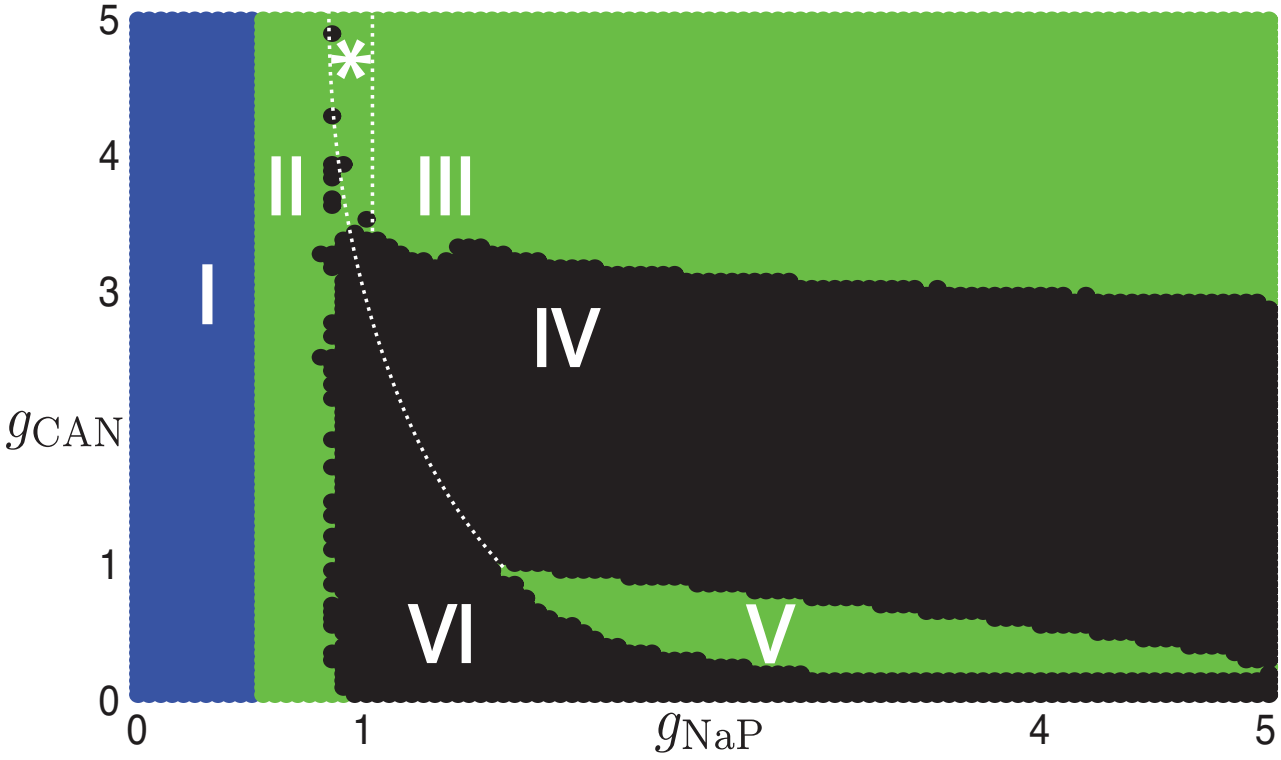


Figure 3.6: Partition of $(g_{NaP}, g_{CAN})$ parameter space based on the dynamics of the unified model for a self-coupled neuron. Blue dots represent quiescent solutions. Black dots represent tonic activity. Green dots represent bursting activity, either of DB bursting or square-wave bursting type. See Figure 3.7 for example voltage traces corresponding to non-quiescent labeled regions.

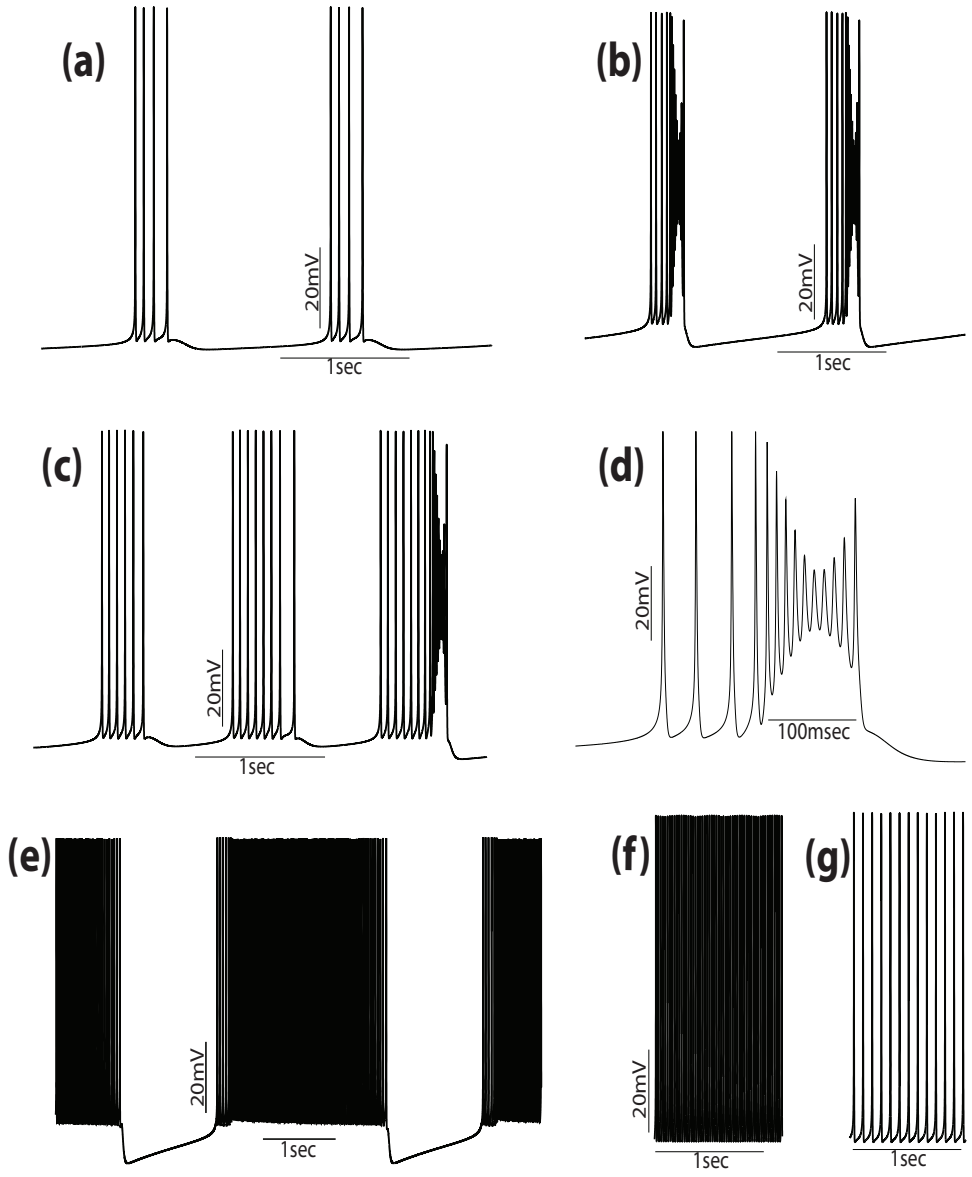


Figure 3.7: Example voltage traces of select regions from Figure 3.6. Panel (a) corresponds to region II, (b) to region III, and (c) to region *, while panel (d) shows the typical structure of a DB burst from region III or region *. Panel (e) shows activity from region V, (f) from region IV, and (g) from region VI.

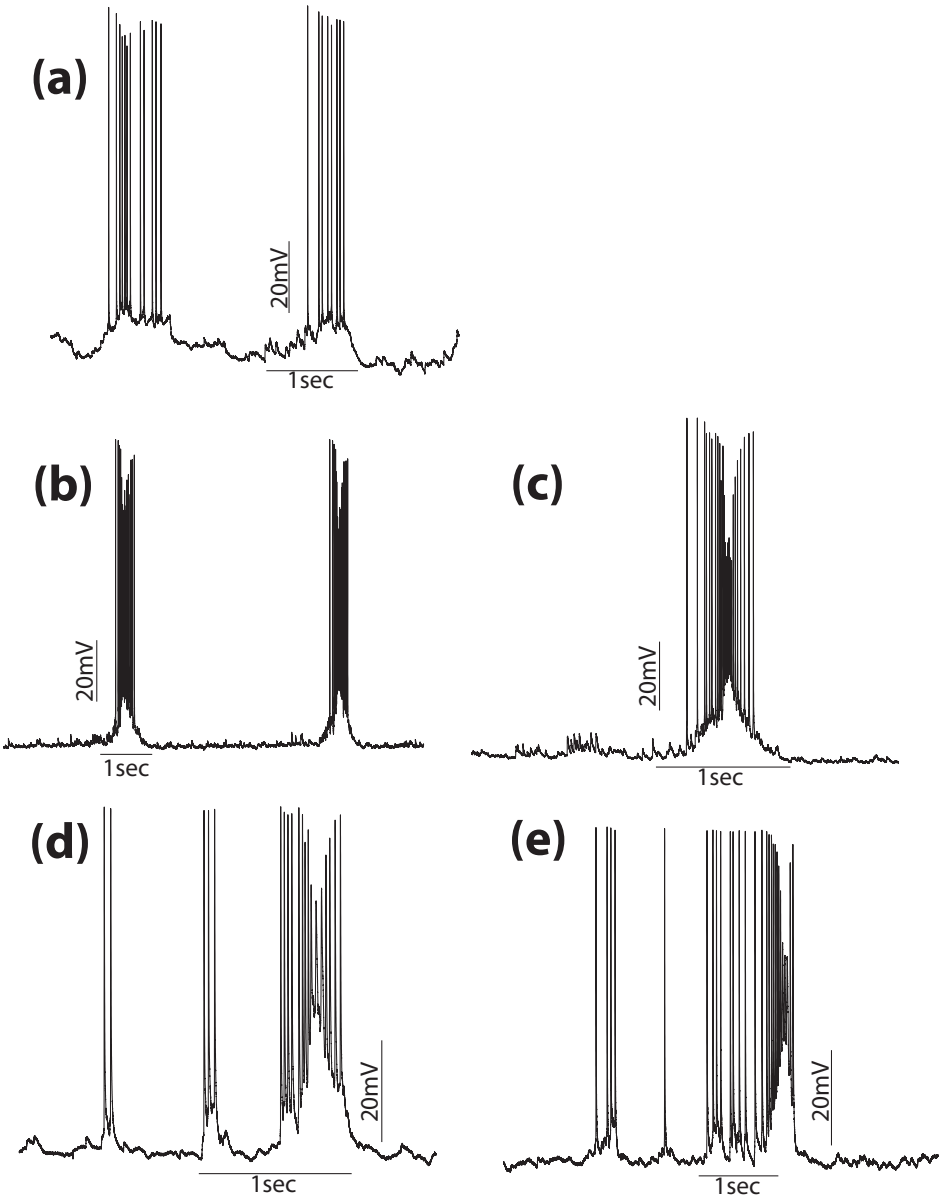


Figure 3.8: Examples from typical *in vitro* recordings from the mouse. Panel (a) corresponds to region II (Figure 3.7(a)), panels (b) and (c) to region III (Figure 3.7(b)), and panels (d) and (e) to region * (Figure 3.7(c)).

## 3.5 ANALYSIS OF UNIFIED MODEL DYNAMICS FOR A SELF-COUPLED NEURON

In this section, we analyze the mechanisms by which the solutions observed in each marked region of Figure 3.6 come about. Figure 3.6 was generated with $E_L = -61$ and with initial conditions corresponding to the quiescent state, as described in Section 3.4. We elected $E_L = -61$ for this analysis because when $g_{CAN} = 0$, we have quiescent, bursting, and tonic spiking solutions, depending on the values of other parameters, in the presence of self-coupling.

For $g_{NaP} \neq 0$, for fixed $hp > 0$ and for fixed $Na > Na_{base}$, the bifurcation diagram for the fast subsystem generated by treating $Ca$ as a bifurcation parameter is similar to Figure 3.4. When $g_{NaP} \neq 0$, but $hp = 0$, the bifurcation diagram is the same as Figure 3.4, because $hp$ and $g_{NaP}$ are multiplied together in equation (3.1) and do not appear anywhere else in the fast subsystem. However, for $hp > 0$, the SNIC bifurcation from the $hp = 0$ case decomposes down into a SN bifurcation and a separate homoclinic bifurcation as in Figure 3.2. The unstable critical point to which the homoclinic orbit converges as $t \to \pm\infty$ will be called a homoclinic point. Thus, for sufficiently small $hp$, we may approximate the $Ca$ and $Na$ coordinates of the homoclinic point with those coordinates of the SN bifurcation. Again, we will work in the $(\varepsilon_{Ca}, \alpha, \varepsilon_{hp}) = (0, 0, 0)$ limit and allow $F(Ca, Na, hp, x_0) = \{x$: for fixed $(Ca, Na, hp)$ and any given $\delta > 0$ there exists $t_n \to \infty$ such that for each $t_n$, $d(x_0 \cdot t_n, x) < \delta\}$. As before, $F(Ca, Na, hp, x_0)$ may be a critical point or a nontrivial orbit. In Figure 3.9, by treating $Ca, Na, hp$ as bifurcation parameters, we present some examples of bifurcation structures for the fast subsystem; in particular, we include a surface of SN bifurcations (SN surface), a surface of AH bifurcations (AH surface), as well as a surface of homoclinic points (HC surface). Indeed, except for the different values of $E_L$ used when generating Figure 3.5 and Figure 3.9, these figures are closely related; Figure 3.5 corresponds to the $hp = 0$ plane of Figure 3.9. We set $Ca_{SN}(Na, hp)$, $Ca_{AH}(Na, hp)$, and $Ca_{HC}(Na, hp)$ to be the $Ca$ coordinate of the SN surface, AH surface, and HC surface for each given $(Na, hp)$. We will also define $Ca_{ISNP}(Na, hp)$ and $Ca_{OSNP}(Na, hp)$ to be the $Ca$ coordinates of the two SNP surfaces, analogous to the corresponding curves in Figure 3.5.

For $X \in \{SN, AH, HC, ISNP, OSNP\}$ we say that the trajectory intersects or reaches the surface $X$ if the trajectory's $Ca, Na, hp$ coordinates satisfy $Ca = Ca_X(Na, hp)$. In general, a transition from the silent phase to the active phase occurs when the trajectory intersects the SN surface transversely, and hence crosses through it, through increases in $hp$ or $Ca$ or decreases in $Na$. A transition from the active phase to the silent phase occurs when the trajectory crosses the HC surface via decreases in $hp$ or $Ca$. An increase in $Na$ promotes such a transition by bringing the surface to larger $hp$ and $Ca$ values (Figure 3.9 and Figure 3.10 below) but will not achieve this transition on its own due to the curvature of the relevant part of the HC surface.

For the following, we assume that initially, $Na > Na_{base}$ and $0 \leq hp \leq 1$. As in Sections 3.3.1 and 3.3.2, for $(Ca, Na, hp)$ such that $Ca < Ca_{SN}(Na, hp)$, there is a unique stable critical point for the fast subsystem corresponding to hyperpolarized quiescence, $Q(Ca, Na, hp)$.

For $(Ca, Na, hp)$ such that $Ca_{HC}(Na, hp) < Ca < Ca_{OSNP}(Na, hp)$ there is a unique large amplitude high voltage stable periodic orbit of the fast subsystem, $P(Ca, Na, hp)$, corresponding to spiking. When $(Ca, Na, hp)$ satisfy $Ca_{ISNP}(Na, hp) < Ca < Ca_{AH}(Na, hp)$, there is a unique small amplitude high voltage stable periodic orbit of the fast subsystem, $L(Ca, Na, hp)$, corresponding to sub-threshold oscillations. Finally, for $(Ca, Na, hp)$ such that $Ca_{AH}(Na, hp) < Ca$, there is a unique stable critical point of the fast subsystem, $DB(Ca, Na, hp)$, corresponding to depolarization block.

### 3.5.1 Region I

As described in Figure 3.6, parameter values from region I yield quiescent solutions. We begin the analysis with $g_{CAN} = 0$. Increasing $g_{NaP}$ lowers $hp_{SN}$, possibly so that the $hp$-nullcline no longer intersects the family of quiescent critical points. We call $g^*_{\text{NaP}}$ the critical $g_{NaP}$ such that when $g_{CAN} = 0$ the quiescent solution exists if and only if $g_{NaP} < g^*_{\text{NaP}}$. We note that $g^*_{\text{NaP}}$ is the value for $g_{NaP}$ such that the $hp$-nullcline intersects the surface of fast subsystem critical points precisely at the SN bifurcation point. When $g_{NaP} < g^*_{\text{NaP}}$, allow $hp_{max}(g_{NaP})$ to be the $hp$ coordinate of the intersection of the $hp$-nullcline and branch of

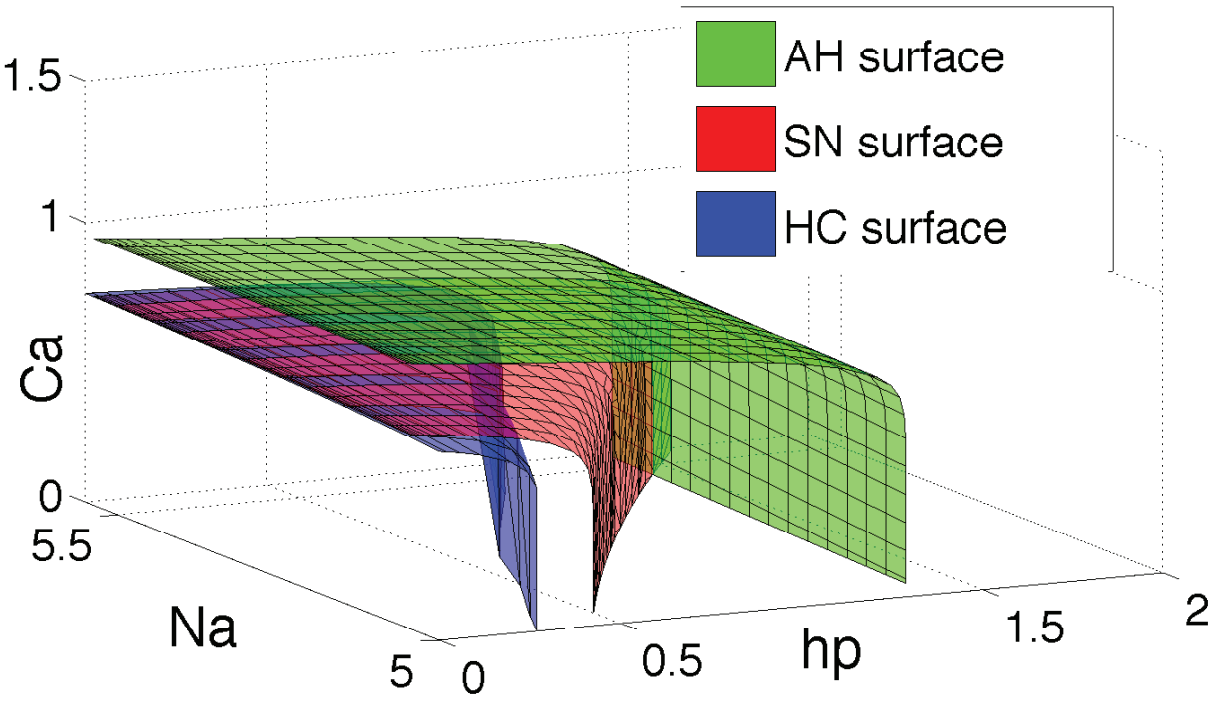


Figure 3.9: SN bifurcation surface (red), AH bifurcation surface (green), and homoclinic points (blue) of system (3.1)–(3.4),(3.8), treating $Ca$, $Na$ and $hp$ as bifurcation parameters. Notice that as $hp$ decreases toward 0, the blue and red surfaces combine to form a SNIC bifurcation surface. We also note that for $Ca = 0$ and $hp = 0$, $Na_{SN} < Na_{base} = 5$, so the slow subsystem cannot pass through the SN surface unless $hp$ or $Ca$ increases. The MATLAB figure file is available as electronic supplementary material.

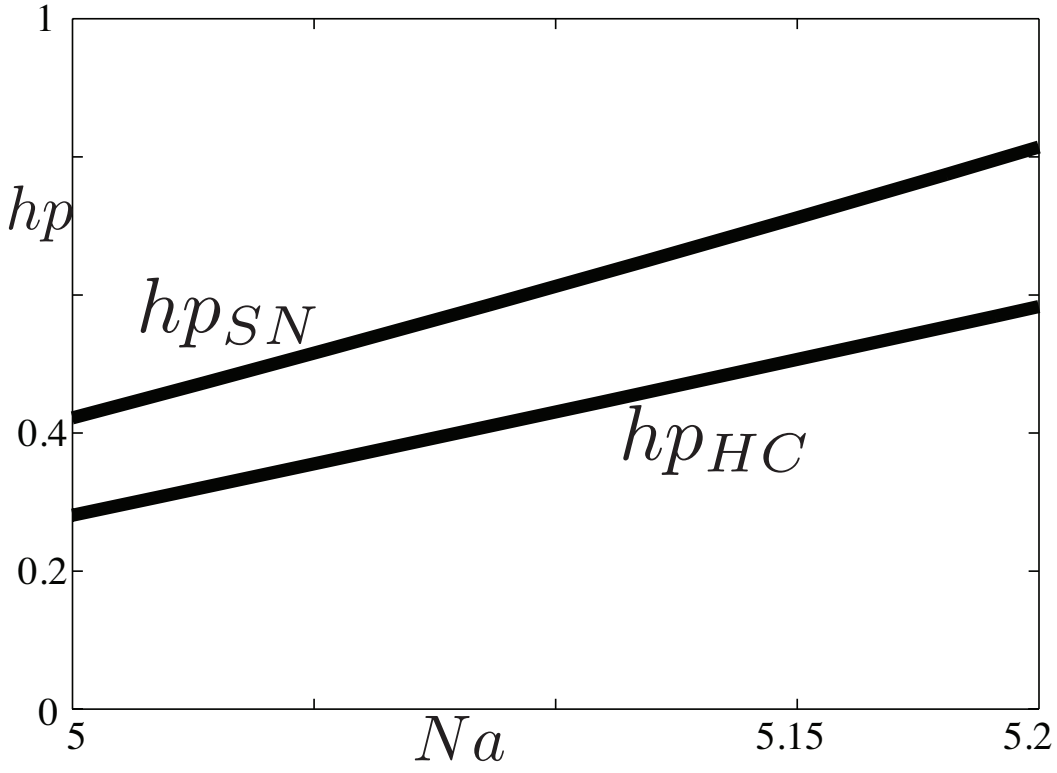


Figure 3.10: Bifurcation curves with fixed $Ca \approx Ca_{base}$. The top curve is $hp_{SN}$ as a function of $Na$. The bottom curve is $hp_{HC}$ as a function of $Na$. Note that the functions increase, so that a small increase in $Na$ may cause $hp_{HC}$ to be crossed, resulting in an early return to and an extended time in the silent phase.

quiescent critical points.

When $E_L = -61$ in the case $g_{NaP} = 0$, the solution is unable to escape quiescence because $Na_{base} > Na_{SNIC}$. Modulation of $g_{CAN}$ will not change this, because $I_{\mathrm{CAN}}(v, Ca)$ does not contribute to $\dot{v}$ when $Ca$ is small. With $Ca$ decaying to $Ca_{base}$ the slow subsystem evolves toward the point $(Ca_{base}, Na_{base}, hp_{max})$, and $Ca_{base} < Ca_{SN}(Na_{base}, hp_{max})$ so that $F(Ca, Na, hp, x_0) \to Q(Ca_{base}, Na_{base}, hp_{max})$ and the solution exhibits quiescent dynamics forever, see Figure 3.11. Similar coordinates for $0 < g_{NaP} < g^*_{\mathrm{NaP}}$ yield the vertical right boundary of region I in Figure 3.6, representing independence from $g_{CAN}$.

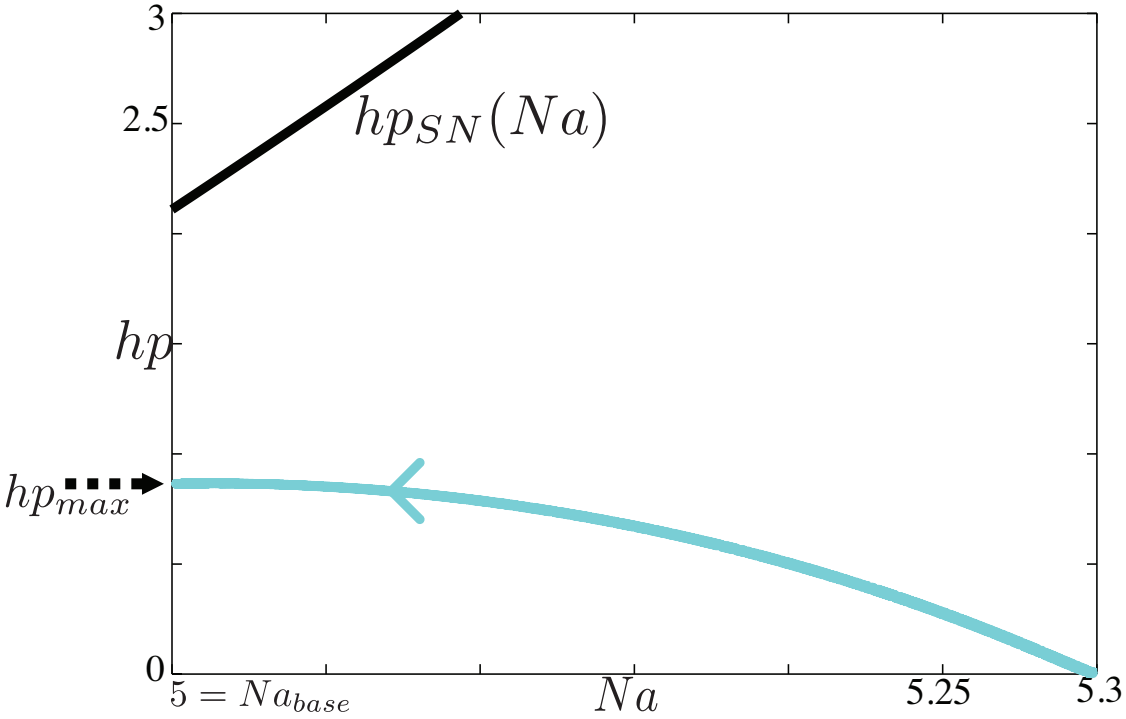


Figure 3.11: SN surface projected onto $(Ca = Ca_{base}, Na, hp)$ coordinates is colored black. The colored curve with the arrowhead is the projection of the trajectory of the full system. The trajectory converges to $(Ca_{base}, Na_{base}, hp_{max})$ without crossing the SN surface, yielding a quiescent steady state.

### 3.5.2 Region II

Trajectories found for parameter values in region II exhibit square-wave bursts typical of the Butera model, even in the presence of elevated $g_{CAN}$. Indeed, the dynamics here is not very different from the dynamics described in Section 3.3.1, with $g_{CAN} = 0$. Here, we will show how this dynamics is preserved when $g_{CAN} > 0$. With $E_L = -61$, since $Na_{base} > Na_{SN}$, we rely on $hp$ increasing enough to cause the singular solution to cross the SN surface to initiate spiking, see for instance the $Ca = Ca_{base} = 0.05$ plane in Figure 3.9. That is, after $Na$ has decayed to $Na_{base}$ and $Ca$ has decayed to $Ca_{base}$, we need $hp$ such that $Ca_{SN}(Na_{base}, hp) < Ca_{base}$ in order for the solution to exit the silent phase. As in Section 3.3.2, once the solution exits the silent phase, $F(Ca, Na, hp, x_0) = P(Ca, Na, hp)$, the solution begins spiking, and $hp$ begins to decay. Across each spike, $Ca$ rises to a higher level, and then $Ca$ decays after the spike. However, the CAN current requires a certain level of $Ca$, namely $Ca \approx k_{\text{CAN}}$, to become active and qualitatively change the dynamics. Until $Ca \approx k_{\text{CAN}}$, $Na$ remains near $Na_{base}$ and the dynamics is qualitatively as in the $g_{CAN} = 0$ case.

To activate the CAN current, then, we need a certain number of spikes of $F(Ca, Na, hp, x_0)$ to occur within a certain window of time to increase s and overwhelm the decay of $Ca$ to $Ca_{base}$ (see Equation (3.5)). The bursts in region II do not yield enough spikes to meet this condition, and decreasing $hp$ causes a return to the silent phase exactly as with $g_{CAN} = 0$. In fact, the presence of the CAN current, even if not fully activated due to low $Ca$, actually aids in this transition to the silent phase. The small rise in $Ca$ induced by the spiking activity causes enough $I_{\text{CAN}}$ activation to increase $Na$ slightly, especially for high $g_{CAN}$. Numerically, we observe that, for $Ca$ fixed, both $hp_{HC}$ and $hp_{SN}$ are increasing functions of $Na$, see Figure 3.10. Thus, the spiking activity that increases $Na$ slightly will increase $hp_{HC}$ and cause an earlier crossing of $hp_{HC}$ and return to the silent phase. Further, since $hp_{SN}$ is an increasing function of $Na$, $hp$ may be unable to cross $hp_{SN}$ until $Na$ decays. This has two key effects. First, the dependence on the slow decay of $Na$ causes the solution of the full system to spend a longer time in the silent phase. Second, the singular solution crosses the SN surface with a higher $hp$ value, which may cause more spikes to occur; however,

in region II, these extra spikes never appreciably activate the CAN current. So, increasing $g_{CAN}$ within region II changes the interburst interval, and the spike counts within bursts, but does not yield the DB bursts seen in region III (Figure 3.7).

### 3.5.3 Region III

Region III contains DB bursts similar to those seen in the Rubin-Hayes model from interactions of $I_{\text{CAN}}$ and $I_{pump}$. Again, the key difference arising for DB bursts in the unified model (3.1)–(3.8), compared to the Rubin-Hayes model, is that the SNIC bifurcation transforms into two separate entities, a SN bifurcation of critical points and a homoclinic bifurcation. Nevertheless, when a solution spends an extended time in the active phase, we may use the SN bifurcation as an approximation to the homoclinic orbit once the CAN current is activated. This approximation is reasonable because $hp$ becomes very small during an extended active phase and $g_{NaP}$ and $hp$ are multiplied in $I_{\text{NaP}}(v, hp)$ in Equation (3.1), so that during an extended active phase, the bifurcation structures approach those from the $g_{NaP} = 0$ case, where the saddle node and homoclinic do combine to form a SNIC bifurcation. In Figure 3.9, we see that for $hp = 0$, the homoclinic surface and SN surface coincide as expected, supporting our claim that for low $hp$ we may approximate the homoclinic surface by the SN surface. This approximation can also be justified by the interpretation of $hp$ as an inactivation variable for $I_{\text{NaP}}$, so when $hp$ is low there is little contribution from $I_{\text{NaP}}$ due to inactivation. This approximation will come into play in understanding the transition to the silent phase in region III, as described below.

While $F(Ca, Na, hp, x_0) = Q(Ca, Na, hp)$, decreasing $Na$ and increasing $hp$ cause a decrease in $Ca_{SN}(Na, hp)$, until $Ca_{SN}(Na, hp) < Ca_{base}$, allowing the trajectory exit the silent phase. As in both Section 3.3.1 and Section 3.3.2, once $Ca_{SN}(Na, hp) < Ca_{base}$, the fast subsystem no longer has a branch of critical points corresponding to quiescence as an attractor, and $F(Ca, Na, hp, x_0) = P(Ca, Na, hp)$. The difference between region II and region III is that region III has higher $g_{NaP}$ than region II, resulting in faster spikes along solutions in $F(Ca, Na, hp, x_0)$, which occur fast enough to build up $Ca$ and activate the CAN current.

By the time that $Ca$ builds up, $hp$ has decayed significantly, so that we may approximate the HC surface by the SN surface. With this approximation, the dynamics is similar to Section 3.3.2. $Ca$ continues to build up, until $Ca > Ca_{OSNP}(Na, hp)$ holds. For $Ca > Ca_{OSNP}(Na, hp)$, $F(Ca, Na, hp, x_0) = DB(Na, hp)$, and the full system enters depolarization block. Spike attenuation due to depolarization block causes $Ca$ to decrease and eventually $Ca < Ca_{AH}(Na, hp)$ holds, such that the solution exits depolarization block. As the trajectory exits depolarization block, $F(Ca, Na, hp, x_0) = L(Ca, Na, hp)$ and the solution has small amplitude high voltage periodic orbits, as in Section 3.3.2. The small amplitude of the periodic orbits do not produce enough voltage variation to yield an increase in $Ca$. Thus, at least until $Ca < Ca_{ISNP}(Na, hp)$ holds (and so $F(Ca, Na, hp, x_0) = P(Ca, Na, hp)$), $Ca$ continues to decrease. Meanwhile $Na$ has been increasing, so that it is possible that as $Ca$ decreases, $Ca < Ca_{SN}(Na, hp) \approx Ca_{HC}(Na, hp)$ results and correspondingly $F(Ca, Na, hp, x_0) = Q(Ca, Na, hp)$. The full system returns to quiescence until $Na$ decreases and $hp$ increases enough to start another burst, as described above.

The variable $hp$ plays two roles in generating a DB burst in region III. First, $hp$ combines with $Na$ to allow escape from the silent phase. Second, $hp$ contributes to the spike speed-up that yields the $Ca$ increases needed for a DB burst. One of the key features of the trajectory of the full system for region III is that in the active phase, although $hp$ becomes small, the decrease in $hp$ alone could not trigger a return to the silent phase. As $g_{NaP}$ is decreased, this feature may be lost, and this brings us to region *.

### 3.5.4 Region *

Region * is characterized by solutions that feature both square-wave bursts and DB bursts. As described in Section 3.5.3, while the full system is in the silent phase, a sufficient decrease in $Na$ together with an adequate rise in $hp$ allows $Ca_{SN}(Na, hp) < Ca$, causing $F(Ca, Na, hp, x_0) = P(Ca, Na, hp)$, and the solution transitions to the active phase. During the active phase, $Ca$ increases and $hp$ decreases. These effects result in a race between $Ca$ and $hp$. On one hand, if $hp$ decreases so that $Ca_{HC}(Na, hp) > Ca$, the full system may return to quiescence without going into the full burst that incorporates greater plateau-like

voltages, higher spiking rates, and ultimately depolarization block. Thus, this outcome results in a square-wave burst as in region II. On the other hand, if $Ca$ increases enough to activate the CAN current, then decreasing $hp$ alone will be unable to trigger a return to the silent phase; to terminate the burst, $Ca$ must be decreased by the full system entering depolarization block as in region III. The winner of the race is influenced by the level of $Na$ when the full system enters the active phase, as we shall now describe.

For $Ca$ fixed, $hp_{HC}$ increases as $Na$ increases, see Figure 3.10. When the trajectory enters the active phase with elevated $Na$, the decreasing variable $hp$ may be able to drop to the elevated value of $hp_{HC}$ and the net drift of $hp$ at the homoclinic orbit may be negative. In this case, $hp$ triggers a return to the silent phase before the CAN current can activate and cause a DB burst. The result is a square-wave burst. Such square-wave bursts, due to the fact that $Ca$ does not exhibit a large increase, yield a net decrease in $Na$. After one or more square-wave bursts, the full system enters the active phase with $Na$ low enough that $hp$ cannot drop below $hp_{HC}$ to trigger a return to the silent phase, resulting in a DB burst. After a DB burst, $Na$ is elevated, and thus so is $hp_{HC}$, so the subsequent bursts may be square-wave. In this way, we may observe solutions with varying sequences of square-wave and DB bursts. These solutions may not be periodic. Indeed, for at least some parameter values in region * we have noted a positive Lyapunov exponent, which may indicate that they are chaotic.

To illustrate this mechanism, we have plotted a trajectory of the full system projected into $hp, Ca$ space, along with two slices of the homoclinic surface, one for lower $Na$ and one for higher $Na$, see Figure 3.12. We begin on the orange section of the trajectory shown in Figure 12(b). Here, the full system has crossed through the SN surface and entered the active phase with $hp = .8$ and $Na = 5.3$ ("start" in Figure 12(a)). As the solution spikes, $Ca$ experiences several abrupt but transient increases while $hp$ decreases. The trajectory passes through the blue curve, which is the slice of the homoclinic surface corresponding to $Na = 5.1$, and even though several subsequent spikes occur, they are insufficient to keep the trajectory in the active phase. With the subsequent return to the silent phase, a square-wave burst results. In the silent phase, $Na$ decreases to 5.051 and $hp$ increases to about 0.6, and again the trajectory passes through the SN surface, causing the solution to re-enter

the active phase. We illustrate the next part of the solution in Figure 3.12 in black. Again, as the solution spikes, $Ca$ experiences abrupt though transient increases. Now we compare the trajectory of the full system against the slice of the homoclinic surface corresponding to $Na = 5.051$, shown in magenta. This time, the trajectory crosses the homoclinic surface only briefly, immediately returning back to the other side of the surface due to a spike. Indeed, this last spike brings $Ca > k_{\text{CAN}}$, activating the CAN current, and the DB burst progresses as usual, such that $Na$ attains an elevated level (Figure 12(b)) and then the trajectory enters the silent phase. In this way, with $Na$ diminished by each square-wave burst until it becomes small enough to allow a DB burst, which pushes it back up again, the model may continually generate alternating square-wave and DB bursts, or perhaps sequences of two or more square-wave bursts before a DB burst, as in Figures 3.7(c) and 3.8(d).

In recordings from preBötC neurons that alternate between DB and square-wave bursts we observe that the interburst interval following a DB burst is generally longer than the interburst interval after a square-wave burst. We highlight one example of this phenomenon in Figure 3.13(a), and the preceding analysis for region * can shed some light on this situation. During a DB burst, the activated CAN current elevates $Na$, and $hp$ typically decays to $hp \approx 0$ due to the prolonged activity. The next active phase begins when $hp$ crosses $hp_{SN}$, which will take longer due to elevated $Na$ (Figure 3.10), even though $Na$ is slowly decaying during the silent phase. If the subsequent burst is a square-wave burst, $Na$ will have continued to decay, and it need not be the case that $hp \approx 0$ at the start of the silent phase. Thus, following a square-wave burst, $hp$ is initially larger and $hp_{SN}$ is smaller (due to decaying $Na$), so it takes less time for the system to attain $hp > hp_{SN}$ and enter the next active phase, see Figure 3.13(b).

### 3.5.5 Region IV

As before, we begin our analysis with $Na > Na_{base}$, $hp = 0$, $Ca = Ca_{base}$ and $F(Ca, Na, hp, x_0) = Q(Ca, Na, hp)$. A decrease in $Na$ toward $Na_{base}$ and an increase in $hp$ cause $Ca_{SN}(Na, hp) < Ca$, resulting in a transition to the active phase. As in region III, $g_{NaP}$ is high enough so that a decrease in $hp$ alone cannot trigger a return to the silent phase. For fixed $Na, hp$, we

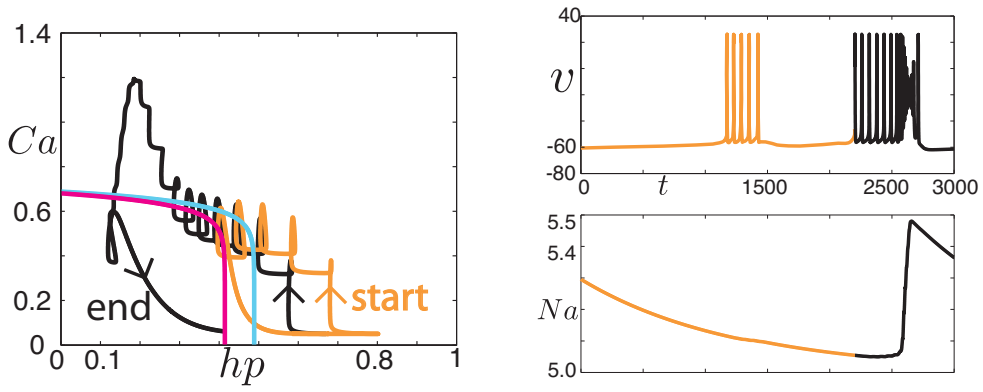


(a) (b)

Figure 3.12: Example trajectory from region *, with projection into $(hp, Ca)$ coordinates to illustrate the analysis of Section 3.5.4. (a) Projection of a trajectory from region * into $(hp, Ca)$ coordinates. The light blue curve is a slice of the homoclinic surface for $Na = 5.1$ and the magenta curve is a slice of the homoclinic surface for $Na = 5.051$. (b) $v$ and $Na$ plotted against time corresponding to the trajectory in (a).

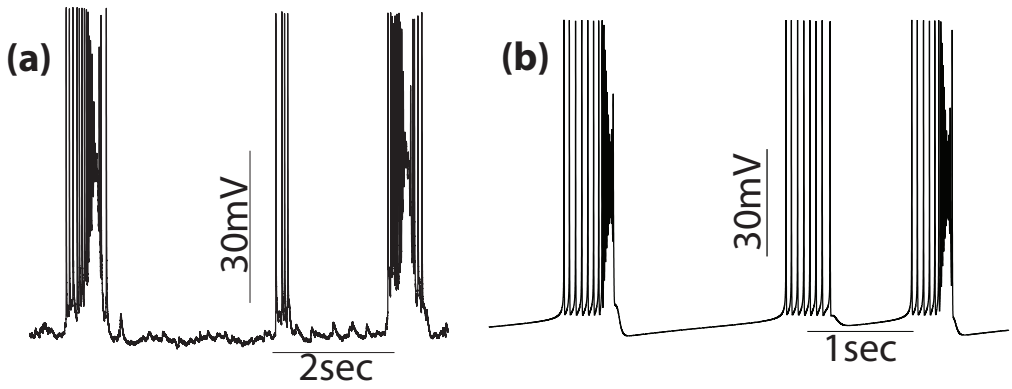


Figure 3.13: Silent phases following DB bursts have longer durations than those following square-wave bursts. Panel (a) shows a sample recording from a preBötC cell that consistently exhibited both square-wave and DB bursts. Panel (b) shows a typical trace from region *. Even though the time scale is not the same, the relative differences between the silent phases in the model agrees well with the data.

observe that $Ca_{AH}(Na, hp)$ is a decreasing function of $g_{CAN}$, see Figure 3.14. Decreasing $g_{CAN}$ may cause $Ca_{AH}(Na, hp)$ to blow up, in which case, $Ca < Ca_{AH}(Na, hp)$ always holds. During an extended active phase, $hp$ decreases to a minimal value, and we are essentially in the situation from Section 3.3.2. Recall from Section 3.3.2 or Section 3.5.3 that to terminate the burst, we required the solution to enter depolarization block so that spike attenuation would lead to a decrease in $Ca$. If $Ca < Ca_{AH}(Na, hp)$ always holds, the only way to depolarization block and corresponding decrease in $Ca$ will never occur, and tonic activity results, unless eventually $Ca_{HC}(Na, hp) > Ca$ holds. However, for most values of $g_{CAN}$, the value of $Ca_{SN}(Na, hp)$, and thus $Ca_{HC}(Na, hp)$, remains low relative to $Ca$ levels of CAN driven tonic activity in region IV, even for extremely high $Na$, see Figure 3.15. Thus, given that $Ca_{AH}(Na, hp)$ is beyond the maximal attainable value of $Ca$ and $Ca_{SN}(Na, hp)$ remains low, $F(Ca, Na, hp, x_0) = P(Ca, Na, hp)$ and the model's activity is indeed tonic.

As we shall see in the next subsection, there are some $g_{CAN}$ values for which $Ca_{SN}(Na, hp)$ does not remain bounded as a function of $Na$ and hence for which significantly different model dynamics emerges.

### 3.5.6 Region V

In this section we explain how the square-wave bursts seen in Figure 3.7(e), corresponding to region V, are realized. As usual, we begin in the silent phase, with $Na$ decreasing toward $Na_{base}$ and $hp$ increasing. Eventually, $Ca > Ca_{SN}(Na, hp)$, $F(Ca, Na, hp, x_0) = P(Ca, Na, hp)$, and the solution enters the active phase. We note that region V has $g_{NaP}$ values similar to those of region III, which implies that the trajectory cannot return to the silent phase simply by virtue of $hp$ decreasing, see Section 3.5.3. Moreover, region V lies below the $g_{CAN}$ value for which $Ca_{AH}(Na, hp)$ blows up, see Figure 3.14. So the trajectory cannot pass through the AH surface, meaning that the full system cannot enter depolarization block and hence $Ca$ cannot decrease to pass back through the HC surface. Instead, we find in region V that $Ca_{HC}(Na, hp)$ actually blows up as $Na$ increases, see Figure 3.16. When this blowup occurs, the trajectory is captured by the HC surface, that is, $Ca < Ca_{HC}(Na, hp)$ holds so that $F(Ca, Na, hp, x_0) = Q(Ca, Na, hp)$ and the full system returns to the silent

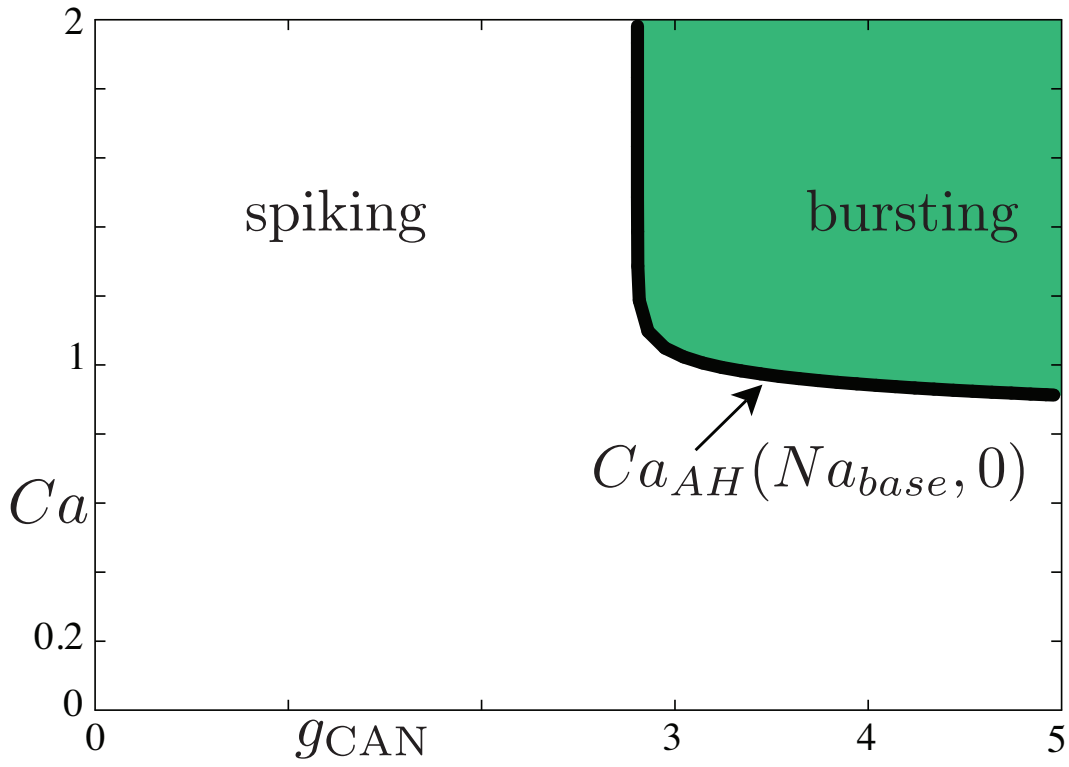


Figure 3.14: $Ca_{AH}(Na_{base}, 0)$ as a function of $g_{CAN}$, with $g_{NaP} = 3$. For fixed $g_{CAN}$, if $Ca_{AH}(Na_{base}, 0)$ is below the maximal value of $Ca$ attainable by the full system, the full system can exhibit a DB burst. Lowering $g_{CAN}$ causes $Ca_{AH}(Na_{base}, 0)$ to blow up, so that depolarization block is never realized, resulting in tonic activity.

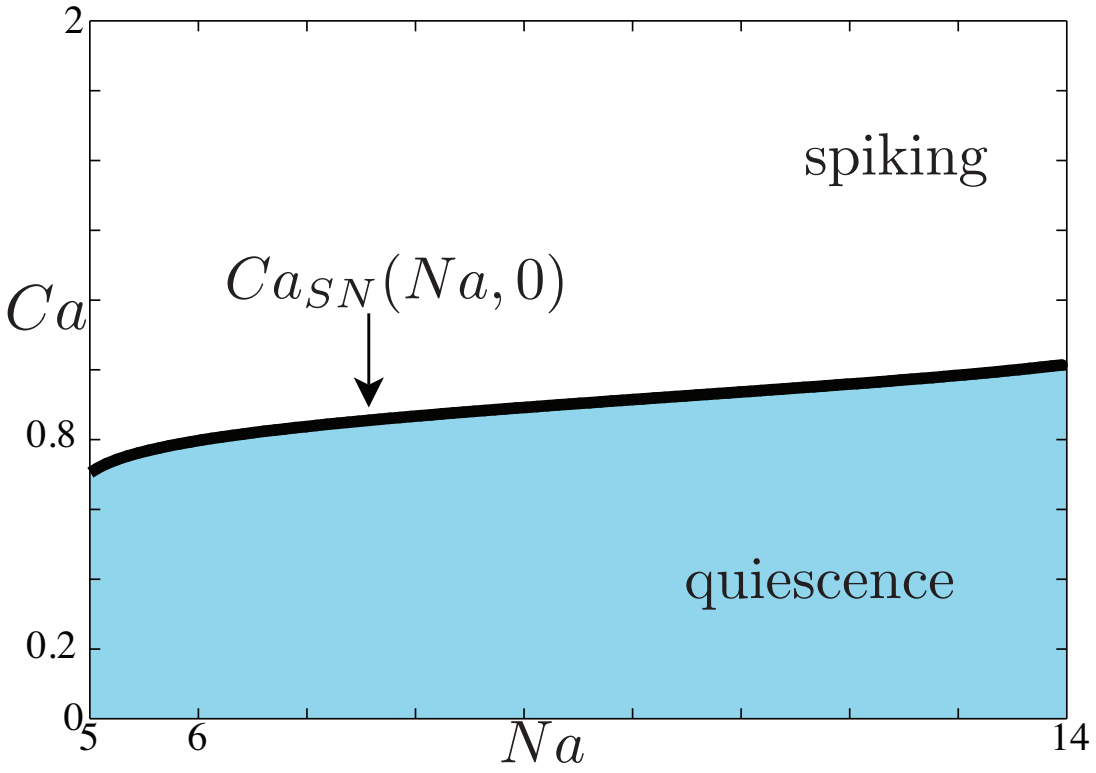


Figure 3.15: $Ca_{SN}(Na, 0)$ plotted for $g_{CAN} = 2.5$ and $g_{NaP} = 3$, a value for which the full system's $Ca$ coordinate cannot attain $Ca_{AH}(Na_{base}, 0)$. For $(Na, Ca)$ below $Ca_{SN}(Na, 0)$, the full system exhibits quiescence, while above it, the full system exhibits tonic spiking.

phase.

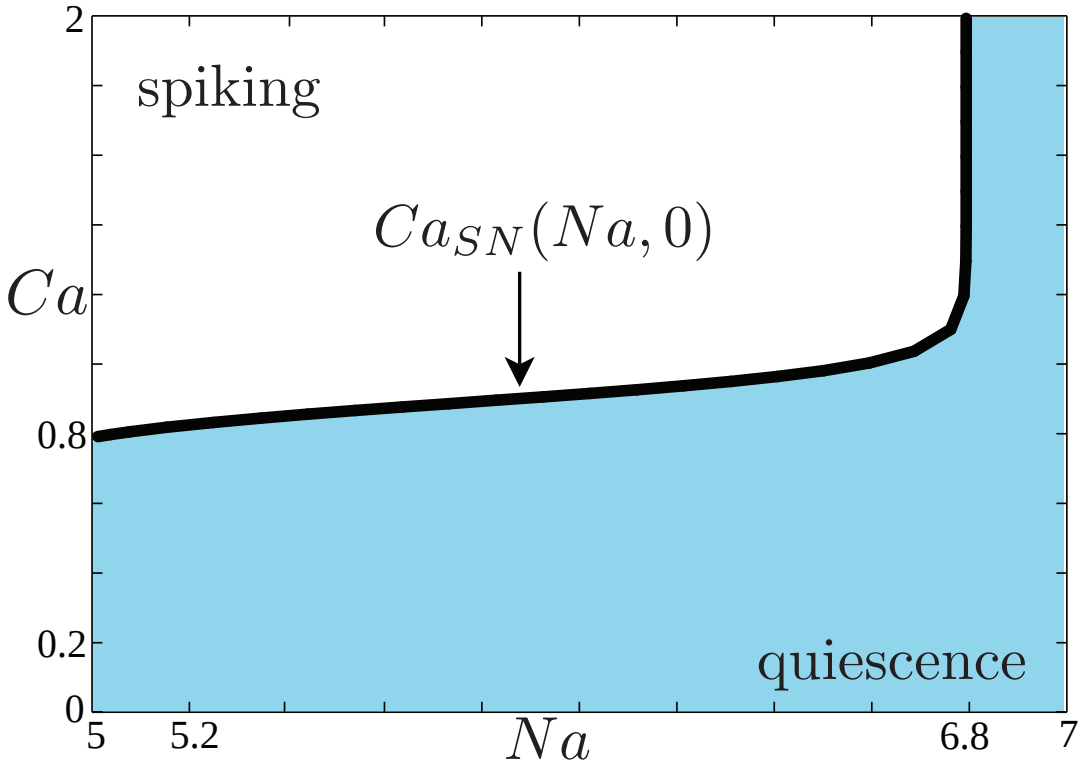


Figure 3.16: $Ca_{SN}(Na,0)$ plotted for $g_{NaP}$ and $g_{CAN}$ corresponding to region V. Note that for values attainable by $Na$ during tonic spiking, $Ca_{SN}(Na,0)$ blows up. Using the approximation $Ca_{HC}(Na,0) \approx Ca_{SN}(Na,0)$, we conclude that $Ca_{HC}(Na,0)$ blows up for finite $Na$ as well. For $(Na,Ca)$ below $Ca_{SN}(Na,0)$ the full system dynamics corresponds to quiescence, while those above $Ca_{SN}(Na,0)$ the full system exhibits tonic spiking.

### 3.5.7 Region VI

Regions IV and VI both feature tonically active solutions. The difference between the two regions is that in region VI, the CAN current does not become active, such that essentially the same tonic spiking dynamics as in Section 3.3.1, with $g_{CAN} = 0$, emerges. When $g_{NaP}$ is low, there are tonic solutions such that the spikes are not fast enough to maintain sustained levels of $s$ sufficient to increase $Ca$ enough to activate the CAN current. When $g_{CAN}$ is low, even if the spike acceleration increases $Ca$ enough to activate the CAN current, the CAN

current is too weak to bring $Na$ to values such that $Ca_{SN}(Na, 0)$ blows up (Section 3.5.6). Also, low values of $g_{CAN}$ prohibit the CAN current from strongly influencing the dynamics. On the other hand, in region IV, the CAN current is strong and active during tonic spiking (Section 3.5.5), which yields solutions with shorter ISI. We summarize these differences graphically in Figure 3.17.

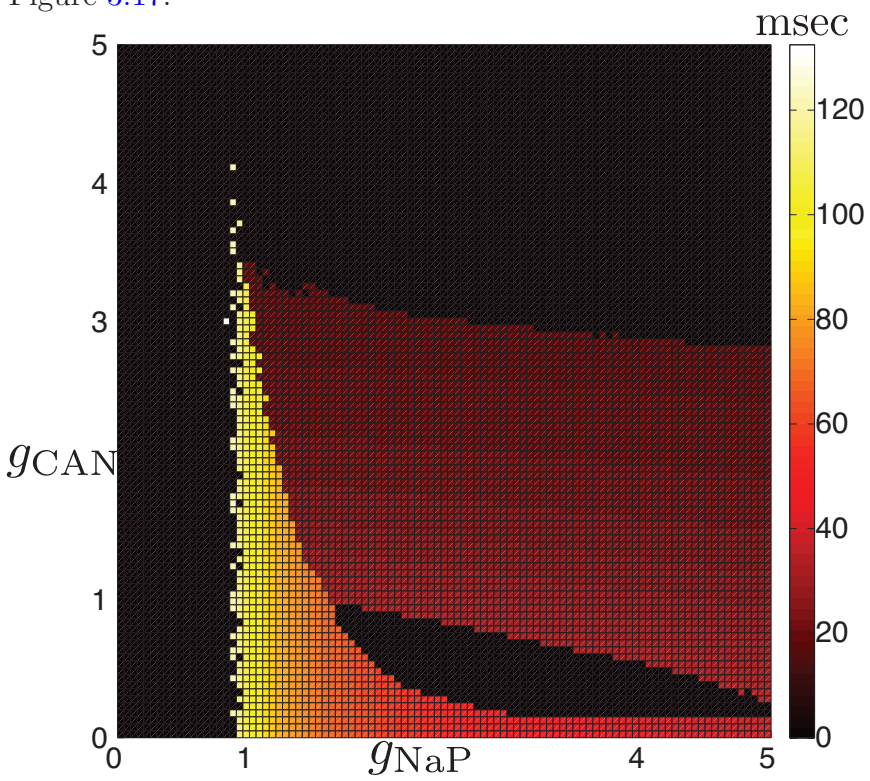


Figure 3.17: Mean interspike interval (ISI) for tonically active model neurons. Black regions indicate that the model neuron was not tonically active. Note the sharp change between high ISI and low ISI within the tonic spiking dynamics that occurs at some $g_{CAN} \in (1, 3.5)$ for each $g_{NaP} \in (1, 2)$.

## 3.6 TRANSITIONS BETWEEN REGIONS

In Section 3.5, we explained how particular bifurcation structures give rise to different forms of model dynamics, as indicated in Figures 3.6 and 3.7. In this section, we estimate where

the borders between dynamic regimes lie in the ($g_{NaP}$, $g_{CAN}$) plane (Figure 3.6) based on criteria derived from insights presented in Section 3.5 and additional numerical calculations. In some cases, we numerically compute estimated boundary curves, the accuracy of which confirms the validity of our analysis. The transition criteria that we provide also allow us to predict the location of regions of bistability in the ($g_{NaP}$, $g_{CAN}$) plane, which we discuss further in Section 3.7.

### 3.6.1 From I to II and from II to VI

The transitions from region I to II and from region II to VI are well understood when $g_{CAN} = 0$ [1]. The transition mechanisms persist when $g_{CAN} > 0$. Starting from region I, an increase in $g_{NaP}$ pushes $hp_{SN}$ low enough that the $hp$-nullcline no longer intersects the family of quiescent critical points, and $F(Ca, Na, hp, x_0) = P(Ca, Na, hp)$ once $hp > hp_{SN}$. This change in the location of the intersection point provides the transition from region I to region II. In the transition from region II to region IV, a further increase in $g_{NaP}$ moves the homoclinic surface enough such that the net drift of $hp$ along the homoclinic is nonnegative, such that $hp$ can never lead the transition back to the silent phase and tonic spiking is attained.

### 3.6.2 From II to *

The transition from region II to region * is similar to the transition from region II to region VI. The key point is that in region II, the CAN current does not sufficiently activate to take control of the active phase before the decrease in $hp$ can terminate it. With an increase in $g_{NaP}$, even without CAN current activation, the trajectory can no longer return to the silent phase simply by virtue of $hp$ decreasing. Without a contribution from $I_{\text{CAN}}$ the resultant solution would be tonically active, as in region VI. Such spiking activity sustains an elevated value for $Ca$. Even if this sustained $Ca < k_{Ca}$, and so may not be enough to activate the CAN current in the traditional sense, it may enable to the CAN current to have a slight influence on the voltage. This influence is amplified by $g_{CAN}$, and for $g_{CAN}$ large enough, it qualitatively changes the dynamics by giving the trajectory the extra spike needed to fully

activate the CAN current. The tipping point for this qualitative change is shown as the lower boundary for region * in Figure 3.6. Thus, as described in Section 3.5.3, alternation of DB and square-wave bursts, depending on levels of $Na$ ensues. Recall from Section 3.3.1 $D = D(hp)$ was the net drift of $hp$ across the homoclinic orbit. In brief, in region II, $D < 0$, and it is increasing $g_{NaP}$ such that $D = 0$, in the presence of enhanced $I_{\text{CAN}}$, that triggers a transition to region *.

### 3.6.3 From * to III

Increasing $g_{NaP}$ further increases $D = D(hp)$, such that in region III, unlike region *, levels of $Na$ attained by typical DB bursts maintain $D > 0$. While $D > 0$, the only way for a solution to return to the silent phase is through a DB burst, and thus DB bursting characterizes region III.

### 3.6.4 From III to IV

The key feature of solutions in region III is that eventually $Ca > Ca_{AH}(Na, hp)$, so that $F(Ca, Na, hp, x_0) = DB(Na, hp)$. $Ca_{AH}(Na, hp)$ is a decreasing function of $g_{CAN}$, see Figure 3.14. As $g_{CAN}$ decreases, $Ca_{AH}(Na, hp)$ blows up for finite $g_{CAN}$. This blowup can be used to indicate a transition from region III to region IV, because for lower $g_{CAN}$ the system cannot go into depolarization block. In Figure 3.18, we plot the predicted boundary between regions III and IV, based on where this blowup occurs. To determine the value of $g_{CAN}$ such that $Ca_{AH}(Na, hp)$ blows up, we must fix $Na$ and $hp$. We fixed $Na$ at 6.5, a value higher than those normally seen in bursting activity, but lower than is seen in tonic activity. We also set $hp = 0$, assuming a prolonged active phase. For each value of $g_{NaP}$, we found $g_{CAN}$ such that $Ca_{AH}(Na, hp) = 1.6$, a typical saturation value for $Ca$ during tonic activity. This scheme gives us the red boundary curve seen in Figure 3.18.

Similarly, $I_{\text{NaP}}(v, hp)$ is a depolarizing current, so $Ca_{AH}(Na, hp)$ is a decreasing function of $g_{NaP}$ as well. This means that an increase in $g_{NaP}$ decreases $Ca_{AH}(Na, hp)$, so that we need a slightly lower $g_{CAN}$ to maintain $Ca_{AH}(Na, hp) = 1.6$. This relationship causes the negative slope of the boundary between regions III and IV.

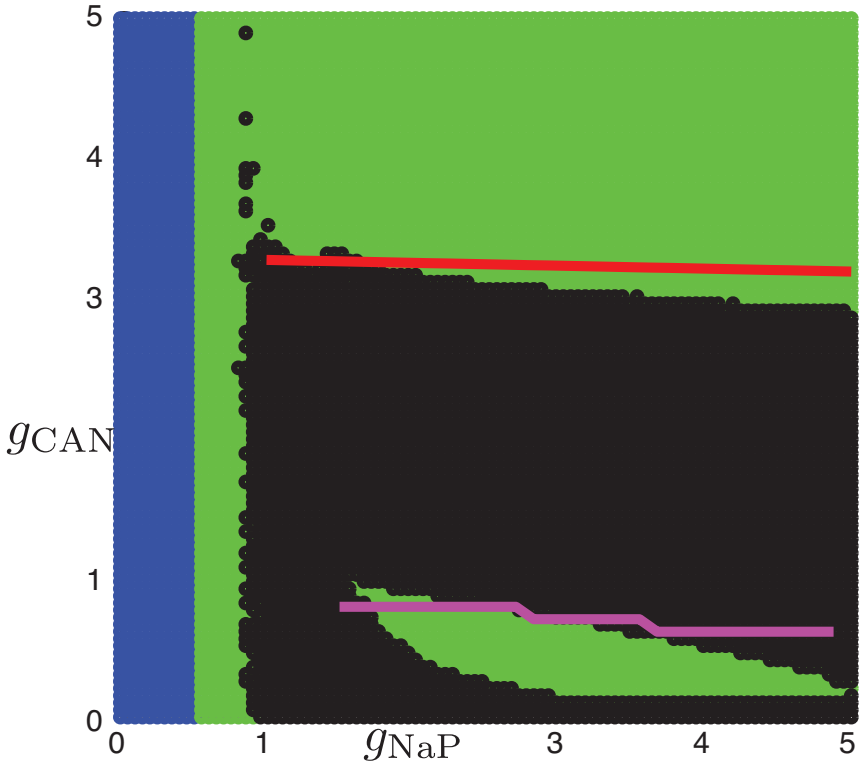


Figure 3.18: Numerical approximations to the boundaries between regions III and IV, and IV and V, as described in Section 3.6.4 and Section 3.6.5, respectively.

### 3.6.5 From IV to V and V to VI

In Figure 3.19, we present an approximation to the boundary between regions IV and V and to the boundary between regions V and VI. These approximations are not based on a slow-fast decomposition, but rather on a bifurcation analysis of the full system. To find these curves, we start with a tonic solution $T$ in region IV and follow $T$ as $g_{CAN}$ is decreased, with $g_{NaP}$ fixed. $T$ loses stability at a torus, or Neimark-Sacker, bifurcation; we color the $(g_{NaP}, g_{CAN})$ at which the torus bifurcation occurs magenta. We continue to follow $T$ until it regains stability at another torus bifurcation, coloring the corresponding bifurcation point blue. We note that the continuation analysis performed by AUTO [19], due to the incidence of limit point of periodic orbit (LPPO) bifurcations, is not necessarily monotonic in $g_{CAN}$, see Figure 3.20. This lack of monotonicity occurs for low $g_{NaP}$ so that even though the magenta point is identified first by the algorithm, the blue point occurs for higher values of $g_{CAN}$. The magenta curve accurately predicts the boundary between regions IV and V, while the blue curve gives an accurate estimate of the boundary between regions V and VI for sufficiently large $g_{NaP}$ and deviates as $g_{NaP}$ decreases (but see Section 3.7).

We can also predict the boundary between regions IV and V based on the slow-fast decomposition. The mechanism that distinguishes regions IV and V is that in in region V, $Ca_{HC}$ blows up to trigger a return to the silent phase. This blow up occurs after an extended time in the active phase, so for the rest of this analysis we assume $hp$ has decreased to a small but nonzero value. Actually, in region IV, $Ca_{HC}(Na, hp)$ blows up for finite $Na$, but such values of $Na$ are not attained. Indeed, solving $\dot{Na} = 0$ for $Na$ yields $Na_{fp}(v, Ca)$, the value that $Na$ will approach based on the activity of the CAN current. For a given $(g_{NaP}, g_{CAN})$ pair, the value $Na = Na^*$ for which $Ca_{SN}(Na, hp)$ blows up may be such that $Na^* > Na_{fp}(v, Ca)$; that is, the $Na$ dynamics will saturate at $Na_{fp}(v, Ca)$ and never reach $Na^*$. As such, the blow up of $Ca_{HC}(Na, hp)$ will never occur for this $(g_{NaP}, g_{CAN})$ pair, so we know that $(g_{NaP}, g_{CAN})$ belongs to region IV. On the other hand, if $Na^* < Na_{fp}(v, Ca)$, then as $Na$ drifts toward its saturation value $Na_{fp}(v, Ca)$, it crosses $Na^*$, causing $Ca_{HC}(Na, hp)$ to blow up and capture the trajectory, triggering a return to the silent phase. This places $(g_{NaP},\ g_{CAN})$ in region V. The border between IV and V therefore

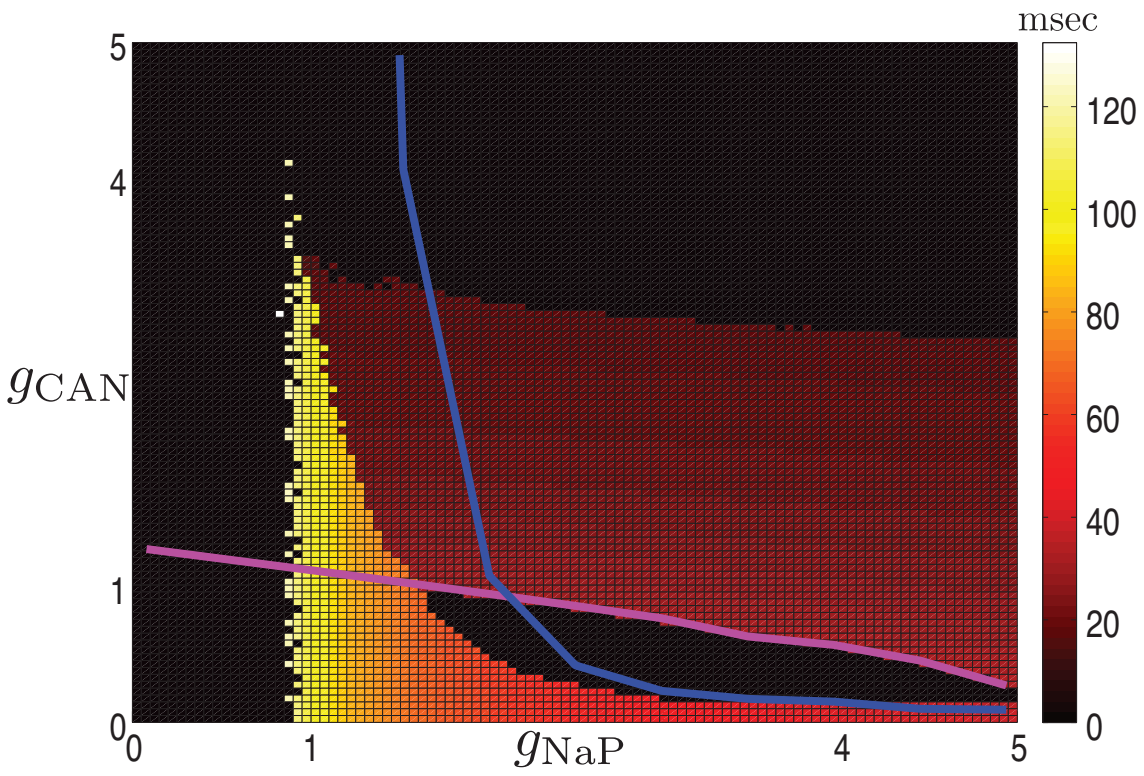


Figure 3.19: Locations of torus bifurcations of tonic solutions from region IV found by decreasing $g_{CAN}$ as described in Section 3.6.5. For $(g_{NaP},\ g_{CAN})$ above the magenta curve, there are stable tonically active solutions. Also, for $(g_{NaP},\ g_{CAN})$ below the blue curve, there are also stable solutions with tonic activity.

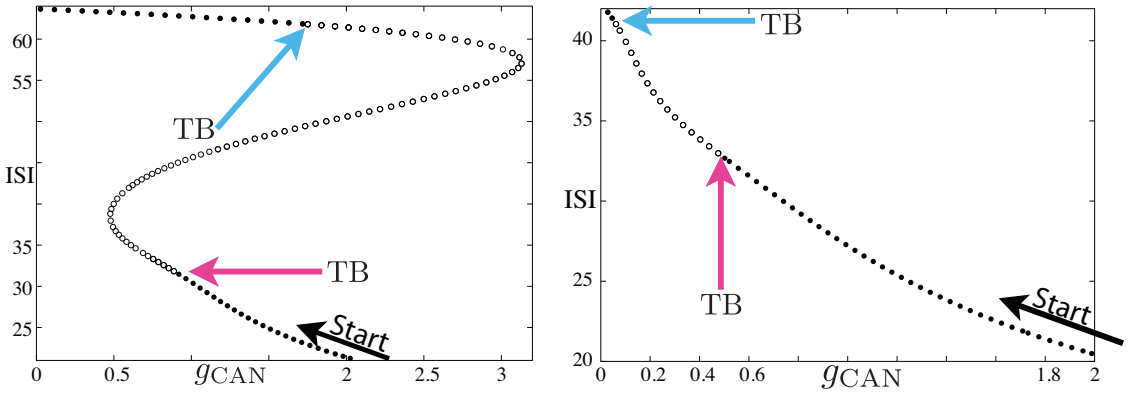


Figure 3.20: Two examples of the bifurcation analysis described in Section 3.6.5. Solid dots correspond to stable tonically active solutions with the corresponding ISI, and open circles are unstable tonic solutions. In each panel above, the continuation analysis begins at $g_{CAN} = 2$ and initially $g_{CAN}$ decreases. The first torus bifurcation found is labeled as TB with a magenta arrow and the second one is labeled with a blue arrow. For Panel (a), $g_{NaP}$ was fixed at $g_{NaP} = 1.8$. Note that after locating the first torus bifurcation the analysis encountered a LPPO bifurcation and the algorithm increased $g_{CAN}$ until another LPPO was encountered. Decreasing $g_{CAN}$ again eventually yielded another torus bifurcation at a higher $g_{CAN}$ value than the first. For Panel (b), $g_{NaP}$ was fixed at $g_{NaP} = 4$. We note that in Panel (b), the continuation analysis was monotonic in $g_{CAN}$.

is the curve of $(g_{NaP}, g_{CAN})$ pairs where $Na^* = Na_{fp}(v, Ca)$. To approximate this border, we first allow $Na^*$ to be the value of $Na$ such that $Ca_{HC}(Na^*, hp) = Ca^*$ where $Ca^*$ must be determined. As $Ca_{HC}(Na^*, hp)$ increases, the fast subsystem approaches a homoclinic orbit, and this increased time between spikes can have subtle effects on the drift for $Ca$ and $Na$. We tried many values for $Ca^*$, and $Ca^* = 1.01$ gave the best fit for the border. We also use the fact that for low $hp$, $Ca_{SN}(Na, hp)$ approximates $Ca_{HC}(Na, hp)$ well. For fixed $Ca$ we calculate the mean $v, s$ over one period of the tonic spiking solution. Using this mean $s$ in Equation (3.5), we calculate the drift of $Ca$, which changes the value of the CAN current. With mean $v$ and adjusted $Ca$, we calculate an approximation for $Na_{fp}(v, Ca)$. This updated $Na$ moves the homoclinic surface, possibly changing the mean $v, s$ for the tonic spiking solutions with updated fixed $Ca$. We iterate this calculation until $Na_{fp}(v, Ca)$ changes by no more than $10^{-3}$, and call this value $Na_{fp}$. In Figure 3.18 we plot in magenta the $(g_{NaP},\ g_{CAN})$ pairs such that $Na_{fp} = Na^*$.

Again, because $I_{\mathrm{NaP}}(v, hp)$ is a depolarizing current, a slight increase to $g_{NaP}$ lowers $Ca_{SN}$, thus requiring slightly higher $Na$ for $Ca_{SN}(Na, hp) \approx Ca_{HC}(Na, hp)$ to blow up. On the other hand, increasing $g_{NaP}$ has little effect on $Na_{fp}(v, Ca)$. Therefore, increasing $g_{NaP}$ from a point on the border of regions IV and V causes $Na^* > Na_{fp}$, resulting in the dynamics of region IV, consistent with the negative slope of the boundary curve between regions IV and V.

## 3.7 BISTABILITY

Figure 3.19 predicts several regions of bistability. Tonic solutions where the CAN current is activated, similar to those solutions commonly seen in region IV, are found for $(g_{NaP},\ g_{CAN})$ above the magenta curve in Figure 3.19. For appropriate values of $(g_{NaP},\ g_{CAN})$, these tonic solutions coexist with the previously described solutions of regions I, II, III, VI and *. Similarly, for $(g_{NaP},\ g_{CAN})$ below (to the left) of the blue curve in Figure 3.19, there are tonic solutions where the CAN current does not play a strong role. These solutions are like those solutions commonly found in region VI and coexist with the previously described

solutions of regions *, III and IV. Such solutions lose stability at the boundary of region II and so they are not observed in regions II or I. We summarize the result of this bistability analysis in Figure 3.21. In Table 3.2, we list the regions of Figure 3.21 together with the regions for which corresponding solutions were originally described.

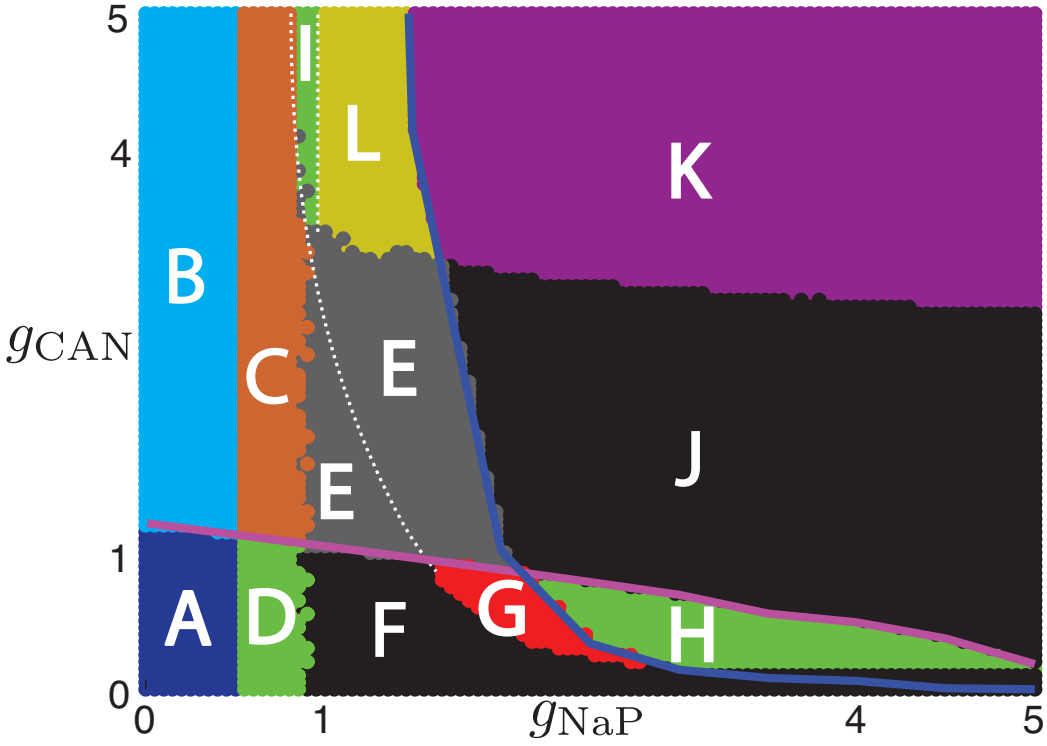


Figure 3.21: Partitioning of parameter space based on bistability analysis. The colors only establish the boundaries of regions A–L.

Therefore, the generalizable modeling framework that incorporates the CAN and NaP currents presented in this specific preBötC model could be useful for adaptation or application to other neuronal systems as well.

## 3.8 RECIPROCAL COUPLING

To facilitate analysis in Sections 3.2–3.7, the unified model considered a self-coupled neuron. However, preBötC neurons do not naturally make autaptic connections. Further, the

Table 3.2: List of stable solutions for each region of Figure 3.21.

| Region of Figure 3.21 | Solutions corresponding to regions of Figure 3.6 |
|---|---|
| A | I |
| B | I, IV |
| C | II, IV |
| D | II |
| E | IV, VI |
| F | IV |
| G | V, VI |
| H | V |
| I | *, IV, VI |
| J | IV |
| K | III, IV |
| L | III, IV, VI |

effects of spike asynchrony for reciprocally coupled neurons can be subtle. For instance, in reciprocally coupled, intrinsically tonic neurons, spike asynchrony can expand the range of external input for which the two-cell network bursts [1]. It is not obvious that the reduction to a self-coupled model neuron will fully capture the behavior of the two-neuron network. In this section we present computational analysis for two identical, reciprocally coupled model neurons and qualify the differences from the self-coupled case.

### 3.8.1 Model

Here, we focus on the same basic model as Equations (3.1)–(3.8) but instead consider two model neurons reciprocally coupled via excitatory synapses. For $i, j \in \{1, 2\}$ the dynamics

for model neuron $i$ are given by:

$$\begin{aligned}\dot{v_i} = -\{&I_L(v_i) + I_{Na}(v_i, h_i, m_i) + I_{\mathrm{K}}(v_i, n_i) + I_{\mathrm{NaP}}(v_i, hp_i) + I_{\mathrm{CAN}}(v_i, Ca_i) \\ &+ I_{pump}(Na_i) - I_{app} + I_{syn}(v_i, s_{j\neq i})\}/C_m\end{aligned} \tag{3.9}$$

$$\dot{h_i} = (h_\infty(v_i) - h_i)/\tau_h(v_i) \tag{3.10}$$

$$\dot{m_i} = (m_\infty(v_i) - m_i)/\tau_m(v_i) \tag{3.11}$$

$$\dot{n_i} = (n_\infty(v_i) - n_i)/\tau_n(v_i) \tag{3.12}$$

$$\dot{Ca_i} = \varepsilon_{Ca}(k_{IP_3}s_{j\neq i} - k_{Ca}(Ca_i - Ca_{base})) \tag{3.13}$$

$$\dot{Na_i} = \alpha(-I_{\mathrm{CAN}}(v_i, Ca_i) - I_{pump}(Na_i)) \tag{3.14}$$

$$\dot{hp_i} = \varepsilon_{hp}(h_{p,\infty}(v_i) - hp_i)/\tau_{hp}(v_i) \tag{3.15}$$

$$\dot{s_i} = ((1 - s_i)s_\infty(v_i) - k_s s_i)/\tau_s \tag{3.16}$$

with all functions and parameters appearing as they did in Section 3.2.

In this section we compare the self-coupled system to a reciprocally coupled system of two model neurons that are identical to each other except for their initial conditions. When the homogeneous, reciprocally coupled pair is perfectly synchronized, it behaves precisely like a self-coupled neuron, hence the reduction to the self-coupled case leaves $gsyn$ and $k_{IP_3}$ unchanged. Figure 3.6 shows the effect of changing $g_{NaP}$, the conductance of the NaP current, and $g_{CAN}$, the conductance of the CAN current, for the self-coupled model neuron. In Subsection 3.8.2, we reproduce that figure in the context of the reciprocally coupled pair of model neurons. We demonstrate that all of the regions of qualitatively distinct dynamics are preserved, and no new dynamics are observed by reducing the reciprocally coupled pair of model neurons to a single self-coupled neuron.

### 3.8.2 Dynamics of reciprocally coupled model neurons

In this section we qualitatively categorize the various dynamic regimes that arise from the two-neuron model given by (3.9)–(3.16) and compare them against the self-coupled case. The first important observation is that spike synchrony between the model neurons is unstable. We illustrate this fact with simulation data. In Figure 3.22 we begin a solution with identical

initial conditions corresponding to the silent phase. Initially the solutions behave as the self-coupled case (Figure 3.22a). Eventually, due to slight numerical error, the voltage traces separate and spike synchrony is broken, see Figure 3.22b.

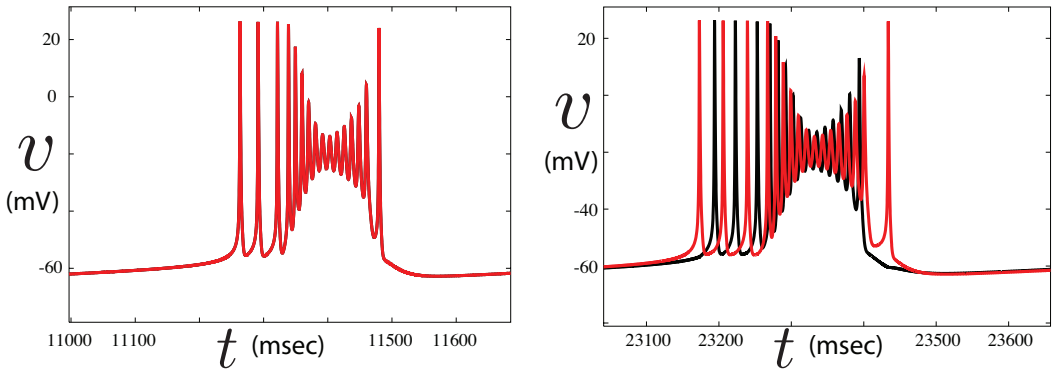


(a) (b)

Figure 3.22: Example model output with $g_{NaP} = 4$, $g_{CAN} = 4$, and initial conditions $(v_1, h_1, m_1, n_1, Ca_1, Na_1, hp_1) = (v_2, h_2, m_2, n_2, Ca_2, Na_2, hp_2) = (-60, 1, 0, 0, Ca_{base}, 0, Na_{base})$. Model output for $v_1$ is colored red, while model output for $v_2$ is colored black. Initially, the solutions remain quite close together, we note that even at $t = 11,000$ milliseconds the traces are virtually indistinguishable in (a). However, eventually the model neurons separate, though they still burst at roughly the same time, with essentially the same burst duration (b).

To classify the dynamics of the two-neuron network, we use the scheme as described in Section 3.4 to qualify the individual model neurons within the network as quiescent, bursting, or tonically active. Even though the solution in Figure 3.22 does not have perfect synchrony, both model neurons burst at roughly the same time. The important feature of the preBötC is that the neurons burst synchronously; the neurons need not be perfectly synchronized as long as the active phases overlap sufficiently.

When both model neurons are classified as bursting, we consider a time window where each model neuron bursts exactly once. In this window, let $F_1$ be the time of the first spike of the first model neuron to enter the active phase, and similarly, let $L_1$ be the time of the last spike of the first model neuron to exit the active phase. Note that $F_1$ and $L_1$ need

not correspond to the same model neuron. Let $F_2$ be the first spike of the second model neuron to enter the active phase, and let $L_2$ be the last spike of the second model neuron to exit the active phase. If $F_2 < L_1$ there is some overlap of the active phases, otherwise, the network is said to exhibit anti-phase bursting. We never observed anti-phase bursting in these simulations. When there is overlap in the active phases, we define the duration of the shared active phase as $S = L_1 - F_2$. Also, we define the total active duration as $T = L_2 - F_1$. We use the ratio $R = S/T$ as a measurement of burst synchrony; if $R > 0.4$, we declare the bursts to be in-phase, otherwise, the bursts are out-of-phase.

At each grid point of Figure 3.23, the initial conditions for each neuron were drawn from a normal distribution corresponding to quiescence. Specifically, each neuron was initialized with $(v_i, h_i, m_i, n_i, Ca_i, Na_i, hp_i) = (\mathrm{N}(-60, 5),\ \mathrm{N}(1, 0.1),\ \mathrm{N}(0.04, 0.1),\ \mathrm{N}(0, 0.1),\ \mathrm{N}(0, 0.0001),\ \mathrm{N}(0.05, 0.01),\ \mathrm{N}(0, 0.1),\ \mathrm{N}(5, 0.1))$, where $\mathrm{N}(x, y)$ is a normal distribution with mean $x$ and standard deviation $y$. Even though some initial conditions drawn from the above distribution will not be physically relevant, the solutions quickly become physical. Note that qualitatively similar results are expected if instead of drawing from the above distribution for each grid point, initial conditions were drawn once from the above distribution and then used for all grid points. We then used the above classification algorithm to partition the $(g_{NaP}, g_{CAN})$ parameter space based on the result of the integration. For sample model output from the various regions of Figure 3.23, refer to Figure 3.24. Regions II, *, III, and V have dynamically distinct bursting patterns. Region IV and region VI both contain tonically active solutions, the only distinction is that in region VI the CAN current is active in both model neurons, which causes the spiking to occur with higher frequency, see Figure 3.24d2 and 3.24f2. The boundaries of region * in Figure 3.23 are where we have observed the existence of solutions with dynamics similar to Figure 3.24c2. For $(g_{NaP}, g_{CAN})$ in region VI and above the dashed white line, there is bistability between bursting solutions and tonic solutions with low frequency (e.g.: Figure 3.24f2), which makes identifying boundaries of region * difficult. This bistability is also seen in the self-coupled case, but spike asynchrony makes the tonically active solutions more prominent here.

The preceding classification algorithm can be used to partition the self-coupled case. In Figure 3.25, we compare the differences between Figure 3.23 and the partitioning for the self-

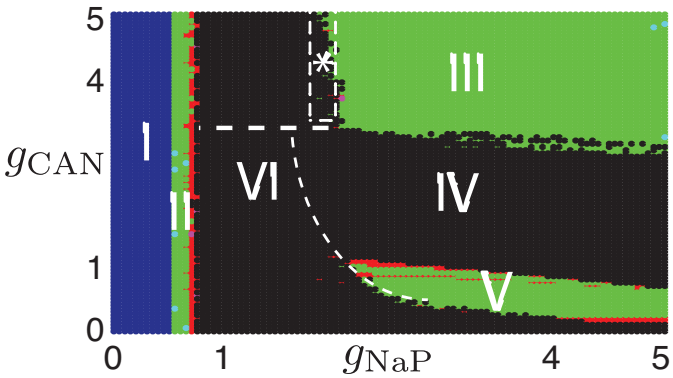


Figure 3.23: Partitioning of parameter space based on resultant dynamics from a network of reciprocally coupled model neurons. Both model neurons start with slightly different initial conditions corresponding to quiescence, but otherwise all parameters are identical. Dark blue dots correspond to solutions where both model neurons remained quiescent. Black dots correspond to both model neurons having tonic activity. When the model neurons have-in phase bursting, we color the dot green. The relatively few times when the model neurons have out-of-phase bursting, the dot is colored light blue. No out-of-phase bursts that were observed were anti-phase; their classification as out-of-phase seems to be a result of one model neuron exhibiting an extra spike before burst termination, which causes the total active phase to increase. Dots are colored red when both model neurons were bursting as defined by the standard deviation criterion but the algorithm was unable to determine the phase relation. Magenta dots correspond to the situation where one model neuron is tonically active and the other is bursting, and are most likely a numerical artifact. The boxed-dashed region marked * features bursts similar to Figure 3.24c2.

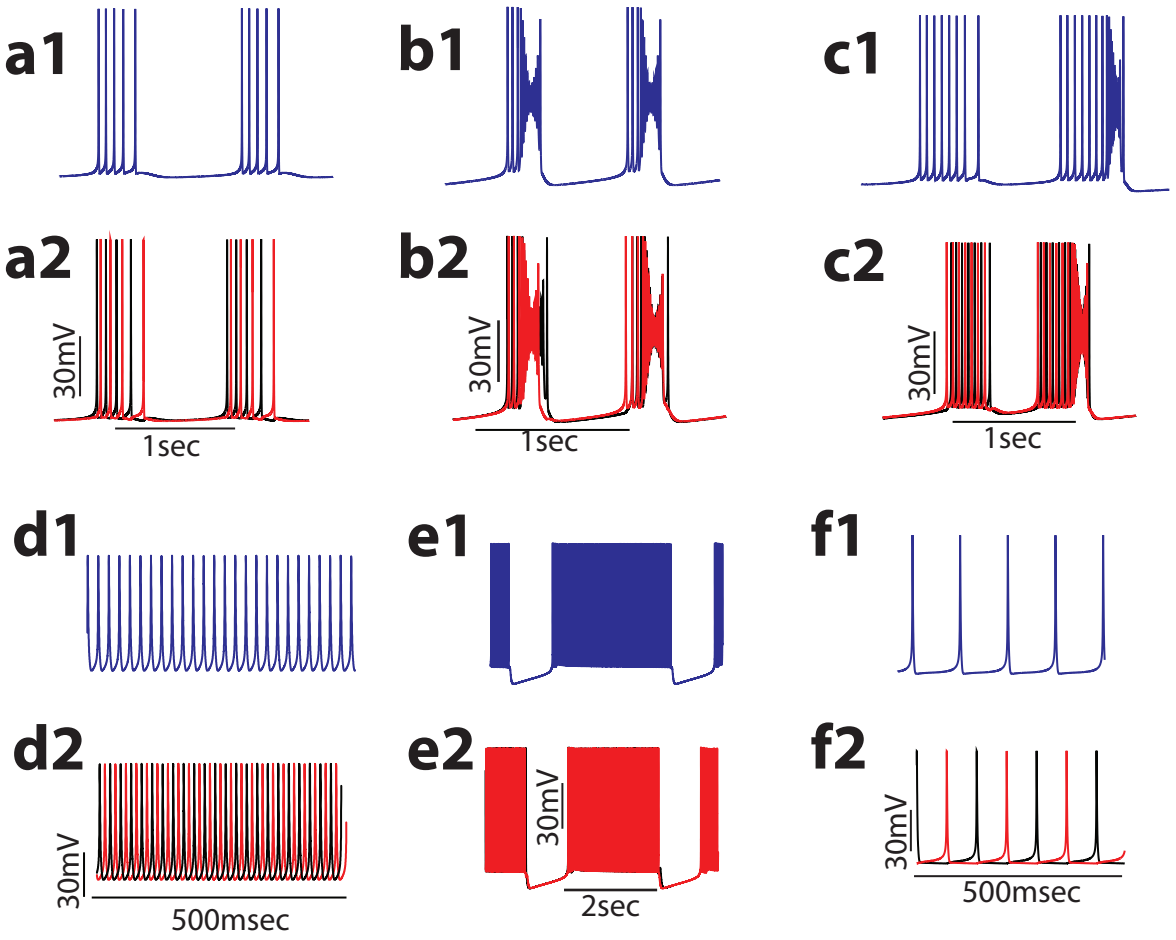


Figure 3.24: Model output for both the self-coupled case as well as the case for a reciprocally coupled pair of model neurons. Panels a1–f1 (blue traces) represent the self-coupled case, while panels a2–f2 (red and black traces) represent the reciprocally coupled case. Specifically, panel a2 corresponds to model output from region II of Figure 3.23, b2 to region III, c2 to region *, d2 to region IV, e2 to region V, and f2 to region VI. Although it cannot be seen at this resolution, the spikes in panel e2 are anti-phase. Note that all of the dynamics of the reciprocally coupled pair are observed in the self-coupled model case, and vice-versa.

coupled case. The primary difference between the self-coupled case and Figure 3.23 is the location of region *. Bursting patterns seen in panels b1, b2, c1 and c2 of Figure 3.24 require activation of the CAN current. Activation of the CAN current relies on sufficient increase of $Ca_i$. This $Ca_i$ buildup is closely related to the spiking frequencies of solutions when they enter the active phase; higher frequencies lead to faster buildup. Asynchronous spiking may lead to lower spiking frequencies for the reciprocally coupled pair because each neuron receives the most synaptic input when it is in the trough between spikes. On the other hand, in the self-coupled case, the neuron receives maximal synaptic input when it is at the peak of a spike. The differences between these two cases is subtle, and is outside of the scope of this work. Numerically, we observe that the self-coupled solution spikes at a higher frequency than the solution for the reciprocally coupled pair. The spiking frequency is directly proportional to $g_{NaP}$, therefore, in the self-coupled case, activation of the CAN current occurs for lower $g_{NaP}$ than it does for the reciprocally coupled pair. This explains the difference in the location of region *. Also, the initiation of each burst requires sufficient deinactivation of the NaP current. The inactivation variable for the NaP current, $hp$, multiplies $g_{NaP}$ in the definition of $I_{\mathrm{NaP}}(v)$. Thus, increasing $g_{NaP}$ shortens the silent phase between bursts, which explains the timing difference in panels c1 and c2 of Figure 3.24. We also note that, in Figure 3.25, the range of $g_{NaP}$ for which there are square-wave bursting solutions of the reciprocally coupled pair (region II) seems to be smaller than the corresponding region for the self-coupled case. In general, introducing asynchronous spiking expands the range of external input, and perhaps other parameters, for which square-wave bursting solutions are observed in traditional models featuring only the NaP current [1]. It has not been quantified whether $g_{NaP}$ is one such parameter. Nevertheless, we have observed bistability between tonically active solutions and square-wave bursting solutions near the low $g_{NaP}$ border of region VI, as well as in region II, which explains why the square-wave bursting region seems smaller for the reciprocally coupled pair.

The unified model has not been calibrated to capture specific voltage traces, rather, the intent is to qualitatively describe the bursting behavior of preBötC neurons. Numerically, we have observed that the reduction from the two reciprocally coupled model neurons to the self-coupled case does not significantly impact statistics such as the burst period, which

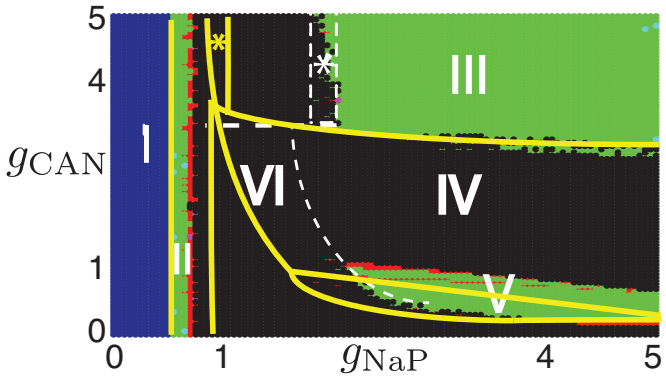


Figure 3.25: Figure 3.23 with partitioning of the self-coupled case overlaid for comparison. Yellow lines indicate the boundaries of various regions of dynamics for the self-coupled case. We observe that, although positions of regions have shifted, all regions of activity in Figure 3.23 are seen in the self-coupled case, and vice versa. The most significant change is region *, which shifted to a much higher range of $g_{NaP}$ due to the spike asynchrony.

indicates that the self-coupled case indeed can inform us about the reciprocally coupled case, and may help elucidate the bursting rhythm of the preBötC. Thus, we summarize some results from the chapter so far to illustrate how one can use insights from the self-coupled case to understand bursting in the reciprocally coupled case. Bursts are primarily initiated and terminated by the drift in the slow variables $Ca_i, Na_i, hp_i$ which, by virtue of geometric singular perturbation theory, can be treated as bifurcation parameters for the fast subsystem $(v_i, h_i, m_i, n_i, s_i)$. For low $g_{NaP}$ corresponding to region II, a burst is initiated when $hp$ crosses a particular threshold corresponding to a fold bifurcation in the fast subsystem, and the burst is terminated when $hp$ later decreases through a homoclinic bifurcation of the fast subsystem [49]. Spike asynchrony modulates the $hp$ coordinate of the homoclinic bifurcation differently from the self-coupled case, however for the $gsyn$ considered here and low $g_{NaP}$, decreasing $hp$ will always terminate the burst. This accounts for the similarities in region II for both the self-coupled and reciprocally coupled cases.

We have already discussed how spike asynchrony requires higher values of $g_{NaP}$ to cause a sufficient $Ca_i$ buildup to ignite the CAN current. In the self coupled case, when the CAN

current turns on, the spike frequency dramatically increases, which causes $Ca$ to build up even higher. Eventually $Ca$ increases through a supercritical Andronov-Hopf bifurcation of the fast subsystem, leading to depolarization block. Meanwhile, the CAN activity has increased the $Na$ variable, which corresponds to increasing the $Ca$ coordinate of the homoclinic bifurcation that must be crossed to terminate the burst. Once in depolarization block, the self-coupled system stops spiking, and thus, $s$ decays, resulting in a decay of $Ca$. Decaying $Ca$ crosses the homoclinic bifurcation of the fast subsystem before returning to spiking behavior. This mechanism generalizes to the reciprocally coupled case. Suppose neuron 1's CAN current is activated first. The activated CAN current causes neuron 1 to bombard neuron 2 with synaptic signals ($s_1$ is high), leading neuron 2's CAN current to ignite, which causes both $s_2$ and $Na_2$ to significantly increase. Elevated $s_2$ further elevates $Ca_1$ (and so also elevates $Na_1$), and eventually $Ca_1$ is high enough to put neuron 1 in depolarization block by crossing the Andronov-Hopf bifurcation of the fast subsystem. During depolarization block, $Ca_2$ decreases because $s_1 = 0$, and since $Na_2$ is elevated, neuron 2's burst terminates as $Ca_2$ decreases through the homoclinic bifurcation of the fast subsystem. Neuron 2's burst termination causes $s_2 = 0$, which yields a decrease in $Ca_1$, and eventually neuron 1 returns to the silent phase.

We have also provided analysis for the boundaries of the various regions of dynamically distinct activity. For instance, we identified the mechanism of crossing from region III to region IV by decreasing $g_{CAN}$. The mechanism involves the Andronov-Hopf bifurcation of the fast subsystem when $Ca$ is treated as a bifurcation parameter. When $g_{CAN}$ is decreased the $Ca$ coordinate of the Andronov-Hopf bifurcation increases, eventually blowing up for finite $g_{CAN}$. With the Andronov-Hopf bifurcation unattainable by $Ca$, the self-coupled cell has no way to enter depolarization block and hence terminate its burst. Thus, the $g_{CAN}$ value for which this blow-up occurs depends on $g_{NaP}$, and can be used to approximate the boundary between regions III and IV. This will carry over into the reciprocally coupled case. If $g_{CAN}$ is sufficiently low such that the $Ca_i$ coordinates of Andronov-Hopf bifurcations of the fast subsystems are beyond the maximal attainable values of $Ca_i$, the system will cease to exhibit synchronous bursting, because neither neuron will enter depolarization block, which is required for the other neuron's $Ca_j$ to begin to decrease and eventually terminate

the bursts. Similar insights can be applied to the transitions between all of the regions of Figure 3.23.

These arguments can be extended to the case when the reciprocally coupled neurons are not from the same region of Figure 3.23. For instance, a reciprocally coupled pair consisting of a region III neuron and a region IV neuron may still exhibit bursting. For region III and region IV neurons, the CAN current of both neurons will eventually become activated. The region III neuron will go into depolarization block, and this sudden loss of synaptic output to the region IV neuron could cause it to suddenly return to the silent phase. Hence, the sudden loss of synaptic input to the region III neuron will cause its return to the silent phase.

## 3.9 DISCUSSION

In this chapter we consider a computational model for respiratory neurons in the preBötC that includes the CAN current and the Na/K ATPase pump, as modeled in the Rubin-Hayes model [56], and the NaP current, all of which are ubiquitous within this population of neurons. By considering varying strengths of $g_{CAN}$, the conductance of the CAN current, and $g_{NaP}$, the conductance of the NaP current, we explain the mechanisms through which the model yields dynamics seen in *in vitro* recordings, such as square-wave bursting (2 different mechanisms), bursts featuring depolarization block (DB bursts), and mixed patterns of square-wave and DB bursts, as well as tonic activity. Although analysis is done for one model neuron, the model is self coupled, and so actually represents the activity of a small, synaptically coupled network. Using our understanding of the bifurcation structure of the fast subsystem, we compute estimates of where transitions between dynamic regimes are predicted to occur, and these agree with direct simulations, validating our analysis. We predict that activity patterns shown in this chapter will be observed in reciprocally coupled pairs of preBötC neurons, as well as preBötC neurons that are manipulated in culture to form autapses.

A multitude of factors influence the activation and magnitude of the CAN current in a biological setting. In the present model, activation of the CAN current depends on in-

tracellular calcium, which is released via a synaptic pathway. Acting through AMPA receptors, glutamate can trigger a small influx of calcium [41], while glutamate binding to metabotropic glutamate receptors (specifically mGluR5s) can induce G protein activation that leads to inositol 1,4,5-trisphosphate ($IP_3$) synthesis and subsequent intracellular calcium release. These two mechanisms work in concert to recruit the CAN current [42, 41]. Phosphatidyl 4,5-bisphosphate ($PIP_2$) is required to synthesize $IP_3$ and is generally abundant in the preBötC neurons [7]. Levels of $PIP_2$ in the membrane surrounding the channels may fluctuate or be regulated and thus affect channel availability, however, which impacts the magnitude of the CAN current [35]. Finally, second messengers such as calcium can also adjust the magnitude of the CAN current by affecting the phosphorylation state of relevant ion channels [40, 7]. Given the variety of factors that could contribute to the heterogeneity in CAN current magnitude and activity across neurons in the preBötC, it was most convenient simply to use variations in the parameter $g_{CAN}$ to represent these effects, as a means to explore how changes in the CAN current characteristics influence preBötC neuron dynamics. The characteristics of the NaP current within the preBötC also exhibit inherent biological variability, which we represent in this chapter by varying $g_{NaP}$.

Rhythmic activity in the preBötC can be influenced by either the NaP current or the CAN current, as shown previously [4, 56], but their combination in this chapter gives a spectrum of additional activity patterns and bistability that are expected to arise in the preBötC network. In particular, alternation of square-wave and DB bursts is seen in experimental data, and is often attributed to intrinsic noise and neuronal variability, but our unified model suggests that such bursting may result from the interactions of the CAN and NaP currents. DB bursts require activation of the CAN current, which also increases $Na$ so that the Na/K ATPase pump leads to eventual burst termination. Although $Na$ decays during the subsequent silent phase, Na may be elevated enough during the next burst that the Na/K ATPase pump and NaP inactivation together may terminate the burst before the CAN current is activated. This interaction may cause one or more square-wave bursts to occur between DB bursts and can also be used to explain the differences in durations of the silent phases between such bursts. Specifically, we observed in our sample of *in vitro* recordings that, in a preBötC neuron that has both DB and square-wave bursts, the silent phase following a DB burst was generally

longer than the silent phase following a square-wave burst (Figure 3.13). We explained this phenomenon by noting that after a DB burst, the Na/K ATPase pump experiences an increased load, which prolongs the silent phase by requiring more NaP deinactivation to occur before the next burst can start. During a subsequent square-wave burst, as noted above, the load on the pump decreases, resulting in a shorter silent phase before NaP deinactivation initiates the next burst. Thus, the model predicts that this link between the nature of a burst and the duration of the subsequent interburst interval should be a general feature of activity of the type generated by the unified model for parameter values from region *.

In addition to underlying square-wave bursting, to contributing to the mixed burst patterns seen in region * and prevalent in electrophysiological recordings (Figure 3.8), and to helping control interburst interval durations, the NaP current plays a role in boosting synaptic activation, due to its voltage-dependence. In the unified model, this boost can promote DB bursts if both $g_{NaP}$ and $g_{CAN}$ are large enough. By increasing the spike rate during tonic activity, the NaP current can contribute to CAN current activation, resulting in a transition through depolarization block and eventually a return to quiescence. Indeed, increasing $g_{NaP}$ increases the range of $g_{CAN}$ for which DB bursting occurs (Figure 3.6), which represents another model prediction.

In this work, we also validated the reduction of the pair of reciprocally coupled neurons (henceforth called "the pair") to a single self-coupled one. This reduction is only valid when both neurons are identical in all parameters except for initial conditions. Perfect synchrony is at least a weakly unstable state for the pair. However, it is not necessary for preBötC neurons to be perfectly synchronous; as long as the active phases have enough overlap, we consider the network to be synchronized. Indeed, almost all bursts observed in this network had sufficient overlap to be called synchronous bursts. We partitioned the pair parameter space into seven different regions containing distinct dynamics. All of the dynamics observed in the pair are qualitatively observed in the self-coupled setting, and vice-versa (Figure 3.24). We also compared the boundaries of the regions in the pair and self-coupled case. The regions for the pair case are qualitatively similar to the self-coupled case (Figure 3.25), which completes the validation of our reduction to the self-coupled case. Numerical exploration suggests that similar results are obtained when $gsyn$ and $k_{IP_3}$ are varied.

Precisely quantifying the effects of spike asynchrony on each neuron's three dimensional slow-subsystem is required to produce computational or analytic boundary curves for many of the regions of Figure 3.23. It is also required, therefore, to explicitly describe the activity patterns of a heterogeneous pair of reciprocally coupled neurons, which is an important step in understanding the activity of large networks of preBötC neurons.

The efforts of Rybak et al. have refined models of the NaP current [59, 58]. We expect that including such refinements would induce some quantitative differences in the locations of the boundaries between regions in Figure 3.6; however, it is unlikely that these relatively minor changes would alter the qualitative bifurcation structures or model dynamics that we have described and analyzed. Toporikova and Butera recently developed a two compartment model including the CAN and NaP currents [70]. Their chapter focuses on individual model neurons that utilize either NaP inactivation, $IP_3$ desensitization, or a combination of these mechanisms to burst in the absence of synaptic input. In this paper, we present a recent experimental result (Figure 3.1) demonstrating that, despite the lack of information regarding the distribution of the NaP and CAN currents, preBötC neurons appear to be electrotonically compact. Given this finding, and the absence of evidence that more compartments are needed to capture the essential mechanisms of burst generation, we here consider the unified model as a one compartment model. Furthermore, intrinsic rhythmicity in individual preBötC neurons is neither necessary for preBötC rhythmicity [14, 15] nor necessarily advantageous for burst synchrony over a broad parameter range (see Chapter 2), and our unified model highlights the diversity of burst-generation mechanisms that emerge through the interaction of synaptically-gated channels with other voltage-dependent channels. It is possible that including desensitization of $IP_3$ in the unified model may alter the locations and burst frequencies associated with regions * and III of Figure 3.6 by delaying activation of the CAN current or yielding earlier burst termination with less $Na$ accumulation, and these effects should be explored in future work. We also note that $E_L$, the reversal potential of the leak current, has been focused on in previous modeling work on the preBötC because it can significantly impact certain forms of model dynamics, it can be manipulated experimentally through alterations in potassium concentrations external to neurons, and it can serve as a proxy for variations in $I_{app}$ (since $g_L E_L$ and $I_{app}$ play identical roles) [4, 54, 56].

If $E_L$ is perturbed, then similar forms of dynamics to those seen in Figure 3.6 arise, albeit with differences in region locations. Larger increases in $E_L$ can push the model away from bursting toward tonic spiking, although DB bursts persist for sufficiently high $g_{CAN}$ until they are transformed into elliptic-like bursts due to the failure of the Na/K ATPase pump to create a prolonged silent phase, as discussed in Section 3.4.

While this chapter is motivated by the dynamics observed in the preBötC (e.g. Figure 3.8), it may be applicable to other rhythmic brain areas as well. In several mammalian locomotor CPGs, the NaP current has been identified as playing a critical role in generating the network rhythm [67, 68, 76]. On the other hand, in other rhythmic brain areas such as entorhinal cortex [18, 23] or the trigeminal system [72], the CAN current plays a critical role in pattern generation. In fact, the trigeminal system features both NaP [74] and CAN currents. Indeed, given that CAN and NaP currents are widespread and can robustly drive the array of rhythmic activity patterns presented and analyzed in this paper, it seems likely that the interaction of these currents is a fundamental component of neuronal rhythmogenesis.

# 4.0 LARGE NETWORKS OF UNIFIED MODEL NEURONS

When embedding models for respiratory neurons in a network, the connectivity architecture is often chosen to be all-to-all [5, 46, 62, 33]. However, recent experimental data indicate that this architecture may not be valid for large networks [25]. In this chapter, we study the unified model from Chapter 3 when it is coupled with an architecture inspired by the data. Heterogeneous networks that adhere to the data and yield synchronous network bursting are trivial to engineer, but there may be other less obvious mechanisms that promote synchronous bursting across the network. We found that randomly generated networks that adhere to the data stand little chance of having synchronous bursting. Thus, it is clear that some mechanisms must be present to support bursting in the preBötC in the face of the dual challenges of neuronal heterogeneity and clustered architecture.

To tease out those mechanisms that promote bursting, in Section 4.3 we develop a genetic algorithm to find families of bursting networks. In Section 4.4 we analyze the networks we found by the genetic algorithm, and show that non-trivial networks that have synchronous bursts do exist, however the quality of the bursting activity is quite limited. Section 4.5 weakens a restriction on the genetic algorithm. By allowing more communication between clusters, we find substantial improvement over Section 4.4. Section 4.6 elucidates the role of the CAN current in communicating bursts throughout the network. We find that intrinsically quiescent neurons are prominent in the networks found through the genetic algorithm; this is discussed in Section 4.7. We found that intrinsically bursting neurons do not play a significant role in the network, see Section 4.8. In Section 4.9 and Section 4.10, we further elucidate the mechanisms underlying synchronous network bursting by simulated blockade of the NaP and CAN currents. Finally, an extension to the model is discussed in Section 4.11.

## 4.1 MODEL NEURONS

For this work, we use the unified model from Chapter 3. The core model is unchanged, except we must account for more synaptic connections than before. Define the matrix $a$ so that $a_{j,i} = 1$ if neuron $j$ is presynaptic to neuron $i$, and 0 otherwise. Let $N$ be the number of neurons in the network. For $i \in \{1, 2, ..., N\}$ the dynamics for model neuron $i$ is given by:

$$\begin{aligned} \dot{v_i} = -\{&I_L(v_i, E_{L,i}) + I_{Na}(v_i, h_i, m_i) + I_{\mathrm{K}}(v_i, n_i) + I_{\mathrm{NaP}}(v_i, hp_i, g_{NaP,i}) \\ &+ I_{\mathrm{CAN}}(v_i, Ca_i, g_{CAN,i}) + I_{pump}(Na_i) - I_{app} + \sum_{j=1}^{N} a_{j,i} I_{syn}(v_i, s_j)\}/C_m \end{aligned} \tag{4.1}$$

$$\dot{h_i} = (h_\infty(v_i) - h_i)/\tau_h(v_i) \tag{4.2}$$

$$\dot{m_i} = (m_\infty(v_i) - m_i)/\tau_m(v_i) \tag{4.3}$$

$$\dot{n_i} = (n_\infty(v_i) - n_i)/\tau_n(v_i) \tag{4.4}$$

$$\dot{Ca_i} = \varepsilon_{Ca}(k_{IP_3} \sum_{j=1}^{N} a_{j,i} s_j - k_{Ca}(Ca_i - Ca_{base})) \tag{4.5}$$

$$\dot{Na_i} = \alpha(-I_{\mathrm{CAN}}(v_i, Ca_i, g_{CAN,i}) - I_{pump}(Na_i)) \tag{4.6}$$

$$\dot{hp_i} = \varepsilon_{hp}(h_{p,\infty}(v_i) - hp_i)/\tau_{hp}(v_i) \tag{4.7}$$

$$\dot{s_i} = ((1 - s_i)s_\infty(v_i) - k_s s_i)/\tau_s \tag{4.8}$$

where $\varepsilon_{Ca}$, $\alpha$, and $\varepsilon_{hp}$ are small and cause $Ca_i, Na_i$ and $hp_i$ to evolve on a separate timescale from $v_i, h_i, m_i, n_i, s_i$ (see Subsection 4.1.1). All remaining functions and parameter values can be found in Subsection 4.1.1, and are in general very similar to those in Chapter 3. We now use $\varepsilon_{hp} = 0.003$ instead of 0.001 to add spikes for intrinsically bursting neurons. Also note that $g_{CAN,i}$, $g_{NaP,i}$ and $E_{L,i}$ are no longer constant across all neurons.

### 4.1.1 Function definitions and parameter values

In equations (4.1)–(4.8), for each $x \in \{h, hp, m_p, n, s\}$, the function $x_\infty(v)$ takes the form $x_\infty(v) = \{1 + \exp[(v - \theta_x)/\sigma_x]\}^{-1}$. Also for each $x \in \{h, hp, m, n\}$, the function $\tau_x(v)$ is given by $\tau_x(v) = \bar{\tau}_x / \cosh[(v - \theta_x)/(2\sigma_x)]$. We used the following functions in equations (4.1)–(4.8): $I_L(v, E_L) = g_L(v - E_L)$, $I_{Na}(v, h, m) = g_{Na} m^3 h(v - E_{Na})$, $I_{\mathrm{K}}(v, n) = g_{\mathrm{K}} n^4 (v -$

$E_{\mathrm{K}})$, $I_{syn}(v,s) = g_{syn}s(v-E_{syn})$, $I_{\mathrm{CAN}}(v,Ca,g_{CAN}) = g_{CAN}(v-E_{\mathrm{CAN}})/(1+\exp((Ca-k_{\mathrm{CAN}})/\sigma_{\mathrm{CAN}}))$, $I_{\mathrm{NaP}}(v,hp,g_{NaP}) = g_{NaP}m_{p,\infty}(v)hp(v-E_{Na})$, $I_{pump}(Na) = \phi(Na)-\phi(Na_{base})$, where $\phi(x) = x^3/(x^3+k_{Na}^3)$. In Table 4.1 we record the parameter values used for equations (4.1)–(4.8). Values of $g_{CAN}$, $g_{NaP}$, and $E_L$ vary across all neurons, so these parameters do not appear in Table 4.1, see Subsection 4.3.2.

Table 4.1: Common parameter values for Equations (4.1)–(4.8)

| Parameter | Value | Parameter | Value | Parameter | Value |
|---|---|---|---|---|---|
| $\alpha$ | $6.6\times10^{-5}$ mM pA$^{-1}$ms$^{-1}$ | $g_L$ | 3 nS | $r_{pump}$ | 200 pA |
| $Ca_{base}$ | 0.05 µM | $g_{Na}$ | 160 nS | $\sigma_{\mathrm{CAN}}$ | −0.05 µM |
| $C_m$ | 45 pF | $g_{syn}$ | 2.5 nS | $\sigma_h$ | 5 mV |
| $E_{\mathrm{K}}$ | −75 mV | $I_{app}$ | 0 mV | $\sigma_{hp}$ | 6 mV |
| $E_{Na}$ | 65 mV | $k_{IP_3}$ | 1200 µM ms$^{-1}$ | $\sigma_m$ | −8.5 mV |
| $\varepsilon_{Ca}$ | 0.0007 | $k_s$ | 1 | $\sigma_{m,p}$ | −6 mV |
| $\varepsilon_{hp}$ | 0.003 | $k_{Na}$ | 10 mM | $\sigma_n$ | −5 mV |
| $E_{\mathrm{CAN}}$ | 0 mV | $k_{Ca}$ | 22.5 ms$^{-1}$ | $\sigma_s$ | −3 mV |
| $E_{syn}$ | 0 mV | $k_{\mathrm{CAN}}$ | 0.9 µM | $\bar{\tau}_h$ | 15 ms |
| $g_K$ | 30 nS | $Na_{base}$ | 5 mM | $\bar{\tau}_{hp}$ | 1 ms |
| $\bar{\tau}_m$ | 1 ms | $\bar{\tau}_n$ | 30 ms | $\tau_s$ | 15 ms |
| $\theta_h$ | −30 mV | $\theta_{hp}$ | −40 mV | $\theta_m$ | −36 mV |
| $\theta_{m_p}$ | −40 mV | $\theta_n$ | −30 mV | $\theta_s$ | 15 mV |

## 4.2 METHODS FOR ANALYZING LARGE NETWORKS OF MODEL NEURONS

The numerical simulations in this chapter involve integrating large systems of differential equations. Each network contains approximately 50 model neurons, each with 8 dynamic variables. Separation of timescales in the neuronal dynamics yields a model that is stiff, so we employed the CVODE routine from SUNDIALS, with absolute and relative tolerances set to $10^{-6}$. For computational speed, the CVODE routine was used in custom C++ code compiled for MATLAB via the mex command. We used MATLAB to implement the genetic algorithm described in Section 4.3 and produce simulated raster plots of the results. Most of the administrative code was written in MATLAB. For networks that result from the genetic

algorithm, graphical depictions of the connectivity structure were produced using the iGraph library in the R programming language[8]. This chapter involves the simulation of a large number of independent systems, so the code was parallelized using the pMATLAB package [71]. Finally, simulations of small clusters and example voltage traces were generated using XPP [19].

## 4.3 GENETIC ALGORITHM

The data gathered on the network connectivity of the preBötC indicate that the neurons are collected into spatial clusters [25]. Neurons within a spatial cluster have high synaptic connectivity with each other. A few neurons within each spatial cluster have far reaching synaptic connections to neurons in one or more different clusters; we say that these clusters are connected via "intercluster connections." At first glance, an artificial network adhering to these statistics stands little chance of synchronizing well, due to the relative sparseness of the intercluster connections. Indeed, we found that out of the 240 networks that were randomly generated while adhering to the statistics from the data (see Subsection 4.3.2), we found only 12.5% of networks exhibited a bursting pattern in the summed synaptic output of all neurons in the network (see Subsection 4.3.1). From those 12.5% bursting networks, we did not find any networks that exhibited a particularly strong bursting pattern. A search of 240 networks is far from exhaustive. To perform an exhaustive search, two factors must be considered. The first factor is the connectivity architecture; simply changing the direction on a select handful of connections could massively affect synchrony (see Section 4.4). The second factor arises from the heterogeneity of the neuronal population within the preBötC. The individual neurons can be intrinsically quiescent, intrinsically bursting, or intrinsically tonic (we model this by varying the strength of the NaP current), and neurons also independently express the CAN current in various strengths. To represent this heterogeneity, we must at least vary in $g_{NaP}$ and $g_{CAN}$; in this chapter we will also consider limited heterogeneity in $E_L$, the reversal potential of the leak current. Thus, for networks of approximately 50 neurons, an exhaustive search is out of the scope of this work. In light of this, we developed a genetic

algorithm to search parameter space for networks that simultaneously fit the connectivity data and yield good bursting patterns across the population.

The genetic algorithm is a map that takes a collection of networks, hereafter called a "generation," to a new generation. This transformation occurs in two stages. First, each network of the current generation must be assigned a "fitness score," see Subsection 4.3.1. The top twenty networks with high-scoring fitness are then combined to produce a new generation, see Subsection 4.3.3. We found that choosing the top twenty networks strikes an acceptable balance between heterogeneity in the new generation and computational feasibility.

### 4.3.1 Evaluating the fitness of a network

Fitness of a particular network was measured by looking at statistics pertaining to the summed synaptic output of all neurons in the network ("population activity"). We define the population activity for a network of $N$ model neurons as $p(t) = \sum_{i=1}^{N} s_i(t)$. We recorded the population activity of a network for 15 seconds of simulated time, after discarding a 5 second transient. The theoretical maximal population activity, $p_{max}$, is defined to be $p_{max} = N \cdot s_{max}$, where $s_{max} = \max_v s_\infty(v)/(k_s + s_\infty(v))$. If the population increased through a threshold of 25% of $p_{max}$, we marked that the population started a burst. Later, if the population decreased through 20% of $p_{max}$, we declared that the population ended the burst. Burst duration is defined to be the end time minus the start time of the burst. The burst period, on the other hand, is the difference between consecutive start times. Burst amplitude is calculated by finding the maximal value of the $p(t)$ during the burst and subtracting off the average population activity during the middle third of the quiescent period before the next burst. Therefore, the last burst in the 15 second window does not always have its amplitude measured. We exclude the first third of the silent phase because we set the burst termination point to be 20% of $p_{max}$, and so should allow some time for the burst to fully terminate. On the other hand, preBötC neurons do not enter the active phase simultaneously. Such activity should not be penalized, so we exclude the last third of the silent phase from consideration to calculate the relative amplitude of the burst. Therefore, this method of calculating the amplitude rewards synchrony during the active phase of a burst and penalizes large numbers

of neurons for being active during much of the silent phase. Instead of using the maximal value of $p(t)$, we also considered the average value of $p(t)$ during middle third of the active phase. This did not produce significantly different results, so we will continue to use the maximal value for scoring in the remainder of the work.

During the 15 second window, if a network displayed at least 3 complete bursts, we then gathered statistics on this network; otherwise, the network is declared to be a failure. The statistics that we gathered were the coefficient of variation (CV) of the burst duration, the CV of the burst period, the CV of the burst amplitude, and the mean of the burst amplitude. Using these statistics, we compile two separate fitness scores: the CV score and the amplitude score. To form the CV score we add together the CV of the burst durations, the CV of the burst periods, and the CV of the amplitudes of the bursts in the network. The amplitude score is the average of the amplitudes for the bursts in the network, as described above, except it is normalized by $p_{max}$. Thus, a network with a low CV score has bursts that have regular shape and occur with a regular frequency, but the amplitude of those bursts might be universally low. On the other hand, a network with a high amplitude score has high participation from the entire network during each burst, with low participation during the network's silent phase, but the bursts may not have regular shape or regular frequency. The best networks will have a low CV score and a high amplitude score.

To select the twenty networks that would engender the next generation, we formulated two lists. One list contains networks with the 10 best CV scores, and other list contains the networks with the 10 best amplitude scores. Once a network was placed on a list, it was precluded from appearing on the other list. These two lists form the top twenty networks that will be combined and mutated to form the next generation. The combination and mutation process will be referred to as "mating" the networks. A priori, it is not clear which score is more important, therefore mating was performed randomly within the top twenty networks; we did not preferentially mate the networks from the CV list with those from the amplitude list. Each network in the top twenty mated with two other networks in the top twenty, selected at random, and each mating pair produced three child networks; thus the next generation contains 120 new networks. Due to asymmetries and randomness in the mating procedure described in Subsection 4.3.3, repeated mating pairs, reversed mating

pairs, and even self-mating pairs were permitted. As an example, let $\{A,\ B,\ C,\ D\}$ be networks. Each network will get two mates; we will use $XY$ to signify $X$ mated with $Y$. The mating pairs $XY$ could be $\{AB,\ AC,\ BA,\ BB,\ CB,\ CC,\ DA,\ DA\}$. Before detailing the mating procedure, we describe how the initial generation is formed.

### 4.3.2 Creating a network

We used the following algorithm to construct networks that adhere to the connectivity data in [25]. First, a target number of neurons must be chosen; in these simulations we set a target number of 50 neurons. We define the size of a cluster as the number of neurons within it. The histogram figure for cluster size in [25] yields a few classes of cluster sizes: $\{3\}$, $\{4, 5, 6, 7\}$, $\{8, 9, 10, 11\}$, and $\{12, 13, 14, 15\}$. The data do not distinguish individual probabilities of occurrence for members within a class. Therefore, we will use these classes as a sort of equivalence class in the mating procedure, see Subsection 4.3.3 for details. We approximated the histogram data with the probabilities given in Table 4.2. These probabilities were derived by counting the height, in pixels, for each bar in the histogram. When a new cluster is created, the size is chosen randomly using those probabilities. Once the size of the cluster is chosen, we add this new cluster to the collection of clusters, repeating this process until the total number of neurons meets or exceeds the target number. Each cluster is also assigned a unique ID, which will be utilized in the mating process. Each ID is unique across all networks, and all generations, of the simulation. At this time, the algorithm does not account for neurons that reside outside of all clusters, because we elected to focus on clusters as the functional units of the network and most preBötC neurons reside within clusters [25].

Table 4.2: Number of neurons for a newly created cluster

| # neurons | probability | # neurons | probability | # neurons | probability |
|---|---|---|---|---|---|
| 3 | 10.7784% | 8 | 11.976% | 12 | 4.7904% |
| 4 | 10.7784% | 9 | 10.7784% | 13 | 4.1916% |
| 5 | 10.7784% | 10 | 5.988% | 14 | 1.1976% |
| 6 | 11.3772% | 11 | 4.7904% | 15 | 0.5988% |
| 7 | 11.976% | | | | |

Each neuron is assigned a random number of open connections, where this number is chosen from a distribution that approximates the histogram data in the literature, see Table 4.3; these open connections will be closed pairwise when two neurons are synaptically connected. Again, the approximation was obtained by counting the height in pixels of the histogram bars from the appropriate figure in [25]. For each cluster within the collection of clusters, we will form a small network containing all the neurons within that cluster, and intercluster connections will be formed from the remaining open connections for neurons in each cluster.

In the absence of data to the contrary, we selected the intrinsic dynamics for each neuron randomly, instead of having neurons have similar parameters based on spatial locations (e.g. within the same cluster). With a probability of 25% the neuron is chosen to be intrinsically bursting, while 37.5% of neurons were intrinsically quiescent and the remaining 37.5% of the neurons are intrinsically tonic. To represent intrinsically quiescent neurons, we set $E_{L,i} = -61.5$, and $g_{NaP,i}$ was chosen from a uniform distribution ranging between 0.55 and 0.75. Intrinsically bursting neurons were generated such that $E_{L,i} = -61.5$ and $g_{NaP,i}$ was chosen from a uniform distribution ranging between 0.85 and 1.25. For intrinsically tonic neurons, we allowed $E_{L,i}$ to vary so that some neurons would become active even without the NaP current, see Section 4.9. Intrinsically tonic neurons therefore had $g_{NaP,i}$ chosen from a uniform distribution ranging between 1.3 and 4 while $E_{L,i}$ was chosen from a uniform distribution ranging between $-61.5$ and $-57$. No matter what intrinsic dynamics were elected for the neuron, $g_{CAN,i}$ was chosen from a uniform distribution ranging between 0 and 5.

Table 4.3: Initial number of open connections for a newly created neuron

| # open connections | probability | # open connections | probability | # open connections | probability |
|---|---|---|---|---|---|
| 2 | 5.6604% | 4 | 25.4717% | 6 | 5.6604% |
| 3 | 11.3208% | 5 | 51.8858% | | |

To form the small network consisting of neurons from only one cluster we iterate the following procedure, see Figure 4.1 for an illustration of the process. We first find the

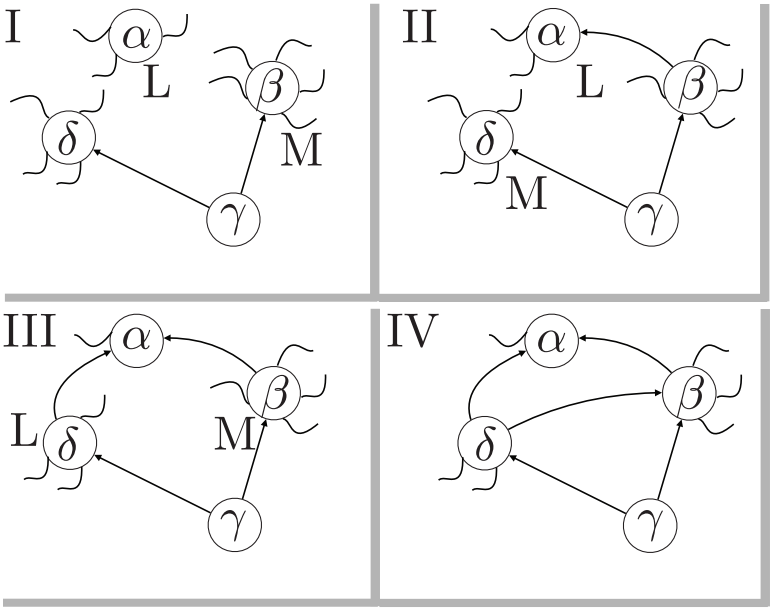


Figure 4.1: Creation of an example cluster by connecting neurons with open connections. Circles represent neurons of the network, arrows connecting them are unidirectional synaptic connections, and S shaped segments represent open connections. A few connections are assumed to have been made already, and the creation of the cluster proceeds through Panels I-IV. Panel I: find the neuron with the least number of open connections ($\alpha$), and label it L. Find the node with the most open connections ($\beta$), that is already not already connected to L, and label it M. Panel II: Form a connection between $\alpha$ and $\beta$, choosing the direction randomly. Again, find the node with the least number of open connections ($\alpha$), label it L. Find the node with the most number of open connections, that is not already connected to L ($\gamma$, since $\beta$ is already connected to $\alpha$), and label it M. Panel III: form a connection between $\beta$ and $\delta$. Find the node with the least number of open connections. This would typically be $\alpha$, but there are no legal neurons for it to connect to, so it is removed from consideration, and so we label $\delta$ as L instead. Find the neuron with the most open connections that is not already connected to L ($\beta$) and label it M. Panel IV: form a connection between $\delta$ and $\beta$, choosing the direction randomly. Each neuron with open connections is already connected to every other neuron with open connections, so the cluster is completed. The remaining open connections will be used to form intercluster connections.

neuron with the least number of open connections, L, as well as the neuron with the greatest number of open connections that it is not already connected to, M, and form a connection between L and M. L and M are never the same neuron. Connections are directed edges on a graph, with the direction determined by an unbiased coin toss. When a neuron has no open connections remaining, or there are no neurons remaining that have open connections that it is not yet connected to, the neuron is removed from consideration. In the latter case, when the removed neuron still has open connections, the neuron will become a candidate for intercluster connections. This process is repeated until there are a prescribed number of open connections left, or until no more connections can be made without having a pair of neurons connected to each other more than once. The prescribed number of open connections to be preserved at this stage is same as the maximum number of intercluster connections per cluster allowed, which is usually 2 or 3 (see Section 4.4 and Section 4.5).

Experimental results suggest that each cluster has, on average, 2 connections to other clusters (personal communication, Mironov). In this algorithm, we enforce a rule that each cluster will have at least two connections to other clusters, and may have more depending on the circumstances of the simulation. To ensure connectedness of the network, clusters are placed into a ring structure (that is, if there are N clusters: cluster 1 is connected to cluster 2 and cluster N, cluster 2 is also connected to cluster 3, etc.). Note that with only 2 intercluster connections per cluster, the only other connected structure is a long chain where cluster 1 is not connected to cluster N, but this would be terrible for synchronization and therefore is not considered here. Intercluster connections are selected by randomly choosing one neuron with remaining open connections from each of the two clusters, and determining the direction of the connection by an unbiased coin toss, see Figure 4.2. If more than two intercluster connections are permitted, then these extra connections are formed after the clusters have been placed into the ring. There are no restrictions on which clusters these intercluster connections may connect, other than the rule that no neuron may be connected with any other single neuron more than once. Once all intercluster connections are created, there may be some neurons with remaining open connections. These open connections are not forgotten, and may be utilized during the mating process, although they have no functional impact when the network is integrated.

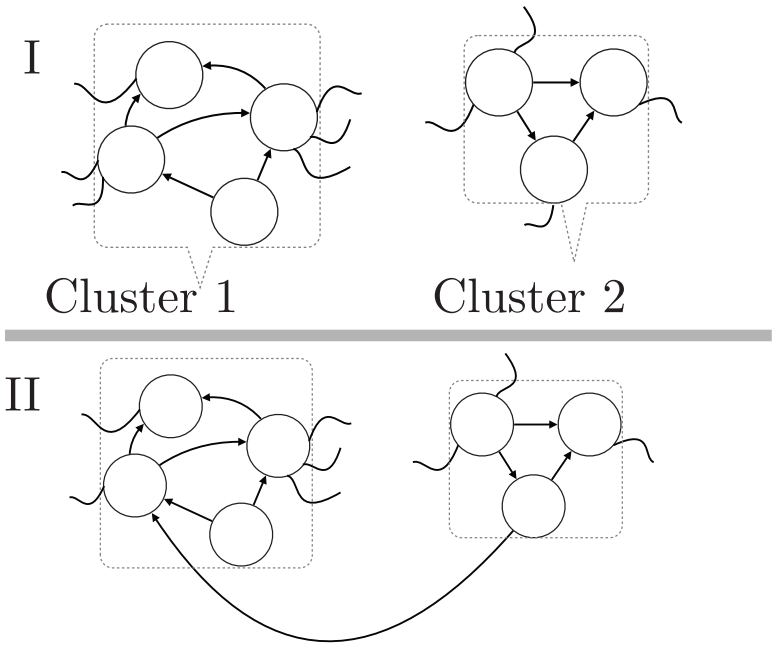


Figure 4.2: Formation of intercluster connections. Panel I: Consider Cluster 1 and Cluster 2, each with varying number of open connections (S shaped segments). Panel II: An intercluster connection is formed between the two clusters by closing one open connection from each cluster at random.

### 4.3.3 Production of a child network from a mated pair

Let $XY$ be a mating pair. We will see below that the order is important; $XY$ is very likely to yield a significantly different network from $YX$. Now we can describe how $X$ and $Y$ are mated to form a child network for the next generation.

An exact copy of $X$ is created, which we will call $S$, see Figure 4.3. $S$ will serve as a sort of scaffolding and its clusters will change to distinguish it from $X$ and $Y$. $S$ will be modified several times as some of its are clusters replaced with clusters from $Y$, or with mutant clusters that may have not yet appeared in any network. Let $T$ be a cluster not already appearing in $S$. When the cluster in $S$ is replaced by $T$, we say that $T$ is transplanted into $S$. Each initial cluster in $S$ has a 50% chance to be replaced. Let $R$ be a cluster in $S$ that has been chosen to be replaced. Recall from Subsection 4.3.2 that the cluster sizes are divided into classes. $R$ will be replaced with a cluster that is in the same class size as $R$. For example, suppose $S$ initially adheres to the data and $R$ has 7 neurons, if we replace $R$ with a cluster of size 4, 5, 6 or 7, then $S$ will still be consistent with the data. Therefore, to keep $S$ consistent with the data, we compile a list, $C$, of clusters from $Y$ that are in the same size class as $R$.

We remove clusters from $C$ if they have IDs already appearing in the current version of $S$; this prevents a network, and perhaps an entire generation, from being dominated by one cluster through repeated mating, see Figure 4.3. If there are no clusters remaining in $C$, we generate a new mutant cluster using the rules described for cluster creation of the first generation, except that its size will be randomly selected from those within $R$'s size class, and the number of open connections the mutant cluster has is at least the number of intercluster connections that $R$ had. This also means that if the mating pair is $XX$, the first cluster replaced will be guaranteed to be replaced by a mutant cluster, but that replaced cluster could then be transplanted into the network at a different location. Even if there are still clusters in $C$ after checking for repeated IDs, $R$ is replaced by a mutant cluster 5% of the time, while the other 95% of the time we randomly select one of the clusters from $C$ to transplant into $S$. The neurons in a mutant cluster have intrinsic dynamics that are randomly generated, as in Section 4.3.2.

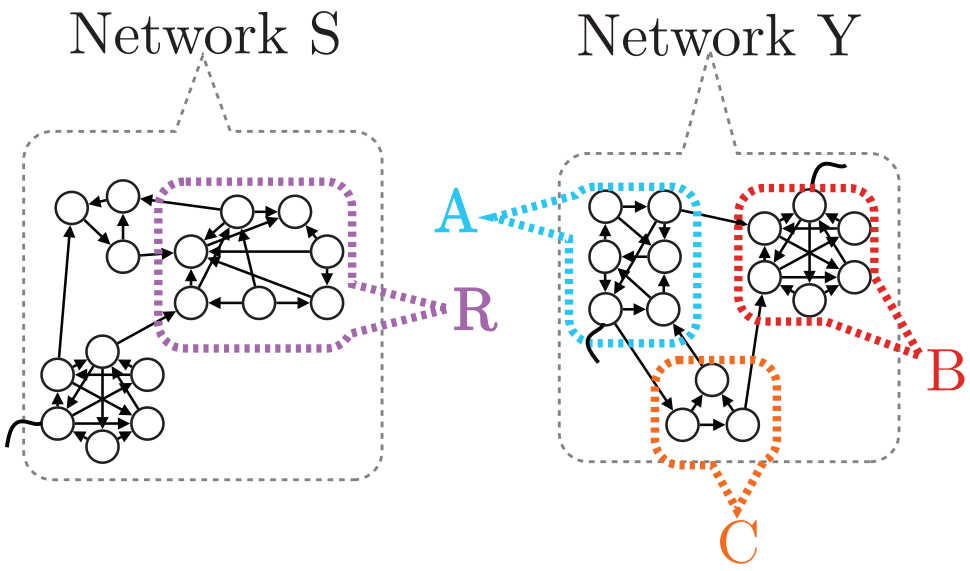


Figure 4.3: Setup for illustration the illustration of transplanting a cluster from Y into the network S. Three intercluster connections per cluster are allowed. The purple cluster R will be replaced. The blue cluster A is within R's size class, so it is a candidate to replace R. The red cluster B is also in R's size class, but already appears in S (albeit with different remaining open connections), so it is rejected. The orange cluster C is not in R's size class, so it too is rejected. Therefore, R will be replaced by A or by a mutant. Note that the network Y will not be altered.

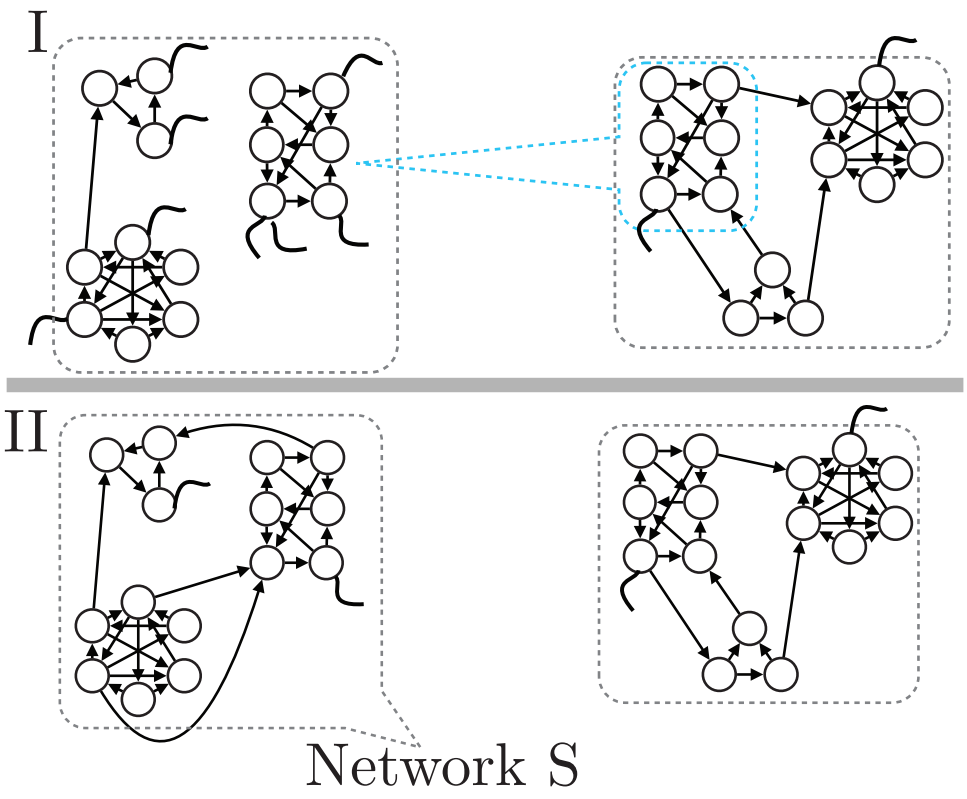


Figure 4.4: Illustration of transplanting cluster A from Figure 4.3 into network S. Panel I: R is deleted, and the intercluster connections that connected it to the other clusters in S are converted to open connections on neurons in those other clusters. The cluster A from network Y is copied, and we refer to this copy as T. Any intercluster connections the original A had are converted to open connections in T, and its already existing open connections are preserved. Panel II: The open connections in T are closed by connecting to neurons with open connections in S. These connections are joined first by forming the ring, and then filling out the rest of the connections until as many clusters as possible have 3 intercluster connections. Note that the network on the right in panels I and II of this figure has not been changed; it is preserved for future mating within this generation.

When a cluster, $T$, is transplanted into the scaffold network S, it keeps its intracluster connectivity structure, as well as the intrinsic dynamics of all of its neurons. If $T$ came from $Y$, then the intercluster connections it had in $Y$ will be recovered as open connections, see Figure 4.4 panel I. The remembered open connections of $T$ are utilized when connecting $T$ to the other clusters in $S$. First, the ring structure of $S$ is preserved by closing random open connections from each appropriate cluster. That is, if $R$ was the $i^{th}$ cluster, $T$ will be connected to clusters $i-1$ and $i+1$. If $R$ had more than two intercluster connections, we attempt to utilize the remaining open connections in $T$ to restore those intercluster connections, see Figure 4.4 panel II. Some open connections in $T$ may not be utilized, since multiple connections between neurons are forbidden, or perhaps the other clusters in $S$ do not have enough open connections remaining. Another alternative is that the maximum number of intercluster connections allowed for $T$ has already been obtained. No matter the cause, the remaining open connections in $T$ are recorded for possible later use.

After all clusters have been replaced or preserved for the next generation network $S$, we attempt to connect as many pairs of neurons with open connections as possible, while working within the restraints concerning maximum numbers of intercluster connections and continuing to forbid self-coupling and multiple connections between neurons. Open connections that could not be closed are remembered for future generations, and $S$ is now a next generation network.

## 4.4 THE GENETIC ALGORITHM PRODUCES BURSTING NETWORKS

In the preBötC it is hypothesized that each cluster is connected to two other clusters (private communication, Mironov). We ran the genetic algorithm while requiring each cluster to be connected to exactly two other clusters. Recall that a network exhibits population bursting if $p(t)$ features repeated (though not necessarily periodic) activity of alternating phases above 25% of $p_{max}$ with phases below 20% of $p_{max}$. The 11th and final generation of this run of the genetic algorithm will be called GA(2) (Genetic Algorithm, 2 intercluster connections per cluster). Out of the initial 120 networks for the genetic algorithm, only 14 exhibited any

bursting patterns, and 6 non-bursting networks were chosen at random to fill out the top twenty. The next generation substantially improved upon this, containing 49 networks with bursting population activity. The final generation contained 80 networks with population bursting.

The directionality of intercluster connections cannot be deduced from the data in [25]. Therefore, with only two intercluster connections per cluster, an individual cluster has a 50% chance to fail to influence, or fail to be influenced by, the rest of the network. Another ramification of having only two intercluster connections per cluster, is that the clusters are arranged in a ring, which results in a long path length between some clusters, which can interfere with synchrony (see also [24]). Some networks from GA(2) achieve a low CV score by avoiding this issue, see Figure 4.5. In Figure 4.5, the red and light blue clusters are tonically active, and keep the population output at about 10% of $p_{max}$. The yellow cluster receives no input from the rest of the network, but has a short path length to the dark blue, green, brown, and purple clusters. In this case, those clusters respond well to bursting input, so the bursting behavior of the yellow cluster controls the remaining clusters. This results in a low CV score, because the clusters that do burst, burst well together. However, the excessive tonic activity is penalized in the amplitude score.

In contrast to the network in Figure 4.5, other networks in GA(2) may achieve periods of lower population activity if they do not contain clusters that are tonically active. With only two intercluster connections per cluster, the path length between clusters can be long enough to interfere with synchronization, see Figure 4.6. Even though each cluster in this network is bursting in some capacity, the population does not cross the 25% threshold unless sufficiently many clusters coincidentally burst. Relying on coincidence yields high CVs for burst amplitude and burst period, and therefore a high CV score. The amplitude score in this network is not a significant improvement over the amplitude score for the network in Figure 4.5, due to the population "bursts" that failed to cross the 25% threshold. Notice that for the network in Figure 4.6, the population activity does regularly fall below 5% of $p_{max}$. Would more intercluster connections per cluster shorten the path length enough to engender networks where each cluster bursts with tighter synchrony?

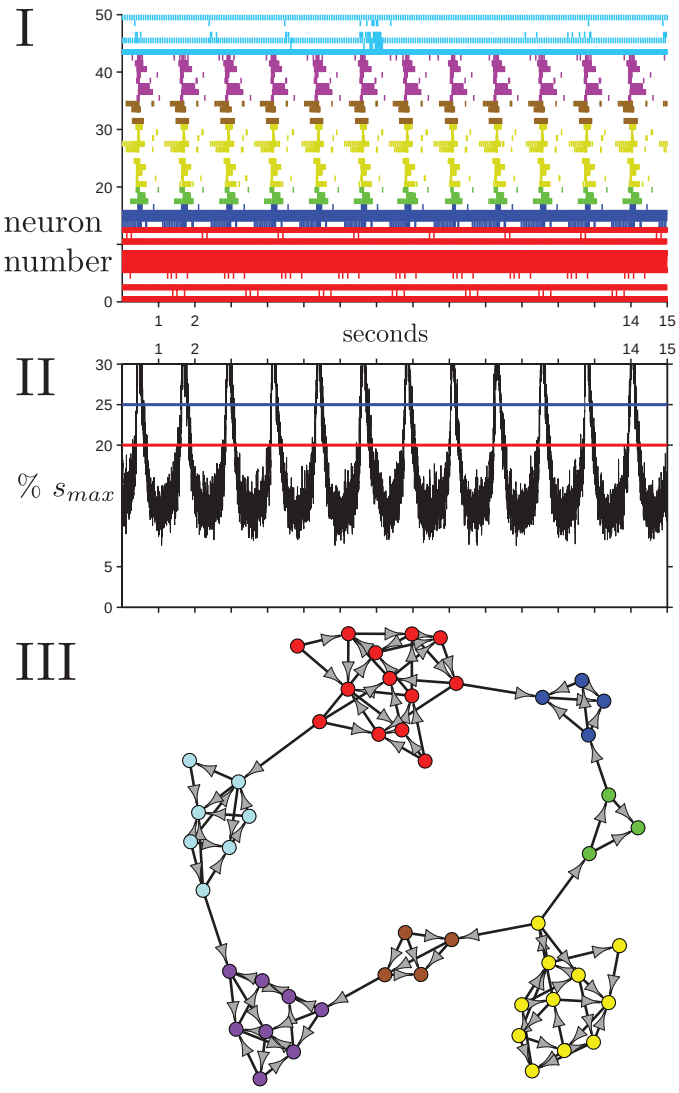


Figure 4.5: A network from GA(2) with a low CV score but also a low amplitude score. Panel I: simulated raster plot. Neuron number is given on the y axis, and a tick at that y value is made at each time (x axis) that neuron spiked. Like colors indicate that the neurons are in the same cluster. Panel II: $p(t)/p_{max}$, the amplitude score is lowered by the fact that the population still has a large amount of activity during the "silent" phase. Panel III: network architecture. Nodes of the graph represent individual neurons, and directed edges are synaptic connections. Colors of the nodes correspond to those colors in panel I.

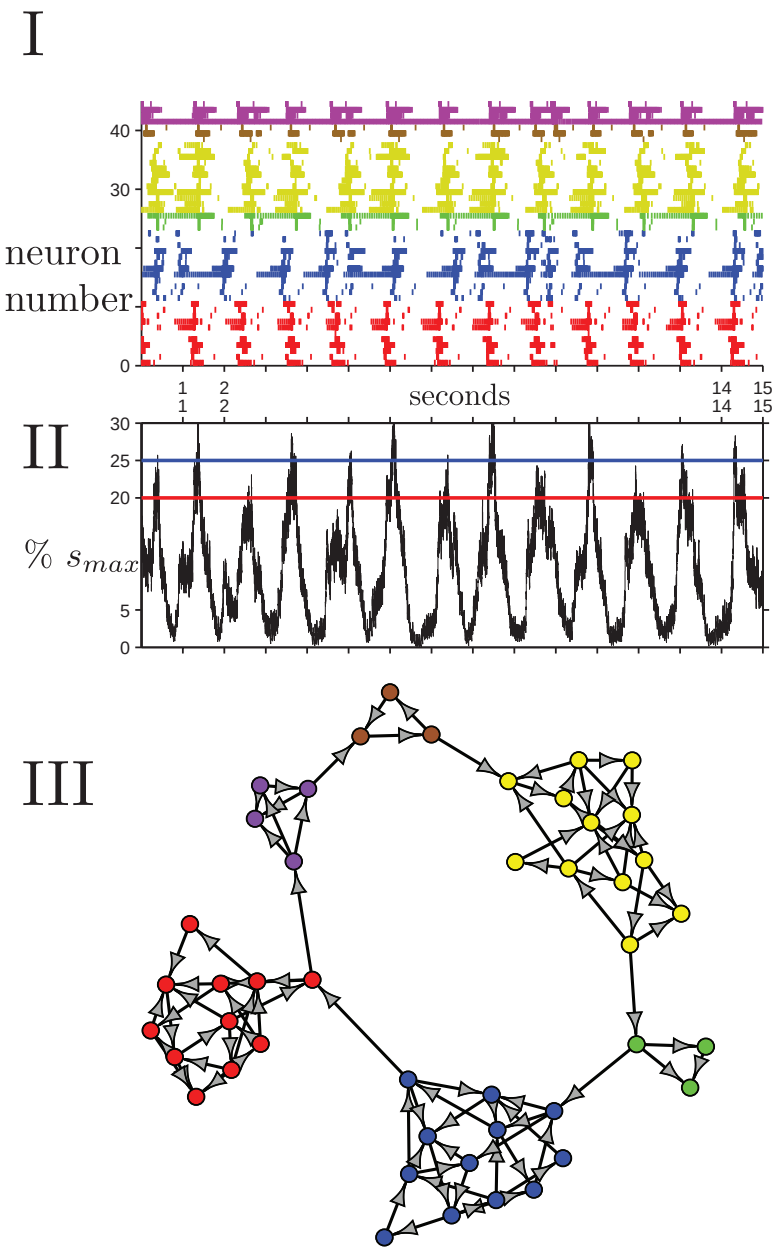


Figure 4.6: A network from GA(2) with a high amplitude score but also a high CV score. Panel I: simulated raster plot. Neuron number is given on the y axis, and a tick at that y value is made at each time (x axis) that neuron spiked. Like colors indicate that the neurons are in the same cluster. Panel II: $p(t)/p_{max}$. Panel III: network architecture. Nodes of the graph represent individual neurons, and directed edges are synaptic connections. Colors of the nodes correspond to those colors in panel I.

## 4.5 THREE INTERCLUSTER CONNECTIONS PER CLUSTER YIELD STRONGER POPULATION ACTIVITY

In this section, we allow the genetic algorithm to establish three intercluster connections per cluster, instead of two. The first 120 networks created this way did not fare much better than the first 120 from Section 4.4: 16 had bursting in their population activity. The subsequent generation again had a marked improvement in performance: 49 networks were bursting. The 11th and final generation yielded 103 networks that were classified as bursting. The final generation of this run of the genetic algorithm will be called GA(3), to signify that it allowed 3 intercluster connections per cluster. The top twenty networks from GA(3) yielded a few networks with high amplitude score while keeping the CV score low, although for the most part, the CV and amplitude scores between GA(3) and GA(2) are comparable at first glance, see Figure 4.7. Networks that received similar scores can look quite different. For instance, the network $GA_3^*$ (Figure 4.8) emerged from GA(3); every cluster participates in bursting behavior, which is well synchronized across the network; hereafter this network will be referred to as $GA_3^*$. However, the amplitude scores of the networks from $GA_3^*$ and Figure 4.5 differ only by 0.03 (11% relative change) in Figure 4.7. This similarity is primarily a reflection of how amplitude scores are calculated: the penalty for activity between bursts differentiates these two networks, but not by enough for it to be apparent from Figure 4.7 that GA(3) outperforms GA(2).

To clarify the separation between GA(2) and GA(3) we performed an additional test. During the scoring process, we recorded the start time of a burst when the population activity increased through 25% of $p_{max}$, and the end time was marked when the population activity decreased through 20% of $p_{max}$. For the additional test, we made the definition of bursting activity much more restrictive. We kept the burst initiation threshold at 25%, but we now mark the end of a burst when it falls below 5% of $p_{max}$. This means that networks such as those in Figure 4.6 and $GA_3^*$ (Figure 4.8) will still be labeled as bursting, but the network in Figure 4.5 will not, since its population activity never dips below 5%. For the top twenty networks from GA(2) and GA(3), if they continued to be classified as bursting under this new test, the CV and amplitude scores of are plotted in Figure 4.9. Interestingly, only 2

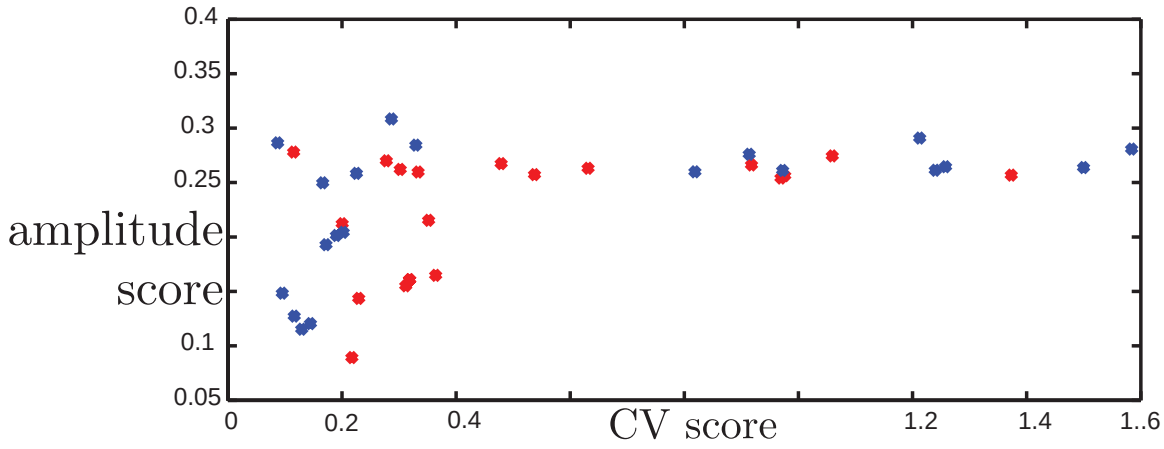


Figure 4.7: Scatterplot of amplitude score vs CV score. Red marks indicate the scores for top twenty networks of GA(2), while blue marks correspond to the top twenty networks from GA(3). Recall that low CV scores and high amplitude scores are desirable. Although the blue marks seem to be concentrated at slightly lower CV scores than the red marks, it is not obvious that the difference between GA(2) and GA(3) is significant.

out of the top twenty for GA(2) continued to be classified as bursting, while 9 of the top twenty from GA(3) were still found to be bursting. Even though the fitness algorithm did not condition GA(2) or GA(3) for increased performance on this test, it is interesting that GA(3) did significantly better. What properties of GA(3) yield this performance increase?

GA(3) is characterized by allowing 3 intercluster connections per cluster, instead of the 2 allowed in GA(2). In Section 4.4 we discussed that for a network to improve its amplitude score, there would need to be less activity between registered bursts. The network in Figure 4.6 managed this, although the CV score was lowered by the lack of synchrony of the bursting clusters. There is a lack of synchrony between clusters due to the long path length, which cannot be shortened without more intercluster connections. For instance, by the time one cluster finishes bursting, a cluster four positions further on the ring may have just received the bursting input; Figure 4.10 demonstrates this phenomenon in a toy network of 4 neurons. Let the black neuron represent the neuron in cluster 1 that has an intercluster connection. An external burst (presumably from the rest of the black neuron's cluster) is fed into the black neuron at time $t = 100ms$. Suppose there are two clusters for which input from and output to the rest of the network occurs from the same neuron; let those neurons correspond to the white neurons in the toy network of Figure 4.10. Finally, allow the red neuron to represent the input neuron of the fourth cluster down the ring from the black neuron's cluster. Notice that the red neuron does not burst until after the black neuron has finished bursting, which risks asynchronous behavior between the first and fourth clusters of the represented network. If the black neuron was allowed one extra connection, perhaps one that reaches the red neuron, the bursts can become synchronous.

The high interconnectivity of the neurons within the clusters means that a bursting input to the cluster will quickly be felt by the rest of the cluster. Certainly, smaller clusters are easier to synchronize. Indeed, a large cluster like the red cluster from Figure 4.6 is difficult to synchronize because long path lengths can exist within the cluster; the path from the north-most neuron to the east-most neuron has length 4. To achieve synchrony across the whole network, then, there should be small clusters with more than 2 intercluster connections per cluster to serve as shortcuts around the ring. In GA(3), this is achieved by networks like $GA_3^*$ (Figure 4.8), whereas in GA(2) smaller clusters may not be practical due to the long

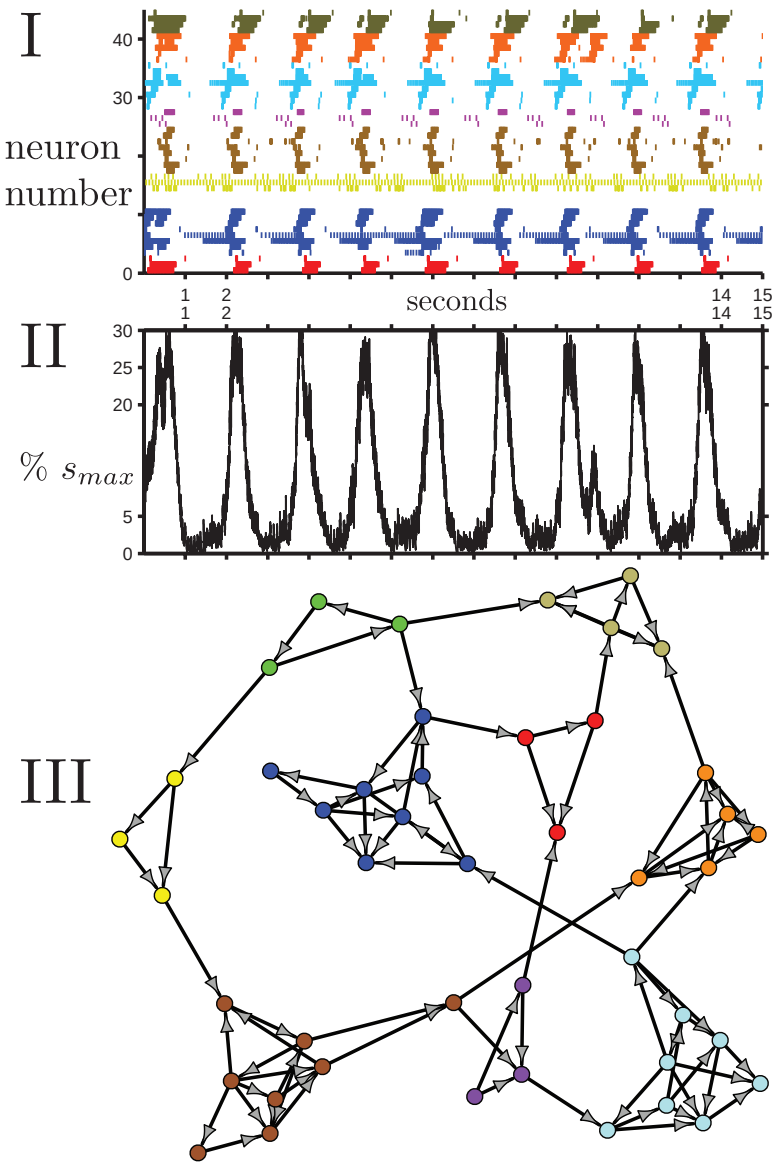


Figure 4.8: A network from GA(3) with high amplitude score and a low CV score, hereafter referred to as $GA_3^*$. Panel I: simulated raster plot. Neuron number is given on the y axis, and a tick at that y value is made at each time (x axis) that neuron spiked. Ticks of the same color indicate that the neurons are in the same cluster. Panel II: $p(t)/p_{max}$. Panel III: network architecture. Nodes of the graph represent individual neurons, and directed edges are synaptic connections. Colors of the nodes correspond to those colors in panel I.

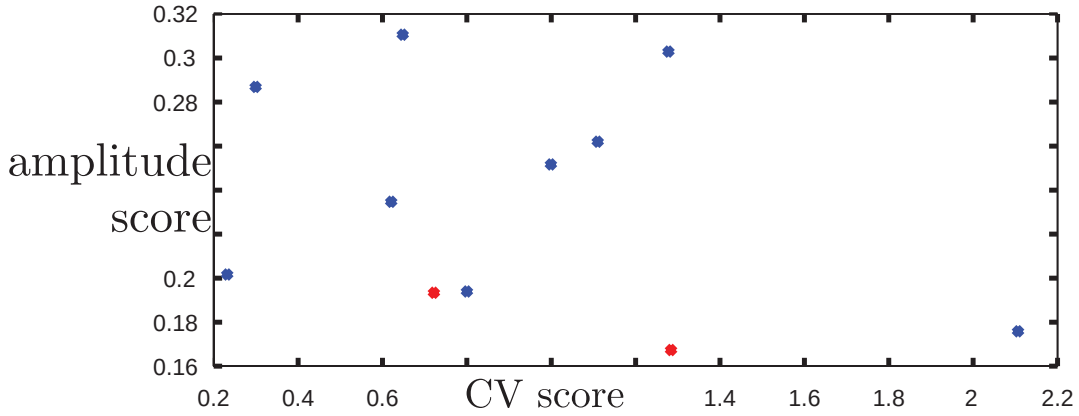


Figure 4.9: Scatterplot of amplitude score vs CV score, when the thresholds for the definition of bursting are set to be 25% and 5% of $p_{max}$, instead of 25% and 20%. Most networks from GA(3) and GA(2) failed to burst under this definition; those that do meet this harsher definition are plotted here. Red marks indicate the scores for top twenty networks of GA(2), while blue marks correspond to the top twenty networks from GA(3). Note that only 2 out of the top twenty networks from GA(2) met the harsher criterion for bursting, while 9 from the top twenty networks in GA(3) bursted under these harsher restrictions.

path length between clusters. Indeed, clusters in GA(3) have, on average, 2 less neurons than clusters in GA(2).

Considering the clusters of the top 20 networks of GA(3) in isolation from each other, 57% of the clusters burst in phase with a supplied bursting input. On the other hand, for GA(2), only 33% of clusters burst under the same conditions. The bursting input had an activated CAN current and was supplied to a neuron that previously had an incoming intercluster connection. For GA(3), only 13% of clusters were tonically active when disconnected from the rest of the network. Therefore, clusters that persist through the generations leading to GA(3) are likely to burst when they receive bursting input, or burst themselves. Combined with the decreased path length between clusters, this helps lower the CV score by promoting synchrony and increase the amplitude score by reducing tonic activity between bursts.

## 4.6 DISTRIBUTIONS OF $g_{CAN}$

In Section 4.5, we concluded that short path lengths are important for synchronization between clusters. However, the dynamics of the neurons are also very important. In the unified model, a lot of information is carried by the CAN current; for a single neuron, CAN current activation is indicative of the activity of its presynaptic neurons. Activation of a neuron's CAN current causes it to, at least for a short time, bombard its postsynaptic neurons with sufficient activity to activate the postsynaptic CAN currents, if they have sufficiently high $g_{CAN}$ (around 0.6 or higher). No matter what intrinsic dynamics are selected when a new model neuron is created, the strength of its CAN current is chosen uniformly from the interval $[0,\ 5]$. Interestingly, the center of the distribution of $g_{CAN}$ changes by the final generation of the genetic algorithm.

For the top twenty networks in GA(2) and GA(3), the average value of $g_{CAN}$ across all neurons is lower than the initial average. For GA(2), the average $g_{CAN}$ is $2.081 \pm 0.1321$, and in GA(3) it is $1.9323 \pm 0.2679$, both of which are statistically significantly different from the initial average of 2.5. Statistical significance was given by a series of t-tests. Each t-test involved 20 samples of 50 randomly selected $g_{CAN}$ values from a uniform distribution ranging

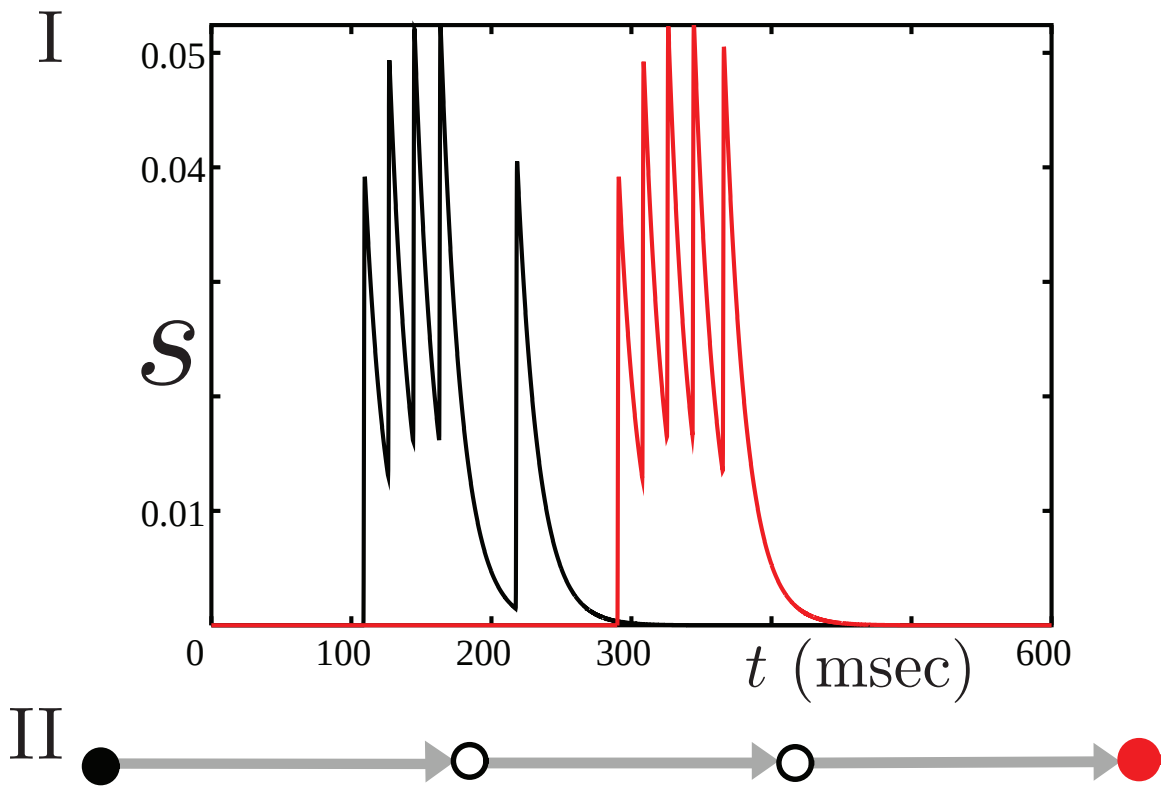


Figure 4.10: Long path lengths can cause bursts to lose synchrony. Panel I: synaptic output from black and red neurons of the four neuron network shown in Panel II. All neurons in the network are intrinsically quiescent, with $g_{NaP} = g_{CAN} = 0.6$. The black neuron receives a burst from the rest of its cluster and the activity propagates through the chain. By the time the red neuron enters the active phase, the black neuron has returned to quiescence. Panel II: The neurons for are arranged in a chain to represent the minimum time it would require for a cluster's bursting output to reach a cluster further down the ring.

from 0 to 5. The average of each sample was computed, and these 20 averages were compared against the average for GA(2) by using the "ttest" command in MATLAB. This gave a $p$ value which was typically around $p = 10^{-}8$. We performed $500,000$ such t-tests, and the maximum $p$ was such that $p < 10^{-5}$, yielding that the differences in $g_{CAN}$ distributions from GA(2) and GA(3) are statistically significant from their initial populations. Interestingly, the average $g_{CAN}$ value has drifted towards an ideal value for relaying a presynaptic burst, see Figure 4.11. In Figure 4.11 we plot the result of simulating a toy network with two neurons: one neuron is self coupled and generates a DB burst, the second neuron (indexed as '$r$' for response) is intrinsically quiescent, but responds with a burst of its own. In panel I of Figure 4.11 we vary $g_{CAN,r}$ and plot a blue dot at the amplitude of this response by averaging $s_r$ over a 300ms window. The window of 300ms was chosen based on the duration of the self-coupled burst. For intermediate values of $g_{CAN}$, we note that the amplitude of the burst in the response is actually increased. Notice that the amplitude of the response is weaker than amplitude of the input for $g_{CAN,r} > 3$. The response neuron is capable of entering depolarization block when $g_{CAN,r} > 3$. Presynaptic activation of the CAN current causes the responding neuron to quickly enter depolarization block, resulting in decreased burst amplitude. The speed of the transition to depolarization block is enhanced by the CAN current, which is why the response continues to decrease as $g_{CAN}$ increases toward 5; the averaging process causes the the amplitude of the response to be mitigated by the short duration.

Nevertheless, the ability of some neurons to enter depolarization block is also important for network functionality. To elucidate the role of depolarization block in these networks, we performed an additional numerical experiment on the top twenty networks from GA(2) and GA(3). For each neuron of the network, if $g_{CAN,i} > 3$, we set $g_{CAN,i} = 2$. This removes the capability of the neuron to enter depolarization block and gives it the ability to boost signals. In most cases, when we make this change in any of the top twenty networks from GA(2) or GA(3), the rhythm of the network is destroyed; it becomes tonically active. Those networks that do continue to burst do so in a very irregular way; this bursting is explained in Section 4.10. Clearly, the ability for some neurons to enter depolarization block is a good thing for the networks we found through the genetic algorithm. Can you have too much of

a good thing?

We performed an analogue of the previous experiment: for each neuron in the network, if $g_{CAN,i} < 3$ we set $g_{CAN,i} = 3.5$. Thus, virtually all neurons will be capable of entering depolarization block. Although not as severe as preventing all neurons from entering depolarization block, the outcome was that a great deal of the amplitude and regularity of the bursts was lost. Thus, the strength of the CAN current across the network needs to be distributed; both neurons that are capable of entering depolarization block, as well as those that are incapable, are important for network functionality.

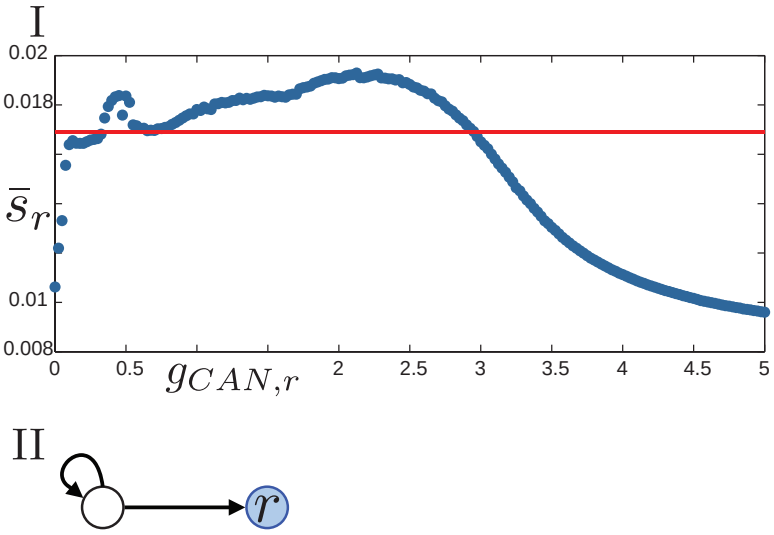


Figure 4.11: The amplitude of a neuron's response to a burst depends on the conductance of its CAN current. Panel I: On the x axis, we plot the strength of $g_{CAN,r}$ the conductance of the postsynaptic CAN current. On the y axis, we plot $\bar{s}_r = \frac{1}{300}\int_0^{300} s_r(t)dt$, the average of the synaptic activity across the burst. The red line is the average of the synaptic activity for the presynaptic burst. Notice that there appears to be a maximum of the average of the postsynaptic neuron's response around $g_{CAN,r} = 2.25$ and for $g_{CAN,r} > 3$ the response is weaker than the input. The strange increase in amplitude around $g_{CAN,r} = 0.5$ appears to be an artifact of the averaging process. Panel II: Network architecture for this toy network. For the self-coupled neuron, $g_{CAN} = 4$ and $g_{NaP} = 2$, $E_L = -61.5$, while for the response neuron $g_{NaP,r} = 0.06$ and $E_{L,r} = -61.5$.

For GA(2) and GA(3), most neurons will not go into depolarization block, but their CAN current will activate when they receive sufficient synaptic input. Also, the CAN current in the average neuron is activated when a presynaptic CAN current is active. However, the CAN current can also be recruited by as few as one presynaptic tonically active neuron, even without that presynaptic neuron's CAN current being active. A tonically active neuron that is presynaptic to a neuron in another cluster, therefore, could activate that neuron's CAN current, regardless of the overall activity of the cluster to which the presynaptic neuron belongs. A quiescent neuron on the other hand sends a pure signal to other clusters since it will only be active when its cluster is active. Similarly, a quiescent neuron that is on the postsynaptic side of an intercluster connection accurately reports the activity of other clusters in the network. Thus, for synchronized cluster behavior, we would expect quiescent neurons to serve as the neurons with intercluster connections.

## 4.7 QUIESCENT NEURONS ARE MORE COMMON IN LATER GENERATIONS

When a new neuron is created (when the networks for the first generation are created, or when a cluster is replaced by a mutant cluster), it has a 25% chance to have intrinsic bursting dynamics, a 37.5% chance of being intrinsically quiescent and a 37.5% chance of being intrinsically tonic. However, in the 20 best networks from the GA(3), on average, 41% of neurons are intrinsically quiescent, see Figure 4.12. If the distribution of the intrinsic dynamics is approximated by a normal distribution, then this is a statistically significant skew towards intrinsically quiescent neurons; a t-test (the MATLAB function "ttest" was used) rejects the hypothesis that GA(3)'s neurons were drawn from a normal distribution with a mean of 37.5% of neurons are intrinsically quiescent ($p < 0.01$). Some of the best networks boast a makeup of more than 50% quiescent neurons, such as $GA_3^*$ (Figure 4.8).

Perhaps quiescent neurons become prominent due to the way input strength is handled in the simulations. In the absence of evidence to the contrary, we did not scale the strength of synaptic connections according to the number of those connections. If a neuron has a

high level of $g_{CAN}$, numerous tonic inputs can hold the neuron in depolarization block. Any neuron pinned in depolarization block will reduce the amplitude of the population activity, because the voltage in depolarization block is below the synaptic threshold. Being pinned in depolarization block also prevents the neuron from responding to bursting input. In particular, if the pinned neuron has an intercluster connection, this behavior can cause the loss of burst regularity across the network. However, the average level of $g_{CAN}$ is low, so most neurons cannot be pinned in depolarization block.

Quiescent neurons are ideal for relaying signals; quiescent neurons only send synaptic output when they receive synaptic input. Indeed, with intermediate levels of $g_{CAN}$ they can increase the amplitude and duration of a burst, which can rekindle a weak burst input into a strong output, see Section 4.6. There is little cause for concern that the bursts will be eternally extended by quiescent neurons; any neuron with sufficiently high values of $g_{CAN}$ will almost immediately enter depolarization block upon receiving a sufficiently strong burst. This fast entry into depolarization block will result in the neuron's output being a very short, high amplitude, burst. Quiescent neurons endowed with this property can halt runaway activity without affecting the rest of the network first, and so send a short signal that is still an accurate reflection of the activity presynaptic to it.

In Section 4.6 we concluded that quiescent neurons are well suited to be the neurons with intercluster connections. In most networks of GA(3), there are more intrinsically quiescent neurons than any other type, so we would expect there to be more quiescent neurons with intercluster connections than other intrinsic dynamics. If GA(3) had increased numbers of quiescent neurons with intercluster connections, this may help explain why its clusters are well synchronized. In support of our analysis of the synchrony of clusters in GA(3), we do see that even though there are more intrinsically quiescent neurons in GA(3) than other kinds, there are disproportionately more intrinsically quiescent neurons serving as neurons with intercluster connections, see Figure 4.13.

On the other hand, intercluster connections are less important for networks from GA(2). Frequently, only a few clusters need to burst together to generate the bursting rhythm of the population. Therefore the property of pure communication that quiescent neurons have does not need to be emphasized in the network. Our analysis predicts that GA(2) should

not have a preference for intrinsically quiescent neurons, nor should intrinsically quiescent dynamics stand out for neurons with those rare intercluster connections. We display the makeup of the top twenty networks from GA(2) in Figure 4.14. The average number of intrinsic quiescent, bursting, and tonic dynamics are as expected from the initial distribution of neurons. Interestingly, there is a preference for intrinsically bursting dynamics for neurons with intercluster connections and intrinsically quiescent neurons are underrepresented in this role. Do these intrinsically bursting neurons play a special role in GA(2) that is not observed in GA(3)?

## 4.8 INTRINSICALLY BURSTING NEURONS MAY NOT IMPACT THE NETWORK DYNAMICS

Recall from Chapter 2 that we did not find a significant advantage to having intrinsically bursting neurons in a three cell network. Is their prominence in GA(2) merely chance? To test this, for every intrinsically bursting neuron in GA(2) or GA(3), we changed its intrinsic dynamics to quiescence by setting $g_{NaP,i} = 0.6$; $g_{CAN,i}$ was unchanged. We plot the effect of this change on the CV and amplitude scores in Figure 4.15. We note that for the most part, the relative changes are clustered around 0%, indicating that intrinsically bursting neurons are not playing a very strong role in these networks. Indeed, all of the top twenty networks in GA(3) continued to burst in the absence of intrinsically bursting neurons, while 16 of the top twenty networks in GA(2) burst; by way of example, see Figure 4.16. In the unified model in the absence of synaptic input, inactivation of the NaP current is required to return to the silent phase. Therefore, the NaP current is required for intrinsically bursting dynamics in the unified model. If intrinsically bursting neurons are not necessary for the network rhythm, perhaps the same can be said for the NaP current.

## 4.9 SIMULATED RILUZOLE

Applying Riluzole to the preBötC quickly results in the blockade of the NaP current [15]. In the preBötC, network bursting can persist in the presence of Riluzole, although the burst frequency and burst amplitude are reduced [15]. Recall from Chapter 3 that neurons modeled by the unified model have two mechanisms that can create bursts: the NaP current or the combination of the CAN current with the Na/K pump. The parameters in Chapter 3 were such that some level of $g_{NaP}$ was required to enter the active phase. When creating networks for the genetic algorithm, we introduced heterogeneity in $E_L$, which allows for some neurons to be intrinsically tonic even when the NaP current is blocked. $E_L$ is a natural parameter to vary, because it can be manipulated by changing $[K^+]_o$ in experimental settings[4]. Therefore, simulated blockade of the NaP current need not necessarily destroy the network bursting rhythm in all networks.

We simulated the blockade of NaP by first discarding a transient of 5 s, then allowing the network to be active for 5 seconds of simulated time. Over the next 5 seconds of simulated time, we linearly reduced the value of $g_{NaP,i}$ to 10% of its original value for all $i = 1 \dots N$. Finally, we recorded population activity for 10 more seconds of simulation time. By our definition of bursting, most networks failed to burst under these conditions. The effect of blocking the NaP current on the amplitude and CV scores of the top twenty of GA(2) and GA(3) is summarized in Figure 4.17.

From GA(3), only 5 out of the top twenty networks continued to burst when NaP is blocked, while GA(2) had 9 of its top twenty networks sustain bursting. $GA_3^*$ (Figure 4.8) stands out again as an interesting example from GA(3), see Figure 4.18. This is the ideal scenario; even though the algorithm doesn't detect the bursts because they never go above 25% of $p_{max}$, it is clear that both the burst amplitude and burst frequency are lowered, but the bursting rhythm endures. The cause for this behavior is clear: the brown, yellow and purple clusters relied on NaP drive to generate bursts, which then synchronized with the rest of the network. Most of the networks do not have this behavior, however. The networks that fail to burst generally have persistent activity that does not regularly fall below 20% of $p_{max}$, or highly irregular bursting with an amplitude that never exceeds 25% of $p_{max}$.

Networks that have population activity that never falls below 20% of $p_{max}$ seem to require the extra excitation from the NaP current to push some neurons into depolarization block to trigger the bursting cascade. Those networks that cannot regularly exceed 25% of $p_{max}$ were irregular to begin with, the loss of the NaP current prevents some clusters from having enough drive to burst. Such bursts previously were coincidental with other clusters' bursts, resulting in an increase through 25% of $p_{max}$, and without them, the network fails to burst.

The networks that manage to sustain bursting under blockade of NaP are ones whose activity look like the network in Figure 4.5. Recall from Chapter 3 that for intermediate values of $g_{CAN}$ we found that some neurons will not go into depolarization block, but will have an activated CAN current. For the self-coupled model neuron, when the CAN current was activated, we were able to observe tonically active solutions that were stable even when $g_{NaP} = 0$ (Figure 3.21 in Chapter 3). The recurrent excitation activates the CAN current for many of the neurons in some of the clusters, as is the case for the red cluster of Figure 4.5, and these neurons were not predisposed to enter depolarization block. These neurons no longer rely on the NaP current for excitation, so this behavior persists as $g_{NaP}$ is gradually reduced. In Figure 4.19 we see that the clusters that continue to burst did not require the NaP current to do so in the first place, though we do observe a reduction in frequency because, before being blocked, the NaP current hastened their entry into the active phase.

In light of this evidence, it is not surprising that GA(2) had more networks continue to burst in the presence of simulated Riluzole; we noted in Section 4.4 that some tonically active clusters mixed with a few bursting ones was a method that emerged from the genetic algorithm for optimizing the CV score. Blockade of the NaP current doesn't significantly impact this behavior, so for the most part, there is not a significant change in score, as reflected in Figure 4.17.

## 4.10 SIMULATED FLUFENAMIC ACID

Flufenamic acid (FFA) is a pharmacological agent that blocks the CAN current. However, excessive doses of FFA interfere with other neuronal properties, such as gap junctions. This

interference occurs at doses lower than those required to completely block the CAN current. In real preBötC networks, the rhythm persists under application of FFA, although its regularity and amplitude are altered. In this section, we simulate the incomplete blockade of the CAN current in the top twenty networks of both GA(2) and GA(3).

First we discard a transient of 5 seconds of simulation time, and then allow the network to proceed as normal for 5 more seconds. Then, across the next 5 s, we linearly reduce $g_{CAN,i}$ in all neurons to 25% of its original value. Finally, we recorded the population activity for the next 10 seconds. For the networks that continued bursting under this condition, we plot the relative change in the CV and amplitude score in Figure 4.20. Note that even though there are more networks bursting than in Section 4.9, the relative change in score is much higher in this case.

In Section 4.6 we discussed the importance of the depolarization block state for generating network bursts. We showed this by replacing virtually every neuron that was capable of entering depolarization block, with one of equivalent $g_{NaP}$ and $E_L$, but reduced $g_{CAN} = 2$. From that analysis, we might expect that the reduction of all $g_{CAN,i}$ to values below 1.25 would cause a cessation of bursting. This is mostly correct. However, in the presence of the simulated incomplete block of the CAN current, 8 networks from GA(3) and 9 networks from GA(2) maintained a bursting rhythm. Those networks that did not maintain bursts behave much like we expect from Section 4.6; with no way of entering depolarization block, the CAN current does not shut off, leading to persistent tonic activity as in Figure 4.21.

For the network to burst, the CAN current must be shutting off, but not through a depolarization block mechanism. The mechanism terminating the burst in networks such as the one in Figure 4.22 was described in Section 3.5.6 of Chapter 3. The CAN current remains active, and sodium slowly increases until the saddle-node bifurcation blows up and captures the trajectory of one of the neurons. This neuron will return to quiescence, which may cause a cascade and terminate the activity of the rest of the network, if the conditions are right; otherwise, there is a delay until another neuron's trajectory is captured by its saddle-node bifurcation. This mechanism occurs in some neurons in Figure 4.21, but such neurons do not trigger a cascade strong enough to quiet the population activity. This behavior was not noted in Section 4.6 because we set $g_{CAN} = 2$, where this behavior does not occur (see

Figure 3.6 in Chapter 3).

The bursts in this section and Section 4.9 are not particularly appealing and activation of the CAN current for durations as long as shown here is not necessarily biophysical. To correct this, the model needs to be extended, and this is the focus of the next section.

## 4.11 MODEL EXTENSION

So far, we have established that the CAN current is an important mechanism for generating the bursts we see in the top twenty networks of GA(2) and GA(3). However, some neurons in these networks, like those in the red cluster of Figure 4.5, have CAN current activation for the entirety of the simulation. This situation is probably not biophysical. The CAN current model we use in the unified model, and was originally used in the Rubin-Hayes model, works based on $IP_3$ mediated calcium-induced calcium- release. Over time, the $IP_3$ receptors on the ER may become desensitized [70]. Thus, if a neuron receives prolonged synaptic input that ignites the CAN current, eventually the CAN current activation should wear off when $IP_3$ receptors can no longer respond. This phenomenon was originally modeled by Toporikova et al [70], but their work focused on calcium oscillations as an intrinsic bursting mechanism. Here we introduce a new dynamic variable to the unified model, and while it is equivalent to the basic implementation in [70], it serves a very different function here.

For $i \in \{1, 2, ..., N\}$ the dynamics for model neuron $i$ are given by:

$$\dot{v_i} = -\{I_L(v_i, E_{L,i}) + I_{Na}(v_i, h_i, m_i) + I_{\mathrm{K}}(v_i, n_i) + I_{\mathrm{NaP}}(v_i, hp_i, g_{NaP,i}) + I_{\mathrm{CAN}}(v_i, Ca_i, g_{CAN,i}) + I_{pump}(Na_i) - I_{app} + \sum_{j=1}^{N} a_{j,i} I_{syn}(v_i, s_j)\}/C_m \tag{4.9}$$

$$\dot{h_i} = (h_\infty(v_i) - h_i)/\tau_h(v_i) \tag{4.10}$$

$$\dot{m_i} = (m_\infty(v_i) - m_i)/\tau_m(v_i) \tag{4.11}$$

$$\dot{n_i} = (n_\infty(v_i) - n_i)/\tau_n(v_i) \tag{4.12}$$

$$\dot{Ca_i} = \varepsilon_{Ca}(k_{IP_3}(1 - D)\sum_{j=1}^{N} a_{j,i} s_j - k_{Ca}(Ca_i - Ca_{base})) \tag{4.13}$$

$$\dot{Na_i} = \alpha(-I_{\mathrm{CAN}}(v_i, Ca_i, g_{CAN,i}) - I_{pump}(Na_i)) \tag{4.14}$$

$$\dot{hp_i} = \varepsilon_{hp}(h_{p,\infty}(v_i) - hp_i)/\tau_{hp}(v_i) \tag{4.15}$$

$$\dot{D_i} = \varepsilon_D(D_\infty(Ca_i) - D) \tag{4.16}$$

$$\dot{s_i} = ((1 - s_i)s_\infty(v_i) - k_s s_i)/\tau_s \tag{4.17}$$

with all functions as in Section 4.1, and $D_\infty(x) = 1/(1 + \exp((x - \theta_D)/\sigma_D))$, $\varepsilon_D = 0.001$, $\theta_D = 0.9$, and $\sigma_D = -0.0006$. $D_i$ is a dynamic variable with no units that represents the desensitization of the $IP_3$ receptors in the neuron. As $Ca_i$ in the cell increases, so too does $D_i$ until it shuts off the $IP_3$ term in equation (4.13), so that further synaptic activity will not increase intracellular calcium.

$D_i$ operates on a slow timescale, and therefore does not interfere with "normal" bursting patterns, like those seen in $GA_3^*$ (Figure 4.8), indeed, see Figure 4.23. A quantification of the effect of including dynamics for the desensitization of $IP_3$ can be found in Figure 4.24. With these new dynamics, 17 of the top twenty networks of GA(3), and 18 of the top twenty networks of GA(2), maintained a bursting rhythm.

We note that adding the desensitization dynamics improves the quality of bursts for the networks undergoing simulated partial blockade of the CAN current, see Figure 4.25. Indeed, for networks that were incapable of bursts during simulated blockade of the CAN current, adding $IP_3$ desensitization can recover a bursting rhythm, see Figure 4.26. In every network

of the top twenty networks from GA(2) and GA(3), adding the desensitization dynamics recovered a bursting rhythm during simulated partial blockade of the CAN current.

## 4.12 DISCUSSION

In this chapter, we consider large scale simulations of the unified model from Chapter 3. Many works consider all-to-all connectivity architectures [5, 46, 62, 33], but this is not necessarily an appropriate approximation for the preBötC network topology [25]. Introducing heterogeneity in the network architecture is sure to give rise to complications in analysis [66], and has been recently studied in model preBötC networks [24]. In fact, in their recent study, Gaiteri and Rubin demonstrated that the architecture inspired by the data, they call it the "Hartelt" architecture, yielded irregular bursting and high numbers of neurons out of sync with the global rhythm, especially when compared against other well studied architectures, such as the small-world network[24, 25]. That study did not consider the CAN current, which is known to be important for rhythmicity in the preBötC [7, 37, 42, 43]. Even if the architecture is suboptimal for synchronous bursting across the preBötC, we continue to breathe in the face of this handicap; this inspires further study of the "Hartelt" architecture.

Out of the gate, we encountered a hurdle: only 12.5% of randomly generated networks that adhere to the data generate synchronous bursts. On the other hand, heterogeneous, data based networks that burst synchronously are easy to engineer. Such networks seem unrealistic, so we need to seek out less obvious design principles that will promote network bursting. To illuminate some of these design principles, we developed a genetic algorithm to search for families of networks that have strong bursting patterns. An important feature of the genetic algorithm is that every network it creates adheres to the data, so that we can be confident that the networks we find are biologically sound. As we search through networks, we score them based on two criteria: a CV score that measures the regularity of the shape of the burst, and the amplitude score which rewards synchrony and penalizes too much activity during the silent phase. These scores were kept separate, a network was chosen for mating if it excelled in either one.

The analysis of the networks found through the genetic algorithm were divided into two classes, which we called GA(2) and GA(3). Inspired by private communication with Mironov, we initially required the genetic algorithm to establish precisely two intercluster connections per cluster. The 11th and final generation of this network was called GA(2). We found that GA(2) was split between two classes of networks. Some networks optimized the CV score by having some clusters be fully tonic, and then synchronizing the bursting of the remaining clusters. Other networks did not have any tonic clusters, instead, all clusters were bursting, but the long path length between clusters interfered with synchrony. Nevertheless, occasionally the bursts overlapped, which drove the amplitude up, and the low activity during the silent phase helped the amplitude score, but the CV score was penalized because of the irregular bursting.

To create GA(3), we increased the number of allowed intercluster connections per cluster to 3, and in simulated 11 generations of the genetic algorithm. The networks in GA(3) were significantly better than those in GA(2). A viable strategy for optimizing the CV score for GA(3) was to contain tonically active clusters with a few bursting clusters. The networks that achieved optimal amplitude scores were capable of having every cluster burst synchronously. These bursts were possible due to the reduced path lengths between clusters for GA(3) relative to GA(2). Indeed, no networks of this quality were found in GA(2). With these superior networks in hand, we described some of their interesting underlying mechanisms.

We showed that intercluster connections were much more important in GA(3) than in GA(2). We also discussed how intrinsically quiescent dynamics are optimal for neurons that have intercluster connections. The reasoning for this was that intrinsically quiescent neurons "only speak when spoken to," and as such, send a less noisy signal than an intrinsically tonic or intrinsically bursting neuron. The importance of intrinsically quiescent neurons for synchronization was highlighted by their elevated presence in GA(3). Indeed, in GA(3) for a neuron with an intercluster connection, it was more likely than pure chance that the neuron would have intrinsically quiescent dynamics. On the other hand, intrinsically quiescent neurons were not more prominent in GA(2), and intrinsically bursting neurons served as neurons with intercluster connections. However, when we replaced all of the intrinsically

bursting neurons in GA(2) and GA(3) with intrinsically quiescent neurons (keeping $g_{CAN}$ unchanged), we saw little effect on most of the networks; in fact, every network in GA(3) continued to burst, and only 4 networks from GA(2) failed to burst.

This led us to question the role of the NaP current in the network, because intrinsically bursting neurons rely on the NaP current. When we blocked the NaP current, we found that, in most cases, it was actually providing important excitation to the rest of the network that allowed the CAN current to generate DB bursts.

This is reinforced by our study on the distribution of $g_{CAN}$ across the networks. We found the average of $g_{CAN}$ in GA(2) and GA(3) was significantly different than the average at the onset of the search. This was interesting, because the average $g_{CAN} = 2$, occurring in generation 11, provides a strong burst in response to a bursting input; we argued that this was important for intercluster communication, as it could rekindle a weaker burst into a strong one. However, some population of neurons still had $g_{CAN} > 3$, which can actually dampen the response of a burst. Those neurons ended up being crucial to the activity in the network; when we lowered $g_{CAN}$ in those neurons so that they could not go into depolarization block, the rhythm was destroyed. On the other hand, neurons that are incapable of depolarization block were also important, as increasing their value of $g_{CAN}$ also destroyed the rhythm. This suggested that a mechanism for synchronization lies in distributing the strength of the CAN current across the network.

We also simulated the blockade of the CAN current and found that the rhythm need not dissolve. To simulate the experiments more closely, we only partially blocked the CAN current by reducing its strength in each cell to 25% of the initial strength. This allowed some neurons to fall into Region V behavior as described in Chapter 3, and in some cases, these neurons could drive the rhythm. On the other hand, the prolonged activation of the CAN current may not be biophysically relevant.

To halt prolonged CAN current activation, we presented an extension of the model to include desensitization of the $IP_3$ receptors that enable calcium-induced calcium release. This has been modeled by Toporikova et al., but their model focuses on intrinsic calcium oscillations, rather than the group pacemaker mechanism developed in the Rubin-Hayes and unified models [70, 56]. We found that our implementation of the desensitization phenomenon

did not significantly interfere with the normal bursting mechanisms in many networks of GA(2) and GA(3), but allowed these networks to more graciously endure blockade of the NaP current or partial blockade of the CAN current.

Ultimately, we identified three major mechanisms underlying the networks that we found to have the best synchronous bursting behavior. The first one is that short path lengths between clusters promote synchronous behavior, this was also shown in recent work by Gaiteri and Rubin[24]. Another mechanism is that intrinsically quiescent neurons promote synchronous bursts, which was also the one of the results of Chapter 2. We concluded that the strength of the CAN current needs to be heterogeneous across the network. Additionally, the mean strength of the CAN current should sit at a level that amplifies synaptic input, if that input is strong enough to invoke the CAN current. Interestingly, the persistent sodium current interacts with the CAN current to help sustain network bursting, and control frequency, as was discussed in Chapter 3. Finally, reminiscent of Chapter 2, we found no significant advantage to having intrinsically bursting neurons within the network.

There are many ways to extend this work. One important direction is to study the architecture of the networks from GA(2) and GA(3). Specifically, what are the connectivity structures within clusters that yield good performance? We approached this problem through a variety of graph theoretic tools. For instance, in graph theory, a motif is a collection of three nodes together with the edges linking them [36]. In this study, neurons were not allowed to be reciprocally coupled, or self-coupled, which greatly reduced the variety of motifs to 5 basic types: convergence (2 nodes output the same node), divergence (one node outputs to two nodes), loop (each node outputs to exactly one other node), asymmetric (two nodes have two outputs each, one has two inputs), or chain (one node has exactly one output and one output, no connections between the other two nodes). We predicted that clusters containing many loops would promote bursting, due to the recurrent excitation available to the system. On the other hand, for large networks, chains represent correlated input and output degrees for the nodes, which can lead to a feed-forward structure. Such structures have been shown to have synchronizing effects [17]. We were unable to use any of these features to distinguish good clusters from poorly performing ones. Nevertheless, there may be second order statistics for these structures, or other ways to analyze them that we have

not yet found, that will help identify what architectures promote burst synchrony in clusters.

We can also build on our findings for the roles of intrinsically quiescent neurons. Confident that intrinsically bursting neurons can be downplayed somewhat, we could increase the initial number of intrinsically quiescent neurons. Would later generations become further skewed in their distribution of intrinsic dynamics? A systematic approach could be used to generate testable hypotheses about the distribution of intrinsic dynamics in the preBötC. Another approach is to focus on the role of intrinsically quiescent neurons within the networks. We found that intrinsically quiescent dynamics are preferred for neurons with intercluster connections. This could be pushed one step further by creating new networks that have only intrinsically quiescent dynamics for such neurons. We predict that this would improve network performance, or perhaps allow for better networks to evolve.

In the absence of evidence to the contrary, we did not scale the synaptic conductance strength based on the number of connections. This lack of normalization means that intercluster connections affect the postsynaptic neuron as strongly as the other neurons in its cluster, which aids the synchronization of the two clusters. What networks would emerge when the genetic algorithm allows for randomization of the strengths of the connections of the architecture could be considered in future work.

We made two assumptions when defining the rules to create both new clusters and new networks. Altering these assumptions may lead to very different networks. The first assumption was utilized when creating new clusters; whenever possible, we connect the neuron with the least number of remaining open connections to the neuron with the greatest number of remaining open connections. This assumption ensures connectedness of the cluster. It also means that there will be a short path length from any node to a node with an intercluster connection, before directionality is considered. An alternate method is to arrange the neurons within a ring; this is similar to the organization of clusters within the network. This also ensures connectivity within the cluster, but it remains to be seen if such a paradigm will improve the networks found within the genetic algorithm. The second assumption that we made was that we were to focus on the role of clusters as the functional unit of the network. In doing so, we ignored the population of neurons that exist without clusters [25]. Such neurons almost never connect to each other, and so must connect to clusters. Therefore,

these neurons decrease the number of intercluster connections, an already precious resource. There is another explanation, however. Perhaps these neurons without clusters are only rendered as such by the experimental methods used to gather the data. We predict that such neurons were actually within a cluster that is lost in the experimental preparation. This viewpoint may support our claim that more intercluster connections are needed significantly promote synchrony; perhaps these connections are there, just misinterpreted by the experimental method.

Improvements can be made upon the genetic algorithm for future work. Initially thresholds of 25% of $p_{max}$ and 20% of $p_{max}$ are required to produce useful initial generations. On the other hand, we'd like to penalize sustained activity above 5% of $p_{max}$ in later generations. Thus, an evolving bursting scale could be deployed; each generation could face stricter definitions of bursting than its forebears. We could also find other ways to combine the scores, or more strictly penalize activity that is out of phase with the burst. In particular, gathering CV information on just 3 bursts may not give an accurate representation of the regularity of the rhythm. Therefore, we could also require more bursts during the 15 second window before assigning CV and amplitude scores. Another valid direction is to consider the $IP_3$ desensitization mechanics of Section 4.11 from the first generation of the genetic algorithm. Gap junctions could also be added to the unified model, as such connections may promote intercluster synchronization [61]. Alternate scoring methods to determine what networks are best can also be developed; for instance, a network that responds well to frequency modulation by a tonic drive is much preferable.

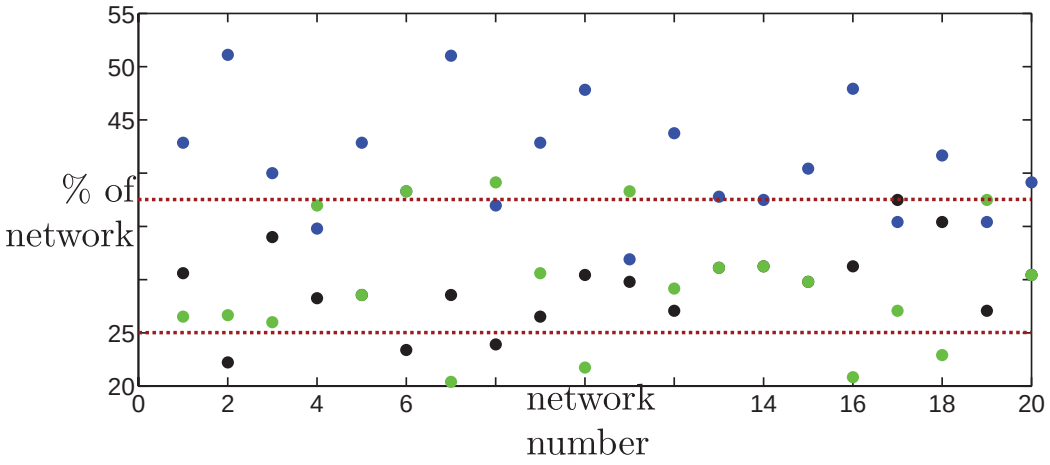


Figure 4.12: Distribution of intrinsic dynamics in GA(3). Blue dots correspond to the percentage of the network's neurons that are intrinsically quiescent. Black dots correspond to the percentage of neurons that are intrinsically tonic. Green dots correspond to intrinsically bursting neurons. Red dashed lines correspond to 25% and 37.5%.

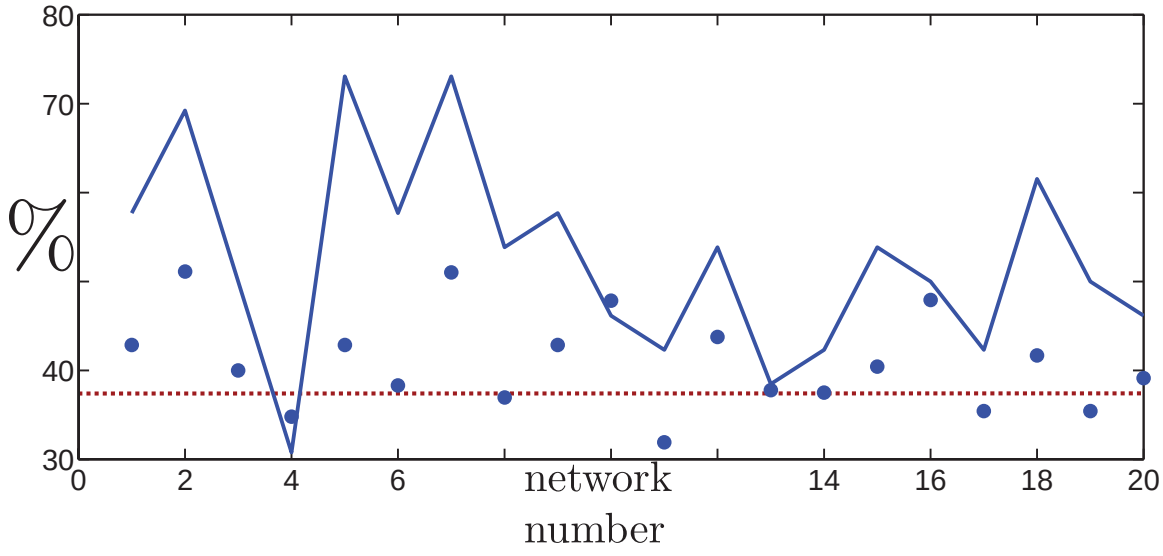


Figure 4.13: Distribution of intrinsic dynamics in GA(3) across the network, and across neurons that have intercluster connections. The blue dots represent the percentage of neurons in the entire network that have intrinsically quiescent dynamics. The blue line shows the percentage of the subset of neurons with intercluster connections that have intrinsically quiescent dynamics. Red dashed lines correspond to 25% and 37.5%. Notice that for most networks in GA(3), the neurons with intercluster connections are more likely to be intrinsically quiescent than would be expected from the makeup of the network.

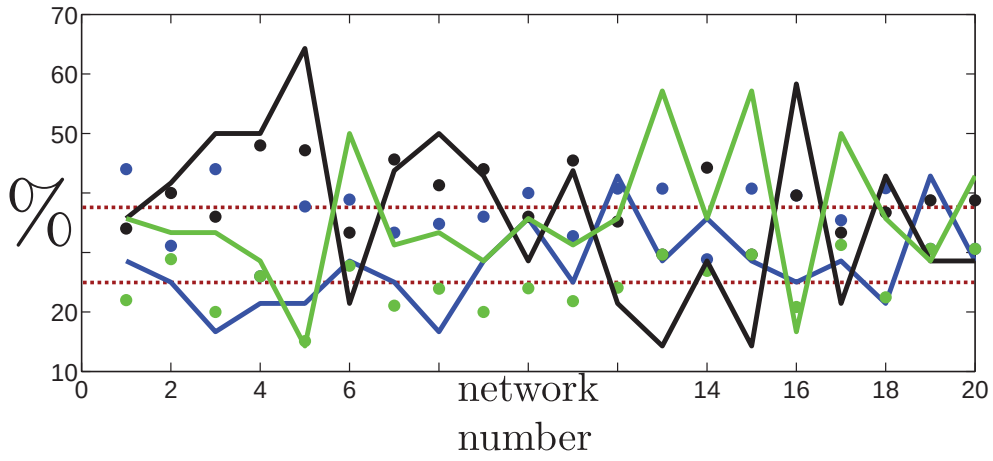


Figure 4.14: Distribution of intrinsic dynamics in GA(2) across the network, and across neurons that have intercluster connections. The blue dots represent the percentage of neurons in the entire network that have intrinsically quiescent dynamics. The blue line shows the percentage of the subset of neurons with intercluster connections that have intrinsically quiescent dynamics. Green dots correspond to the proportion of intrinsically bursting dynamics in the network, and the green line represents the percentage of neurons with intercluster connections that also have intrinsically bursting dynamics. Similarly, black dots are for tonic neurons in the network, and the black line is the percentage of neurons with intercluster connections that are intrinsically tonic. Red dashed lines correspond to 25% and 37.5%. A striking difference from GA(3) is that intrinsically quiescent dynamics is underrepresented and intrinsically bursting dynamics is overrepresented when it comes to neurons with intercluster connections.

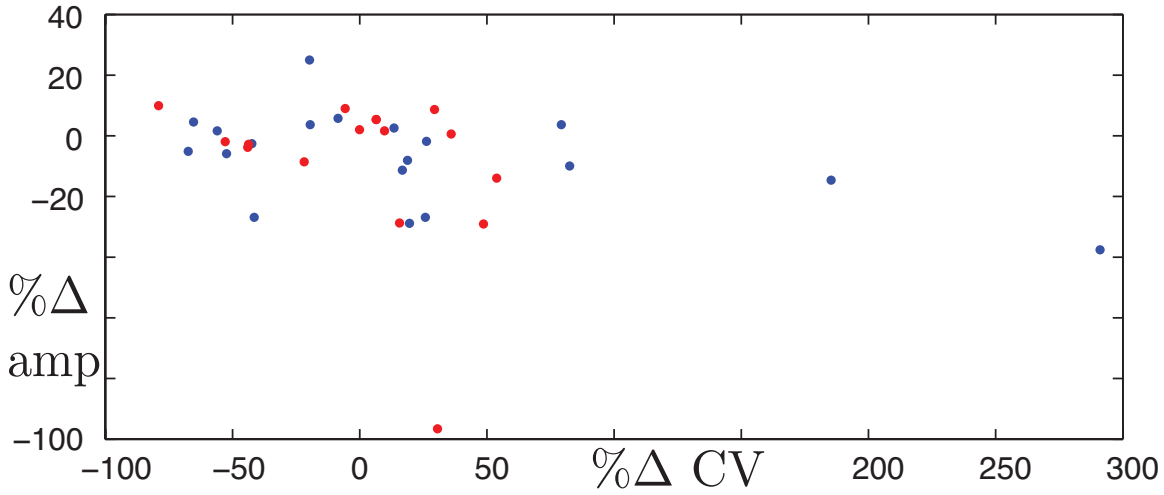


Figure 4.15: Relative change for the scores of the top twenty networks from GA(2) and GA(3) when intrinsically bursting neurons were replaced with intrinsically quiescent neurons. Blue dots correspond to GA(3), and red dots correspond to GA(2). For each neuron, the value of $g_{CAN}$ was not changed. Notice that although a few scores were significantly changed, most of the new scores are clustered around a 0% change. Impressively, for the top twenty networks in GA(3), every network continued to burst despite this drastic change in dynamics. For GA(2), 16 of the top twenty networks continued to burst. This indicates that intrinsically bursting dynamics are not necessary for the bursting rhythm of the networks found through the genetic algorithm, even though they formed 25% of the initial neuronal population.

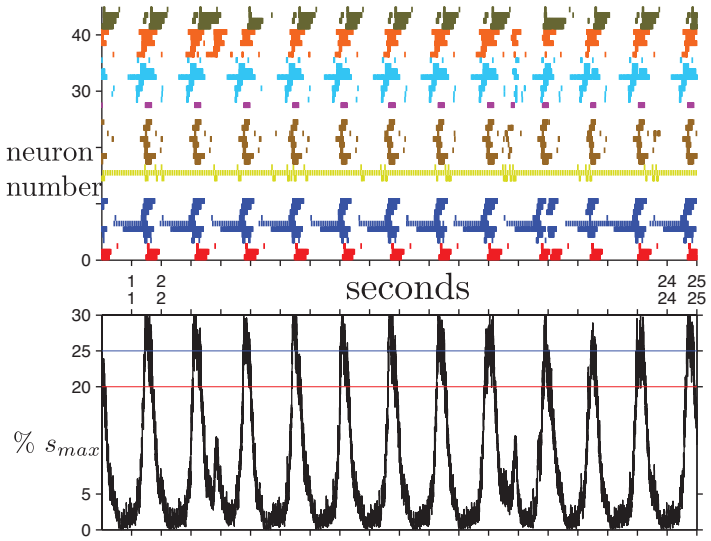


Figure 4.16: The same network as $GA_3^*$ (Figure 4.8), except every intrinsically bursting neuron has been replaced by a quiescent neuron. Notice that this does not change the rhythm very much; it looks like the burst frequency increased, but notice this simulation was longer than the one for $GA_3^*$.

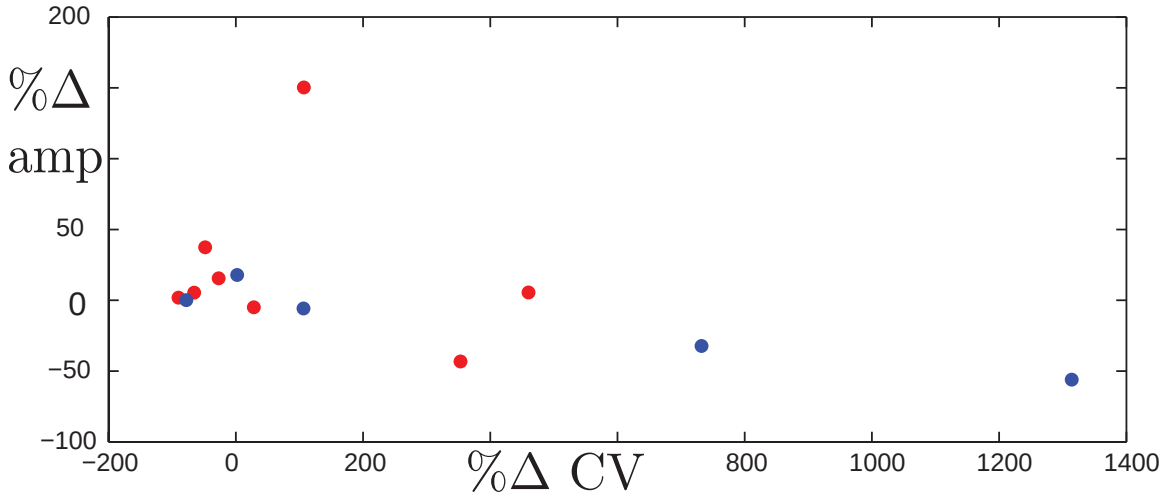


Figure 4.17: Result of the simulation of blocking the NaP current in the top twenty networks of GA(2) and GA(3). Only 5 networks from GA(3) continued to burst, the relative change of the amplitude and CV score is plotted as a blue dot. From GA(2), 9 networks continued to burst, their relative changes in scores are plotted in red. Notice that for the networks that continue to burst, the relative changes are mostly around 0% in both scores.

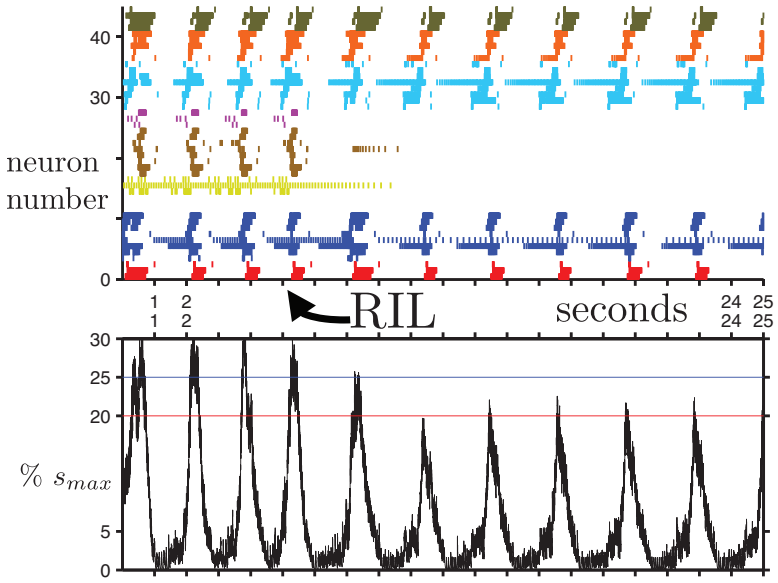


Figure 4.18: The same network as $GA_3^*$ (Figure 4.8), except we simulate the addition of Riluzole to the network to block the NaP current. Above is a raster plot, with colors corresponding to the clusters of panel II from Figure 4.8. At 5 seconds on the recorded time, we simulate blocking the NaP current by gradually reducing $g_{NaP,i}$ for all neurons to 10% of their original value. The brown, yellow, and purple clusters lose the drive that initiated their bursts, but the remaining clusters continue to burst, albeit with a lower frequency. Below is the population activity, and we observe a loss of amplitude and frequency for the network, which is seen in experimental data. [15]

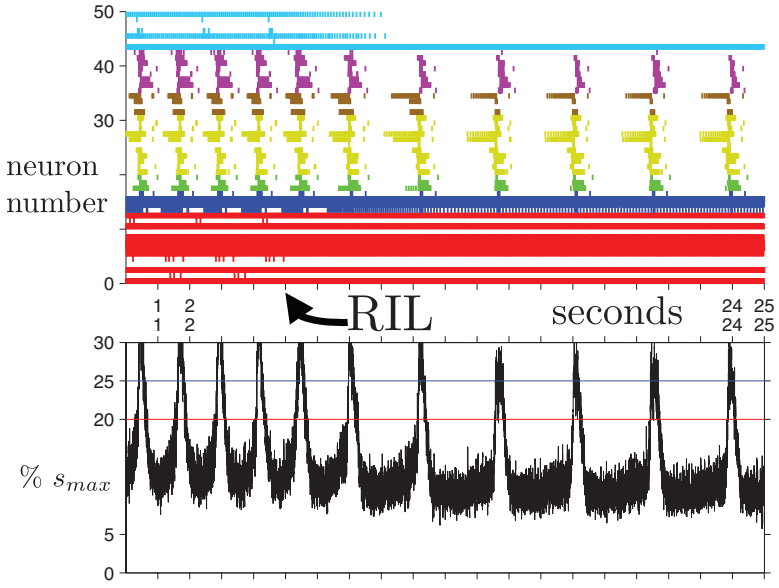


Figure 4.19: The same network as from Figure 4.5, except we simulate the addition of Riluzole to the network to block the NaP current. Above is a raster plot, with colors corresponding to the clusters of panel II from Figure 4.5. At 5 seconds on the recorded time, we simulate blocking the NaP current by gradually reducing $g_{NaP,i}$ for all neurons to 10% of their original value. Some neurons, like those in the light blue cluster stop spiking, but otherwise the activity is largely unchanged except for a slightly lower frequency. Below is the population activity, and we observe a slight loss of amplitude and frequency for the network, which is seen in experimental data. [15]

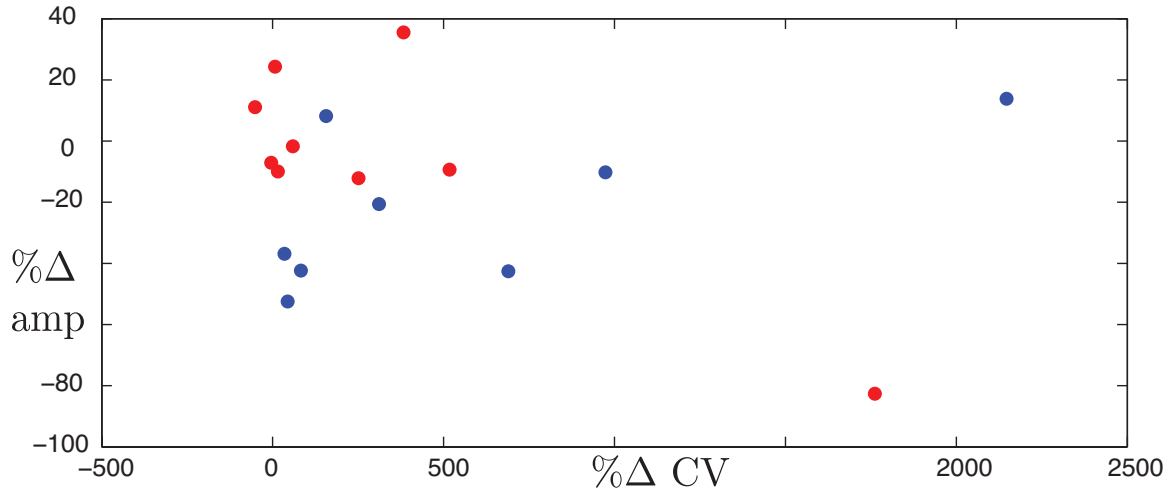


Figure 4.20: Relative change for the scores of the top twenty networks from GA(2) and GA(3) under incomplete blockade of the CAN current. From GA(3), 8 networks continued to burst, we have plotted the relative change in scores for these networks as blue dots. On the other hand, 9 networks from GA(2) continued to burst (red dots). In almost all cases, the relative changes were significant, indicating a significant reliance on the CAN current for bursting.

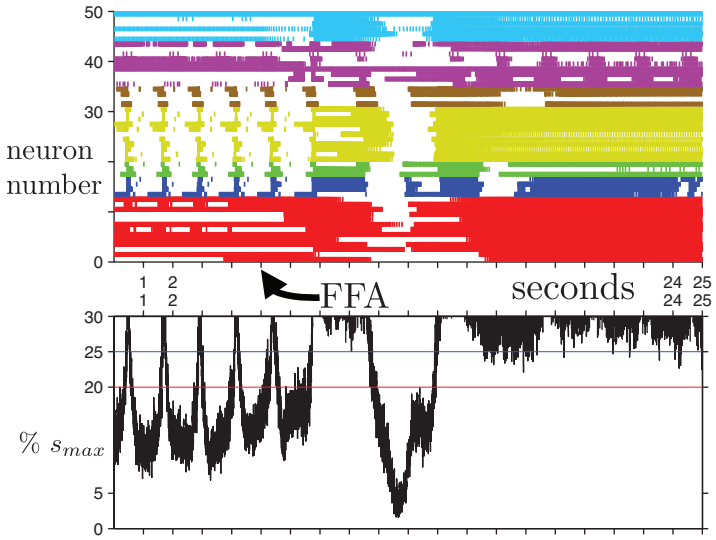


Figure 4.21: A typical result of the incomplete blockade of the CAN current in a top twenty network from GA(2) or GA(3). Once the CAN current is sufficiently weak, tonic activity dominates all clusters.

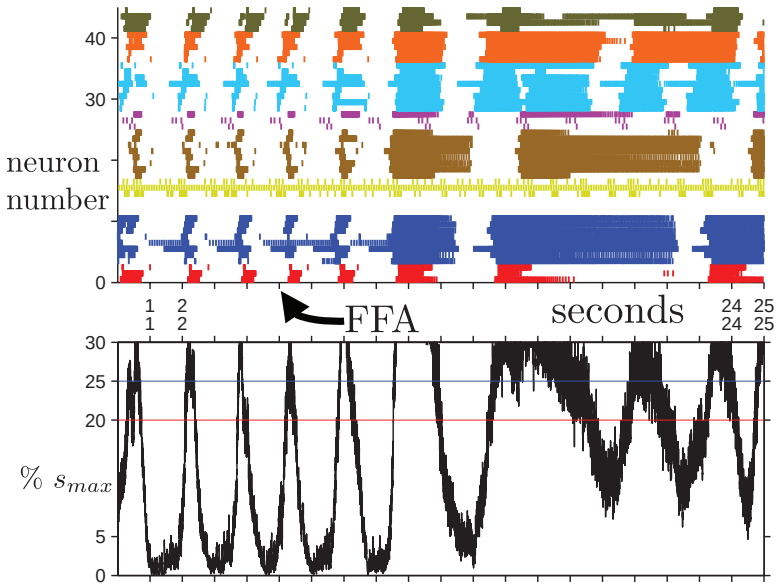


Figure 4.22: Some networks do burst when the CAN current is weakened. This network is the same as in $GA_3^*$ (Figure 4.8), but with the CAN current significantly weakened. The burst termination mechanism is the one described in Section 3.5.6 of Chapter 3.

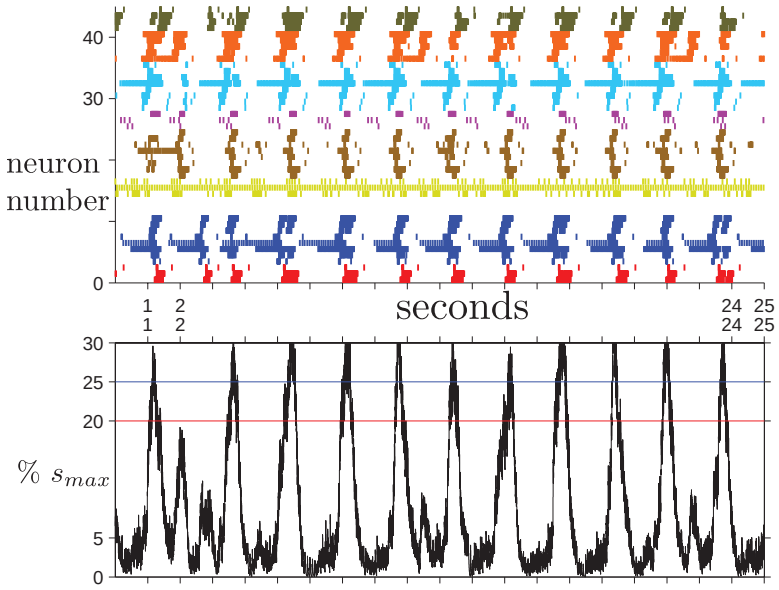


Figure 4.23: The same network as $GA_3^*$ (Figure 4.8), but now the dynamics are modeled instead by equations (4.9)–(4.17). Note that because $D_i$ evolves on a slow timescale and requires the CAN current to be active before taking effect, it does not have a large impact on the dynamics here.

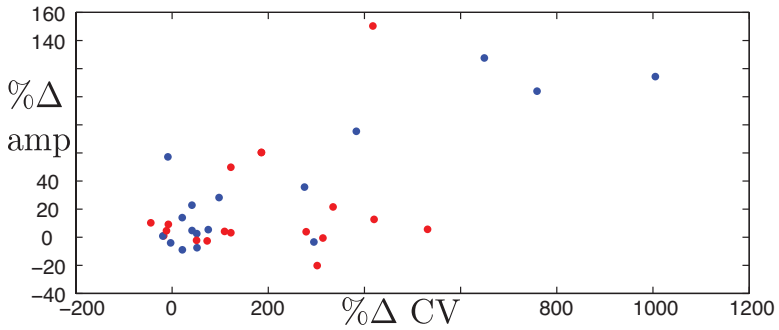


Figure 4.24: Relative change in CV and amplitude score when networks from GA(2) and GA(3) have dynamics for desensitization of $IP_3$. Blue dots correspond to the relative change in score for GA(3), and red dots correspond to GA(2). Notice that there is a large cluster around (0,0), indicating that the additional dynamics do not significantly effect these networks. Networks with large, tonically active clusters have their CV score changed significantly, because these clusters now burst, but at a different frequency than the rest of the network.

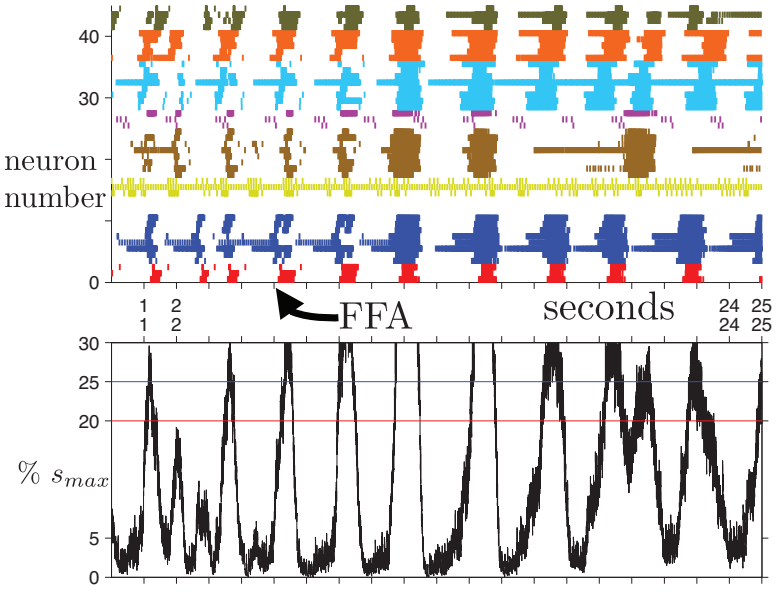


Figure 4.25: The same network as $GA_3^*$ (Figure 4.8), undergoing simulated partial blockade of the CAN current as in Figure 4.22, except now with model dynamics that include $IP_3$ desensitization. The runaway CAN current activity is halted by the $IP_3$ desensitization. Note the marked improvement of the synchrony of the bursts.

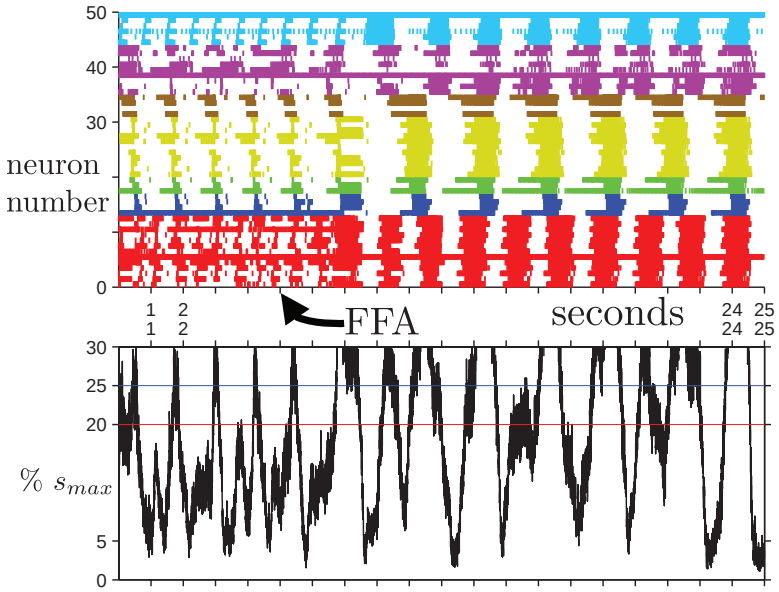


Figure 4.26: The same network undergoing blockade of the CAN current as in Figure 4.21, except now model dynamics include $IP_3$ desensitization. Notice the emergence of bursting due to the new dynamics, despite these harsh conditions.

# 5.0 DISCUSSION

In this dissertation, we provide insight regarding the emergence of network-wide, synchronous bursting within the preBötC. The study is spread across three chapters. Chapter 2 was inspired by the debate regarding heterogeneity in the preBötC. In it, we evaluated the roles of different intrinsic dynamics in small networks of three neurons. The bursting mechanism in Chapter 2 relies on inactivation of the NaP current. Another mechanism relevant to the preBötC was described in [56]; this mechanism involved the CAN current's activation through recurrent excitation. In Chapter 3 we systematically explore the interactions of the CAN and NaP currents. We detail how bursting can emerge from a reciprocally coupled pair of identical neurons. Finally, Chapter 4 extends the methodology of both preceding chapters. We study the effects of heterogeneity in networks of larger than two or three neurons. We found families of networks that sustain robust bursting rhythms by employing a genetic algorithm designed to create networks that adhere to known connectivity data for the preBötC.

There are three types of intrinsic dynamics that are well represented in the preBötC: quiescence, bursting, and tonic activity; however, only 5-15% of neurons in the preBötC are intrinsically bursting. Recently, the role of intrinsically bursting neurons has come into question [20]. We constructed three-neuron networks to analyze the roles of the various intrinsic dynamics. To represent the prevalence of intrinsically tonic and intrinsically quiescent neurons, every three-neuron network contained one of each. The third neuron could have any of the three types of intrinsic dynamics, which allowed us to compare the effects of each type of intrinsic dynamics on the rest of the network. We found that intrinsically bursting neurons did not offer any significant advantage for synchronous bursting in the three-cell network; in fact, due to their ability to return to the silent phase prematurely, they were

often detrimental to the activity of the network. When we studied a pair of reciprocally coupled neurons, we found that intrinsically bursting neurons were incapable of recruiting the postsynaptic CAN current. In our simulations of larger networks, 25% of the initial neurons were intrinsically bursting neurons. By overemphasizing their presence, we sought to find networks that relied on such behavior. Nevertheless, most networks we found through the genetic algorithm did not necessarily need their intrinsically bursting neurons. Indeed, 36/40 networks continued to exhibit synchronous, network-wide bursts when all intrinsically bursting dynamics were replaced with intrinsic quiescence. Ultimately, this study concludes that intrinsically bursting neurons may not significantly contribute to rhythmogenesis in the preBötC.

On the other hand, we have consistently shown that intrinsically quiescent neurons play a very important role in creating synchronous bursts across the preBötC. In our study of three-cell networks, we discovered that it is ideal to endow the third cell with intrinsically quiescent dynamics. The added quiescent neuron supported general bursting, but could also be selected to yield a broad frequency of bursting rhythms through input from a tonic source. Our work in studying the interaction of the CAN and NaP currents did not focus on intrinsically quiescent neurons, since the reciprocally coupled pair were identical. However, we noted that a quiescent neuron's CAN current will become active when the CAN current for a presynaptic neuron becomes active. In this way, intrinsically quiescent neurons can communicate a pure signal to the rest of the network. Thus, intrinsically quiescent neurons would be the best candidate for neurons with intercluster connections. The best networks in GA(3) have more intrinsically quiescent neurons than the other two types. Further, intrinsically quiescent dynamics occurred more frequently in neurons with intercluster connections than would have happened by chance. The abundance of intrinsically quiescent neurons was an evolved trait; for the networks used to initiate the search intrinsically quiescent neurons were approximately 37.5% of the population, but by the 11th generation, there was a statistically significant increase to 41%. In fact, some of the best networks had 50% or more of their neurons endowed with intrinsically quiescent dynamics. Of course, tonically active neurons are required to provide baseline excitability for the network. Further, the best networks of GA(2) and GA(3) relied on the NaP current for rhythmogenesis; the bursting activity was often destroyed

when $g_{NaP}$, the strength of the NaP current, was decreased in all cells. Intrinsically bursting neurons are not needed by the networks, but a distribution of intrinsically quiescent and tonic neurons are required for synchronous bursting. Perhaps the prevalence of intrinsically bursting neurons can be attributed to the fact that, in $g_{NaP}$ parameter space, intrinsic bursting dynamics lie between intrinsically tonic and intrinsically bursting dynamics.

The distribution of the strength of the CAN current, $g_{CAN}$, was modified by the genetic algorithm during the search. A statistically significant decrease of the mean value of $g_{CAN}$ from 2.5 to 2.0 occurred in the progress to the 11th generation. We found that heterogeneity was critical in this case; even though the average neuron was incapable of entering depolarization block (DB) for GA(2) and GA(3), the network rhythm failed if no neuron was capable of entering DB. On the other hand, neurons incapable of entering DB were also vital to the population's bursting activity. Such a distribution of $g_{CAN}$ may therefore be required for bursting in the preBötC.

Mathematically, this work primarily employed the techniques of geometric singular perturbation theory and bifurcation theory. Indeed, without this analysis we would very much be in the dark about the mechanisms underlying the bursting in the large networks. The analysis has been nontrivial. When we considered networks of three neurons, each neuron had an associated slow variable, but the interaction was restricted to the fast subsystem. This allowed us to consider the evolution of the trajectory in three separate phase planes that updated when the trajectory entered the active phase corresponding to any plane. On the other hand, when we studied the interactions of the CAN and NaP currents, the self-coupled neuron also had three slow variables but they could not be so easily separated. Indeed, it was through the interaction of these three slow variables that we were able to show how the subtle modulation of the surface of homoclinic points for the fast subsystem created alternating patterns of DB and square-wave bursts; this novel bursting pattern had been seen in data, but not in any prior model. Even though hope of analysis through geometric means was abandoned when we moved to larger networks, insights from the self-coupled case continued to light the way. The NaP current played a role in promoting DB bursting through the CAN current, as well as increasing the frequency of such bursts. This explained the loss of population bursting, or the slowing of the frequency of bursts when it remained, when

the NaP current was blocked. Bifurcation analysis from the self-coupled system, yielded regimes of bistability that also became very relevant when we blocked the NaP current. The slow-fast decomposition also yielded the interesting bursting regime, region V, which was characterized by the saddle-node bifurcation of the fast subsystem blowing up to capture the trajectory. The behavior of this mechanism became relevant when we partially blocked the CAN current; it was the cause of burst termination across the network. However, the timescale of these bursts require activation of the CAN current for a duration which may not be biophysically relevant. We took a step toward correcting this by adding $IP_3$ desensitization to the unified model in the form of another dynamic variable. This added a fourth slow variable to the unified model, the analysis of which is a very important future direction for this work. Finally, prior work has established methodology for quantifying the effects of spike asynchrony for two reciprocally coupled Butera model neurons [1]. The situation is more complicated in our work because each neuron has 3 (or 4!) slow variables, instead of two as was previously considered. Therefore, a nontrivial direction to pursue for future work is the analysis of the effects of spike asynchrony in the unified model.

Another important direction for mathematical work is in the analysis of the connectivity structures found through the genetic algorithm. We tried many different approaches to categorize the best networks from GA(2) and GA(3). In graph theory, three-node networks fall into one of many motifs, based on the connections between them. Initially, these seem like an ideal way to describe clusters; loops (not self-coupling) can represent recurrent excitation that is beneficial for CAN current activation, and chains (correlated input degree and output degree) correspond to a feed-forward structure that can boost synchronization [17]. We found no significant correlation between the distributions of the motifs and the performance of the cluster.

Directionality analysis is another potentially fruitful direction. Networks are more likely to synchronize when information flows in one direction [75]. Determining a direction in our networks was a difficult problem because of the abundance of potential feedback for each neuron. One must consider pairs of neurons, neither of which is postsynaptic, through any sequences of synapses, to the other. If, eventually, they share a postsynaptic neuron, the information they send could be competitive (one terminates the burst, so the other can

have no effect), or cooperative (both inputs are necessary to terminate the burst). What is the direction of such situations? What about pairs that have no interaction, such as neurons in separate clusters, both of which have no output to the rest of the network? In the face of these challenges, our characterizations of direction were too weak to distinguish well-performing networks from GA(3) with poor performing networks from GA(2).

Of biological importance and mathematical interest is the study of the effects of noise on the preBötC. The study of noise in this system ultimately leads to stochastic switching times between the silent and active phases. Noise can be incorporated into the model in a variety of ways, including the membrane potential and synaptic transmission rate. Are the networks from GA(2) and GA(3) robust to noise? Noise could also provide a stochastic method for terminating bursts, which may actually improve the population bursting of some networks during the simulated application of Riluzole or FFA.

Also of importance is frequency modulation of the preBötC by an outside source. The preBötC is surrounded by a ring of other neuronal networks, many of which provide inhibition to the preBötC during normal respiration. Such networks have been studied in the absence of the CAN current [63]. Given that both the CAN current and the heterogeneity in connectivity architecture play an extremely important role in this work, the larger network studies in [63] may need to be revisited.

## BIBLIOGRAPHY


[1] J. Best, A. Borisyuk, J. Rubin, D. Terman, and M. Wechselberger, *The dynamic range of bursting in a model respiratory pacemaker network*, SIAM Journal on Applied Dynamical Systems **4** (2005), no. 4, 1107–1139.

[2] A. Bose, N. Kopell, and D. Terman, *Almost-synchronous solutions for mutually coupled excitatory neurons*, Physica D: Nonlinear Phenomena **140** (2000), no. 1-2, 69–94.

[3] J. Brockhaus and K. Ballanyi, *Synaptic inhibition in the isolated respiratory network of neonatal rats*, European Journal of Neuroscience **10** (1998), no. 12, 3823–3839.

[4] R. Butera, J. Rinzel, and J.C. Smith, *Models of respiratory rhythm generation in the pre-Botzinger complex. I. Bursting pacemaker neurons*, Journal of neurophysiology **82** (1999), no. 1, 382–397.

[5] ———, *Models of respiratory rhythm generation in the pre-Botzinger complex. II. Populations of coupled pacemaker neurons*, Journal of neurophysiology **82** (1999), no. 1, 398–415.

[6] R. Butera, J. Rubin, D. Terman, and J. Smith, *Oscillatory bursting mechanisms in respiratory pacemaker neurons and networks*, Bursting: The Genesis of Rhythm in the Nervous System (S. Coombes and P.C. Bressloff, eds.), World Scientific, Singapore, 2006, pp. 303–346.

[7] E.A. Crowder, M.S. Saha, R.W. Pace, H. Zhang, G.D. Prestwich, and C.A. Del Negro, *Phosphatidylinositol 4, 5-bisphosphate regulates inspiratory burst activity in the neonatal mouse preBotzinger complex*, The Journal of Physiology **582** (2007), no. 3, 1047–1058.

[8] G. Csárdi and T. Nepusz, *The igraph software package for complex network research*, InterJournal Complex Systems **1695** (2006), no. 1695.

[9] S. Daun, J.E. Rubin, and I.A. Rybak, *Control of oscillation periods and phase durations in half-center central pattern generators: a comparative mechanistic analysis*, J. Comput. Neurosci. (2009).

[10] C.A. Del Negro, J.A. Hayes, and J.C. Rekling, *Dendritic Calcium Activity in Pre-Botzinger Complex Neurons in Neonatal Mice Studied In Vitro. (Submitted)*, (2010).

[11] _____, *Dendritic calcium activity precedes inspiratory bursts in preb "otzinger complex neurons*, The Journal of Neuroscience **31** (2011), no. 3, 1017.

[12] C.A. Del Negro, S.M. Johnson, R.J. Butera, and J.C. Smith, *Models of respiratory rhythm generation in the pre-Botzinger complex. III. Experimental tests of model predictions*, Journal of Neurophysiology **86** (2001), no. 1, 59–74.

[13] C.A. Del Negro, N. Koshiya, R.J. Butera Jr, and J.C. Smith, *Persistent sodium current, membrane properties and bursting behavior of pre-botzinger complex inspiratory neurons in vitro*, Journal of neurophysiology **88** (2002), no. 5, 2242–2250.

[14] C.A. Del Negro, C. Morgado-Valle, and J.L. Feldman, *Respiratory Rhythm:: An Emergent Network Property?*, Neuron **34** (2002), no. 5, 821–830.

[15] C.A. Del Negro, C. Morgado-Valle, J.A. Hayes, D.D. Mackay, R.W. Pace, E.A. Crowder, and J.L. Feldman, *Sodium and calcium current-mediated pacemaker neurons and respiratory rhythm generation*, Journal of Neuroscience **25** (2005), no. 2, 446–453.

[16] A. Dhooge, W. Govaerts, and Y.A. Kuznetsov, *MATCONT: a MATLAB package for numerical bifurcation analysis of ODEs*, ACM Transactions on Mathematical Software (TOMS) **29** (2003), no. 2, 164.

[17] B. Doiron, J. Rinzel, and A. Reyes, *Stochastic synchronization in finite size spiking networks*, Physical Review E **74** (2006), no. 3, 030903.

[18] A.V. Egorov, B.N. Hamam, E. Fransén, M.E. Hasselmo, and A.A. Alonso, *Graded persistent activity in entorhinal cortex neurons*, Nature **420** (2002), no. 6912, 173–178.

[19] G.B. Ermentrout, *Simulating, analyzing, and animating dynamical systems: a guide to XPPAUT for researchers and students*, Society for Industrial Mathematics, 2002.

[20] J.L. Feldman and C.A. Del Negro, *Looking for inspiration: new perspectives on respiratory rhythm*, Nature Reviews Neuroscience **7** (2006), no. 3, 232–241.

[21] J.L. Feldman and J.C. Smith, *Cellular mechanisms underlying modulation of breathing pattern in mammals*, Annals of the New York Academy of Sciences **563** (1989), no. Modulation of Defined Vertebrate Neural Circuits, 114–130.

[22] N. Fenichel, *Geometric singular perturbation theory for ordinary differential equations*, Journal of Differential Equations **31** (1979), no. 1, 53 – 98.

[23] E. Fransén, B. Tahvildari, A.V. Egorov, M.E. Hasselmo, and A.A. Alonso, *Mechanism of graded persistent cellular activity of entorhinal cortex layer v neurons*, Neuron **49** (2006), no. 5, 735–746.

[24] C. Gaiteri and J.E. Rubin, *The interaction of intrinsic dynamics and network topology in determining network burst synchrony*, Frontiers in computational neuroscience **5** (2011).

[25] N. Hartelt, E. Skorova, T. Manzke, M. Suhr, L. Mironova, S. K
"ugler, and SL Mironov, *Imaging of respiratory network topology in living brainstem slices*, Molecular and Cellular Neuroscience **37** (2008), no. 3, 425–431.

[26] A.C. Hindmarsh, P.N. Brown, K.E. Grant, S.L. Lee, R. Serban, D.E. Shumaker, and C.S. Woodward, *SUNDIALS: Suite of nonlinear and differential/algebraic equation solvers*, ACM Transactions on Mathematical Software (TOMS) **31** (2005), no. 3, 363–396.

[27] SM Johnson, JC Smith, GD Funk, and JL Feldman, *Pacemaker behavior of respiratory neurons in medullary slices from neonatal rat*, Journal of neurophysiology **72** (1994), no. 6, 2598–2608.

[28] C. Jones, *Geometric singular perturbation theory*, Dynamical systems (Montecatini Terme, 1994) **1609**, 44–118.

[29] J. Karbowski and G.B. Ermentrout, *Synchrony arising from a balanced synaptic plasticity in a network of heterogeneous neural oscillators*, Physical Review E **65** (2002), no. 3, 31902.

[30] RB Kellogg, TY Li, and J. Yorke, *A constructive proof of the Brouwer fixed-point theorem and computational results*, SIAM Journal on Numerical Analysis (1976), 473–483.

[31] H. Koizumi and J.C. Smith, *Persistent Na+ and K+-dominated leak currents contribute to respiratory rhythm generation in the pre-Botzinger complex in vitro*, Journal of Neuroscience **28** (2008), no. 7, 1773–1785.

[32] A.Y. Kolesov, E.F. Mishchenko, and N.K. Rozov, *Asymptotic methods of investigation of periodic solutions of nonlinear hyperbolic equations*, Trudy Matematicheskogo Instituta im. VA Steklova **222** (1998), 7–191.

[33] A. Lal, Y. Oku, S. H
"ulsmann, Y. Okada, F. Miwakeichi, S. Kawai, Y. Tamura, and M. Ishiguro, *Dual oscillator model of the respiratory neuronal network generating quantal slowing of respiratory rhythm*, Journal of computational neuroscience (2011), 1–16.

[34] R.H. Lee and C.J. Heckman, *Essential role of a fast persistent inward current in action potential initiation and control of rhythmic firing*, Journal of Neurophysiology **85** (2001), no. 1, 472–427.

[35] D. Liu and E.R. Liman, *Intracellular Ca2+ and the phospholipid PIP2 regulate the taste transduction ion channel TRPM5*, Proceedings of the National Academy of Sciences of the United States of America **100** (2003), no. 25, 15160–15165.

[36] R. Milo, S. Shen-Orr, S. Itzkovitz, N. Kashtan, D. Chklovskii, and U. Alon, *Network motifs: simple building blocks of complex networks*, Science **298** (2002), no. 5594, 824.

[37] S.L. Mironov, *Metabotropic glutamate receptors activate dendritic calcium waves and TRPM channels which drive rhythmic respiratory patterns in mice*, The Journal of Physiology **586** (2008), no. 9, 2277–2291.

[38] C. Morgado-Valle, L. Beltran-Parrazal, M. DiFranco, J.L. Vergara, and J.L. Feldman, *Somatic Ca2+ transients do not contribute to inspiratory drive in preB "otzinger Complex neurons*, The Journal of Physiology **586** (2008), no. 18, 4531.

[39] W.H. Nesse, C.A. Del Negro, and P.C. Bressloff, *Oscillation Regularity in Noise-Driven Excitable Systems with Multi-Time-Scale Adaptation*, Physical Review Letters **101** (2008), no. 8.

[40] B. Nilius, F. Mahieu, J. Prenen, A. Janssens, G. Owsianik, R. Vennekens, and T. Voets, *The Ca2+-activated cation channel TRPM4 is regulated by phosphatidylinositol 4, 5-biphosphate*, The EMBO journal **25** (2006), no. 3, 467–478.

[41] R.W. Pace and C.A. Del Negro, *AMPA and metabotropic glutamate receptors cooperatively generate inspiratory-like depolarization in mouse respiratory neurons in vitro*, European Journal of Neuroscience **28** (2008), no. 12, 2434–2442.

[42] R.W. Pace, D.D. Mackay, J.L. Feldman, and C.A. Del Negro, *Inspiratory bursts in the preBotzinger complex depend on a calcium-activated non-specific cation current linked to glutamate receptors in neonatal mice*, The Journal of Physiology **582** (2007), no. 1, 113–125.

[43] ———, *Role of persistent sodium current in mouse preBotzinger complex neurons and respiratory rhythm generation*, The Journal of Physiology **580** (2007), no. 2, 485–496.

[44] J.F.R. Paton, A.P.L. Abdala, H. Koizumi, J.C. Smith, and W.M. St-John, *Respiratory rhythm generation during gasping depends on persistent sodium current*, Nature neuroscience **9** (2006), no. 3, 311–313.

[45] K. Ptak, G.G. Zummo, G.F. Alheid, T. Tkatch, D.J. Surmeier, and D.R. McCrimmon, *Sodium currents in medullary neurons isolated from the pre-Botzinger complex region*, Journal of Neuroscience **25** (2005), no. 21, 5159–5170.

[46] L. K. Purvis, J. C. Smith, H. Koizumi, and R. J. Butera, *Intrinsic Bursters Increase the Robustness of Rhythm Generation in an Excitatory Network*, J Neurophysiol **97** (2007), no. 2, 1515–1526.

[47] J.M. Ramirez, A.K. Tryba, and F. Pena, *Pacemaker neurons and neuronal networks: an integrative view*, Current opinion in neurobiology **14** (2004), no. 6, 665–674.

[48] J. Ren and J.J. Greer, *Modulation of respiratory rhythmogenesis by chloride-mediated conductances during the perinatal period*, Journal of Neuroscience **26** (2006), no. 14, 3721–3730.

[49] J. Rinzel, *A formal classification of bursting mechanisms in excitable systems*, Proceedings of the International Congress of Mathematicians, 1987, pp. 1578–1593.

[50] P. Rowat and A. Selverston, *Synchronous bursting can arise from mutual excitation, even when individual cells are not endogenous bursters*, J. Comput. Neurosci. **4** (1997), 129–139.

[51] J. Rubin and K. Josic, *The firing of an excitable neuron in the presence of stochastic trains of strong synaptic inputs*, Neural computation **19** (2007), no. 5, 1251–1294.

[52] J. Rubin, N. Shevtsova, B. Ermentrout, J. Smith, and I. Rybak, *Multiple rhythmic states in a model of the respiratory cpg*, J. Neurophysiol. **101** (2009), 2146–2165.

[53] J. Rubin and D. Terman, *Geometric singular perturbation analysis of neuronal dynamics, in Handbook of Dynamical Systems*, Elsevier Science **2** (2002), 93–146.

[54] ———, *Synchronized activity and loss of synchrony among heterogeneous conditional oscillators*, SIAM Journal on Applied Dynamical Systems **1** (2002), no. 1, 146–174.

[55] J. E. Rubin, *Bursting induced by excitatory synaptic coupling in nonidentical conditional relaxation oscillators or square-wave bursters*, Physical Review E (Statistical, Nonlinear, and Soft Matter Physics) **74** (2006), no. 2, 021917.

[56] J. E. Rubin, J. Hayes, J. Mendenhall, and C. Del Negro, *Calcium-activated nonspecific cation current and synaptic depression promote network-dependent burst oscillations*, Proceedings of the National Academy of Sciences **106** (2009), no. 8, 2939–2944.

[57] I.A. Rybak, A.P.L. Abdala, S.N. Markin, J.F.R. Paton, and J.C. Smith, *Spatial organization and state-dependent mechanisms for respiratory rhythm and pattern generation*, Progress in brain research **165** (2007), 201–220.

[58] I.A. Rybak, N.A. Shevtsova, K. Ptak, and D.R. McCrimmon, *Intrinsic bursting activity in the pre-Botzinger complex: role of persistent sodium and potassium currents*, Biological cybernetics **90** (2004), no. 1, 59–74.

[59] I.A. Rybak, N.A. Shevtsova, W.M. St-John, J.F.R. Paton, and O. Pierrefiche, *Endogenous rhythm generation in the pre-Botzinger complex and ionic currents: modelling and in vitro studies*, European Journal of Neuroscience **18** (2003), no. 2, 239–257.

[60] XM Shao and JL Feldman, *Respiratory rhythm generation and inhibition of expiratory neurons in pre-Botzinger complex: differential roles of glycinergic and GABAergic neuronal transmission*, J Neurophysiol **77** (1997), 1853–1860.

[61] A. Sherman and J. Rinzel, *Model for synchronization of pancreatic beta-cells by gap junction coupling*, Biophysical journal **59** (1991), no. 3, 547–559.

[62] NA Shevtsova, K. Ptak, DR McCrimmon, and IA Rybak, *Computational modeling of bursting pacemaker neurons in the pre-b
"otzinger complex*, Neurocomputing **52** (2003), 933–942.

[63] J.C. Smith, A.P.L. Abdala, H. Koizumi, I.A. Rybak, and J.F.R. Paton, *Spatial and functional architecture of the mammalian brainstem respiratory network: a hierarchy of three oscillatory mechanisms*, J. Neurophysiol. **98** (2007), 3370–3387.

[64] JC Smith, HH Ellenberger, K. Ballanyi, DW Richter, and JL Feldman, *Pre-Botzinger complex: a brainstem region that may generate respiratory rhythm in mammals*, Science **254** (1991), no. 5032, 726.

[65] D. Somers and N. Kopell, *Rapid synchronization through fast threshold modulation*, Biological Cybernetics **68** (1993), no. 5, 393–407.

[66] S.H. Strogatz, *Exploring complex networks*, Nature **410** (2001), no. 6825, 268–276.

[67] S. Tazerart, J.C. Viemari, P. Darbon, L. Vinay, and F. Brocard, *Contribution of persistent sodium current to locomotor pattern generation in neonatal rats*, Journal of neurophysiology **98** (2007), no. 2, 613–628.

[68] S. Tazerart, L. Vinay, and F. Brocard, *The persistent sodium current generates pacemaker activities in the central pattern generator for locomotion and regulates the locomotor rhythm*, Journal of Neuroscience **28** (2008), no. 34, 8577–8589.

[69] D. Terman, N. Kopell, and A. Bose, *Dynamics of two mutually coupled slow inhibitory neurons*, Physica D: Nonlinear Phenomena **117** (1998), no. 1-4, 241–275.

[70] Natalia Toporikova and Robert Butera, *Two types of independent bursting mechanisms in inspiratory neurons: an integrative model*, Journal of Computational Neuroscience (2010), 1–14, 10.1007/s10827-010-0274-z.

[71] N. Travinin Bliss and J. Kepner, *'pmatlab parallel matlab library'*, International Journal of High Performance Computing Applications **21** (2007), no. 3, 336.

[72] K. Tsuruyama, H. Chie-Fang, V. Nguyen, and S. Chandler, *Intracellular calcium signaling modulates rhythmical burst activity in rat trigeminal principal sensory neurons*, Society for Neuroscience abstract (2008).

[73] J.A. White, C.C. Chow, J. Rit, C. Soto-Trevino, and N. Kopell, *Synchronization and oscillatory dynamics in heterogeneous, mutually inhibited neurons*, Journal of Computational Neuroscience **5** (1998), no. 1, 5–16.

[74] N. Wu, A. Enomoto, S. Tanaka, C.F. Hsiao, D.Q. Nykamp, E. Izhikevich, and S.H. Chandler, *Persistent sodium currents in mesencephalic v neurons participate in burst generation and control of membrane excitability*, Journal of neurophysiology **93** (2005), no. 5, 2710–2722.

[75] An Zeng, Seung-Woo Son, Chi Ho Yeung, Ying Fan, and Zengru Di, *Enhancing synchronization by directionality in complex networks*, Phys. Rev. E **83** (2011), no. 4, 045101.

[76] G. Zhong, M.A. Masino, and R.M. Harris-Warrick, *Persistent sodium currents participate in fictive locomotion generation in neonatal mouse spinal cord*, Journal of Neuroscience **27** (2007), no. 17, 4507–4518.